Collective Dynamics of Large-Scale Spiking Neural Networks by Mean-Field Theory

by

Liang Chen

A thesis
presented to the University of Waterloo
in fulfillment of the
thesis requirement for the degree of
Doctor of Philosophy
in
Applied Mathematics

Waterloo, Ontario, Canada, 2024

Examining Committee Membership

The following served on the Examining Committee for this thesis. The decision of the Examining Committee is by majority vote.

External Examiner: Stephen Coombes
Professor, School of Mathematical Sciences
University of Nottingham

Supervisor: Sue Ann Campbell
Professor, Department of Applied Mathematics
University of Waterloo

Internal Member: N Sri Namachchivaya
Professor, Department of AppliedMathematics
University of Waterloo

Marek Stastna
Professor, Department of AppliedMathematics
University of Waterloo

Internal-External Member: Jeff Orchard
Associate Professor
David R. Cheriton School of Computer Science
University of Waterloo

Author's Declaration

This thesis consists of material all of which I authored or co-authored: see Statement of Contributions included in the thesis. This is a true copy of the thesis, including any required final revisions, as accepted by my examiners.

I understand that my thesis may be made electronically available to the public.

Statement of Contributions

Liang Chen was the sole author of this thesis, although substantial portions of the content were adapted from collaborative publications and preprints.

Chapters 1, 2 and 6 were written by Liang Chen under the supervision of Prof. Sue Ann Campbell and were not written for publication.

Chapter 3 is based on published work in collaboration with Prof. Sue Ann Campbell.

- Liang Chen and Sue Ann Campbell. Exact mean-field models for spiking neural networks with adaptation. Journal of Computational Neuroscience, 50(5):445–469, 2022, `https://doi.org/10.1007/s10827-022-00825-9`.

Chapter 4 is a result of collaboration with Prof. Sue Ann Campbell. The manuscript has been accepted by the SIAM Journal on Applied Dynamical Systems.

- Liang Chen and Sue Ann Campbell. Synaptic delay induced macroscopic dynamics of the large-scale network of Izhikevich neurons, 2023, `http://arxiv.org/abs/2310.04596`.

Chapter 5 is based on unpublished work in collaboration with Prof. Sue Ann Campbell and Prof. Emily Stone (University of Montana).

Abstract

The brain contains a large number of neurons, each of which typically has thousands of synaptic connections. Its functionality, whether function or dysfunction, depends on the emergent collective dynamics arising from the coordination of these neurons. Rather than focusing on large-scale realistic simulations of individual neurons and their synaptic coupling to understand these macroscopic behaviors, we emphasize the development of mathematically manageable models in terms of macroscopic observable variables. This approach allows us to gain insight into the underlying mechanisms of collective dynamics from a dynamical systems perspective. It is the central idea of this thesis.

We analytically reduce large-scale neural networks to low-dimensional mean-field models that account for spike frequency adaptation, time delay between neuron communication, and short-term synaptic plasticity. These mean-field descriptions offer a precise correspondence between the microscopic dynamics of individual neurons and the macroscopic dynamics of the neural network, valid in the limit of infinitely many neurons in the network. Bifurcation analysis of the mean-field systems is capable of predicting network transitions between asynchronous and synchronous states, or different patterns of synchronization, such as slow-fast nested collective oscillations. We discuss how these dynamics are closely related to normal brain functions and neurological disorders. We also investigate the influence on these dynamic transitions induced by current heterogeneity, adaptation intensity, and delayed coupling. By integrating a kinetic model of synapses into the neural network, we describe calcium-dependent short-term synaptic plasticity in a relatively simple mathematical form. Through our mean-field modeling approach, we explore the impact of synaptic dynamics on collective behaviors, particularly the effect of muscarinic activation at inhibitory hippocampal synapses. Together, this thesis provides a tractable and reliable tool for model-based inference of neurological mechanisms from the perspective of theoretical neuroscience.

Acknowledgments

I wish to express my deepest gratitude to my supervisor, Prof. Sue Ann Campbell, who reignited my enthusiasm for research. I thank her for the countless meetings and conversations we have had over the years. Her guidance, wisdom, and patience have been indispensable in shaping my research and academic growth. Without her support, I would not have made it this far, and I am truly grateful.

I would also like to express my gratitude to my committee members, Prof. Stephen Coombes, Prof. Marek Stastna, Prof. N Sri Namachchivaya, and Prof. Jeff Orchard, in addition to my collaborators Prof. Wilten Nicola and Prof. Isam Al-Darabsah, for their valuable time, feedback and suggestions.

Furthermore, I am thankful to the instructors of the courses I took during my doctoral studies. Their insightful lectures and commitment to fostering a stimulating learning environment have greatly enriched my academic experience. I am especially thankful for Prof. Marek Stastna, Prof. Brian Ingalls, and Prof. Hans De Sterck.

I also want to extend my gratitude to Maureen and Erin for consistently providing me with the resources and information I needed at every stage of my journey. Additionally, I would like to thank all my friends and colleagues in Waterloo, Russell, Stéphanie, Maliha, Marina, and Megha, for the collaborative efforts we shared while working on coursework and engaging in discussions.

Dedication

This is dedicated to my husband, Mark, and our children, Bristol and Tim.

Table of Contents

List of Figures

List of Tables

List of Abbreviations

ACh acetylcholine 100, 129, 130

CFC cross-frequency-coupling 97

CO collective oscillation xv, 66, 82–91, 94–96, 123, 127–129

DDE delay differential equation 72, 79, 80, 128

EEG electroencephalogram 28, 60

EP equilibrium point xi–xvi, 9–11, 13, 14, 17, 26, 45–47, 53, 54, 57, 66, 73–76, 79, 82–84, 86–94, 116–118, 120, 122, 123

ERP event-related potentials 28

HP Andronov-Hopf xii, xv, 45, 46, 55, 56, 77, 78, 82, 90

HWHM half-width at half-maximum 25, 39, 41, 63, 69, 113

ISI interspike interval 14, 102

mAChR muscarinic acetylcholine receptor 3, 100, 116, 129

OA Ott-Antonsen 4, 17, 29, 30, 58, 63, 66, 69, 74, 76, 80, 94, 98, 113, 123, 127, 128

ODE ordinary differential equation 3, 30, 31, 33, 36, 44, 61, 63, 70, 71, 80, 82, 110, 124, 128

PDE partial differential equation 3

PO periodic orbit xi–xvi, 10, 11, 26, 45–47, 53, 54, 56, 57, 62, 82, 90–93, 96, 117, 118, 120, 122, 123

POFold Fold bifurcation of periodic orbits xv, 90, 96

PSC postsynaptic current 7, 18, 21, 24, 104, 105, 107, 110, 117, 120

QIF quadratic integrate-and-fire xi, xvi–xviii, 4, 5, 8, 12–15, 17, 27, 29, 30, 60, 61, 63, 64, 94, 96, 98, 100, 107, 110, 116–120, 122–124, 126, 127

SFA spike frequency adaptation 3, 4, 15, 26, 27, 30, 50, 58, 63, 66, 82, 95–98, 126, 127, 129, 130

SNIC saddle-node bifurcation on invariant circle 11, 13, 56, 59, 60, 63, 127

SNLC saddle-node bifurcation of limit cycles xii, 45, 46, 55

STD short-term depression 99

STF short-term facilitation 99

STP short-term plasticity xvi–xviii, 3, 5, 21, 22, 96, 98–100, 102, 105–107, 109, 110, 112, 115–120, 122–126, 128, 130

TM Tsodyks-Markram 21, 22, 99

WC Wilson-Cowan 28, 127

WS Watanabe-Strogatz 29, 30, 94

Chapter 1

Introduction

There are approximately 100 billion neurons in a mature human brain [166]. These neurons are hierarchically organized into regions, layers and nuclei, each part being relatively distinct and specialized for specific functions [64]. Each small part typically contains thousands of neurons, each with thousands of connections, known as synapses, organized in a network-like fashion [189]. Large-scale analyses of the brain come at many levels of scale, ranging from genetic regulatory and protein interaction networks inside of neurons to the highest level relating to the entire or a substantial part of the brain [170]; see Fig. 1.1. The networks at each level perform fundamentally different functions.

A longstanding challenge in computational neuroscience is the development of mathematically tractable models with experimentally measurable parameters, allowing for insights into the neural dynamics associated with both normal functions, such as working memory or spatial navigation, and neurological disorders like epilepsy or Parkinson's disease. This problem can be approached from various perspectives. For example, one can construct a neural network with meticulous attention to detail and utilize modern computing resources to simulate the full network's behaviors. This is the approach taken by the Blue Brain Project [143], which is dedicated to simulating the detailed structure and behavior of the brain at the cellular and synaptic levels. Additionally, various software tools, such as NEURON [109], GENESIS [30] and BRIAN [100], have been developed to render numerical model analysis. They support the setup and simulation of multi-compartment models of single neurons, including realistic dendritic structures and subcellular processes. Large-scale realistic simulations based on these computational platforms can offer a wealth of valuable information, especially for experiments that may be infeasible or ethically impractical with actual neural networks. Unfortunately, this approach is predominantly

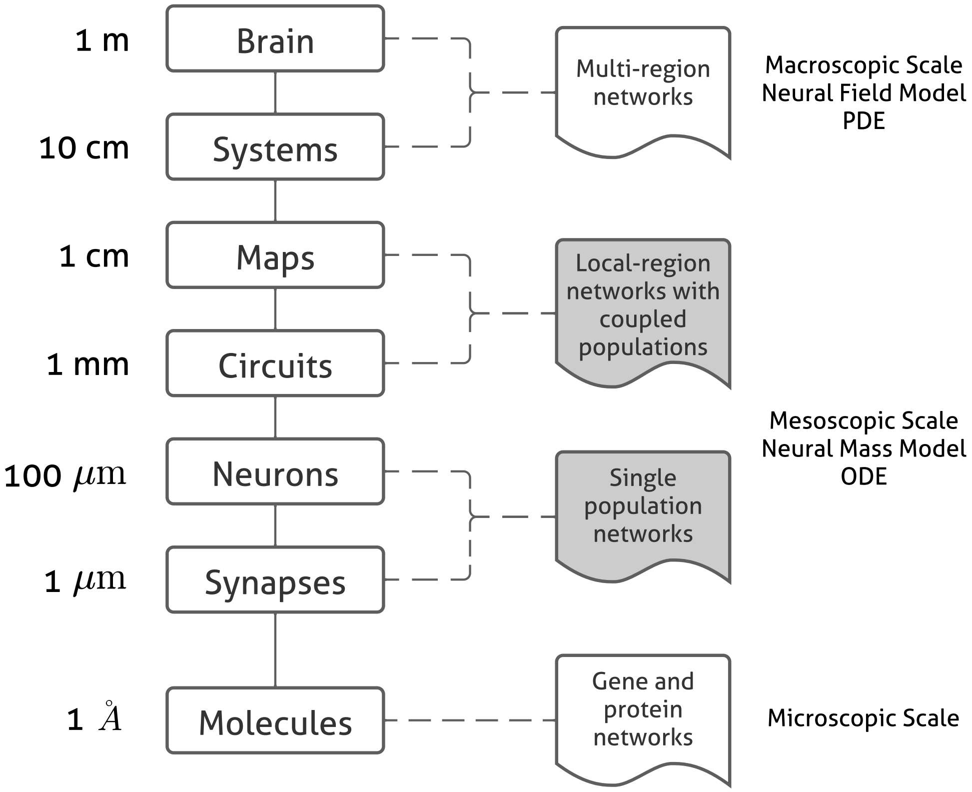

Figure 1.1: Network hierarchy in the neural system. The large scale analyses discussed in the thesis focus on the levels of shaded areas. Adapted from [170].

restricted to simulations. Beyond posing daunting computational issues, it offers a limited analytical understanding of the network function and the underlying mechanisms.

The functionality, whether function or dysfunction, of neural networks depends on the collective dynamics of the interacting individual neurons [28]. For example, the firing of action potentials is a fundamental aspect of neural communication. The exact timing of individual action potentials is not always crucial to comprehending the function of the network. Instead, the population firing rate – averaging across the entire network – captures the fundamental mechanism through which neurons communicate and process information in the brain. This insight has motivated the development of mean-field models, which seek to describe the coarse-grained activity of populations of neurons by reducing the degree of freedom from many to a few macroscopic variables, e.g., the population firing rate. Mean-field approximations have proven to be valuable analytical tools in terms of low-dimensional dynamical systems and have demonstrated powerful capability in various fields of neuroscience, including the description of wave propagation across the cortex, interpretation of neuroimaging data, and insights into patterns of functional connectivity [110, 62, 59, 39]. Furthermore, such mathematically tractable models have become an integral part of software tools, for example, DCM [154], TVB [187] and NNMT [130], which aim to provide simulation platforms for model-based inference of neurophysiological mechanisms across different brain scales.

In general, mean-field models fall into two main categories: neural mass and neural field models, as shown in Fig. 1.1. Neural field models, typically characterized by partial differential equations (PDEs), prescribe how a state of a neural population evolves over both space and time by taking into account the fact that neural dynamics play out on a spatially extended cortical sheet. These models allow us to accommodate lateral interactions in terms of wave equations when trying to understand brain organization and function across multiple regions. To gain a complete understanding of this subject, we recommend consulting the works of Bressloff [31] and Coombes [60]. By comparison, neural mass models, formulated primarily with ordinary differential equations (ODEs), characterize the average neural activity over time only by assuming that all neurons are approximately located at the same point and ignoring the spread and propagation of neural activity in continuous space. A comprehensive review of this field can be found in [64, 28, 219].

In this thesis, we concentrate on the temporal dynamics of neural networks with local connectivity, with particular emphasis on the intermediate two levels (shaded boxes) as depicted in Fig. 1.1. The thesis is based on three projects. First, we employ mean-field theory to analytically derive a neural mass model for neural networks with spike frequency adaptation (SFA). SFA refers to the phenomenon where the firing rate of a neuron decreases over time in response to an input current. It is a fundamental neural process and significantly contributes to the synchronous behaviors of neurons. Furthermore, we examine the influence of time delays, a key characteristic of the neural system arising from the finite conduction velocity in neuron communication. Time delays are crucial in shaping various collective behaviors of neural networks, including rhythms and their synchronization [43, 84]. Our investigation includes the time delay effect, along with the impact of heterogeneous current parameter and SFA intensity, through bifurcation analysis of the derived mean-field system. Finally, we develop a mean-field model for neural networks that incorporates calcium-dependent synaptic short-term plasticity (STP) and study the effect of muscarinic acetylcholine receptors (mAChRs) activation at inhibitory synapses in the CA1 region of the hippocampus. STP refers to transient changes in synapse transmission efficacy, induced by presynaptic activity, which subsequently influences the spike frequency of the postsynaptic neuron [225]. Some researchers [20, 95] view STP, especially synaptic depression, as a type of SFA mechanism, different from that induced by the adaptation current, which is represented as a slow variable in the Izhikevich neuron [115] used in our first project. Moreover, short-term synaptic dynamics implies noninstantaneous communication between neurons, which we account for in the second project by introducing time delays in the coupling of neurons.

The thesis is structured into six chapters, each outlined and summarized as follows.

Chapter 1. Introduction

A general introduction to this thesis.

Chapter 2. Biological and Mathematical Prerequisites

We introduce fundamental concepts and different approaches to modeling neurons and large networks. We also present typical microscopic and macroscopic behaviors, interpreting them from a dynamical systems perspective.

Chapter 3. Mean-Field Modeling for Neural Networks with Spike Frequency Adaptation

In this chapter, we employ mean-field theory to analytically derive a neural mass model that approximates the collective dynamics of a network of Izhikevich neurons. Each neuron is characterized by a two-dimensional system, consisting of a canonical quadratic integrate-and-fire (QIF) equation and an equation that implements SFA. We extend the approach to a network of two populations of neurons and discuss the qualitative and quantitative accuracy and efficacy of our mean-field approximations by examining all assumptions that are imposed during the derivation. This collaborative research, conducted with Prof. Sue Ann Campbell, has been published in [53]. My contribution included proposing the mean-field approach, conducting all the numerical simulations and bifurcation analysis, and writing the first draft of the paper.

Chapter 4. Collective Dynamics of Izhikevich Neural Networks with Synaptic Delay

Chapter 4 extends the study from Chapter 3 to a network of Izhikevich neurons with global delayed coupling. We thoroughly investigate the impact of the heterogeneity of the quenched input current, the adaptation intensity, and the synaptic delay on the collective dynamics of the neural network. Furthermore, we study the Ott-Antonsen (OA)-based mean-field approximation in the limit of extremely weak heterogeneity. The collaborative research in this chapter was conducted with Prof. Sue Ann Campbell and has been accepted by SIAM Journal on Applied Dynamical Systems [54]. My contribution was derivation of the mean-field system, numerical bifurcation analysis, and drafting the manuscript.

Chapter 5. Mean-Field Modeling for Spiking Neural Networks with Short-Term Synaptic Plasticity

In this chapter, we improve the realism of neural networks by incorporating STP in synaptic connections between QIF neurons. Synaptic dynamics is characterized by measurable calcium-dependent processes that occur in synapses. We develop a discrete microscopic synaptic model and construct a neural network with kinetic synapses. Expanding on the approach in Chapter 3, we derive the corresponding mean-field system, in addition to exploring the muscarine effect at hippocampal inhibitory synapses through the developed mean-field model. This collaborative effort includes Prof. Sue Ann Campbell and Prof. Emily Stone (University of Montana). Parameter values are based on experimental data from Prof. Stone's work [195]. My contribution included developing the synaptic model, constructing the neural network with STP, deriving the mean-field system, and performing the numerical analysis.

Chapter 6. Conclusions and Outlook

We summarize the main findings of this thesis and discuss possible future work and the open problems associated with the presented research.

Chapter 2

Biological and Mathematical Prerequisites

This chapter highlights fundamental concepts and common phenomena in neuroscience, illustrating how to understand them from a dynamical systems perspective, which is the central theme throughout the thesis.

2.1 Biological Background

A neuron is the brain's primary computational unit, with cells coupled together to perform functions in the form of neural networks. A typical neuron receives signals from more than 10,000 other neurons via electrochemical contacts on its dendrites, called synapses [129]. As an example, Fig. 2.1 illustrates the connection between two neurons in (a) and a magnified view of synaptic transmission in (b). Neurons communicate by sending action potentials, or spikes, which are abrupt and transient voltage changes across the membrane that propagate via long biological cables called axons. When a spike train reaches the axon terminal of the sending cell, the presynaptic neuron, it triggers the opening of voltage-gated calcium channels, allowing an inflow of calcium ions (Ca^{2+}). This influx causes a brief surge in calcium concentration, which triggers the release of neurotransmitters into the synaptic cleft. These neurotransmitters diffuse across the cleft, binding to receptors on the receiving cell, the postsynaptic neuron, and either opening or closing ion channels in its membrane. This leads to a localized change in the membrane potential of the postsynaptic neuron. Depending on the ions involved, this change can make the inside of the cell more positive, causing an excitatory postsynaptic current (PSC), or more negative, causing an inhibitory PSC. The cumulative effects of all synapses on the postsynaptic neuron sum in the soma. This summation may or may not lead to the generation of action potentials in the postsynaptic neuron, depending on the relative magnitude and direction of the currents.

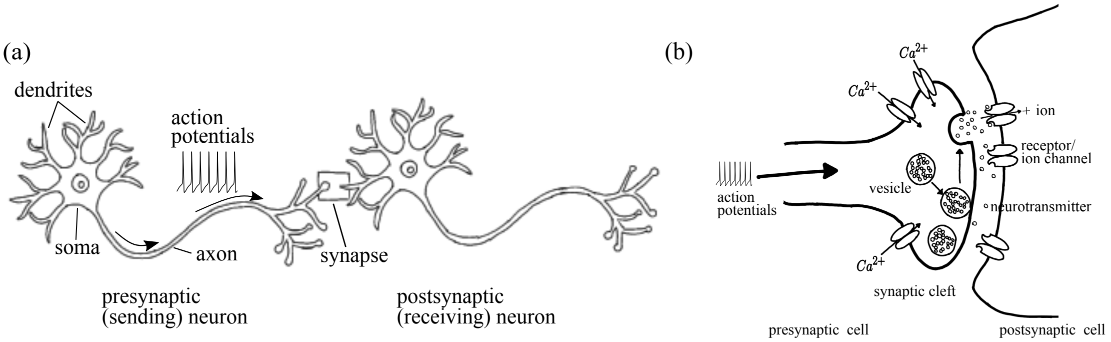

Figure 2.1: Communication between two neurons via a synapse (blow up in (b)) by sending action potentials.

2.2 Dynamical Systems Perspective

Two neurons with similar physiological features and located in the same brain region may exhibit different responses to the same input current due to their dynamical properties. Conversely, neurons with different physiological properties may undergo identical dynamical changes, leading to similar neurocomputational properties [117]. Therefore, both physiological and dynamic characteristics are crucial in influencing neural activities. The concept that neurons and neural networks coupled by them are regarded as dynamical systems originated from the seminal work of Rinzel and Ermentrout [182]. They showed that the differences in neural behavior arise from different bifurcation mechanisms of excitability. Today, the dynamical systems approach has become the core of computational neuroscience research. Bifurcation theory, in particular, is a powerful tool for studying the system around dynamic transitions. These transitions are associated with bifurcations, which take place when a minor adjustment to the parameter values (referred to as bifurcation parameters) of a system results in an abrupt 'qualitative' or topological shift in its behavior [125]. In the following sections, we will explain the specific concepts and phenomena in neuroscience from a dynamical systems point of view, focusing on those most relevant to the results in subsequent chapters.

2.3 Neuron Models

Neurons are the basic units of complex neural networks, and various models have been proposed to characterize them, varying in their level of abstraction, biological detail, and mathematical complexity [116]. The most abstract models are those commonly used in artificial neural networks, where actual spiking behaviors of neurons are ignored. Instead, the average rate of spiking is encoded as an instantaneous input-output relationship, typically governed by the Heaviside step function or any sigmoidal function [139, 146]. The most biologically detailed models are conductance-based models, exemplified by the Hodgkin-Huxley model and its modifications. They are based on the underlying biophysics of action potential generation and describe the dynamics of changes in conductance along the neuron membrane. While these models exhibit most of the major neural computational properties with biophysically meaningful and measurable parameters [116], their mathematical complexity, involving multiple differential equations and tens of parameters, makes studying large-scale network dynamics challenging both analytically and numerically. Integrate-and-fire models provide a significant reduction in the dimensionality of conductance-based models. Although not based on biophysical principles, these models retain central dynamical properties that can be fitted to real neurons. They are phenomenological models. For this thesis, we aim to strike a balance between the extreme abstraction of artificial neural network models and the high biological detail of the Hodgkin-Huxley model. We seek a model for a single neuron that is computationally simple enough to construct the neural network, yet capable of exhibiting the rich spiking behaviors observed in real biological neurons.

In this section, we start with the conductance-based models, and then introduce two classical integrate-and-fire models: the quadratic integrate-and-fire (QIF) neuron and the Izhikevich neuron. We offer a conceptual understanding and a dynamical system analysis for each model. This discussion will lay the foundation for studying networks composed of these models in subsequent chapters.

2.3.1 Conductance-Based Neuron

According to the Nobel Prize-winning work of Hodgkin and Huxley [111], the variation of the membrane potential of a neuron, V, is modeled as an RC circuit. The currents in this model consist of I_{Na} resulting from sodium ions (Na^+) flowing across the membrane, I_{K} from potassium ions (K^+), the leak current I_L from other ions, and the applied input current I_{app}. It is given by

$$\begin{aligned} CV' &= -I_{\text{Na}} - I_{\text{K}} - I_{\text{L}} + I_{\text{app}} \\ &= -\bar{g}_{\text{Na}} m^3 h (V - E_{\text{Na}}) - \bar{g}_{\text{K}} n^4 (V - E_{\text{K}}) - \bar{g}_{\text{L}} (V - E_{\text{L}}) + I_{\text{app}} \\ m' &= \alpha_m(V)(1-m) - \beta_m(V) m \\ n' &= \alpha_n(V)(1-n) - \beta_n(V) n \\ h' &= \alpha_h(V)(1-h) - \beta_h(V) h \end{aligned} \tag{2.1}$$

where $' = d/dt$ denotes the time derivative, C is the membrane capacitance, $\bar{g}$ is the maximal value of the conductance (the reciprocal of the resistance), and E is the reversal potential at which a particular ion has no net flow across the membrane. The gating variables m, h and n represent the proportion of ion channels that are in any particular state with the rate constants α and β dependent on V.

Since the original Hodgkin-Huxley model, different currents have been described using a conductance-based formalism. At the same time, simplifications have been suggested by assuming instantaneous dynamics of certain ion channels or by aggregating them into lumped variables through methods such as the quasi-steady state approximation or perturbation theory [114]. Instances of such models include the Morris-Lecar model [155], the Wang-Buzsáki model [211], and the Chay-Cook model [51], among others. As an example, we present a modified Chay-Cook model [22], given by

$$\begin{aligned} C_m V' &= -I_{\text{Ca}} - I_{\text{Ca2}} - I_{\text{K}} - I_{\text{L}} \\ &= \bar{g}_{\text{Ca}} m_\infty (V - E_{\text{Ca}}) - \bar{g}_{\text{Ca2}} \frac{1}{1 + \exp(2A(V,c))} (V - E_{\text{Ca}}) \dots \\ &\quad - \bar{g}_{\text{K}} n (V - E_{\text{K}}) - \bar{g}_{\text{L}} n (V - E_{\text{L}}) \\ n' &= \lambda \left[n_\infty(V) - n \right] / \tau_n(V) \\ c' &= \beta \left[-\alpha (I_{\text{Ca}} + I_{\text{Ca2}}) - k_{\text{Ca}} c \right]. \end{aligned} \tag{2.2}$$

This model is composed of a potassium current I_{K}, a leak current I_{L}, a fast calcium current I_{Ca}, and a slow calcium current I_{Ca2}, both carried by calcium ions (Ca^{2+}). The gating variable for potassium and leak currents is represented by n, while the gating variable for the fast calcium current is assumed to be in steady state m_∞ and the one for the slow calcium current depends on V and the intracellular free calcium concentration c.

Fig. 2.2 shows typical spiking behaviors of a single neuron. A small stimulus, such as $I_{\text{app}} = 12.2$ in (a), results in small excursions from equilibrium point (EP); a larger stimulus,

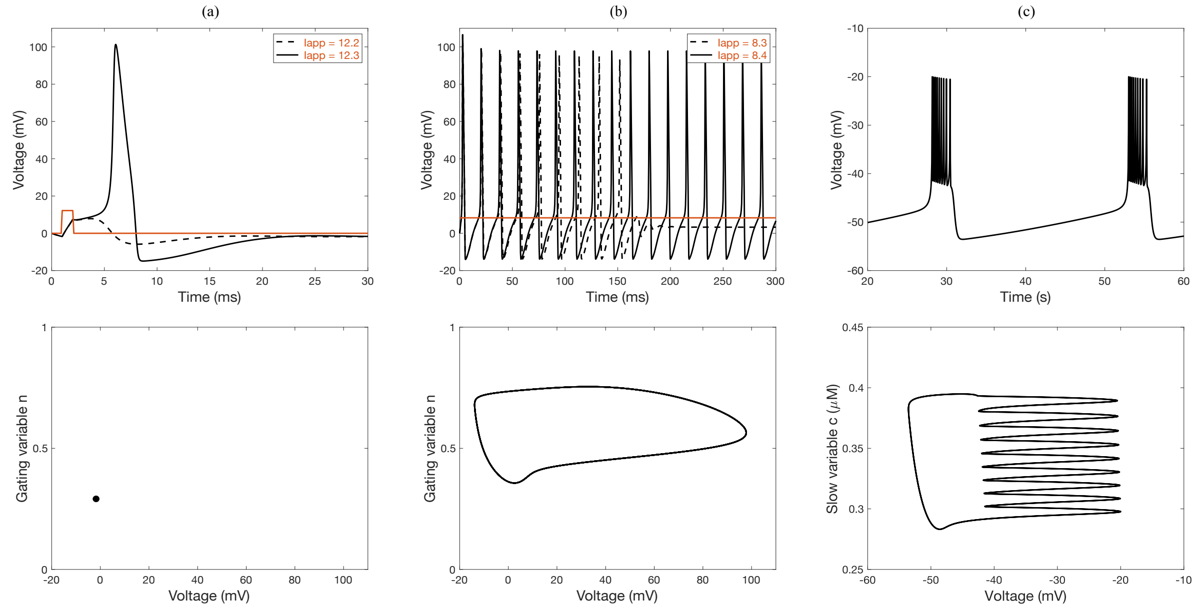

Figure 2.2: Typical microscopic behaviors of a single neuron. (a): one spike, (b): tonic firing, (c): bursting. The applied current is shown in orange. Curves in (a) and (b) are simulations of the Hudgkin-Huxley model (2.1) with parameter values $E_{\mathrm{Na}} = 117.5$, $E_{\mathrm{K}} = -15.8$, $E_{\mathrm{L}} = 7.9$, $\bar{g}_{\mathrm{Na}} = 120$, $\bar{g}_{\mathrm{K}} = 36$ and $\bar{g}_{\mathrm{L}} = 0.3$. For further details, see the paper [111]. Curves in (c) depict simulations of the modified Chay-Cook model (2.2) with parameter values $\lambda = 0.95$, $\beta = 0.002$ and $k_{\mathrm{Ca}} = 0.027$. For further details, see the paper [22].

such as $I_{\mathrm{app}} = 12.3$ in (a) and $I_{\mathrm{app}} = 8.3$ in (b), triggers a spike response characterized by a rapid upward spike followed by a rapid fall. These up-and-down cycles are called action potentials. To characterize and compare neural spiking behaviors, one can examine the geometry of the phase portrait through phase plot analysis, a valuable technique within the field of dynamical systems, where we can gain insights into a system without requiring a complete understanding of all the details that govern the system evolution. For the spiking behaviors in Fig. 2.2(a) and the dashed line in (b), the neuron undergoes a transient process and finally converges to the same state, which is indicated by an EP in the phase portrait (V, n) depicted in Fig. 2.2(a). If we inject a different current, the neuron exhibits tonic firing activity, as in Fig. 2.2(b) for $I_{\mathrm{app}} = 8.4$. From the dynamical system point of view, the state of such a neuron has a stable limit cycle, also known as stable periodic orbit (PO). Furthermore, the alternation between the resting and spiking modes results in the bursting behavior, as shown in Fig. 2.2(c). This neural activity is biologically induced by processes with different time scales. Specifically, in the modified Chay-Cook model (2.2), it arises from the interaction between the fast variables V and n and the slow variable c.

Fig. 2.2 also shows that small changes in the parameter values can push the system past a critical point and induce a qualitative change in the phase portrait of the system. Next, we will perform a bifurcation analysis for the modified Chay-Cook model (2.2) to illustrate the underlying mechanism of the bursting generation in Fig. 2.2(c).

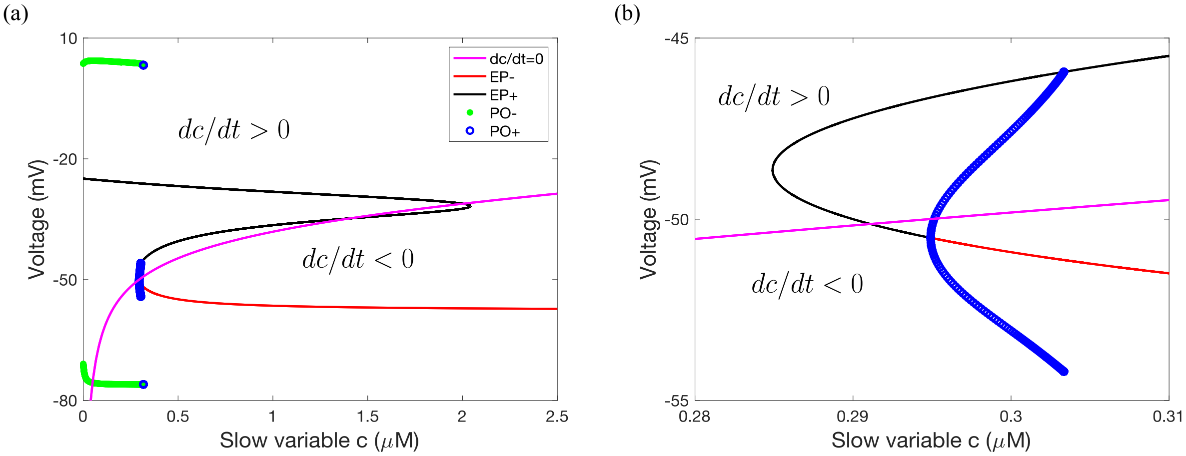

Figure 2.3: Bursting analysis for the modified Chay-Cook neuron (2.2) with $k_{\mathrm{Ca}} = 0.022$. Panel (b) is a magnified view of panel (a). Stable/unstable PO is shown in green/blue, stable/unstable EP in red/black, and the nullcline $dc/dt = 0$ in pink.

Figure 2.3 illustrates the bifurcation diagram and its magnification for the rapid subsystem (V, n), with c being constant and representing the c nullcline ($dc/dt = 0$) for the slow subsystem. It is important to observe that $dc/dt > 0$ above the nullcline and $dc/dt < 0$ below it. The burst event is explained below. In the scenario where c has a small value, the system has an unstable EP (depicted in black) alongside a stable PO. As c gradually increases due to $dc/dt > 0$, the neuron fires action potentials until it reaches a critical point known as the saddle-node bifurcation on invariant circle (SNIC). Subsequently, the system transitions to the stable EP (illustrated in red) and remains in a state of rest without any firing activity. However, currently, the rate of change of c is negative ($dc/dt < 0$). Consequently, the system remains in a static state until c decreases to the subcritical Hopf bifurcation point (the point where the blue curve intersects the red curve), at which point it switches to the stable PO and resumes firing action potentials. This cyclic process leads to the bursting behavior in Fig. 2.2(c).

2.3.2 Quadratic Integrate-and-Fire Neuron

Various models have been suggested to mimic the spiking patterns observed in actual neurons, such as the FitzHugh–Nagumo neuron [93], the Adaptive Exponential (AdEx) neuron [32, 156], and more. Of these models, the QIF stands out as the most basic and has established itself as a fundamental model in computational neuroscience.

The QIF neuron is defined as

$$C\frac{dV}{dT} = k_1(V - V_T)(V - V_R) + I_{\text{sum}}(t), \quad \text{if V} \geq \text{V}_{\text{peak}}, \quad \text{then V} \leftarrow \text{V}_{\text{reset}} \tag{2.3}$$

where C is the capacitance of the cell, k_1 is the scaling factor, V_R is the resting membrane potential and typically negative, V_T is the threshold potential, and $I_{\text{sum}}(t)$ is a lumped representation of all current inputs to the cell. When the voltage reaches a cut-off value, denoted as the peak of a spike V_{peak}, it is reset to the value V_{reset}. Via the transformations

$$v = \frac{V}{|V_R|} + \frac{1}{2}\left(1 - \frac{V_T}{|V_R|}\right), \quad t = \frac{k_1|V_R|}{C}T, \quad I = \frac{I_{\text{sum}}}{k_1 V_R^2} - \frac{(V_T + |V_R|)^2}{4k_1 V_R^2} \tag{2.4}$$

we can simplify the expression as

$$\frac{dv}{dt} = v^2 + I(t), \quad \text{if } v \geq v_{\text{peak}}, \quad \text{then } v \leftarrow v_{\text{reset}}. \tag{2.5}$$

The QIF model involves an intrinsic spike generation mechanism through a nonlinear one-dimensional process and a resetting rule. Following quadratic dynamics, the membrane potential v increases rapidly until it reaches a preset peak value v_{peak}. A spike is generated and the neuron is reset immediately at v_{reset}; see Fig. 2.4(a) and (d). In the limit $v_{\text{peak}} = -v_{\text{reset}} \to \infty$, the QIF neuron is equivalent to the theta neuron [85, 104] defined in the domain $\theta \in [-\pi, \pi)$ via the transform $v = \tan(\theta/2)$,

$$\theta' = 1 - \cos\theta + (1 + \cos\theta)I, \tag{2.6}$$

where the neuron fires an action potential whenever θ crosses π; see Fig. 2.4(c). The theta neuron is a phase oscillator characterized by a single phase variable that effectively captures the periodic process. This equivalence allows neural networks composed of QIF neurons to be studied using tools for the Kuramoto model, which is a well-established framework for understanding synchronization phenomena [163].

The QIF system (2.5) is the topological normal form for the saddle-node bifurcation. We show its qualitative dynamics in Fig. 2.4(a) and (b) by varying the current parameter

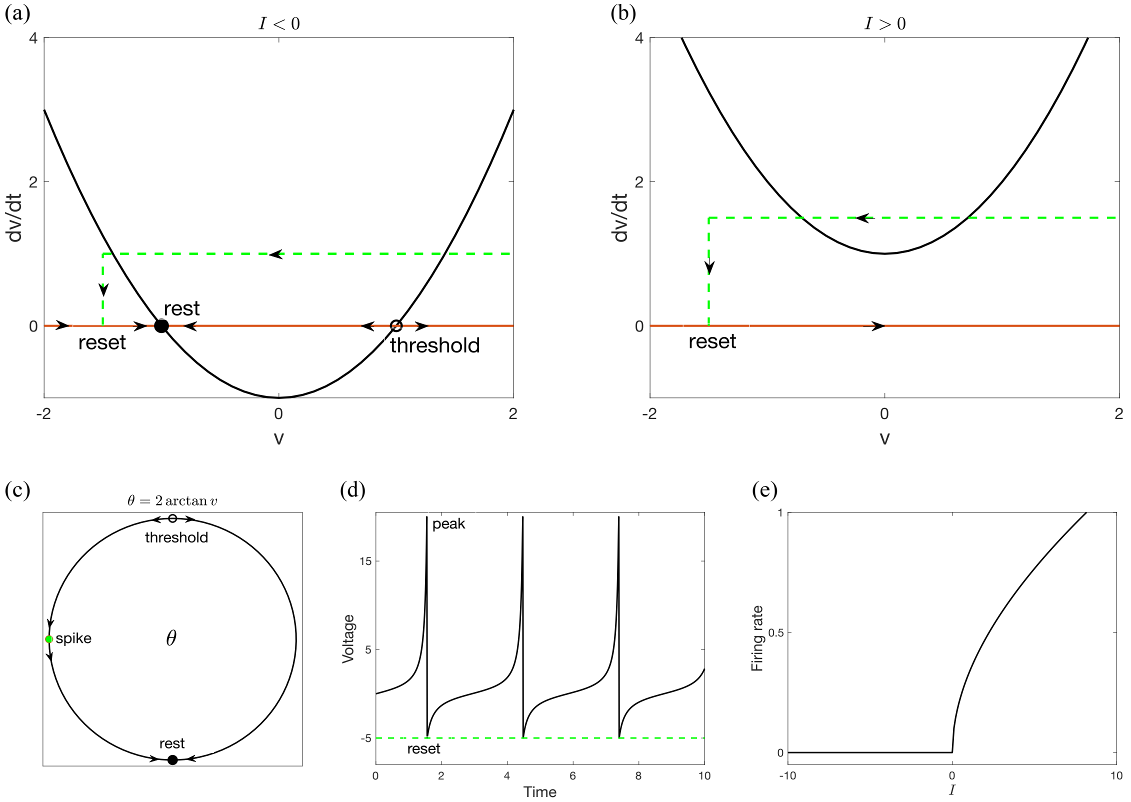

Figure 2.4: Dynamics of a single QIF neuron. (a)-(b): Relationship between dv/dt and v for negative and positive input current I, respectively. (a): QIF dynamics for $I < 0$ are governed by a stable EP (filled circle), corresponding to the resting potential, and an unstable EP (empty circle), corresponding to the threshold potential. (b): For $I > 0$, no EP exists and the QIF neuron exhibits tonic firing behavior; see (d). (c): Relationship between the QIF neuron and the theta neuron. We take $I = -1$ and $v_{\text{peak}} = -v_{\text{reset}} \to \infty$ as an example. (d): Tonic firing behavior with $v_{\text{peak}} = 20$ and $v_{\text{reset}} = -5$. (e): Relationship between the current I and the firing rate r from Eq. (2.8) with $v_{\text{peak}} = -v_{\text{reset}} = 20$.

I, which we consider to be constant for now, that is, $I(t) = I$, $\forall t$. From Eq. (2.5), we find that there are two equilibria for $I < 0$, one stable node at $v = -\sqrt{-I}$, denoted by the filled circle, and an unstable saddle at $v = \sqrt{-I}$, denoted by the empty circle. By increasing the value of the input parameter I, the two equilibria approach and annihilate each other at the saddle-node bifurcation point $I = 0$. Thus, no equilibria exist anymore when $I > 0$. From the perspective of the theta neuron (see Fig. 2.4(c)), such a bifurcation is called SNIC. In the case of $I < 0$, as illustrated in Fig. 2.4(a), the neuron is resting at the stable EP (the filled circle). Small perturbations via transient input result in small excursions from the EP. If this perturbation is strong enough such that $v > \sqrt{-I}$, the threshold denoted by the empty circle, it will drive the system out of the attraction basin of the stable EP. In this scenario, v can escape to infinity in finite time due to the quadratic dynamics. This corresponds to the firing of an action potential, more precisely, to its upstroke. When v reaches the preset value v_{peak}, the state of the system is reset immediately by the resetting rule, which corresponds to the downstroke of the action potential. Thus, a spike is generated before the trajectory is finally attracted to the stable resting state. In the case of $I > 0$, as shown in Fig. 2.4(b), there is no stable equilibrium and $dv/dt \geq I$. v increases and reaches v_{peak}. The resetting rule brings v back to v_{reset}, and then v increases again. Thus, the QIF neuron exhibits periodic spiking (also called tonic firing) behavior; see Fig. 2.4(d).

When comparing the configuration of a single action potential depicted in Fig. 2.4(d) produced by the QIF neuron with that shown in Fig. 2.2(a) generated by the Hodgkin-Huxley neuron, it is evident that the downstroke of the action potential of the QIF neuron is simplified as a straight line due to the resetting rule. This simplification arises because, in many cases, especially those involving the collective behaviors of large-scale networks of spiking neurons, the precise shape of the action potential holds less significance than the subthreshold dynamics leading to this action potential. In other words, the shape of the downstroke of the action potential is less critical than that of the upstroke [117]. This concept of simplification underpins the essence of many integrate-and-fire neuron models.

In addition, we can obtain the solution to Eq. (2.5) with initial condition $v(t_0)$,

$$v(t) = \sqrt{I} \tan\left(t\sqrt{I} + \arctan\frac{v(t_0)}{\sqrt{I}}\right). \tag{2.7}$$

The firing rate of the spiking activity, that is, the number of spikes in unit time or the inverse of the mean interspike interval (ISI), can be found by choosing $v(t_0) = v_{\text{reset}}$ and solving Eq. (2.7) for the time t_{ISI} it takes until $v(t_{\text{ISI}}) = v_{\text{peak}}$, given by

$$r = \frac{1}{t_{\text{ISI}}} = \frac{\sqrt{I}}{\arctan\frac{v_{\text{peak}}}{\sqrt{I}} - \arctan\frac{v_{\text{reset}}}{\sqrt{I}}}. \tag{2.8}$$

In the limit $v_{\text{peak}} = -v_{\text{reset}} = \infty$, we have $r = \sqrt{I}/\pi$. As shown in Fig. 2.4(e), the QIF neuron produces spiking with an arbitrarily small frequency and is therefore said to exhibit Class I excitability [88].

The QIF neuron is simple and canonical in the sense that any Class I excitable system close enough to the onset of oscillations can be transformed into this form [85, 82, 128]. Therefore, the QIF neuron is appropriate to be used for the study of dynamics of large-scale networks of neurons exhibiting Class I excitability.

2.3.3 Izhikevich Neuron

The QIF neuron alone does not suffice to replicate all spiking activities, particularly the bursting behavior, which commonly arises from the interplay between fast and slow dynamics. Recall that the Hodgkin-Huxley type model usually has two variables that evolve on a fast time scale (m and V) and two that evolve on a slow time scale (n and h). Some two-dimensional spiking neuron models have been proposed to retain the central dynamical properties, such as the FitzHugh–Nagumo neuron [93], the Adaptive Exponential (AdEx) neuron [32, 156], the Izhikevich neuron [115], etc. The Izhikevich model is a straightforward extension of the QIF neuron by including a slower recovery variable. Derived from bifurcation theory and normal form reduction, this model can reproduce a much larger class of neurodynamics, including spike frequency adaptation (SFA). Although not based on biophysical principles, experimental data can be used to fit the parameters so that the model accurately replicates the neural spiking behaviors of biological neurons.

The Izhikevich neuron is governed by

$$\begin{aligned} CV' &= k_1(V - V_R)(V - V_T) - W + I_{\text{sum}}, & &\text{if } V \geq V_{\text{peak}},\ \text{then} \\ \tau_W W' &= \beta(V - V_R) - W, & &V \leftarrow V_{\text{reset}},\ W \leftarrow W + W_{\text{jump}}, \end{aligned} \tag{2.9}$$

where V is the membrane potential, evolving on a fast time scale, W is a phenomenological recovery variable, representing the sum of all slow currents that modulate the spike generation mechanism, τ_W is the recovery time constant, β is the scaling factor, and W_{jump} is the after-spike reset of W, representing the effect of the total amount of net currents activated during the spike. The remaining parameters are of the same significance as those mentioned in Eq. (2.3). Similarly, via the transformations

$$v = 1 + \frac{V}{|V_R|}, \quad w = \frac{W}{k_1 V_R^2}, \quad t = \frac{k_1|V_R|}{C}T,$$

we can obtain a compact form,

$$\begin{aligned} v' &= v(v - \alpha) - w + I, & &\text{if } v \geq v_{\text{peak}},\ \text{then} \\ w' &= a(bv - w) & &v \leftarrow v_{\text{reset}},\ w \leftarrow w + w_{\text{jump}}. \end{aligned} \tag{2.10}$$

with

$$\alpha = 1 + \frac{V_T}{|V_R|}, \quad a = \frac{C}{\tau_W k_1 |V_R|}, \quad b = \frac{\beta}{k_1|V_R|}, \quad I = \frac{I_{\text{sum}}}{k_1 V_R^2}.$$

Compared with the QIF neuron, the great difference of the Izhikevich neuron is the introduction of a slow variable w, which allows the system to exhibit much richer neurocomputational properties, including the most fundamental one: bursting.

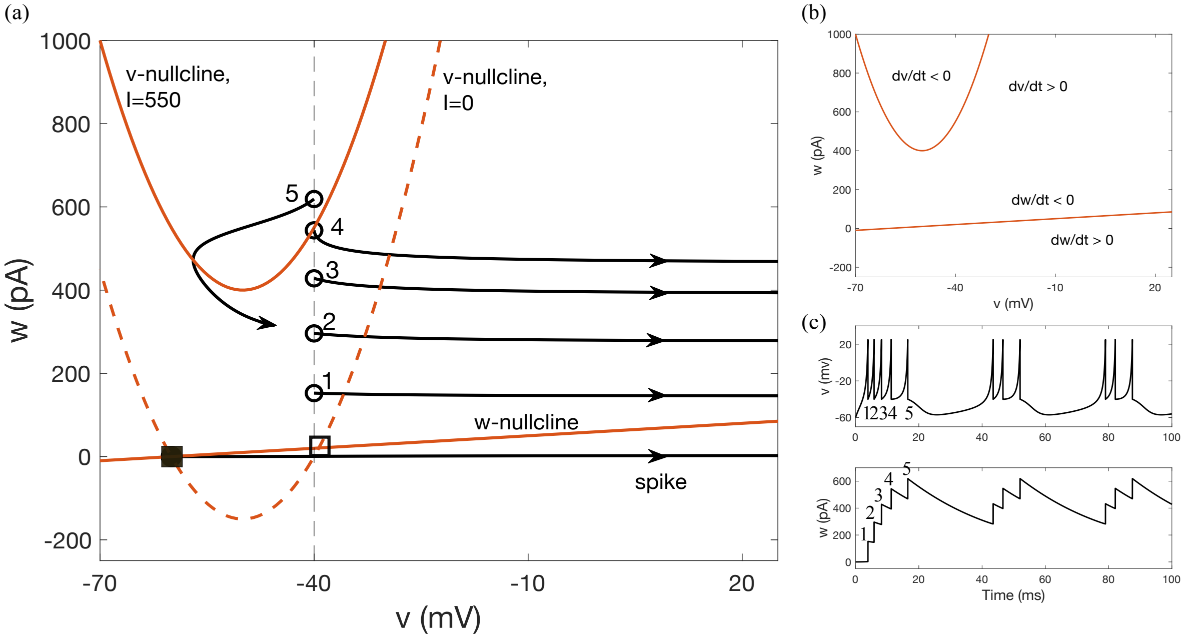

Figure 2.5: Dynamics of a single Izhikevich neuron $50v' = 1.5(v+60)(v+40) - w + I$, $w' = 0.03(v + 60 - w)$, if $v \geq 25$, then $v \to -40$, $w \to w + 150$. (a): Phase portrait of the model and nullclines for $I = 550$ (solid line) and $I = 0$ (dashed line), respectively. (b): Nullclines for $I = 550$ and rates of change with time. (c): Time evolutions. Adapted from Fig. 8.24 of [117].

There are many types of bursting initiated by different bifurcation mechanisms [117]. As an example, the phase portrait in Fig. 2.5 illustrates the mechanism of bursting generation in the Izhikevich neuron. In general, every bursting pattern involves two time-scale oscillations: a fast spiking within the burst and a slow oscillation between the bursts modulated by the slow current; see Fig. 2.5(c). From $dv/dt = 0$ and $dw/dt = 0$, we can obtain the nullclines for v and w, respectively; see the orange lines in Fig. 2.5(a) and (b). The v nullcline takes the form of a quadratic parabola that shifts upward as I increases, while the w nullcline is a linear function that remains unaffected by changes in I. The arrows in the lines indicate the temporal changes of the variables. When the system state lies within the parabolic v nullcline, the variable v will experience a decrease over time as $dv/dt < 0$; conversely, if the state is located outside the v nullcline, v will increase over time as $dv/dt > 0$. Similarly, when the system remains above the w nullcline, w will decrease over time, whereas if it stays below the w nullcline, w will increase over time. It should be noted that w undergoes significantly less movement than v due to the substantial disparities in their time constants. When $I = 0$ (the dashed v nullcline in Fig. 2.5(a)), the system has one stable EP (denoted by the filled square) and one saddle-type EP (denoted by the empty square), resulting from intersection of the two nullclines. Similarly to the analysis of QIF as shown in Fig. 2.4, the Izhikevich neuron rests at the stable EP or generates a single spike depending on the strength of the perturbation. A constant input current $I > 0$ shifts the v nullcline upward (the solid line in Fig. 2.5(a)), but leaves the w nullcline fixed. The trajectory (black lines) starting from the resting quickly moves rightward to fire a spike. The after-spike reset point (the empty circle marked "1" in Fig. 2.5(a) and (c)) is outside the v nullcline and up the w nullcline. So, with increasing v, another spike is fired immediately, and so on, until the upward strength of w moves the after-spike reset point inside the v nullcline (the empty circle marked "5"). After that, the trajectory makes a brief excursion to the left and down. The slow part of the solution comes from where the trajectory is close to the v nullcline. When it exits the parabola nullcline, the trajectory moves rightward again, initiating another series of spikes.

The Izhikevich neuron is an excellent model to be used in the study of large-scale network dynamics since it combines the capability of reproducing variety of neurocomputational properties, tractability and efficiency of the numerical and theoretical implementation. More important, the QIF-version of the fast subsystem in the Izhikevich model allows us to extend the Ott-Antonsen (OA) theory, a well-known mean-field reduction approach, to a more complicated situation. In subsequent chapters, we will take the Izhikevich model as the individual neuron to investigate collective behaviors of large-scale neural networks through the mean-field approximation.

2.4 Synapse Models

Neurons communicate with each other through specialized points of connection known as synapses, which can be classified into two types: chemical and electrical. Chemical synapses are more prevalent and complicated, transmitting signals using chemical messengers. Other synapses are electrical and ions flow directly between cells. In this section, we will focus on modeling chemical synapses.

Similarly to modeling neurons, there are also two strategies for modeling chemical synapses for different purposes and applications. One is kinetic modeling, which predicts system behavior based on knowledge of its components' properties. However, overly detailed biological representations can make this approach challenging for simulating large-scale neural networks. The other is phenomenological modeling, which describes the empirical relationship of phenomena based on experimental observations and mathematical reduction theory. While not as accurate as kinetic modeling, it is computationally friendly for studying large networks. Sometimes, these two approaches are involved in one framework to model different system components.

2.4.1 Kinetic Models

As illustrated in Fig. 2.1(b), the firing of the presynaptic neuron sends a train of action potentials to its axon terminal, causing the release of neurotransmitters into the synaptic cleft. The neurotransmitters then diffuse and bind to receptors on the postsynaptic cell, triggering the opening or closing of ion channels, and finally resulting in a change in the voltage of the postsynaptic neuron's membrane.

The simplest kinetic model for synapses, proposed by Destexhe et al. [66], focused on modeling the temporal dynamics of ion channels associated with the concentration of neurotransmitters $[T]$ in the synaptic cleft. The chemical reaction takes the form

$$C + T \xrightleftharpoons[\beta]{\alpha} O$$

where C and O represent the closed and open states of the ion channel, respectively. Denote s the fraction of ion channels that are in the open state. The resulting model is given by

$$s' = \alpha[T](1 - s) - \beta s, \tag{2.11}$$

where α and β are the channel opening and closing rate. Then, the PSC is modeled as

$$I_{\text{syn}} = \bar{g}_{\text{syn}} s(V_{\text{post}} - E_r), \tag{2.12}$$

where V_{post} is the voltage of the postsynaptic cell, $\bar{g}_{\text{syn}}$ is the maximal conductance and E_r is the reversal potential. These models are valid for synapses involving the neurotransmitters AMPA and GABA_A and slight modifications are necessary to account for other types of receptor and neurotransmitter [67]. Regarding the models for $[T]$, a simple function associated with the presynaptic voltage v_{pre} was suggested in [66], given by

$$[T] = \frac{T_{\max}}{1 + \exp(-(v_{\text{pre}} - v_p)/K_p)}, \tag{2.13}$$

where $T_{\max}$, v_p and K_p are parameters. In addition, a simpler model was proposed in [65, 67], given by

$$[T] = \begin{cases} T_{\max} & t_k < t < t_k + \bar{t} \\ 0 & t_k + \bar{t} \le t < t_{k+1}. \end{cases} \tag{2.14}$$

It is a step-shaped pulse with width $\bar{t}$. Pulses start at specific spike times t_k of action potentials from the presynaptic cell. In this case, the gating variable in Eq. (2.11) can be solved analytically, given by

$$s(t) = \begin{cases} s_\infty + (s(t_k) - s_\infty)e^{-(t-t_k)/\tau_s}, & t_k \le t < t_k + \bar{t}, \\ s(t_k + \bar{t})e^{-\beta(t-t_k-\bar{t})}, & t_k + \bar{t} \le t < t_{k+1}, \end{cases}$$

with

$$s_\infty = \frac{\alpha T_{\max}}{\alpha T_{\max} + \beta} \quad \tau_s = \frac{1}{\alpha T_{\max} + \beta}. \tag{2.15}$$

Through induction and algebraic manipulations, we can conclude that when $1 \le s(0) \le s_\infty$, the inequality $0 \le s(t) \le 1$ holds for all t. This makes sense, as s represents the proportion of open ion channels. Based on experimental observations, these two formulations for $[T]$, Eq. (2.13) and (2.14), produce a similar impact on the postsynaptic neuron [67]. As an example, Fig. 2.6(a) illustrates the temporal evolution of s in Eq. (2.11) generated using the pulse model for $[T]$ (2.14). The top one shows the effect of a single spike at $t_k = 1$, while the bottom one shows the cumulative effect of action potentials spiking at $t_k = 1$, 1.5, 2, and 2.5, respectively. It is evident that s remains within the range $[0, 1]$ for all t.

2.4.2 Phenomenological Models

Phenomenological models, first introduced by Rall [177], were proposed to approximate the change in the postsynaptic conductance $s(t)$ due to a spike-train stimulus from the presynaptic cell. In this case, s is defined as a convolution of the spiking activity of the presynaptic cell with a postsynaptic response kernel $E(t)$, given by

$$s(t) = \sum_k \int_{-\infty}^{t} E(t - t')\delta(t' - t^{(k)})dt' = \sum_k E(t - t^{(k)}), \tag{2.16}$$

where $\delta(\cdot)$ is the Dirac delta function and $t^{(k)}$ is the time of the kth action potential of the presynaptic cell.

Different forms of the function $E(t)$ were chosen in the literature [88]. Typical examples include the single exponential synapse,

$$E(t) = s_{\text{jump}} \exp(-t/\tau_s), \tag{2.17}$$

where τ_s is the time constant, the double exponential synapse,

$$E(t) = \frac{1}{\tau_{r1}\tau_d}\big(\exp(-t/\tau_{r1}) - \exp(-t/\tau_d)\big), \tag{2.18}$$

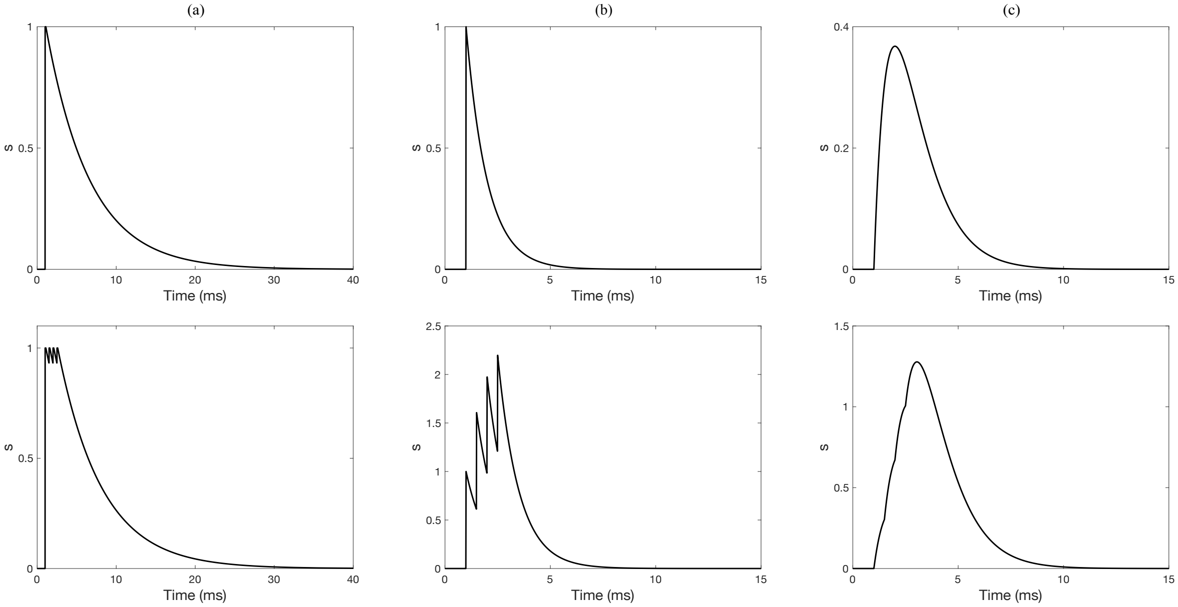

Figure 2.6: Time evolution of the gating variable s generated via Column (a): the kinetic synapse model (2.11) and (2.14) with $\bar{t} = 0.1$ ms, $\alpha = 5000$ $\mathrm{M}^{-1}\mathrm{ms}^{-1}$, $\beta = 0.18$ ms^{-1} and $T_{\max} = 2.84$ mM for the GABA_A synapse [67]. Column (b): the single exponential synapse (2.16) and (2.17) with $\tau_s = 1$ and $s_{\text{jump}} = 1$. Column (c): the alpha synapse (2.16) and (2.19) with $\alpha = 1$. The first row depicts one-spike effect occurring at $t_k = 1$, and the second row depicts the accumulation effect of a spike train occurring at $t_k = 1,\ 1.5,\ 2$ and 2.5.

where τ_{r1} is the rise time and τ_d is the decay time, and the alpha synapse

$$E(t) = \alpha^2 t \exp(-\alpha t), \tag{2.19}$$

where $1/\alpha$ is related to both the rise and decay times. Substituting Eq. (2.17) into (2.16) and differentiating it yield a differential equation

$$\tau_s s' = -s + \tau_s s_{\text{jump}} \sum_k \delta(t - t^{(k)}). \tag{2.20}$$

Similarly, the double exponential function and the alpha function will yield a system of two first-order ODEs [88].

The motivation for these phenomenological models arises from the exponential-like pulses observed experimentally, as shown in the first row of Fig. 2.6 for one spike. The simple form is particularly useful for the construction and simulation of large networks of synaptic-coupled neurons. Note that the constraint $s \in [0, 1]$ should be included when applying these phenomenological models, since there is a chance that s may exceed 1 if the spikes are close enough to each other, as shown in the second row of Fig. 2.6(b) and (c). Here, panel (b) illustrates the single exponential synapse, while panel (c) shows the alpha synapse.

2.4.3 Synapse with Short-Term Plasticity

More accurate synapse models can be obtained by considering short-term plasticity (STP). STP refers to dynamic changes in the strength or efficacy of synaptic transmission due to the firing of presynaptic cells. This process is typically associated with the dynamic properties of neurotransmitter release and subsequent recovery. Synaptic depression occurs when the postsynaptic response decreases with repetitive presynaptic activity, while synaptic facilitation increases synaptic efficacy.

Since the 1950s, there have been increasing efforts to develop mathematical models for STP [134, 108]. A simple phenomenological model, proposed by Tsodyks and Markram [205], has been widely accepted and used in many studies, e.g., [149, 171, 199]. This model is described as

$$\tau_d X' = 1 - X - \tau_d X^- U^+ s, \tag{2.21}$$

$$\tau_f U' = U_0 - U + \tau_f U_0 (1 - U^-) s, \tag{2.22}$$

where $X \in [0, 1]$ represents the proportion of available presynaptic resources recovered from the refractory state, $U \in [0, 1]$ represents the fraction of these available resources utilized to generate the postsynaptic current, τ_d and τ_f are the depression and facilitation time constants, respectively, and U_0 is the baseline utilization. Here, the superscript "$-$" denotes a quantity just before the presynaptic neuron spikes (left limit), and "$+$" denotes a quantity just after a spike occurs (right limit). Having the STP dynamics, we can rewrite the PSC, Eq. (2.12), by adding a modulation factor $X^- U^+$,

$$I_{\text{syn}} = X^- U^+ \bar{g}_{\text{syn}} s (V_{\text{post}} - E_r) \tag{2.23}$$

Note that only the values at left- and right-limit spike times matter for the PSC. The idea behind the Tsodyks-Markram (TM) model is that when the presynaptic neuron emits a spike, neurotransmitters are released, leading to a decrease in X; simultaneously, calcium accumulates at the presynaptic axon terminals, increasing the probability of neurotransmitter release at the next spike emission and thus enhancing the fraction U of utilized resources; see Fig. 2.1(b).

Like other phenomenological models, the TM model, despite its mathematical simplicity, includes parameters and variables that are not experimentally measurable or physiologically well-defined. In chapter 5, we will introduce a kinetic STP model [132, 195] which incorporates descriptions of the calcium dynamics involved in the neurotransmitter release process. This kinetic model is simple enough to allow us to develop a mean-field model, which we will use to investigate the synaptic dynamics within the context of large neural networks. In addition, STP usually occurs on a time scale of milliseconds to seconds [144, 225] and results in a time delay between the firing of the presynaptic cell and the response in the postsynaptic cell. Maex and De Schutter [141] proposed that the specific nature of the delay is insignificant; rather, the crucial factor is the temporal gap established between neurons. Hence, in Chapter 4, we will explicitly incorporate a delay term in neural connections to simulate delayed synaptic transmission and investigate its impact on the collective dynamics of Izhikevich neural networks using mean-field models.

2.5 Neural Networks

2.5.1 Two Coupled Neurons

In this section, we will examine the firing patterns of a pair of coupled neurons described by the conductance-based Wang and Buzśaki model [211], connected by a GABA$_A$ synapse represented by the kinetic model (2.11) and (2.13). The specific parameter settings can be found in [67]. Let neuron 1 be the presynaptic neuron and neuron 2 be the postsynaptic neuron. Then the system is governed by

$$\begin{aligned} C_1 V_1' &= -I_{\text{ion},1} + I_1, \\ C_2 V_2' &= -I_{\text{ion},2} + I_2 - I_{\text{syn}}, \end{aligned} \tag{2.24}$$

where I_1 and I_2 are the applied currents; $I_{\text{ion},1}$ and $I_{\text{ion},2}$ are composed of the leaky current and the Hodgkin–Huxley type currents of Na^+ and K^+ with the same parameter values; the coupling is

$$\begin{aligned} I_{\text{syn}} &= \bar{g}_{\text{syn}} s (V_2 - E_r) \\ s' &= \alpha \frac{T_{\max}}{1 + \exp(-(V_1 - V_p)/K_p)} (1 - s) - \beta s. \end{aligned} \tag{2.25}$$

These equations are supplemented by equations for the gating variables of the ionic currents for each neuron, similar to those found in Eq. (2.1). Fig. 2.7 illustrates the temporal

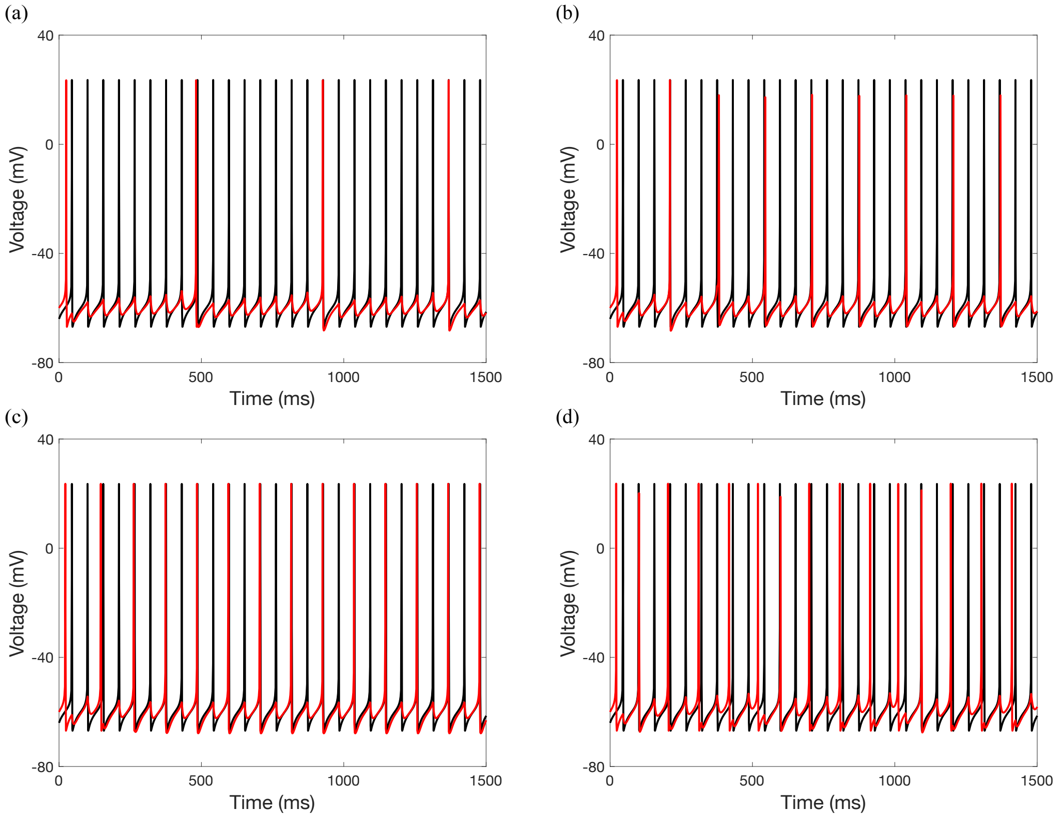

Figure 2.7: Two neurons coupled with a GABA_A synapse. The neuron is modeled as the conductance-based Wang Buzśaki model [211]. The synapse is modeled as a kinetic model (2.11) and (2.13). Parameter values: $I_1 = 0.3$ and (a): $I_2 = 0.28$, (b): $I_2 = 0.29$, (c): $I_2 = 0.31$, and (d): $I_2 = 0.32$. See other parameter values in [67]. Neuron 1/2: black/red.

evolution of the membrane potentials of two neurons. It can be observed that for $I_2 = 0.28$ in Fig. 2.7(a), after a brief transient period, the two neurons become phase locked (synchronized), with neuron 2 firing once for every eight spikes of neuron 1. For $I_2 = 0.29$ in Fig. 2.7(b), the two neurons remain phase locked, but with neuron 2 firing once for every three spikes of neuron 1. For $I_2 = 0.31$ in Fig. 2.7(c), the two neurons are phase locked, with neuron 2 firing once for every two spikes of neuron 1, resembling the behavior in $I_2 = 0.3$ (not shown) but with a slightly different amplitude for neuron 2. At $I_2 = 0.32$ in Fig. 2.7(d), the two neurons are not synchronized.

2.5.2 Network Models

Brain functions are carried out through neural networks that typically comprise thousands of neurons. Although conductance-based neuron models include biophysical details, simplified integrate-and-fire models are better suited for studying the collective dynamics of large-scale neural networks.

For the ith postsynaptic neuron in the network, its integrate-and-fire form is generally described as

$$v_i' = f(v_i) + I_i - I_{\text{syn},i}. \tag{2.26}$$

Its PSC, $I_{\text{syn},i}$, is the cumulative outcome of contributions from all the coupled presynaptic neurons j, given by

$$I_{\text{syn},i} = (v_i - e_r)\bar{g}_i s_i = (v_i - e_r)\sum_{j=1}^{N} \bar{g}_{ij} s_{ij}, \tag{2.27}$$

where $\bar{g}_{ij}$ is the maximal synaptic conductance between the postsynaptic neuron i and the presynaptic neuron j. Taking $\bar{g}_{ij} = g_{\text{syn}}/N$ yields

$$I_{\text{syn},i} = (v_i - e_r)\frac{g_{\text{syn}}}{N}\sum_{j=1}^{N} s_{ij} = (v_i - e_r) g_{\text{syn}} s_i = (v_i - e_r) g_{\text{syn}} s, \tag{2.28}$$

where $\bar{g}_i = g_{\text{syn}}$ is the maximal synaptic conductance of the neuron i and we assume it is homogeneous across the network [158]. $s_i = 1/N \sum_{j=1}^{N} s_{ij}$ is the network-average synaptic activation. For all-to-all connectivity, that is, the neuron i is coupled with all N neurons in the network, including itself, we have $s_i = s$ for all i since every postsynaptic neuron receives the same sum of inputs from all presynaptic neurons. For sparsely coupled networks with a distributed connection or distributed coupling strength, we can set $\bar{g}_{ij} = \bar{g}_i$ with probability $p \ll 1$ in Eq. (2.27). For further details, refer to [89, 50, 127]. In this thesis, we focus on the all-to-all connection scenario. As an example, the Izhikevich neural network is governed by

$$\begin{aligned}
&v_i'(t) = v_i(v_i - \alpha) - w_i + I_i - (v_i - e_r) g_{\text{syn}} s(t),\\
&w_i'(t) = a(b v_i - w_i),\\
&\text{if } \ v_i \geq v_{\text{peak}}, \ \text{ then } v_i \leftarrow v_{\text{reset}}, w_i \leftarrow w_i + w_{\text{jump}},
\end{aligned} \tag{2.29}$$

with the single exponential synapse

$$\tau_s s'(t) = -s(t) + \tau_s s_{\text{jump}} \frac{1}{N}\sum_{j=1}^{N}\sum_{k} \delta(t - t_j^{(k)}) \tag{2.30}$$

for $i = 1, 2, \ldots, N$. Each neuron has a different current parameter I_i drawn from the Lorentzian distribution with center $\bar{I}$ and half-width at half-maximum (HWHM) Δ_I, i.e.,

$$\mathcal{L}(I) = \frac{1}{\pi} \frac{\Delta_I}{(I - \bar{I})^2 + \Delta_I^2}. \tag{2.31}$$

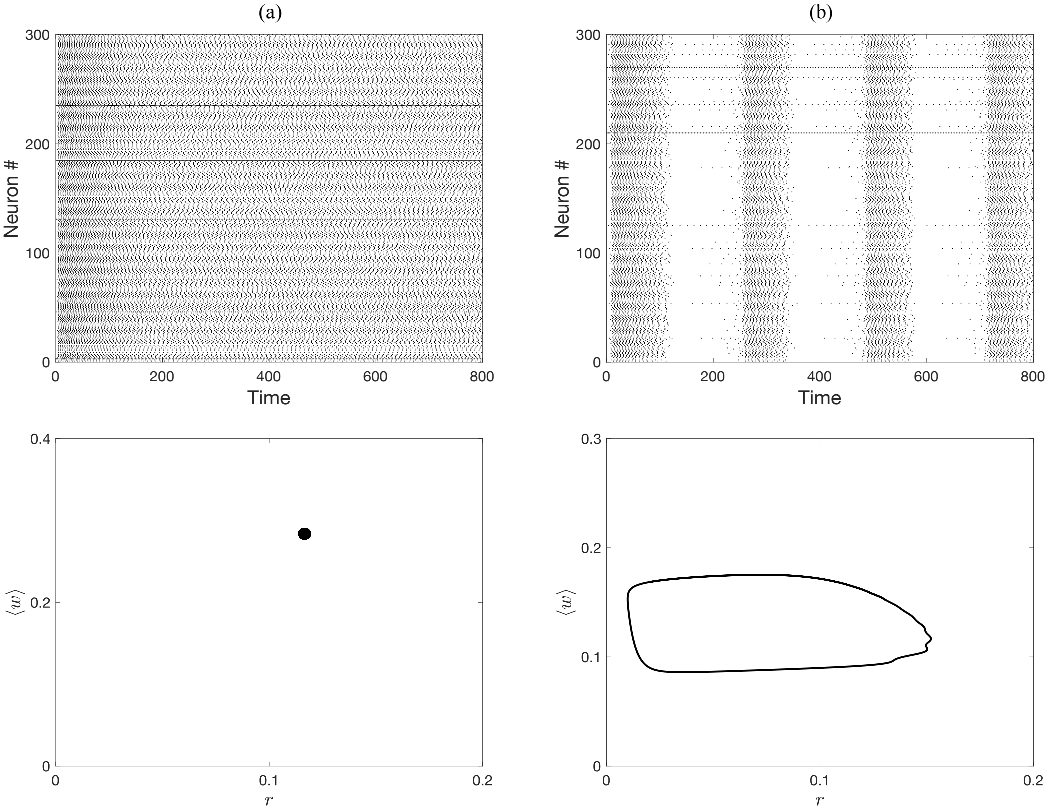

Figure 2.8: Typical macroscopic behaviors of the Izhikevich neural network. (a): asynchronous tonic firing with $\bar{I} = 0.25$, (b): synchronous bursting with $\bar{I} = 0.12$. Parameter values: $N = 10^4$, $\Delta_I = 0.02$ and $\Delta t = 0.02$. See others in Fig. 1 of [53].

A network of neurons performs its function via emergent collective behaviors, such as the average rate of spiking and the synchrony of spiking across neurons in the network. The emergence of these macroscopic phenomena results from interactions among a large number of isolated microscopic units and is distinct from individual microscopic dynamics. Fig. 2.8 shows two typical macroscopic behaviors by simulating a network of $N = 10^4$ Izhikevich neurons described by Eqs. (2.29)-(2.31). We randomly choose 300 neurons and plot their spike times with black dots in the raster plots; each dot along the row indicates a spike event at a specific time; see the first row of Fig. 2.8. Furthermore, we depict the macroscopic behaviors in phase portraits in terms of the population firing rate $r(t)$ and the mean adapting current $w(t)$, averaged across the entire network, as shown in the second row of Fig. 2.8. Note that we calculate the instantaneous population firing rate $r(t)$ at time t by counting the number of spikes $N_{\mathrm{spike}}(t)$ fired by neurons within the time window $[t-\Delta t, t]$, that is,

$$r(t) = \frac{N_{\mathrm{spike}}(t)}{\Delta t \cdot N}.$$

Here, we choose $\Delta t = 0.02$ in the numerical simulation. In column (a) of Fig. 2.8, individual neurons exhibit asynchronous tonic firing while the network settles on a stable EP. If we adjust the value of $\bar{I}$, as shown in column (b), the network transitions to synchronous bursting, where most neurons alternate synchronously between firing a volley of spikes and a quiescent state periodically, and the network settles on a stable PO. In fact, there exist various forms of synchronous activity, including different phase-locked behaviors illustrated in Fig. 2.7 for two coupled neurons, and population-bursting behaviors similar to those depicted in Fig. 2.2(c) for an individual neuron, which will be discussed in Chapter 4.

Transitions between synchronous and asynchronous neural dynamics, or between different patterns of synchronization, are arguably of utmost importance for the study of brain function [186, 34]. In some instances, synchronization of neural activity is beneficial and serves as a crucial mechanism, such as for integrating separate pieces of information into unified representations [80], and for efficient information transmission [105]. However, in other cases, neural synchronization can be detrimental and has been observed in a variety of neurological disorders, e.g., epilepsy [153] or Parkinson's disease [180]. From Fig. 2.8, we can see that it is feasible to predict the collective dynamics of the neural network by using mean-field variables. This concept forms the basis for the mean-field approximation, which constructs a dynamical system in terms of average variables across the network. Due to its low dimensionality, this approach allows for tractable bifurcation analysis, a powerful tool for studying dynamic transitions. This analysis can help uncover the underlying mechanisms of brain functions and dysfunctions, leading to the development of potential treatments. In subsequent chapters, we apply the mean-field approach to large-scale neural networks with SFA, time delays in neuron communication, and short-term synaptic plasticity. Through mean-field models, we aim to deepen our understanding of brain function and dysfunction from a dynamical systems perspective.

Note that in this chapter, the numerical simulations in Fig. 2.2, Fig. 2.4-2.8 were created using MATLAB [145], while the bifurcation diagrams in Fig. 2.3 were generated with XPPAUT [83].

Chapter 3

Mean-Field Modeling for Neural Networks with Spike Frequency Adaptation

This chapter aims to analytically derive a set of mean-field equations for the Izhikevich neural network. Each neuron in this network is represented by a two-dimensional system that comprises a quadratic integrate-and-fire (QIF) equation and an equation that implements spike frequency adaptation (SFA). The challenge lies in achieving a closed mean-field system that incorporates the dynamics of the adaptation variable without assuming that it operates on a sufficiently slow timescale. To address this problem, we propose using the Lorentzian ansatz to remove the assumption of a separation of time scales, as commonly done in the literature, and using the moment closure method to release the dependence of the adaptation variable on the membrane potential to help close the mean-field system (Sec. 3.3). This approach allows us to derive a mean-field system that is valid in the limit of infinitely many neurons in the network. This system can qualitatively and quantitatively describe the collective dynamics of the neural network, including transitions between asynchronous tonic firing and synchronous bursting states (Sec. 3.4). We further extend this approach to a network consisting of two populations of neurons with different adaptation intensities. Through numerical bifurcation analysis, we identify bifurcations not previously observed in existing models, including a novel mechanism for the emergence of bursting in the network, highlighting the utility and significance of our proposed mean-field framework (Sec. 3.5). Finally, we assess the accuracy and effectiveness of our mean-field approximations by examining all assumptions made during the derivation process in Sec. 3.6.

3.1 Mean-Field Approaches in Neuroscience

A central topic of computational neuroscience research is to develop computationally and analytically tractable models that describe the collective activities of neural networks underlying normal brain functions such as memory and decision-making, as well as brain disorders like epilepsy or Parkinson's disease. Various approaches rooted in mean-field theory have been proposed to model these low-dimensional neural dynamics using mean-field variables such as population firing rates and mean membrane potentials.

The development of mean-field models has a long history that spans more than a half century, e.g. [25]. Models in this field can generally be classified into two types: phenomenological models and exact models. Phenomenological models, which have been active since the 1970s, are not derived from specific neural network structures, but are designed to resemble macroscopic features of neural dynamics observed in physiology, disregarding individual neuron behaviors. The Wilson-Cowan (WC) model [217, 218] and its three well-known variants [224, 119, 135] are examples of such phenomenological models. The standard WC model describes the macroscopic evolution equations for the rate dynamics of two coupled populations of excitatory and inhibitory neurons, given by

$$\begin{aligned}\tau_e \frac{dE}{dt} &= -E + S_e(c_1 E - c_2 I + P),\\ \tau_i \frac{dI}{dt} &= -I + S_i(c_3 E - c_4 I + Q),\end{aligned}$$

where E is the time coarse-grained variable representing the proportion of excitatory cells firing at time t, I for the population of inhibitory cells, P and Q are external inputs. The WC models are essentially phenomenological. Their core part is that the average input-output firing rate relationship $S(\cdot)$ is approximated by a nonlinear, instantaneous function, typically a sigmoidal function. While this choice is consistent with physiology and commonly used in neuronal dynamics modeling, it is based on experimental observations and lacks a direct connection to individual neurons. Consequently, these mean-field descriptions cannot account for spike synchronization arising from dynamic interactions between neurons [70]. Furthermore, the WC models lack a description of the mean membrane potential, which is a crucial variable to capture the macroscopic evolution of neural networks. This potential carries equivalent information to electroencephalogram (EEG)s, event-related potentials (ERP)s and local field potentials [147] and is frequently used to characterize brain activity in electrophysiological studies such as working memory [209, 199]. Despite these limitations, the WC models have inspired many theoretical developments. For a historical perspective on the development of these ideas, see [10, 68, 219].

As an alternative, exact macroscopic descriptions have been analytically developed through mean-field reduction of neural network models, using concepts from statistical physics. These models bridge the microscopic properties of individual neurons with the collective dynamics of the neural network. Thus, they can account for phenomena that the phenomenological models cannot and have been called the "next generation" mean-field models [38]. The development of exact mean-field models has followed two threads, both based on the population density approach from statistical physics. This approach yields a conservation law for the population density function, which represents the dynamics of the network. In one thread, the population density approach was applied to networks of spiking neurons [2, 204, 160, 161, 11, 140, 158, 14, 41]. In the other thread, this approach was applied to networks of coupled phase models [196, 213, 214, 163, 164, 165, 173]. Recently, these two threads have started to converge when it was shown that the Ott-Antonsen (OA) theory [163, 164, 165] could be applied to networks of coupled QIF neurons using the link between the QIF model and the theta model and the equivalence between the low-dimensional OA manifold and the Lorentzian ansatz [150]. A general description of such a mean-field model is given by

$$\begin{aligned} r' &= f(r, \langle v\rangle, \bar{p}, \Delta_p), \\ v' &= g(r, \langle v\rangle, \bar{p}, \Delta_p), \end{aligned} \tag{3.1}$$

where r is the population firing rate and $\langle v\rangle$ is the mean membrane potential, both averaged across the network; p is the parameter representing a heterogeneous source, that is, each neuron in the network has a different parameter value drawn from a distribution function with the mean $\bar{p}$ and deviation Δ_p. Note that the OA theory (or Lorenzian ansatz) only defines an invariant manifold for system dynamics. The stability of this manifold has been a matter of debate for years until recent works, [49] for the phase model and [172] for the QIF model, confirmed what researchers had already seen in numerical simulation: the OA manifold is attractive for the heterogeneous network, i.e., $\Delta_p > 0$. These articles [49, 172] essentially extend the Watanabe-Strogatz (WS) method from the homogeneous network, i.e., $\Delta_p = 0$, to the heterogeneous network. The WS theory, proposed by Watanabe and Strogatz [213, 214], is also an important mean-field theory developed for networks of coupled phase models. It has a complete description of the stability of the system, but only for the homogeneous network. By establishing the connection between the WS mean-field model and the OA model with $\Delta_p = 0$, Pikovsky and Rosenblum [173, 174] proved that the OA manifold for $\Delta_p = 0$ is only marginally stable, meaning the system must be initialized within the OA manifold for the homogeneous network. In summary, the OA theory is suitable for heterogeneous neural networks. The OA manifold for $\Delta_p > 0$ has been theoretically shown to be attractive. However, implementing the WS method, especially in closing the mean-field equations, is complex, as it requires expressing mean synaptic activation through mean-field variables [126]. For homogeneous neural networks where $\Delta_p = 0$, one should use the WS method for coupled phase models or the population density approach directly applied to spiking neural networks, e.g., [158]. In this thesis, we employ the theoretical framework of OA theory since the biological neural network exhibits significant heterogeneity across neurons and synaptic couplings. In Chapter 4, we investigate the OA-based mean-field model in the limit $\Delta_p \to 0$.

3.2 Izhikevich Neural Network

The Izhikevich neuron comprises a fast subsystem based on the QIF model and a slow subsystem modeling the mechanism of SFA. Details of the Izhikevich neuron are provided in Chapter 2. The SFA has been shown to enhance neural coding and computation at a lower metabolic cost [103, 92, 185]. It has also been demonstrated to play a crucial role in the emergence of network bursting and synchronization [207, 157, 122, 89, 96]. Recent work has focused on deriving mean-field descriptions for neural networks with SFA [14, 41, 47, 72]. These descriptions vary in the neuron models employed, the types of approximations used, and the behaviors the mean-field models can analyze. In this chapter, we utilize the Izhikevich neuron. The resulting Izhikevich network has been extensively used to investigate brain function [118, 78] and dysfunction [181]. Its numerical and theoretical efficiency makes it well suited for exploring the collective dynamics of neural networks through mean-field descriptions.

The network model for a population of Izhikevich neurons is described by the following discontinuous ordinary differential equations (ODEs),

$$\begin{aligned}
&v_i'(t) = v_i(v_i - \alpha) - w_i + I_{\text{ext}}(t) + \eta_i + I_{\text{syn},i}(t),\\
&w_i'(t) = a(bv_i - w_i),\\
&\text{if } \ v_i \geq v_{\text{peak}}, \ \text{ then } v_i \leftarrow v_{\text{reset}}, w_i \leftarrow w_i + w_{\text{jump}},
\end{aligned} \tag{3.2}$$

for $i = 1, 2, \ldots, N$. Here, $' = d/dt$ denotes the time derivative, $v_i(t)$ is the membrane potential of ith neuron and w_i is the recovery current, which serves as an adaptation variable. By construction, $v_i \in (-\infty, v_{\text{peak}}]$, while w has no constraints, $w_i \in (-\infty, \infty)$. The parameter η_i is the intrinsic current, while I_{ext} is the external common current. We will assume that η_i is drawn from a distribution $\mathcal{L}(\eta)$ defined on $(-\infty, \infty)$. The term I_{syn} represents the total synaptic current due to the other neurons in the network. When the voltage reaches a cut-off value, denoted as the peak of a spike v_{peak}, it is reset to the value

v_{reset}. At the same time, the adaptation variable jumps by an amount w_{jump}, which affects the after spike behavior. When in the limit of $v_{\mathrm{peak}} = -v_{\mathrm{reset}} \to \infty$, the Izhikevich model (3.2) can be transformed into the theta model with adaptation, where the neuron fires a spike whenever θ crosses π; see Fig. 2.4(c).

The neurons in the network are connected by synapses using the standard conductance-based synaptic current model [88]

$$I_{\mathrm{syn},i} = g_{\mathrm{syn}} s_i (e_r - v_i), \tag{3.3}$$

where e_r is the reversal potential and g_{syn} the maximum synaptic conductance, both assumed to be the same for all neurons. The synaptic gating variable, s_i, lies between 0 to 1 and represents the proportion of ion channels open in the postsynaptic neuron as the result of the firing in presynaptic neurons. For simplicity, we assume that neurons are all-to-all coupled. This assumption has been widely used in the literature [88, 150, 39]. Specifically, it is reasonable for the application to the CA3 region of hippocampus we will consider later, since this region is highly recurrently coupled [8, 9, 35]. We will discuss the necessity of all the assumptions we make and possible extensions that relax some of these requirements in Sec. 3.6. For a network with all-to-all connectivity, s_i is homogeneous across the network as every postsynaptic neuron receives the same summed input from all presynaptic neurons, thus $s_i = s$. The mechanism of synaptic transmission can be formally described by a linear system of ODEs with a sum of delta pulses corresponding to the times a neuron fires an action potential [88]. For simplicity, we consider the single exponential synapse, given by

$$s' = -\frac{s}{\tau_s} + \frac{s_{\mathrm{jump}}}{N} \sum_{j=1}^{N} \sum_{k} \delta(t - t_j^{(k)}), \tag{3.4}$$

where $\delta(t)$ is the Dirac delta function, and t_j^k represents the time of the kth spike of the jth neuron. We assume that the parameters s_{jump} and τ_s are the same for every synapse. It is straightforward to extend our approach to the double exponential synapse and the alpha synapse; see Sec. 2.4.2.

Here, the network system of (3.2)-(3.4) is dimensionless, which is appropriate for mathematical and numerical exploration of the neurodynamics. However, neuroscientists are normally accustomed to the dimensional form with parameters that have physiological interpretation, e.g., [78, 181]. Here is the dimensional form of the Izhikevich network, given by

$$\begin{aligned}
C\frac{dV_i}{dT} &= k_1(V_i - V_T)(V_i - V_R) - W_i + I_{\text{sum},k} + G_{\text{syn}}s(E_r - V_i), \\
\tau_W\frac{dW_i}{dT} &= \beta(V_i - V_R) - W_i, \\
\frac{ds}{dT} &= -\frac{s}{\tau_{\text{syn}}} + \frac{S_{\text{jump}}}{N}\sum_{j=1}^{N}\sum_{k}\delta(t - t_j^{(k)}), \\
&\text{if } V_i \geq V_{\text{peak}}, \text{ then } V_i \leftarrow V_{\text{reset}}, \; W_i \leftarrow W_i + W_{\text{jump}},
\end{aligned} \tag{3.5}$$

where $i = 1, 2, \ldots N$. The parameters are described in Table 3.1 and the values are taken from [158, 159] that were originally fitted by [78] to the data of pyramidal neurons in the hippocampal CA3 region [107]. Table 3.2 gives the whole scaling relationship between the dimensionless and the dimensional systems.

Parameters	Values	Description
C	250 pF	Membrane capacitance
k_1	2.5 nS/mV	Scaling factor
V_R	-65 mV	Resting potential
V_T	-24.6 mV	Threshold potential, $V_T = V_R + 40 - \frac{\beta}{k_1}$
G_{syn}	200 nS	Synaptic conductance
E_r	0 mV	Reversal potential
β	-1 nS	Scaling factor
τ_W	200 mS	Time constant of W
τ_{syn}	4 mS	Time constant of s
S_{jump}	0.8	Coupling strength
W_{jump}	200 pA	After-spike jump size

Table 3.1: Parameters for the dimensional Izhikevich network (3.5) based on [158, 159].

$v_i = 1 + \frac{V_i}{\lvert V_R\rvert}$	$w_i = \frac{W_i}{k_1\lvert V_R\rvert^2}$	$s = s$
$e_r = 1 + \frac{E_r}{\lvert V_R\rvert}$	$v_{\text{peak}} = 1 + \frac{V_{\text{peak}}}{\lvert V_R\rvert}$	$v_{\text{reset}} = 1 + \frac{V_{\text{reset}}}{\lvert V_R\rvert}$
$\alpha = 1 + \frac{V_T}{\lvert V_R\rvert}$	$g_{\text{syn}} = \frac{G_{\text{syn}}}{k_1\lvert V_R\rvert}$	$a = \left(\frac{\tau_W k_1\lvert V_R\rvert}{C}\right)^{-1}$
$b = \frac{\beta}{k_1\lvert V_R\rvert}$	$s_{\text{jump}} = S_{\text{jump}}\frac{C}{k_1\lvert V_R\rvert}$	$w_{\text{jump}} = \frac{W_{\text{jump}}}{k_1\lvert V_R\rvert^2}$
$\eta + I_{\text{ext}} = \frac{I_{\text{app}}}{k_1\lvert V_R\rvert^2}$	$T = \frac{C}{k_1\lvert V_R\rvert}t$	$\tau_s = \frac{\tau_{\text{syn}} k_1\lvert V_R\rvert}{C}$

Table 3.2: Scaling relations between the dimensionless (3.2)-(3.4) and dimensional (3.5) Izhikevich neural networks.

3.3 Derivation of Mean-Field Models

The network model becomes too complex for tractable analysis, particularly with a large number of neurons. In this section, we aim to develop a low-dimensional mean-field model to approximate the behavior of the full network, described by equations (3.2)-(3.4), valid in the thermodynamic limit ($N \to \infty$). We will show how to describe key macroscopic variables and derive their reduced macroscopic dynamics, cast as ODEs, through step-by-step assumptions. Our approach combines ideas from prior works [158, 159, 140, 150].

3.3.1 General Mean-Field Description

The mean-field approximation is essentially a technique that borrows concepts and methods from statistical physics, e.g., the population density approach [140], the continuity equation (or the Fokker-Planck equation when the system is subject to noise) [64, 28]. We define the population density function $\rho(t, v, w, \eta)$ as the density of neurons at a point (v, w) in phase space with the parameter η at time t. In the limit $N \to \infty$, the principle of conservation mass leads to the following evolution equation for the density function, that is, the continuity equation,

$$\frac{\partial}{\partial t}\rho(t, v, w, \eta) + \bigtriangledown \cdot \mathcal{J}(t, v, w, s, \eta) = 0, \tag{3.6}$$

where the probability flux is defined as

$$\mathcal{J}(t, v, w, s, \eta) = \begin{pmatrix} \mathcal{J}^v(t, v, w, s, \eta) \\ \mathcal{J}^w(t, v, w) \end{pmatrix} = \begin{pmatrix} G^v(v, w, s, \eta) \\ G^w(v, w) \end{pmatrix} \rho(t, v, w, \eta),$$

and

$$\begin{aligned} G^v(\cdot) &= v(v-\alpha) - w + \eta + I_{\text{ext}} + g_{\text{syn}} s(e_r - v), && (3.7\text{a}) \\ G^w(\cdot) &= a(bv - w). && (3.7\text{b}) \end{aligned}$$

Note that $\mathcal{J}^v(t, v, w, s, \eta)$ depends on s. The flux is intuitively the mass flow rate along a specific direction in phase space. A boundary condition for the flux, consistent with the resetting rule in Eq. (3.2), is imposed,

$$\mathcal{J}^v(v_{\text{peak}}, w) = \mathcal{J}^v(v_{\text{reset}}, w + w_{\text{jump}}). \tag{3.8}$$

We assume the flux to be vanishing on the boundary ∂w, that is, $\rho(t, v, w, \eta) = 0$ in the limit $w \to \pm\infty$ [140]. Then, we can define macroscopic variables in terms of mean-field description, which are extremely useful in understanding brain function. The population firing rate is the flux through the threshold v_{peak} over the entire range of w in the phase space and η in parameter space, defined by

$$r(t) = \lim_{v \to v_{\text{peak}}} \int_{\partial\eta} \int_{\partial w} \mathcal{J}^v(t, v, w, s, \eta) \mathrm{d}w \mathrm{d}\eta = \int_{\partial\eta} \int_{\partial w} \mathcal{J}^v(t, v_{\text{peak}}, w, s, \eta) \mathrm{d}w \mathrm{d}\eta. \tag{3.9}$$

The mean membrane potential is the average over the population, defined by

$$\langle v(t) \rangle = \int_{\partial\eta} \int_{\partial w} \int_{\partial v} v \rho(t, v, w, \eta) \mathrm{d}v \mathrm{d}w \mathrm{d}\eta.$$

Similarly, the mean adaptation current is given by

$$\langle w(t) \rangle = \int_{\partial\eta} \int_{\partial v} \int_{\partial w} w \rho(t, v, w, \eta) \mathrm{d}w \mathrm{d}v \mathrm{d}\eta.$$

Next, we will derive the differential equation for $\langle w \rangle$. The derivation is modified from [159]. Differentiation with respect to time and application of the continuity equation (3.6) yields

$$\langle w \rangle' = \int_{\partial\eta} \int_{\partial v} \int_{\partial w} w \frac{\partial}{\partial t} \rho(t, v, w, \eta) \mathrm{d}w \mathrm{d}v \mathrm{d}\eta = - \int_{\partial\eta} \int_{\partial v} \int_{\partial w} w \left(\frac{\partial \mathcal{J}^v}{\partial v} + \frac{\partial \mathcal{J}^w}{\partial w} \right) \mathrm{d}w \mathrm{d}v \mathrm{d}\eta \tag{3.10}$$

For the first term, we apply integration by parts and interchange the order of integration as needed, then obtain:

$$\begin{aligned}
\text{Term1} &= \int_{\partial\eta}\int_{\partial v}\int_{\partial w} w\frac{\partial \mathcal{J}^v}{\partial v}\mathrm{d}w\mathrm{d}v\mathrm{d}\eta \\
&= \int_{\partial\eta}\int_{\partial w}\int_{\partial v} w\mathrm{d}\mathcal{J}^v(t,v,w,s,\eta)\mathrm{d}w\mathrm{d}\eta \\
&= \int_{\partial\eta}\int_{\partial w} w\Big(\mathcal{J}^v(t,v_{\text{peak}},w,s,\eta) - \mathcal{J}^v(t,v_{\text{reset}},w,s,\eta)\Big)\mathrm{d}w\mathrm{d}\eta \\
&= \int_{\partial\eta}\int_{\partial w} w\Big(\mathcal{J}^v(t,v_{\text{peak}},w,s,\eta) - \mathcal{J}^v(t,v_{\text{peak}},w-w_{\text{jump}},s,\eta)\Big)\mathrm{d}w\mathrm{d}\eta
\end{aligned}$$

For a constant v, we have $\mathcal{J}^v(t,v_{\text{peak}},w,s,\eta) = G^v(\cdot)\rho(t,w,\eta)$ from Eq. (3.6). We can write $\rho(t,w,\eta)$ in conditional form,

$$\rho(t,w,\eta) = \rho^w(t,w|\eta)\mathcal{L}(\eta),$$

with $\mathcal{L}(\eta)$ defined as the probability that a randomly chosen neuron has a current parameter η. Then, assuming $\langle w|\eta\rangle \gg w_{\text{jump}}$, we apply a Taylor expansion and integration by parts to Term 1, resulting in

$$\begin{aligned}
\text{Term1} &= \int_{\partial\eta}\int_{\partial w} w\Big(w_{\text{jump}}\frac{\partial}{\partial w}\mathcal{J}^v(t,v_{\text{peak}},w,s,\eta) + \mathcal{O}(w_{\text{jump}}^2)\Big)\mathrm{d}w\mathrm{d}\eta \\
&= \int_{\partial\eta} w_{\text{jump}}\int_{\partial w} w\mathrm{d}\mathcal{J}^v(t,v_{\text{peak}},w,s,\eta)\mathrm{d}\eta + \mathcal{O}(w_{\text{jump}}^2) \qquad (3.11)\\
&\approx \int_{\partial\eta} w_{\text{jump}}\Big(w\mathcal{J}^v(t,v_{\text{peak}},w,s,\eta)|_{\partial w} - \int_{\partial w}\mathcal{J}^v(t,v_{\text{peak}},w,s,\eta)\mathrm{d}w\Big)\mathrm{d}\eta
\end{aligned}$$

Then, we assume the flux to be vanishing on the boundary ∂w, yielding

$$\text{Term1} = -\int_{\partial\eta}\int_{\partial w} w_{\text{jump}}\mathcal{J}^v(t,v_{\text{peak}},w,s,\eta)\mathrm{d}w\mathrm{d}\eta.$$

Similarly, for the second term of (3.10), we obtain

$$\text{Term2} = \int_{\partial\eta}\int_{\partial v}\int_{\partial w} w\frac{\partial \mathcal{J}^w}{\partial w}\mathrm{d}w\mathrm{d}v\mathrm{d}\eta = -\int_{\partial\eta}\int_{\partial v}\int_{\partial w}\mathcal{J}^w\mathrm{d}w\mathrm{d}v\mathrm{d}\eta = -\langle G^w(t,v,w)\rangle.$$

Thus, we derive the dynamic system of $\langle w\rangle$ in terms of the flux given by

$$\langle w\rangle' \approx \langle G^w(v,w)\rangle + \int_{\partial\eta}\int_{\partial w} w_{\text{jump}}\mathcal{J}^v(t,v_{\text{peak}},w,s,\eta)\mathrm{d}w\mathrm{d}\eta.$$

Further, considering the linearity of $G^w(\cdot)$ function with respect to v and w, see Eq. (3.7), and the description of the population firing rate in terms of flux (3.9), we finally derive the following ODE describing the evolution of the mean adaptation variable,

$$\langle w\rangle' = G^w\big(\langle v\rangle, \langle w\rangle\big) + w_{\text{jump}} r(t) = a\big(b\langle v\rangle - \langle w\rangle\big) + w_{\text{jump}} r(t). \tag{3.12}$$

Next, we rewrite the synaptic dynamics (3.4) in terms of flux description. The derivation is modified from [158]. The key idea is how to connect the population firing rate r with the description in terms of the number of spikes fired by neurons,

$$u(t) = \frac{1}{N}\sum_{j=1}^{N}\sum_{k}\delta(t - t_j^{(k)}). \tag{3.13}$$

We define the function $n_j(t)$ to be the number of spikes fired by the jth neuron in the time interval $[0, t]$,

$$n_j(t) = \int_0^t \sum_k \delta(t' - t_j^{(k)})\mathrm{d}t'.$$

Then, we can relate $u(t)$ to the average of $n_j(t)$ over the population, given by

$$\lim_{N\to\infty}\int_0^t u(t')\mathrm{d}t' = \lim_{N\to\infty}\frac{1}{N}\int_0^t\sum_{j=1}^{N}\sum_{k}\delta(t' - t_j^{(k)})\mathrm{d}t' = \langle n(t)\rangle.$$

We also define the firing rate as the number of spikes per unit time. Then, the population firing rate in this sense of the limit of population activity as $\Delta t \to 0$ is given by [158, 98]

$$r(t) = \lim_{\Delta t\to 0}\frac{1}{\Delta t}\lim_{N\to\infty}\sum_{j=1}^{N}\frac{n_j(t+\Delta t) - n_j(t)}{N}. \tag{3.14}$$

Rearranging the limits yields

$$r(t) = \lim_{\Delta t\to 0}\frac{\langle n(t+\Delta t)\rangle - \langle n(t)\rangle}{\Delta t} = \frac{d}{dt}\langle n(t)\rangle = u(t). \tag{3.15}$$

Thus, we can rewrite the synaptic dynamics (3.4) in terms of the population firing rate as

$$s' = -s/\tau_s + s_{\text{jump}} r(t), \tag{3.16}$$

where $r(t)$ is equivalent to the flux definitioin (3.9). The two equations (3.12) and (3.16) are an integral part of the final mean-field model for the network of Izhikevich neurons. They depend on two macroscopic variables: the mean membrane potential $\langle v(t)\rangle$ and the population firing rate $r(t)$. In the following, we will derive the dynamical system for these two variables.

3.3.2 Density Function in Conditional Form

In this section, we take advantage of the population density approach and the moment closure assumption to reduce the dependence between the macroscopic variables.

1. Moment closure method For brevity, we consider a homogeneous network, that is, the current η is the same for each neuron. We write the population density function in conditional form

$$\rho(t, v, w) = \rho^w(t, w|v)\rho_0^v(t, v). \tag{3.17}$$

We define the marginal density as

$$\rho_0^v(t, v) = \int_{\partial w} \rho(t, v, w)\mathrm{d}w$$

and the mean of w conditioned on v as $\langle w|v\rangle = \int_{\partial w} w\rho^w(t, w|v)\mathrm{d}w$. Then, the kth conditional moment $\langle w^k|v\rangle$ satisfies

$$\int_{\partial w} w^k \rho(t, v, w)\mathrm{d}w = \langle w^k|v\rangle\rho_0^v(t, v) \equiv \rho_k^v(t, v|\eta)$$

Integrating Eq. (3.6) with respect to w yields

$$\begin{aligned} \frac{\partial}{\partial t}\rho_0^v(t, v) &= -\frac{\partial}{\partial v}\Big[\big(G_1^v(v) - \langle w|v\rangle\big)\rho_0^v(t, v)\Big] \\ &= -\frac{\partial}{\partial v}\Big[G_1^v(v)\rho_0^v(t, v) - \rho_1^v(t, v)\Big], \end{aligned} \tag{3.18}$$

where $G_1^v(v) = v(v-\alpha) + \eta + I_{\mathrm{ext}} + g_{\mathrm{syn}}s(e_r - v)$ is the part of Eq. (3.7a) without w. To obtain this expression, we use the normalization condition on the marginal density of w, that is, $\int_{\partial w} \rho^w(t, w|v)\mathrm{d}w = 1$, and the fact that the flux vanishes on the boundary ∂w. One can see that the evolution equation for $\rho_0^v(t, v)$ depends on the unknown function $\rho_1^v(t, v)$. To derive the equation for $\rho_1^v(t, v)$, we can multiply Eq. (3.6) by w and integrate over w again. Then $\rho_2^v(t, v)$ appears on the right-hand side of the evolution equation for $\rho_1^v(t, v)$. Thus, the system is not closed. To close the system, we adopt the moment closure method, which assumes that the kth centered conditional moment of w is independent of v, that is, $\langle w^k|v\rangle = \langle w\rangle^k$. Thus, the mean-field approximation involves expressing the kth conditioned moment as a linear combination of the $k-1$ conditioned moments and the first k unconditioned moments [140]. For the first-order moment closure where $k = 1$, we have

$$\langle w|v\rangle = \langle w\rangle. \tag{3.19}$$

Then, Eq. (3.18) becomes

$$\begin{aligned}\frac{\partial}{\partial t}\rho_0^v(t,v) &= -\frac{\partial}{\partial v}\Big[G^v\big(v,\langle w|v\rangle\big)\rho_0^v(t,v)\Big]\\ &= -\frac{\partial}{\partial v}\Big[G^v\big(v,\langle w\rangle\big)\rho_0^v(t,v)\Big].\end{aligned} \tag{3.20}$$

by the notation $\rho_1^v(t,v) = \langle w|v\rangle\rho_0^v(t,v)$.

2. Mean-field approximation by first-order moment closure Let us return to the heterogeneous network. We express the population density function in conditional form

$$\rho(t,v,w,\eta) = \rho^w(t,w|v,\eta)\rho^v(t,v|\eta)\mathcal{L}(\eta). \tag{3.21}$$

Then, the population firing rate in the general expression (3.9) can be described by the conditional probability $\rho^v(t,v|\eta)$ as

$$\begin{aligned}r(t) &= \lim_{v\to v_{\text{peak}}}\int_{\partial\eta}\int_{\partial w} G^v(v,w,s,\eta)\rho^w(t,w|v,\eta)\cdot\rho^v(t,v|\eta)\mathcal{L}(\eta)\mathrm{d}w\mathrm{d}\eta\\ &= \lim_{v\to v_{\text{peak}}}\int_{\partial\eta}\mathcal{L}(\eta)\rho^v(t,v|\eta)\cdot\int_{\partial w} G^v(v,w,s,\eta)\rho^w(t,w|v,\eta)\mathrm{d}w\mathrm{d}\eta\\ &= \lim_{v\to v_{\text{peak}}}\int_{\partial\eta}\mathcal{L}(\eta)\rho^v(t,v|\eta)\cdot G^v(v,\langle w|v,\eta\rangle,s,\eta)\mathrm{d}\eta.\end{aligned}$$

To balance the trade-off between accuracy and the practicality of the mean-field approximation, we employ first-order moment closure assumption

$$\langle w|v,\eta\rangle = \langle w|\eta\rangle. \tag{3.22}$$

Then, we have

$$r(t) = \lim_{v\to v_{\text{peak}}}\int_{\partial\eta}\mathcal{L}(\eta)\rho^v(t,v|\eta)\cdot G^v(v,\langle w|\eta\rangle,s,\eta)\mathrm{d}\eta. \tag{3.23}$$

Similarly, the mean membrane potential is rewritten as

$$\langle v(t)\rangle = \int_{\partial\eta}\mathcal{L}(\eta)\int_{\partial v} v\rho^v(t,v|\eta)\mathrm{d}v\mathrm{d}\eta. \tag{3.24}$$

Here, we use the normalization condition on the marginal density of w,

$$\int_{\partial w}\rho^w(t,w|v,\eta)\mathrm{d}w = 1.$$

To obtain the evolution equation for $\rho^v(t,v|\eta)$, we integrate the general continuity equation (3.6) with respect to w and use the conditional form (3.21), yielding

$$\frac{\partial}{\partial t}\rho^v(t,v|\eta) = -\frac{\partial}{\partial v}\big[G^v(v,\langle w|v,\eta\rangle,s,\eta)\rho^v(t,v|\eta)\big].$$

Further, by the first-order moment closure assumption, we have the resulting modified continuity equation,

$$\frac{\partial}{\partial t}\rho^v(t,v|\eta) = -\frac{\partial}{\partial v}\big[G^v(v,\langle w|\eta\rangle,s,\eta)\rho^v(t,v|\eta)\big]. \tag{3.25}$$

Thus, we have derived a closed mean-field system for the evolution of $\rho^v(t,v|\eta)$, $\langle w|\eta\rangle$ and s. It consists of Eq. (3.16), (3.23)-(3.25) and an equation analogous to (3.12) for $\langle w|\eta\rangle$. We can derive the steady-state solution to this system, given by

$$\begin{aligned}\overline{\rho}^v(v|\eta) &= \frac{1}{G^v(v,\overline{\langle w|\eta\rangle},\overline{s},\eta)} \\ &= \frac{1}{v(v-\alpha)-\overline{\langle w|\eta\rangle}+\eta+I_{\text{ext}}+g_{\text{syn}}\overline{s}(e_r-v)},\end{aligned} \tag{3.26}$$

where $\overline{\langle w|\eta\rangle}$ and $\overline{s}$ are the steady state values of $\langle w|\eta\rangle$ and s, respectively.

3.3.3 Lorentzian Ansatz

In this section, we will further reduce the mean-field system and the expressions of the macroscopic variables via the Lorentzian ansatz [150], where the limit $v_{\text{peak}} = v_{\text{reset}} \to \infty$ is considered. To begin, we assume that the conditional probability $\rho^v(t,v|\eta)$ satisfies a time-dependent version of Eq. (3.26) and hence can be written in the form of Lorentzian distribution, also known as the Cauchy distribution, as follows,

$$\rho^v(t,v|\eta) = \frac{1}{\pi}\frac{x(t,\eta)}{\big[v-y(t,\eta)\big]^2+x^2(t,\eta)}, \tag{3.27}$$

where $x(t,\eta)$ and $y(t,\eta)$ are two time-dependent parameters defining half-width at half-maximum (HWHM) and center of the distribution, respectively. Moreover, $y(t,\eta)$ is defined via the Cauchy principal value as

$$y(t,\eta) = P.V.\int_{\partial v} v\rho^v(t,v|\eta)\mathrm{d}v = \langle v(t,\eta)\rangle,$$

the reason being that the Lorentz distribution only has a mean in principal value sense. Therefore, the mean membrane potential is related to $y(t,\eta)$ via

$$\langle v(t)\rangle = \int_{\partial\eta} y(t,\eta)\mathcal{L}(\eta)\mathrm{d}\eta. \tag{3.28}$$

Under the condition

$$v_{\text{peak}} = -v_{\text{reset}} \to +\infty$$

corresponding to $\theta = \pi$ in the theta model, the population firing rate defined as Eq. (3.23) is also related to the Lorentzian coefficient through the intermediate expression,

$$\begin{aligned} r(t,\eta) &= \lim_{v\to v_{\text{peak}}} \rho^v(t,v|\eta)G^v(v,\langle w|\eta\rangle,s,\eta) \\ &= \lim_{v_{\text{peak}}\to\infty} \frac{1}{\pi}\frac{x(t,\eta)}{\big[v_{\text{peak}} - y(t,\eta)\big]^2 + x^2(t,\eta)} \\ &\quad\cdot \big[v_{\text{peak}}(v_{\text{peak}}-\alpha) - \langle w|\eta\rangle + \eta + I_{\text{ext}} + g_{\text{syn}}s(e_r - v_{\text{peak}})\big] \\ &= \frac{1}{\pi}x(t,\eta). \end{aligned}$$

The total firing rate is then

$$r(t) = \int_{\partial\eta} r(t,\eta)\mathcal{L}(\eta)\mathrm{d}\eta = \int_{\partial\eta}\frac{1}{\pi}x(t,\eta)\mathcal{L}(\eta)\mathrm{d}\eta. \tag{3.29}$$

Substituting the Lorentzian ansatz (3.27) into the continuity equation (3.25), we obtain two relevant terms: one is given by

$$\partial_t\rho^v(t,v|\eta) = \frac{1}{\pi}\frac{\dot{x}\big[(v-y)^2 - x^2\big] + 2x(v-y)\dot{y}}{\big[(v-y)^2+x^2\big]^2},$$

the other is given by

$$\begin{aligned} \frac{\partial}{\partial v}\big[G^v(\cdot)\rho^v(\cdot)\big] = (2v-\alpha-gs)\rho^v(t,v|\eta) + \big[v(v-\alpha) - \langle w|\eta\rangle + \eta \\ + I_{\text{ext}} + g_{\text{syn}}s(e_r - v)\big]\partial_v\rho^v(t,v|\eta). \end{aligned}$$

We can also obtain

$$\partial_v\rho^v(t,v|\eta) = -\frac{1}{\pi}\frac{2x(v-y)}{\big[(v-y)^2+x^2\big]^2}.$$

Equating the resulting equation in the powers of v yields

$$
\begin{aligned}
v^2\Big[x' - 2xy + (\alpha + g_{\text{syn}}s)\Big] + v\Big[2xy' - 2x'y + 2x(x^2+y^2) + 2x(\langle w|\eta\rangle - \eta - I_{\text{ext}} - g_{\text{syn}}se_r)\Big] \\
+ \Big[x'(y^2 - x^2) - 2xyy' - (\alpha + g_{\text{syn}}s)(x^2+y^2)x \\
+ 2xy\big(\eta + I_{\text{ext}} - \langle w|\eta\rangle + g_{\text{syn}}se_r\big)\Big] = 0
\end{aligned}
$$

Then, we have

$$
\begin{aligned}
x'(t,\eta) &= 2xy - (\alpha + g_{\text{syn}}s)x, \\
y'(t,\eta) &= y(y-\alpha) - x^2 - \langle w|\eta\rangle + \eta + I_{\text{ext}} + g_{\text{syn}}s(e_r - y),
\end{aligned}
\tag{3.30}
$$

where the first equation is from the coefficient of v^2 equal to zero; the second from the coefficient of v equal to zero. Both of them lead to the disappearance of the leftover terms. By defining a complex variable

$$
z(t,\eta) = x(t,\eta) + iy(t,\eta) = \pi r(t,\eta) + i\langle v(t,\eta)\rangle, \tag{3.31}
$$

we write Eq. (3.30) in complex form as

$$
\frac{\partial}{\partial t}z(t,\eta) = i\Big[-z^2(t,\eta) + iz(t,\eta)(\alpha + g_{\text{syn}}s) - \langle w|\eta\rangle + \eta + I_{\text{ext}} + g_{\text{syn}}se_r\Big]. \tag{3.32}
$$

So far, we have obtained the reduced mean-field system for the dynamics of the two macroscopic variables $r(t,\eta)$ and $\langle v(t,\eta)\rangle$ via Eqs. (3.28), (3.29), (3.31) and (3.32). However, both variables depend on the heterogeneous current η and $\langle w|\eta\rangle$ and therefore on the distribution $\mathcal{L}(\eta)$.

3.3.4 Heterogeneity with Lorentzian Distribution

Further reduction of the mean-field system depends on the distribution of the heterogeneous parameter, η. Specifically, we choose η to have a Lorentzian distribution with center $\bar{\eta}$ and HWHM Δ_η, i.e.,

$$
\mathcal{L}(\eta) = \frac{1}{\pi}\frac{\Delta_\eta}{(\eta - \bar{\eta})^2 + \Delta_\eta^2}. \tag{3.33}
$$

Then we apply the residue theorem to evaluate the integrals of (3.28) and (3.29) for $\eta \in (-\infty, \infty)$.

We begin by denoting the line integral around an oriented rectifiable curve γ,

$$\oint_\gamma f(\eta)\mathrm{d}\eta \equiv \oint_\gamma \frac{1}{\pi}x(t,\eta)\mathcal{L}(\eta)\mathrm{d}\eta.$$

Substituting the Lorentzian distribution (3.33) yields

$$\begin{aligned} f(\eta) &= \frac{1}{\pi^2}x(t,\eta)\frac{\Delta_\eta}{(\eta-\bar{\eta})^2+\Delta_\eta^2} \\ &= \frac{x(t,\eta)}{\pi^2}\cdot\frac{1}{2i}\left(\frac{1}{\eta-(\bar{\eta}+i\Delta_\eta)}-\frac{1}{\eta-(\bar{\eta}-i\Delta_\eta)}\right). \end{aligned}$$

Then, the residue of $f(\eta)$ at the point $\eta_1=\bar{\eta}-i\Delta_\eta$ is

$$\mathrm{Res}(f,\eta_1) = -\frac{x(t,\bar{\eta}-i\Delta_\eta)}{2\pi^2 i}$$

Let's define the clockwise contour γ (shown in Fig. 3.1) that goes along the real line from $-a$ to a and then clockwise along a semicircle centered at the origin from a to $-a$. Take a to be greater than Δ_η, so that the point $\eta_1=\bar{\eta}-i\Delta_\eta$ is enclosed within the curve.

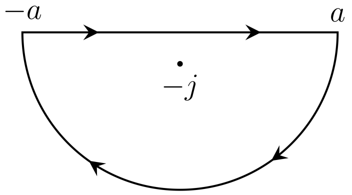

Figure 3.1: The contour γ for the parameter η using to solve the integrals (3.28) and (3.29) when $a\to+\infty$.

According to the residue theorem, we have

$$\oint_\gamma f(\eta)\mathrm{d}\eta = 2\pi i\cdot(-\mathrm{Res}(f,\eta_1)) = \frac{1}{\pi}x(t,\bar{\eta}-i\Delta_\eta)$$

Splitting the contour γ into a straight part and a curved arc, yields

$$\oint_\gamma f(\eta)\mathrm{d}\eta = \int_{straight} f(\eta)\mathrm{d}\eta + \int_{arc} f(\eta)\mathrm{d}\eta$$

and thus

$$\int_{-a}^{a} f(\eta)\mathrm{d}\eta = \frac{1}{\pi}x(t,\bar{\eta}-i\Delta_\eta) - \int_{arc} f(\eta)\mathrm{d}\eta \tag{3.34}$$

Next, we will show that the integral $\int_{arc} f(\eta)\mathrm{d}\eta$ goes to zero as $a \to +\infty$. From the estimation lemma, also known as the ML inequality, we have

$$\begin{aligned}\left|\int_{arc} f(\eta)\mathrm{d}\eta\right| &= \left|\int_{arc} \frac{1}{\pi^2}x(t,\eta)\frac{\Delta_\eta}{(\eta-\bar{\eta})^2+\Delta_\eta^2}\mathrm{d}\eta\right| \\ &\leq l(arc)\cdot\sup_{arc}\left|\frac{1}{\pi^2}x(t,\eta)\frac{\Delta_\eta}{(\eta-\bar{\eta})^2+\Delta_\eta^2}\right|,\end{aligned} \tag{3.35}$$

where $l(arc)$ is the arc length of the contour γ shown in Fig. 3.1. By observing that the arc is half the circumference of a circle with radius a, we have

$$l(arc) = \frac{1}{2}(2\pi a) = \pi a.$$

Then, we seek the upper bound $\sup_{arc}\left|\frac{1}{\pi^2}x(t,\eta)\frac{\Delta_\eta}{(\eta-\bar{\eta})^2+\Delta_\eta^2}\right|$. By the triangle inequality we see that

$$\begin{aligned}|\eta-\bar{\eta}|^2 &= \left|(\eta-\bar{\eta})^2\right| \\ &= \left|(\eta-\bar{\eta})^2+\Delta_\eta^2-\Delta_\eta^2\right| \\ &\leq \left|(\eta-\bar{\eta})^2+\Delta_\eta^2\right|+\Delta_\eta^2.\end{aligned}$$

Thus,

$$\left|(\eta-\bar{\eta})^2+\Delta_\eta^2\right| \geq |\eta-\bar{\eta}|^2-\Delta_\eta^2.$$

When η goes to $\pm\infty$, i.e., $a \to +\infty$, we have

$$\left|\frac{1}{(\eta-\bar{\eta})^2+\Delta_\eta^2}\right| \leq \frac{1}{|\eta-\bar{\eta}|^2-\Delta_\eta^2} = \frac{1}{a^2-\Delta_\eta^2}.$$

Further, assuming that the half-width $|x(\eta,t)|$ is bounded above by a constant C, we obtain

$$\left|\frac{1}{\pi^2}x(t,\eta)\frac{\Delta_\eta}{(\eta-\bar{\eta})^2+\Delta_\eta^2}\right| \leq \frac{C\Delta_\eta}{\pi^2}\cdot\frac{1}{a^2-\Delta_\eta^2}.$$

Then, we have

$$\lim_{a\to+\infty} l(arc)\cdot\sup_{arc}\left|\frac{1}{\pi^2}x(t,\eta)\frac{\Delta_\eta}{(\eta-\bar{\eta})^2+\Delta_\eta^2}\right| = \lim_{a\to+\infty}\pi a\cdot\frac{C\Delta_\eta}{\pi^2}\frac{1}{a^2-\Delta_\eta^2} = 0. \tag{3.36}$$

Finally, from Eqs. (3.34) - (3.36) we derive

$$\int_{-\infty}^{\infty} f(\eta)\mathrm{d}\eta = \frac{1}{\pi}x(t,\bar{\eta}-i\Delta_\eta),$$

that is,

$$r(t) = \int_{-\infty}^{\infty} \frac{1}{\pi} x(t, \eta) \mathcal{L}(\eta) \mathrm{d}\eta = \frac{1}{\pi} x(t, \bar{\eta} - i\Delta_\eta).$$

Similarly, we can derive

$$\langle v(t) \rangle = \int_{-\infty}^{\infty} y(t, \eta) \mathcal{L}(\eta) \mathrm{d}\eta = y(t, \bar{\eta} - i\Delta_\eta).$$

Thus, by introducing Lorentzian distribution for the heterogeneous parameter η (3.33), we can obtain a sharp reduction for the mean-field variables, given by

$$\begin{aligned} r(t) &= \frac{1}{\pi} x(t, \bar{\eta} - i\Delta_\eta), \\ \langle v(t) \rangle &= y(t, \bar{\eta} - i\Delta_\eta). \end{aligned}$$

Further, considering $\pi r(t) + i\langle v(t) \rangle = z(t, \bar{\eta} - i\Delta_\eta)$, evaluating the complex equation (3.32) at $\eta = \bar{\eta} - i\Delta_\eta$ and taking into account the formula that

$$\langle w \rangle = \int_\eta \langle w | \eta \rangle \mathcal{L}(\eta) \mathrm{d}\eta$$

yield the mean-field system of equations given by

$$\begin{aligned} r' &= \Delta_\eta/\pi + 2r\langle v \rangle - \big(\alpha + g_{\text{syn}} s\big) r, \\ \langle v \rangle' &= \langle v \rangle^2 - \alpha \langle v \rangle - \langle w \rangle + \bar{\eta} + I_{\text{ext}} + g_{\text{syn}} s \big(e_r - \langle v \rangle\big) - \pi^2 r^2. \end{aligned}$$

Note that the distribution $\mathcal{L}(\eta)$ can be arbitrary. In particular, if $\mathcal{L}(\eta)$ has n poles in the lower half η-plane, one can readily obtain n sets of complex-valued mean-field ODEs analogous to Eq. (3.32) by evaluating the integrals (3.28) and (3.29) [163]. The Lorentzian distribution is a mere mathematical convenience, since it has only one pole, as required.

Recalling that we have already obtained the dynamical system for the mean adaptation current (3.12) and the synapse (3.16), we finally have the reduction of the network of Izhikevich neurons (3.2)-(3.4) to the following the mean-field system of ODEs,

$$\begin{aligned} r' &= \Delta_\eta/\pi + 2r\langle v \rangle - \big(\alpha + g_{\text{syn}} s\big) r \\ \langle v \rangle' &= \langle v \rangle^2 - \alpha \langle v \rangle - \langle w \rangle + \bar{\eta} + I_{\text{ext}} + g_{\text{syn}} s \big(e_r - \langle v \rangle\big) - \pi^2 r^2 \\ \langle w \rangle' &= a \left(b \langle v \rangle - \langle w \rangle\right) + w_{\text{jump}} r \\ s' &= -s/\tau_s + s_{\text{jump}} r. \end{aligned} \tag{3.37}$$

3.4 Numerical analysis

We now numerically examine the dynamics of the mean-field model and demonstrate its validity in terms of reproducing the macroscopic dynamics of the Izhikevich neural network. The parameter values used in all simulations can be found in Table 3.3, unless otherwise specified in a figure. These values are dimensionless and originally fitted to hippocampal CA3 pyramidal neuron data; see Table 3.1. The exceptions are v_{peak} and v_{reset} which are, respectively, set to large positive and negative numbers. This is to approximate $v_{\text{peak}} \to +\infty$ and $v_{\text{reset}} \to -\infty$ for mathematical convenience [117, 150]. Numerical simulation was done by using the Euler's method in MATLAB with time step $dt = 10^{-3}$ and numerical continuation by using the software XPPAUT [83]. All initial conditions are chosen at the origin. Euler's method allows us to track spike times effectively in order to implement the discontinuity of the Izhikevich neuron model. In our simulations, we found that numerical errors are acceptable, especially when small step sizes are used.

Parameter	Value	Parameter	Value	Parameter	Value	Parameter	Value
α	0.6215	τ_s	2.6	g_{syn}	1.2308	e_r	1
a	0.0077	b	-0.0062	s_{jump}	1.2308	w_{jump}	0.0189
v_{peak}	200	v_{reset}	-200	N	10,000		

Table 3.3: Dimensionless parameters for the Izhikevich neural network (3.2)-(3.4).

We begin with the bifurcation analysis of the mean-field model (3.37). Fig. 3.2(a) and its blow-up (b) show how the population firing rate r qualitatively changes as the mean intrinsic current $\bar{\eta}$ is varied. Fig. 3.2(c) shows the same diagram as (a) in terms of the mean adaptation, $\langle w(t) \rangle$, and includes a bifurcation diagram for full network (3.2)-(3.4) (star symbols). The mean-field model diagrams show two subcritical Andronov-Hopf (HP)s at $\bar{\eta} = \bar{\eta}_{HP} \approx 0.19$ and 0.075, respectively. Unstable limit cycles (blue) emerge from these bifurcations and collide with the stable limit cycles (green) in a saddle-node bifurcation of limit cycles (SNLC) for some $\bar{\eta} = \bar{\eta}_{SNLC} > \bar{\eta}_{HP}$ (right branches) or $< \bar{\eta}_{HP}$ (left branches). The system displays two small ranges of bistability between the Hopf and SNLC bifurcations. The stable periodic orbits (POs) (green) correspond to solutions where individual neurons in the network exhibit synchronous bursting and stable equilibrium points (EPs) (red) correspond to solutions where individual neurons exhibit asynchronous tonic firing. This is clearly reflected in the raster plots and time series of macroscopic variables $r(t)$, $\langle v(t) \rangle$ and $\langle w(t) \rangle$ in Fig. 3.2(d) and (e). The mean-

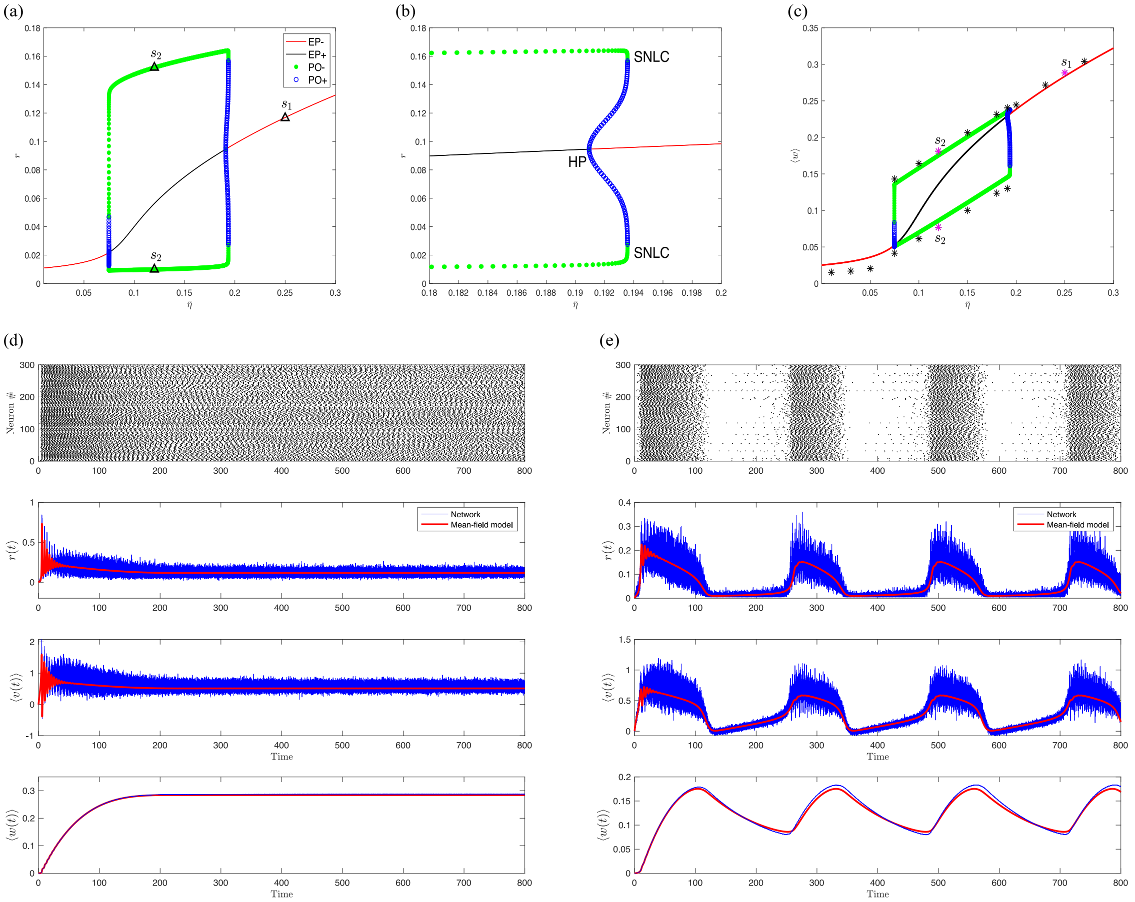

Figure 3.2: The Izhikevich neural network (3.2)-(3.4) and its mean-field model (3.37). (a): Bifurcation diagram of the mean-field system in the plane $(\bar{\eta}, r)$. Stable/unstable EP in red/black and stable/unstable PO in green/blue. (b): Blow-up of (a) near $\bar{\eta} = 0.19$. Bistability is induced by the subcritical HP bifurcation and SNLC. Similar qualitative changes occur at $\bar{\eta} \approx 0.075$. (c): Bifurcation diagram in the plane $(\bar{\eta}, \langle w \rangle)$. The star symbols are simulations of the network. (d) & (e): Time evolutions of the network in blue and its mean-field model in red when $\bar{\eta} = 0.25$ (s_1 in (a) and (c)) and $\bar{\eta} = 0.12$ (s_2 in (a) and (c)). The first rows are the raster plots of 300 randomly selected neurons. The other rows show $r(t)$, $\langle v(t) \rangle$ and $\langle w(t) \rangle$, respectively. Parameters: $\Delta_\eta = 0.02$, $I_{\text{ext}} = 0$, others are given in Table 3.3.

field equations (3.37) predict very accurately the behavior of the entire network, including the damped oscillations in (d) and the frequency of stable oscillations in (e).

Prior work has shown that bursting in a network of Izhikevich neurons is due to a balance between inputs (intrinsic and external applied currents and synaptic inputs), which cause neurons to spike, and the slow adaptation current, which can terminate spiking [78, 158, 159]. For a given level of adaptation, there must be sufficient input, but not too much, to initiate bursting. Hence, the bursting in Fig. 3.2(a) occurs when the mean intrinsic current input $\bar{\eta}$ is not too small and not too large. Note in Fig. 3.2(e) that even when the population is bursting, a small subset of neurons in the population do not burst but remain tonically firing. This is due to the distribution of the heterogeneous input current. A small number of neurons receives an input current large enough that the adaptation is not strong enough to cause these neurons to burst.

In addition, Fig. 3.2(c) demonstrates a great correspondence between a bifurcation diagram generated from numerical simulation of the full network (star symbols) with that obtained from the mean-field model. Here, it is worth paying more attention to the POs (green). This figure shows an excellent amplitude match for a wide range of the bifurcation parameter. Note in Fig. 3.2(c) that we compare behaviors of the variable $\langle w \rangle$ instead of r for clarity, as r exhibits fluctuations due to the spiking of individual neurons (see Fig. 3.2(e)). Employing a larger number of neurons in the network model achieves a narrower spread around the mean-field value, at the expense of increased computational time.

Regarding the frequency match of the POs, Fig. 3.2(e) shows an excellent correspondence at the parameter point s_2. However, in some simulations, especially those with parameter values close to the transition points, the mean-field and network behavior differ quantitatively. Fig. 3.3 shows two examples. In Fig. 3.3(a) the parameter $\bar{\eta}$ is slightly lower than the first bifurcation point. Equivalent initial conditions are chosen for the network model and the mean-field model. However, while the network exhibits a PO, the mean-field model exhibits an EP. This suggests that the bifurcation point leading to the PO in the mean-field model is different from that in the network model. In Fig. 3.3(c) the parameter $\bar{\eta}$ is slightly less than the second bifurcation point, in the region where the mean-field model has only a stable PO. In this case, both the mean-field and network models exhibit a PO, but there is a frequency mismatch. Better agreement in examples can be achieved by slightly tuning the bifurcation parameter of the mean-field model towards higher values. See Fig. 3.3(b) and (d). The same trend can be seen in ([55], Fig. 1). The discrepancies are likely due to the finite size of the network. In summary, for the dynamic comparison between the finite-size network of Izhikevich neurons ($N = 10^4$ here) and the mean-field model derived in the thermodynamic limit ($N \to \infty$), particularly for the behavior of synchronous bursting (POs for the mean-field model), quantitative difference is relatively less visible in terms of the amplitude of the POs than their frequency shift. Further, the discrepancy due to the finite size of the network is more apparent close to the bifurcation

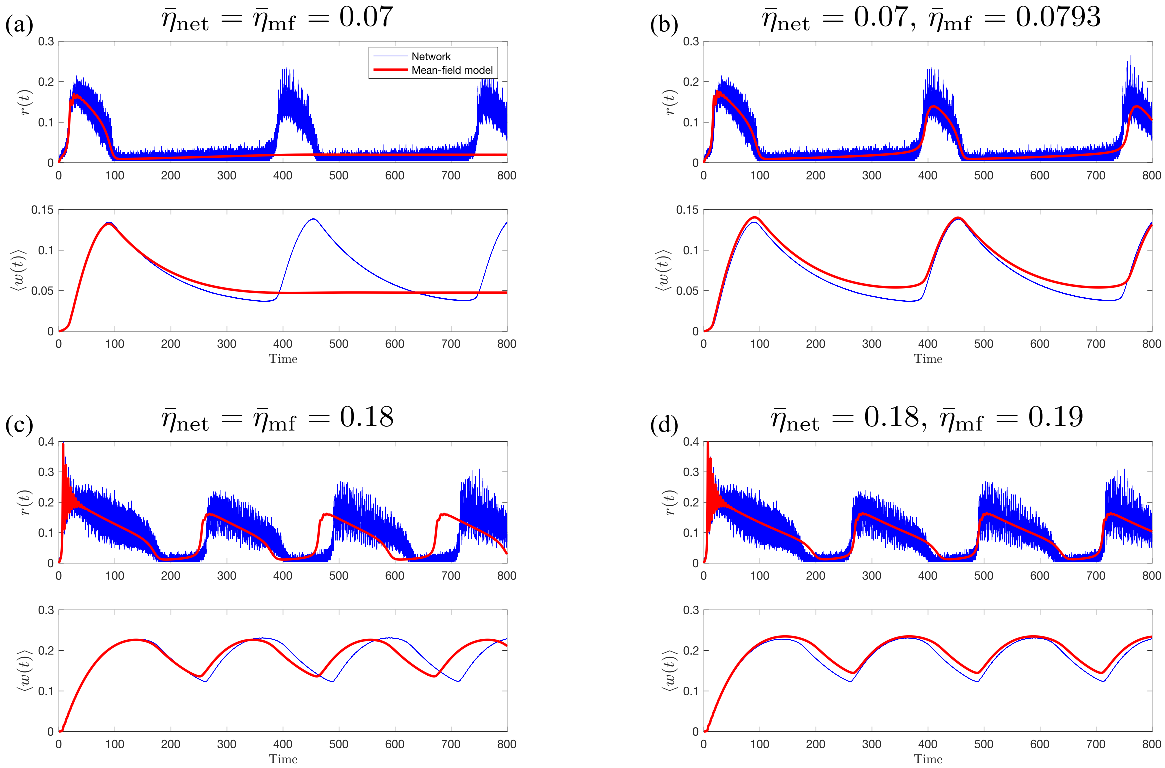

Figure 3.3: Bifurcation shift between the Izhikevich neural network (3.2)-(3.4) (blue) and the mean-field model (3.37) (red). In panels (b) and (d), the network time series $r(t)$ and $\langle w(t) \rangle$ (blue) are the same as those in (a) and (c), while the bifurcation parameters in the mean-field model, $\bar{\eta}_{\text{mf}}$, have been adjusted to match the behaviors of the network. The Hopf bifurcations of the mean-field model occur at $\bar{\eta}_{\text{mf}} \approx 0.075$ and 0.191 in Fig. 3.2. Other parameters are the same as those in Fig. 3.2.

points, where the system is more sensitive to small changes in parameter values.

Furthermore, we can determine the Hopf bifurcation manifolds in the $(\bar{\eta}, \Delta_\eta)$ parameter space for the mean-field model as shown in Fig. 3.4(a) and (b). These curves are associated with the transition between synchronous bursting (inside the curves) and asynchronous tonic firing (outside the curves). Thus, we call the region inside the Hopf bifurcation manifold the bursting region. We see from the network raster plots and time series of $r(t)$ (Fig. 3.4(c)) that the rhythmic regime disappears if the external drive I_{ext} is sufficiently strong. This is a well-known effect observed in many models of adaptation-induced bursting [78, 158, 159]. It is also consistent with the experimental data of [202] on a hippocampal

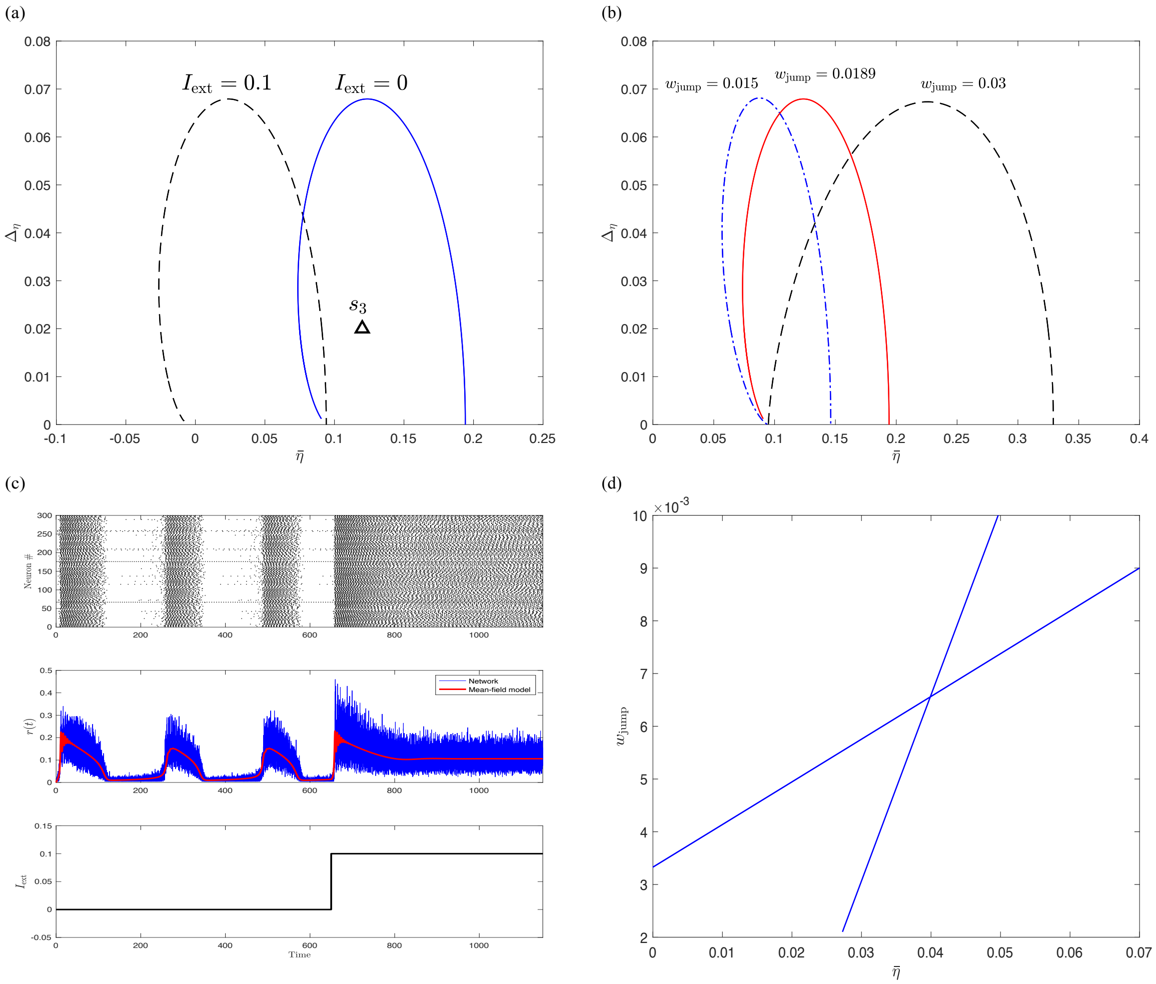

Figure 3.4: The Izhikevich neural network (3.2)-(3.4) and its mean-field model (3.37). (a) & (b): Hopf bifurcations of the mean-field system in the plane $(\bar{\eta}, \Delta_\eta)$ when (a): $w_{\text{jump}} = 0.0189$, $I_{\text{ext}} = 0.1,\ 0$; (b): $I_{\text{ext}} = 0$, $w_{\text{jump}} = 0.015,\ 0.0189,\ 0.03$. (c): Time evolutions when $\bar{\eta} = 0.12$, $\Delta_\eta = 0.02$ (s_3 in (a)). Raster plot in first panel; $r(t)$ in second panel depicted in blue/red for the network/mean-field models; $I_{\text{ext}}(t)$ in last panel. At time $t = 650$, a current $I_{\text{ext}} = 0.1$ is applied to all neurons. (d): Hopf-Hopf bifurcation induced by the intersection of two Hopf bifurcations in the plane $(\bar{\eta}, w_{\text{jump}})$ when $\Delta_\eta = 0.02$. Other parameters are given in Table 3.3.

CA3 slice preparation, which showed that injection of sufficient depolarizing current into pyramidal cells can cause them to transition from bursting to tonic firing. Additionally, Fig. 3.4(d) shows a Hopf-Hopf bifurcation resulting from the intersection of two Andronov-

Hopf bifurcations in the parameter space $(\bar{\eta}, w_{\text{jump}})$. The two curves look like straight lines on such narrow scales. Secondary bifurcations can emanate from this co-dimension two bifurcation point, potentially leading to quasiperiodic behavior [102]. For a detailed investigation, refer to Chapter 4.

3.5 Extension to Two-Coupled Populations of Izhikevich Neurons

A large-scale neural network can be divided into several coupled groups by considering different properties of cells in the network. For example, neurons can be grouped into excitatory and inhibitory populations based on the type of synapses they form [217, 77]; or into strongly and weakly adapting populations based on the amount of SFA they exhibit [158]. In this section, we consider a network of excitatory neurons consisting of two populations: strongly adapting neurons (population p) and weakly adapting neurons (population q). The network is all-to-all connected with single exponential synapses. This model is motivated by the experimental data of [107] on firing properties of CA3 pyramidal neurons and the modeling studies of [78, 158, 159]. Each neuron in the network is characterized by the Izhikevich model given by

$$\begin{aligned}
v'_{m,i} &= v_{m,i}(v_{m,i} - \alpha_m) - w_{m,i} + \eta_{m,i} + I_m^{\text{ext}} + I_{m,i}^{\text{syn}}, \\
w'_{m,i} &= a_m(b_m v_{m,i} - w_{m,i}), \\
\text{if } v_{m,i} &\geq v_m^{\text{peak}}, \text{ then } v_{m,i} \leftarrow v_m^{\text{reset}}, \; w_{m,i} \leftarrow w_{m,i} + w_m^{\text{jump}},
\end{aligned} \tag{3.38}$$

where $m = p, q$ represents the two populations with N_p and N_q cells, respectively. The subscript $\{m, i\}$ denotes the ith neuron in population m. The subscript with only $\{m\}$ represents the corresponding parameter is homogeneous within the population m, but heterogeneous across the two populations. The total synaptic current $I_{m,i}^{\text{syn}}$ depends on the cell type. We require two maximal synaptic conductances, $g_{p,p}^{\text{syn}}$ and $g_{q,q}^{\text{syn}}$, within the populations and two, $g_{p,q}^{\text{syn}}$ and $g_{q,p}^{\text{syn}}$, between the populations. Then, we have

$$\begin{aligned}
I_{p,i}^{\text{syn}}(t) &= \left[\kappa g_{p,p}^{\text{syn}} s_p + (1-\kappa) g_{p,q}^{\text{syn}} s_q\right] \left(e_p^r - v_{p,i}\right) \equiv GS_p \cdot \left(e_p^r - v_{p,i}\right), \\
I_{q,i}^{\text{syn}}(t) &= \left[\kappa g_{q,p}^{\text{syn}} s_p + (1-\kappa) g_{q,q}^{\text{syn}} s_q\right] \left(e_q^r - v_{q,i}\right) \equiv GS_q \cdot \left(e_q^r - v_{q,i}\right),
\end{aligned} \tag{3.39}$$

where $\kappa = \frac{N_p}{N_p + N_q}$ is the proportion of strongly adapting neurons in the network and s_p (respectively, s_q) represents the proportion of open synapses due to neurons in the strongly (respectively, weakly) adapting population. These gating variables are governed by the single exponential synapse model,

$$s_m' = -\frac{s_m}{\tau_m^s} + \frac{s_m^{\text{jump}}}{N_m} \sum_{j=1}^{N_m} \sum_k \delta(t - t_{m,j}^{(k)}). \tag{3.40}$$

Thus, we can apply the approach in the previous section by considering the two populations to be described by their own distinct density functions,

$$\rho_m(t, v_m, w_m, \eta_m) = \rho_m^w(t, w_m|v_m, \eta_m) \cdot \rho_m^v(t, v_m|\eta_m)\mathcal{L}_m(\eta_m).$$

For the population p, we have

$$\frac{\partial}{\partial t}\rho_p^v(t, v|\eta_p) = -\frac{\partial}{\partial v}\left[G_p^v(v, \langle w|\eta_p\rangle, s, \eta_p)\rho_p^v(t, v|\eta_p), \right] \tag{3.41}$$

where $G_p^v(\cdot)$ is defined as Eq. (3.7) with the subscript p for each element. A boundary condition for the flux $\mathcal{J}_p^v(\cdot) = G_p^v(\cdot)\rho_p^v(\cdot)$ is imposed as Eq. (3.8) according to the reset mechanism of the Izhikevich neuron. Assume that the solution of the continuity equation (3.41) has the form of a Lorentzian distribution,

$$\rho_p(t, v|\eta_p) = \frac{1}{\pi} \frac{x_p(t, \eta_p)}{\left[v - y_p(t, \eta_p)\right]^2 + x_p^2(t, \eta_p)}. \tag{3.42}$$

The population firing rate $r_p(t)$ is the flux through the threshold v_p^{peak}. Having set the threshold at infinity and considering the Lorentzian solution (3.42), we obtain

$$\begin{aligned} r_p(t) &= \lim_{v \to v_{\text{peak}}} \int_{\partial \eta_p} \mathcal{L}_p(\eta_p)\rho_p^v(t, v|\eta) \cdot G_p^v(v, \langle w|\eta\rangle, s, \eta_p) \mathrm{d}\eta_p \\ &= \int_{\partial \eta_p} \frac{1}{\pi} x_p(t, \eta_p)\mathcal{L}_p(\eta_p)\mathrm{d}\eta_p, \end{aligned} \tag{3.43}$$

where $\mathcal{L}_p$ defines a probability that a randomly chosen cell in the population p has an intrinsic parameter η_p. In addition, the mean membrane potential has a relationship with $y_p(t, \eta_p)$ via

$$\langle v(t)\rangle_p = \int_{-\infty}^{\infty} y_p(t, \eta_p)\mathcal{L}_p(\eta_p)d\eta_p, \tag{3.44}$$

like that in Eq. (3.28) but with the subscript p. Assume the distribution of the heterogeneous parameter η_p has the form of Lorentzian function,

$$\mathcal{L}_p(\eta_p) = \frac{1}{\pi} \frac{\Delta_p}{(\eta_p - \bar{\eta}_p)^2 + \Delta_p^2}. \tag{3.45}$$

The integrals in (3.43) and (3.44) can be evaluated by using the residue theorem and Eq. (3.45). Then, denoting the complex variable $z_p(t,\eta_p) = x_p(t,\eta_p) + iy_p(t,\eta_p)$, we can derive an explicit relation of the firing rate and the mean membrane potential,

$$\pi r_p(t) + i\langle v(t)\rangle_p = z_p(t, \bar{\eta}_p - i\Delta_p), \tag{3.46}$$

where $z_p(t,\eta_p)$ follows the complex differential equation,

$$\frac{\partial}{\partial t} z_p = i\Big[- z_p^2 + iz_p(\alpha_p + GS_p) - \langle w|\eta_p\rangle_p + \eta_p + I_p^{\text{ext}} + e_p^r GS_p \Big]. \tag{3.47}$$

Here, GS_p, given in Eq. (3.39), is defined as the compound synaptic conductance resulting from the coupling within and between populations. Applying Eq. (3.46) to (3.47) and combining the mean adaptation dynamics in Eq. (3.12) with the subscript p lead to a set of eight differential equations. Among them, three differential equations describe the mean-field quantities for each population,

$$\begin{aligned} r_p' &= \Delta_p^\eta/\pi + 2r_p\langle v\rangle_p - r_p[GS_p + \alpha_p] \\ \langle v\rangle_p' &= \langle v\rangle_p^2 - \alpha_p\langle v\rangle_p - \langle w\rangle_p + \bar{\eta}_p + I_p^{\text{ext}} + GS_p[e_p^r - \langle v\rangle_p] - \pi^2 r_p^2 \\ \langle w\rangle_p' &= a_p[b_p\langle v\rangle_p - \langle w\rangle_p] + w_p^{\text{jump}} r_p \end{aligned} \tag{3.48}$$

for the population p with strong adaptation and

$$\begin{aligned} r_q' &= \Delta_q^\eta/\pi + 2r_q\langle v\rangle_q - r_q[GS_q + \alpha_q] \\ \langle v\rangle_q' &= \langle v\rangle_q^2 - \alpha_q\langle v\rangle_q - \langle w\rangle_q + \bar{\eta}_q + I_q^{\text{ext}} + GS_q[e_q^r - \langle v\rangle_q] - \pi^2 r_q^2 \\ \langle w\rangle_q' &= a_q[b_q\langle v\rangle_q - \langle w\rangle_q] + w_q^{\text{jump}} r_q \end{aligned} \tag{3.49}$$

for the population q with weak adaptation. These two subsystems are coupled through synaptic currents, as given in Eq. (3.39), with the synaptic dynamics governed by

$$\begin{aligned} s_p' &= -s_p/\tau_p^s + s_p^{\text{jump}} r_p, \\ s_q' &= -s_q/\tau_q^s + s_q^{\text{jump}} r_q. \end{aligned} \tag{3.50}$$

In the following we analyze the dynamics of the mean-field system and examine how well it reproduces the macroscopic activities of the two-population network of Izhikevich neurons. The parameter values can be found in Table 3.4. Most of these values are taken from [158, 159], which were originally fit by [78] to data from pyramidal CA3 neurons of the hippocampus [107]. The only parameters that differ between the two populations are those that govern the adaptation levels, i.e., the after-spike jump sizes w_m^{jump} and the time

Parameter	Value	Parameter	Value	Parameter	Value	Parameter	Value
w_p^{jump}	0.0189	w_q^{jump}	0.0095	a_p	0.0077	a_q	0.077
$g_{p,p}^{\text{syn}}$	1.2308	$g_{q,q}^{\text{syn}}$	1.2308	$g_{p,q}^{\text{syn}}$	1.2308	$g_{q,p}^{\text{syn}}$	1.2308
I_p^{ext}	0	I_q^{ext}	0	$N_p + N_q$	10,000		

Table 3.4: Dimensionless parameters for the two-coupled Izhikevich network (3.38)-(3.40).

constants a_m, where $m = p, q$. All parameters that are not shown in Table 3.4 are the same for both populations and can be found in Table 3.3.

Fig. 3.5 compares the behavior of the mean-field model to simulations of the full network. Fig. 3.5(c)-(h) show that the dynamics of the two-population network are very well described by the reduced mean-field description in the asynchronous tonic firing (EPs in Fig. 3.5(c), (e) and (g)) and synchronous bursting (POs in Fig. 3.5(d), (f) and (h)) regimes. Note in the bursting regime that a relatively larger fraction of neurons in the weakly adapting population are tonically firing (compare (f) with (d)). This makes sense since the bursting occurs due to the balance of inputs and adaptation. In the weakly adapting population, a larger fraction of neurons receive sufficient input to prevent them from bursting. In addition to the correspondence found at these two typical parameter settings, Fig. 3.5(a) and (b) show that there is a great correspondence between a bifurcation diagram from numerical simulation of the two-population network (star symbols) with that obtained from the mean-field model in terms of $\langle w \rangle_p$ and $\langle w \rangle_q$, respectively. In spite of the excellent amplitude agreement at each parameter point shown, we should point out that the mean-field dynamics shows some quantitative differences from those of the network model, especially at the points very close to the transition between bursting and firing. The effect is very similar to what is seen for the single population network in Figure 3.3. Improvement can be seen by slightly adjusting the bifurcation parameter of the mean-field model towards higher values, although it is not as effective as that shown in the single-population network.

Additionally, the mean-field model for the network of two coupled Izhikevich populations involves more complicated bifurcations compared with that of the single-population network of strongly adapting Izhikevich neurons studied in the previous section. The bifurcation analysis in Fig. 3.6 reveals that when the proportion of strong adapting neurons is $\kappa = 0.8$, the sequence of bifurcation is largely the same as when there is a single population of strongly adapting neurons (compare Fig. 3.6(a) with Fig. 3.2(a)). With $\kappa = 0.8$, as the mean intrinsic current $\bar{\eta}$ increases, the stable periodic behavior in the mean-field system

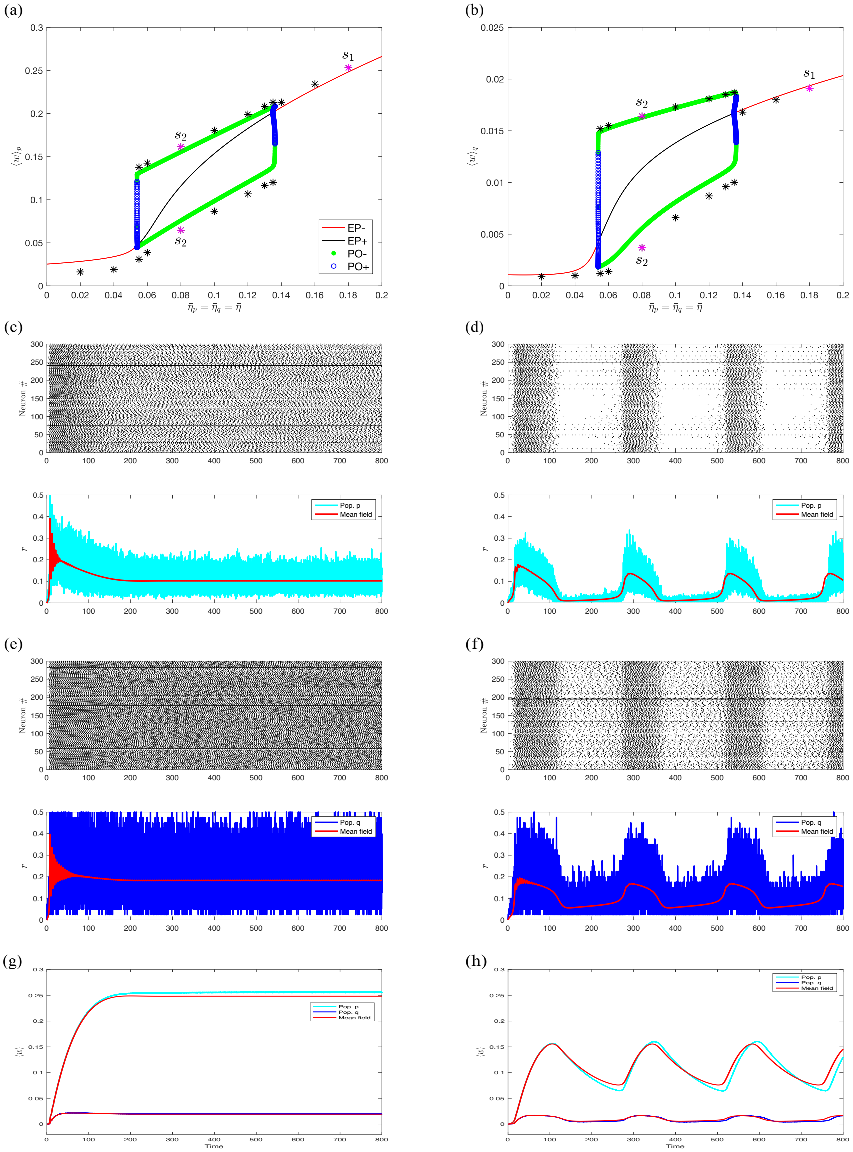

Figure 3.5: Two-coupled Izhikevich neural network (3.38)-(3.40) and its mean-field model (3.48)-(3.50). Bifurcation diagrams in the plane $(\bar{\eta}_p = \bar{\eta}_q = \bar{\eta}, \langle w \rangle)$ for Population p in (a) and Pop. q in (b). Stable/unstable EP in red/black and Stable/unstable PO in green/blue. Star symbols are simulations of the network. Time evolutions in left column: $\bar{\eta}_p = \bar{\eta}_q = 0.18$ (s_1 in (a & b) and Fig. 3.6(a)); in right column: $\bar{\eta}_p = \bar{\eta}_q = 0.08$ (s_2 in (a & b) and Fig. 3.6(a)). Shown in cyan/blue for Pop. p/q are $r(t)$ and $\langle w(t) \rangle$ (g & h) from the network. Shown in red are from the mean-field system. Raster plots are 300 randomly selected neurons. Parameters: $\kappa = 0.8$, $\Delta_p^\eta = \Delta_q^\eta = 0.02$, others are given in Table 3.4.

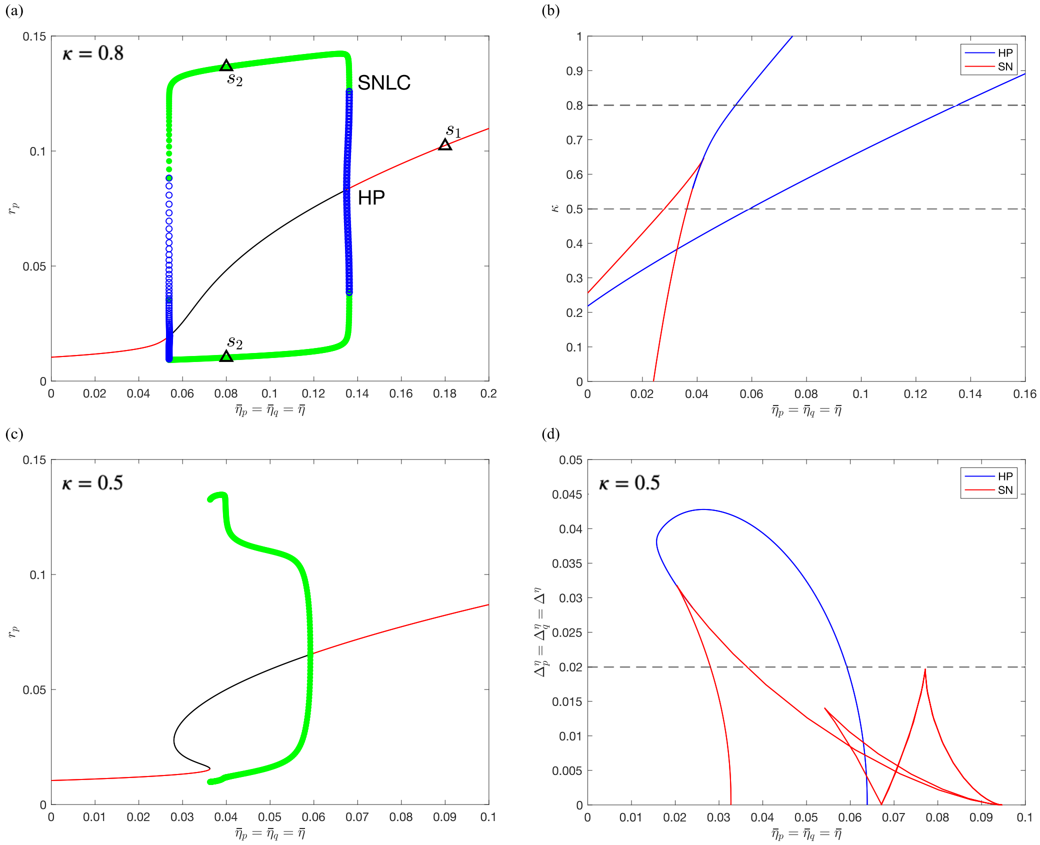

Figure 3.6: Bifurcation diagrams of the mean-field model (3.48)-(3.50) for the two-coupled Izhikevich neural network. (a): The plane $(\bar{\eta}_p = \bar{\eta}_q = \bar{\eta}, r_p)$ when the proportion of strongly adapting neurons $\kappa = 0.8$. (b): The plane $(\bar{\eta}, \kappa)$. Saddle-node bifurcations are in red; Hopf bifurcations are in blue. (c): The plane $(\bar{\eta}_p = \bar{\eta}_q = \bar{\eta}, r_p)$ when $\kappa = 0.5$. A supercritical Hopf bifurcation occurs at $\bar{\eta} \approx 0.06$ and two saddle node bifurcations at $\bar{\eta} \approx 0.028, 0.036$, respectively. (d): The plane $(\bar{\eta}, \Delta^\eta)$ when $\kappa = 0.5$. Saddle-node bifurcations are in red; Hopf bifurcations are in blue. Parameters: $\Delta_p^\eta = \Delta_q^\eta = 0.02$, others are given in Table 3.4.

is initiated by a SNLC connected to a subcritical HP at $\bar{\eta}_p = \bar{\eta}_q \approx 0.054$ and terminated by the same sequence in reverse at the Hopf point $\bar{\eta}_p = \bar{\eta}_q \approx 0.135$. The system shows bistability in the narrow regions between SNLC and HP. However, complex bifurcations occur when changing the value of κ. Fig. 3.6(b) shows the bifurcation curves plotted in the $(\bar{\eta}, \kappa)$ parameter plane. Saddle-node bifurcation curves (red) meet and form cusp points or tangentially intersect the curves of the HP bifurcation (blue) and produce a zero-Hopf bifurcation. When $\kappa = 0.8$, the system has two Hopf points, also shown in Fig. 3.6(a). When the proportion is reduced to $\kappa = 0.5$, the system undergoes two saddle-node bifurcations and one HP bifurcation. These behaviors are also shown in the one-parameter bifurcation diagram Fig. 3.6(c). Further, one can see from Fig. 3.6(c) that the stable period behaviour is now initiated by what appears to be a saddle-node bifurcation on invariant circle (SNIC) or a homoclinic bifurcation (at $\bar{\eta}_p = \bar{\eta}_q \approx 0.036$) and terminated by a supercritical HP bifurcation at $\bar{\eta}_p = \bar{\eta}_q \approx 0.06$. Thus, the stable PO has a very low frequency, which rapidly increases as the $\bar{\eta}$ increases. Finally, Fig. 3.6(d) shows a two-parameter bifurcation diagram in the $(\bar{\eta}, \Delta^\eta)$ parameter plane with κ fixed at 0.5. Complicated bifurcation structures, including the Bogdanov-Takens bifurcation, may occur for nearby parameter values. We leave further investigation of this complex bifurcation structure for future work.

Since periodic solutions in the mean-field model correspond to synchronous bursting in the full network, we can use these results to predict the effects of parameters on network behavior. Comparing the dashed lines in Fig. 3.6(b) (which correspond to Figs. 3.6(a) and (c), respectively) shows that decreasing the proportion of strongly-adapting neurons, κ, makes bursting less likely in the sense that the range of values of the mean current $\bar{\eta}$ for which bursting occurs is decreased. Fig. 3.6(d) shows that decreasing the heterogeneity of the currents, Δ^η, has a similar effect. Further, a new transition to bursting is possible. In the two-parameter diagrams Fig. 3.6(b) and (d), the bursting region is now bounded in part by the HP manifold (blue) and in part by the right-most saddle-node bifurcation (red). The frequency of stable bursting behavior near the saddle-node bifurcation is expected to be strongly dependent on the mean intrinsic current, $\bar{\eta}$, with quite low frequency possible near the transition point. The new transition occurs when the proportion of strongly-adapting neurons, κ, and the heterogeneity of the currents, Δ^η, are both small enough.

Fig. 3.7 further illustrates the impact of the proportion of strongly-adapting neurons in the network. The boundary of the bursting region is shifted into the high mean intrinsic current region for a higher proportion (shown in Fig. 3.7(a)) and the rhythmic regime appears as κ increases (shown in Fig. 3.7(b)). This indicates that stable bursting behavior is more likely in a network with a higher proportion of strongly adapting neurons. Fig. 3.7(c) and (d) show a comparison between the full network dynamics and the reduced mean-field system. The reduced description captures the essential shape of the firing activity of the full network. There is a small discrepancy in the approximation of the mean adaption variable $\langle w \rangle$. This may be due to the failure of the assumption $\langle w | \eta \rangle \gg w_{\text{jump}}$ during the derivation of the dynamics of $\langle w \rangle$ (see Eq. (3.11)).

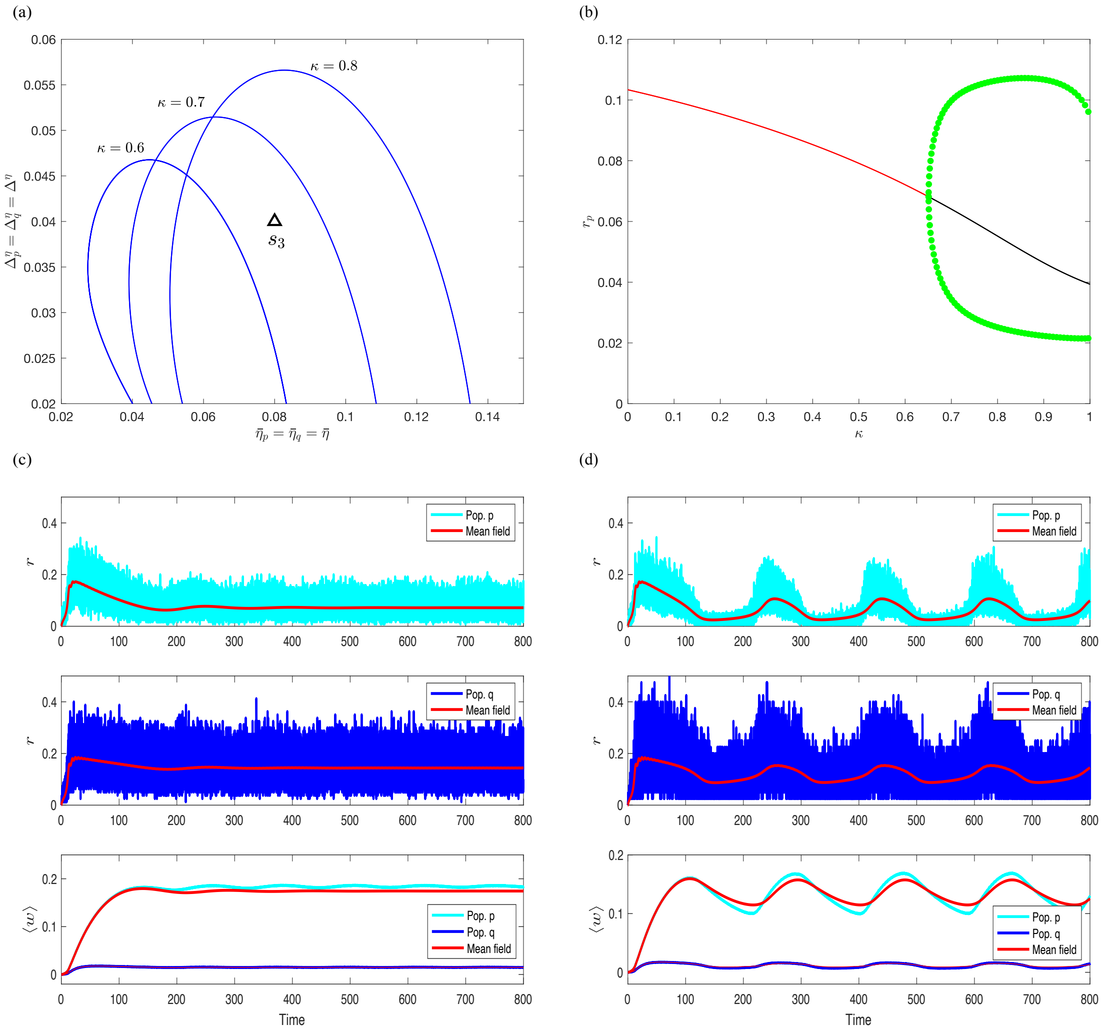

Figure 3.7: The two-coupled Izhikevich neural network (3.38)-(3.40) and its mean-field model (3.48)-(3.50). (a): Hopf bifurcations of the mean-field system with $\kappa = 0.6,\ 0.7,\ 0.8$. (b): Bifurcation diagram in (κ, r_p). Stable/unstable EP in red/black, and stable PO in green. (c) & (d): Time evolutions when $\kappa = 0.6$ (left) and 0.8 (right). Shown in cyan (population p) and blue (population q) are r and $\langle w \rangle$ of the network. Shown in red are from the mean-field system. Parameter values: $\bar{\eta}_p = \bar{\eta}_q = 0.08$, $\Delta_p^\eta = \Delta_q^\eta = 0.04$ (s_3 in (a)), others are given in Table 3.4.

3.6 Discussion

In this chapter, we have shown that it is feasible to extend the OA theory [163] or the equivalent Lorentzian ansatz [150] to the derivation of mean-field models for a network of Izhikevich neurons. The difficulty lies in how to achieve a closed set of mean-field equations with the inclusion of the mean-field expression of the adaptation variable. To do this we turned to the population density approach for spiking neurons, which was extended to two dimensional integrate-and-fire models by [158, 159]. The quasi-steady approximation for the continuity equation in [159] was replaced by the Lorentzian ansatz to remove the assumption of separation of time scales. The moment closure approach [140] was deployed to remove the dependence of the adaptation variable on the membrane potential and close the mean-field system.

We have derived and validated the mean-field model for a network of heterogeneous Izhikevich neurons that display SFA through a recovery variable. Furthermore, we have demonstrated that it is straightforward to apply our approach to multiple populations where the forces of adaptation, inhibition, or excitation interact. The mean-field models have exhibited qualitative and quantitative agreement with the full network. Using bifurcation analysis, we have identified and characterized collective bursting regimes that emerge given appropriate levels of adaptation, external stimulus, and proportion of strongly adapting neurons. The parameter values used in the numerical examples are non-dimensionalization of those fit to actual neuronal data collected in the literature. Bifurcation analysis for the mean-field system can be used to make predictions about the biological networks being studied, e.g. the emergence of synchronous bursting in the CA3b region of the hippocampus in this chapter. Our model, an extension of those proposed by Dur-e-Ahmad et al. [78] and Nicola et al. [158, 159], is motivated by several observations. In their studies of isolated pyramidal cells in the CA3 region of the hippocampus, Hemond et al. [107] observed that approximately 13% of neurons were intrinsically bursting, while the majority exhibited regular spiking, with 37% showing strong SFA and 46% showing weak SFA. Although it is well known that SFA in individual neurons can lead to bursting behavior when neurons are coupled [86, 207], it is less clear whether this phenomenon occurs when a significant proportion of neurons exhibit weak adaptation. Our mean-field model (3.48)-(3.50) allows us to compute bifurcation manifolds and types for the network with varying proportions of strongly and weakly adapting neurons. This helps us to understand the impact of various parameters on the transition between the behavior of asynchronous tonic firing and synchronous bursting in the actual neural network. In particular, we found that the larger proportion of weakly-adapting neurons (small κ) makes bursting less likely and the decreasing heterogeneity of the currents (small Δ^{η}) has a similar effect. While the former conclusion is not surprising, the latter is more interesting. Given the percentage of weakly vs. strongly adapting neurons in the data of [107], our results indicate that adaptation-induced network bursting would only be possible if there is sufficient, but not too much, heterogeneity in the intrinsic applied current. Since the intrinsic current determines the firing rates of the model neurons, this shows that the heterogeneity of the firing rates may be an important factor in the generation of bursting behavior. We also note that increasing the proportion of weakly-adapting neurons changed the bifurcation involved in the transition to bursting behavior. With sufficient weakly-adapting neurons (50%) this transition was a SNIC or homoclinic bifurcation. For the network, this translates into the potential increased variability of the network bursting frequency, including the possibility of quite low bursting frequency.

To assess the validity of our mean-field approximation, we examine all the assumptions that are imposed during the derivation. They are listed in order of appearance as follows.

1. All-to-all connectivity within the population and between different populations.

This assumption is reasonable for the application to the CA3 region of the hippocampus we considered, as this region is highly recurrently coupled [8, 9, 35]. It is possible to expand our approach to sparsely coupled networks with a distributed connection or a distributed coupling strength using the techniques in [89, 50, 127, 27].

2. $N \to \infty$, the thermodynamic limit.

In theory, the mean-field model is a valid description for the network of neurons in the thermodynamic limit. The CA3 region of the hippocampus contains estimated 29,000 neurons in rats and 87,000 neurons in humans [19, 216]. In finite-size numerical experiments, the spread of the network variables around the mean narrows as the number of neurons increases, and thus becomes closer to the dynamics of the mean-field model. One can see Fig. 3.5 for a comparison, where $N_p = 8000$ for the strongly adapting neurons and $N_q = 2000$ for the weakly adapting neurons. The same trend can be seen in [55, Fig. 6].

3. $\langle w|\eta\rangle \gg w_{\text{jump}}$, the mean adaptation variable with the parameter η is sufficiently greater than the homogeneous after-spike jump value.

This assumption is required when deriving the differential equation of $\langle w\rangle$. The small discrepancy between the mean-field model and the population of strongly adapting neurons may result from a partial failure of the requirement; see $\langle w(t)\rangle$ of the population p in Fig. 3.5(g) and (h), Fig. 3.7(c) and (d). However, the mean-field description still captures the essential shape and frequency of the firing activity of the network. The accuracy could be improved by including high-order terms in the Taylor expansion (see Eq. (3.11)). This will give rise to an extra term in the final mean-field equation for $\langle w\rangle'$.

4. $\langle w|v,\eta\rangle = \langle w|\eta\rangle$, first-order moment closure assumption, also called the adiabatic approximation.

This assumption implies fast dynamics of the membrane potential. We could employ a high-order moment closure approximation, although we need to assess the cost of the added effort in terms of improving the accuracy of the resulting mean-field model [140].

5. $\rho^v(t,v|\eta) = \frac{1}{\pi}\frac{x(t,\eta)}{\left[v-y(t,\eta)\right]^2+x^2(t,\eta)}$, the Lorentzian ansatz on the conditional density function.

The derivation of the differential equations of $r(t)$ and $\langle v(t)\rangle$ started by writing the density function in conditional form $\rho(t,v,w,\eta) = \rho^w(t,w|v,\eta)\rho^v(t,v|\eta)\mathcal{L}(\eta)$; see Eq. (3.21). If we rewrite it as $\rho(t,v,w,\eta) = \rho^\eta(t,\eta|v,w)\rho^{vw}(t,v,w)$ and assume that $\rho^{vw}(t,v,w)$ has the Lorentzian shape, we can use the approach in this chapter to obtain a different mean-field system. The paper [159] shows how changing the expansion of the population density function can drastically change the resulting mean-field model. The expansion we used in this chapter corresponds to that used to develop the "Mean-field system III" in [159].

6. $v_{\text{peak}} = -v_{\text{reset}} \to \infty$, limit of the resetting rule when neurons fire.

The parameter values used in this chapter are based on actual neuronal data except the resetting values. This choice is essential for the validity of the Lorentzian ansatz Eq. (3.27). It also facilitates analysis by linking the QIF model to the theta neuron model by changing the variable $v = \tan(\theta/2)$ [117]. Although not precisely biologically realistic, the theta model and its variants have been used in the literature to explore phenomena, such as chaotic dynamics in large, sparse-balanced networks [152], rhythm generation [122], wave propagation in the cortex [162, 87, 39] and models for EEG [40]. For the neuron model that exhibits a bifurcation of SNIC, it is possible to reduce it to the theta model with adaptation [85, 82, 122]. For a system not near a SNIC, but near some other bifurcation satisfying fairly general and biophysiologically plausible conditions, one can still obtain the theta model with adaptation [114]. When dealing with a biological network based on experimental data, we should treat the assumption with caution, as changing v_{peak} and v_{reset} can affect the firing rates and estimation of the mean membrane potential. In numerical experiments, we choose $v_{\text{peak}} = -v_{\text{reset}} = 200$ as in [76], which is far from the normal range of membrane potential v. We have found that different spiking thresholds lead to some bias in averaging v over the full network, even if they meet the assumption requirement. Montbrió et al. [150] attempted to address this by adding a refractory period to the network model, that is, the time for neurons taken from v_{peak} to infinity and minus infinity to v_{reset}. This effectively makes the firing rate and the mean membrane potential of the network match those of the theta model and hence the mean-field model. Gast et al. [97] made a similar compensation for the firing rate in the refractory period by adjusting the external current I_{ext}. In addition, to avoid numerical delicacies near the spiking threshold, one can transform the QIF form into the theta neuron when performing the numerical simulation [175] .

7. $\mathcal{L}(\eta) = \frac{1}{\pi} \frac{\Delta_\eta}{(\eta-\bar{\eta})^2+\Delta_\eta^2}$, distribution of the heterogeneous current.

Many parameters can be sources of heterogeneity in a network. Here we chose the intrinsic current η, but our approach could be applied to other choices, such as the synaptic conductance g_{syn}. In addition, the choice of the Lorentzian distribution function is just a mathematical convenience. It can sharply reduce the complexity of the resulting mean-field model when evaluating the integrals in (3.28) and (3.29). Unfortunately, the Lorentzian distribution is physically implausible since both its expected value and its variance are undefined. Other distributions, including Gaussian distributions, have been discussed in the literature. Particularly, if a distribution $\mathcal{L}(\eta)$ has n complex-conjugate pole pairs, one can easily obtain the mean-field model consisting of n complex-value ODEs in the form (3.32) [163]. Furthermore, both Ott et al. [164] and Montbrió et al. [150] pointed out that mean-field systems obtained using the Lorentzian and Gaussian distributions had qualitatively identical bifurcation structures. However, Klinshov et al. [123] argued that the quantitative difference did matter in terms of both transient and asymptotic dynamics. They also showed how to compute the integrals in (3.28) and (3.29) with the help of rational approximation and residue theory when $\mathcal{L}(\eta)$ is a Gaussian distribution. Certainly, the resulting mean-field model has higher dimensions.

For numerical experiments, Montbrió et al. [150] generated a set of N input currents that accurately reproduced a Lorentzian distribution. The same set of input currents was used for all simulations with N neurons and was given by

$$\eta_i = \bar{\eta} + \Delta_\eta \tan\left(\frac{\pi}{2} \cdot \frac{2i-N-1}{N+1}\right). \tag{3.51}$$

In this chapter, we take a different approach, except for Fig. 3.3. We generated the distribution by using the technique of inverse transform sampling. Specifically, for the ith neuron, we have

$$\eta_i = \bar{\eta} + \Delta_\eta \tan\big(\pi(r_i - 0.5)\big), \tag{3.52}$$

where value of the cumulative distribution function r_i is randomly sampled from the uniform distribution on $(0, 1)$. This is a basic method for pseudo-random number sampling from any probability distribution. The advantage is that the distribution of the heterogeneous currents is more realistic. The drawback is that the number of neurons N involved in the simulation must be large enough to exhibit a good approximation of the Lorentzian distribution. For example, $N = 10^4$ in our simulations. Additionally, the numerical results obtained in each simulation are slightly different, since the current distributed to each neuron is different each time. Specifically, for our mean-field approximations for the network of Izhikevich neurons (both single and two populations), the deterministic rule (3.51) gives a narrower spread of the variable around the value of the mean-field model for a given N than the random algorithm (3.52). However, the random algorithm is still capable of achieving a good match of the amplitude and (usually) frequency of POs between the full network and the mean-field model; see the details in Fig. 3.8. As another example, Ciszak et al. [55] showed that similar accuracy of the mean-field results was observed by employing a network of $N = 10^4$ nodes with the deterministic generation rule and one of $N = 10^6$ nodes with the random algorithm.

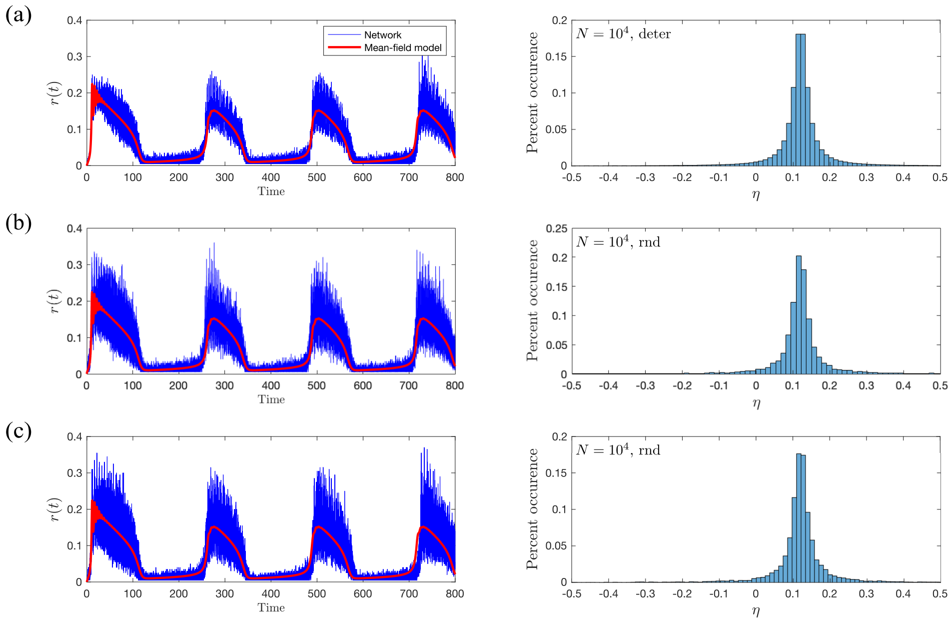

Figure 3.8: Time series of $r(t)$ for the Izhikevich neural network (3.2)-(3.4) (blue) and its mean-field model (3.37) (red). We also show different distributions of the heterogeneous current η when its mean $\bar{\eta} = 0.12$. In (a), the currents are generated deterministically according to the rule (3.51), while (b) and (c) are two independent experiments where the currents are generated in a random way as Eq. (3.52). Other parameters are the same as those in Fig. 3.2(d).

8. $\eta \in (-\infty, \infty)$, range of the heterogeneous current.

This assumption is adopted in the evaluation of integrals (3.28) and (3.29) using the residue theorem. For the neural network to be realistic in spite of this requirement, the distribution range of the heterogeneous parameter should be much wider than its HWHM Δ_η to achieve Eq. (3.36).

In sum, all the above eight requirements are not truly indispensable for the applicability of the developed mean-field models. Some choices are simply mathematical convenience, and insights gained from the macroscopic description are more generally applicable.

To our knowledge, we were the first to analytically derive mean-field models in terms of the population firing rate for a spiking neural network with adaptation without relying on assumptions of explicit separation of time scales, weak coupling, or averaging. Nicola and Campbell [158, 159] proposed a set of mean-field models for the homogeneous and heterogeneous Izhikevich network. They used a quasi-steady approximation for the continuity equation (3.25) by assuming a sufficiently large time scale of adaptation. We replaced it by employing the Lorentzian ansatz (3.27) to remove this limitation. Their resulting mean-field models were a switching system of ODEs and the bifurcation theory of non-smooth systems had to be involved to perform further dynamical analysis. We used similar parameter values, and thus our work can be directly compared. The shape of the bursting region and dependence of bursting on various parameters are consistent, which is satisfactory since the bursting mechanism in the underlying network model is the same. Interestingly, we have found a novel mechanism for the emergence of synchronous bursting in the neural network of two-coupled populations. The bursting behavior was initiated by what appeared to be a SNIC bifurcation or a homoclinic bifurcation (see Fig. 3.6(c)). Moreover, our results greatly improve on those of [158, 159] in the sense of representing the frequency of bursting. Gast et al. [96] developed a smooth mean-field system for the QIF network with adaptation. The SFA mechanism acted additively on the dynamics of the membrane potential, just like the Izhikevich neuron. However, its adaptation variable was specifically expressed as a convolution of the membrane potential with an integral kernel. This treatment facilitates finding the closed set of mean-field equations, but lacks generality. Furthermore, in [96] it was also assumed that the adaptation dynamics was slow enough so that the variable was considered constant, which eventually led to the same derivation process as in [150]. Recently, Bandyopadhyay et al. [15] derived a mean-field model for the network of Hodgkin-Huxley neurons including the effect of ion exchange between the intracellular and extracellular environment. They used quasi-steady state assumptions and numerical fitting to approximate the Hodgkin-Huxley model with a piecewise-defined QIF model and then applied the Lorentzian ansatz [150]. However, their incorporation of the ion-exchange dynamics is ad hoc. By comparison, our approach provides explicit and solid mathematical foundations underlying the derivation process and shows how to incorporate such additional variables into a mean-field model.

In addition to studies built on the OA mean-field framework dedicated to the network of QIF-type neurons with adaptation, there are a few other approaches to derive mean-field models for populations of other models of adapting neurons. Overall, the adiabatic approximation (first- or higher-order statistic moments) is commonly employed to deal with the adaptation variables. The differences lie in developing the dynamics of the population firing rate. For example, di Volo et al. [73] adopted a master equation formalism [79] to obtain a macroscopic Markovian description of the homogeneous network of AdEx integrate-and-fire neurons and subsequently extended it to the corresponding heterogeneous network [72]. Simultaneously, Carlu et al. [47] generalized the approach to networks of more complex neuron models, including Hodgkin-Huxley and Morris-Lecar. The main ingredient of the master equation formalism is the derivation of a stationary transfer function. The key assumptions in the derivation of the mean-field model are that the network dynamics be asynchronous and that the time scale of the adaptation be slower than the spiking dynamics of individual neurons [73]. Therefore, the deduced mean-field model cannot address the emergence of bursting-induced synchronization, but is well suited to describe the response of networks to external stimuli (see Fig. 3 and 4 in [47]). In addition, different from the above mean-field approximation, which takes into account the network with finite neurons, Cakan and Obermayer [41] presented a mean-field model based on a linear-nonlinear cascade [14] of a network of AdEx neurons in the thermodynamic limit $N \to \infty$. The approach begins with the replacement of the synaptic current by a Gaussian white noise process and then formulates the stochastic network using the Fokker-Planck equation as the continuity equation. In our approach, we consider a deterministic network and use the counterpart continuity equation (3.6). Furthermore, in [41], similar to the master equation formalism, pre-computed stationary transfer functions are necessary to derive the cascade-based mean-field model, which indirectly links to the dynamics of the population firing rate and suffers the same incapability to describe neurons that display bursting behaviors. In contrast, our approach introduces a Lorentzian ansatz as the solution to the continuity equation that leads to simpler and direct firing rate equations as the final mean-field description and goes beyond the limitation to bursting.

Interaction between fast and slow processes in a network of spiking neurons can induce much richer dynamics, especially the emergence of population bursting activity and the resulting spike synchronization. Those regimes are of interest to describe both normal and pathological neural network dynamics. The mean-field models developed in this chapter provide a tractable and reliable tool for investigating the underlying mechanism of brain function from the perspective of computational neuroscience. For example, the emergence of bursting in the CA3b region of the hippocampus, which we described before, and the onset of seizures in [181], where a computational analysis was performed for a network of 500 Izhikevich neurons to explore a novel hypothesis about the seizure initiation. We expect that our mean-field reduction models can provide a reasonable interpretation for large-scale numerical simulations and experimental data. In addition, the impact of time delay, gap junctions, and realistic network topology may be considered within the same framework, allowing for the application to more biologically realistic network models. The next chapter will focus on the impact of time-delayed coupling between neurons on collective dynamics.

Chapter 4

Collective Dynamics of Izhikevich Neural Networks with Synaptic Delay

In Chapter 3, we demonstrated the efficacy of mean-field approximations within the Ott-Antonsen (OA) theoretical framework. The resulting low-dimensional dynamical system connects the emergent collective dynamics to microscopic characteristics of individual neurons, valid in the thermodynamic limit. In this chapter, our focus shifts to understanding neural systems' behavior in the presence of time delays. We establish the OA-based mean-field descriptions for Izhikevich neural networks with global delayed coupling (Sec. 4.2), examine the existence of equilibrium points (EPs) and their linear stability (Sec. 4.3). We investigate how the emergence of collective oscillations (COs) is impacted by three main factors: the heterogeneity of the quenched input current, the intensity of spike frequency adaptation (SFA), and the time delay during neuron communications (Sec. 4.4).

4.1 Time Delay in Neural Systems

Time delays are an important element that cannot be ignored when modeling a neural network. They typically range from 10 to 200 ms, comparable to the characteristic time scales of neural systems, which are generally between 10 and 250 ms [36]. Therefore, they can significantly influence the system dynamics. These effects are diverse. Delays can be associated with the emergence or prevention of oscillations [193, 179], control phase locking

[61], and induce multi-stability [192, 52]. There are several sources of time delay in the neural system. These include propagation delays as action potentials travel along the axon or dendrite, as well as delays in signal transmission across synapses. These delays typically affect the neuron's membrane potential through coupling mechanisms. Consider a network of N neurons modeled by the general equations

$$v_i'(t) = F(v_i(t)) + I_{\text{app},i} + \sum_{j=1}^{n} I_{ij}\big(v_i(t), v_j(t)\big), \quad k = 1, \dots, N.$$

Here, v_i is the ith neuron's membrane potential, $I_{\text{app},i}$ is the applied current, the function $F(\cdot)$ represents the intrinsic dynamics of the neuron and the function $I_{ij}(\cdot)$ represents the current input to the ith neuron from the jth neuron because of the coupling. Depending on the cell structures and the specific questions being addressed, time delays can be represented in different ways. The common way is to assume that time delays are constant. In this case, the coupling function becomes

$$I_{ij}\big(v_i(t), v_j(t - \tau_{ij})\big).$$

For a simpler approach, it could be assumed that delays are homogeneous throughout the network. If they are heterogeneous, a probability distribution function could be introduced. A more complicated approach is to integrate a delay plasticity mechanism into the network [168]. It is inspired by evidence that axonal white matter exhibits adaptability through learning and behavior [91], and that myelin continues to form around axons in an activity-dependent manner in the mature neural system [7, 16]. These findings suggest the presence of a state-dependent propagation delay $\tau(t)$. Furthermore, time delays that occur during the transmission of action potentials across synapses are usually implicitly included by adding additional models that represent the chemical kinetics of the synapse, e.g., the models introduced in Sec. 2.4.1. We will consider this scenario in Chapter 5.

The study of the impact of delays, especially on coupled systems of neuronal oscillators, has been an area of active research and posed a significant challenge. When oscillators are weakly coupled, it is possible to reduce the full coupled model with a stable limit cycle to a phase description using the methods of phase reduction [44, 5]. However, this effort is still formidable. In this chapter, we study the delay effect by establishing low-dimensional mean-field systems for the large-scale coupled system of neuronal oscillators. We mainly consider constant delays. For an overview of the role of time delays in neural systems, we refer the reader to the papers [43, 220, 221, 84].

4.2 Mean-Field Modeling for Neural Networks with Synaptic Delay

4.2.1 Mean-Field Systems with General Distributed Delay

We consider the network of heterogeneous, all-to-all coupled Izhikevich neurons given by

$$\begin{aligned} &v_i'(t) = v_i(v_i - \alpha) - w_i + I_{\text{ext}}(t) + \eta_i + I_{\text{syn},i}(t), \\ &w_i'(t) = a(bv_i - w_i), \\ &\text{if } \ v_i \geq v_{\text{peak}}, \ \text{ then } v_i \leftarrow v_{\text{reset}}, w_i \leftarrow w_i + w_{\text{jump}}, \end{aligned} \tag{4.1}$$

for $i = 1,\ 2,\ \ldots,\ N$. The differential equations for v_i and w_i determine the neural activity leading to an action potential. Each neuron has three sources of input current: a common, time-varying external component $I_{\text{ext}}(t)$, a heterogeneous, quenched intrinsic component η_i, drawn from a probability distribution, and a recurrent synaptic component representing input from other neurons via synapses, $I_{\text{syn},i}$. For the connection between neurons, we use the standard conductance-based synaptic current model [88], as introduced in Chapter 2,

$$I_{\text{syn},i}(t) = g_{\text{syn}} s_i(t)\big(e_r - v_i(t)\big) = g_{\text{syn}} s(t)\big(e_r - v_i(t)\big), \tag{4.2}$$

where the maximum synaptic conductance g_{syn} determines the coupling strength and the reversal potential e_r, which is usually 0 mV for excitatory synapses and negative for inhibitory ones, determines whether the synapses increase or decrease the likelihood of firing of the postsynaptic neuron. The term $g_{\text{syn}}(e_r - v_i)$ in Eq. (4.2) is sometimes replaced by a constant for simplicity, e.g., in [150, 178, 90], such that positive/negative I_{syn} represents the excitatory/inhibitory synaptic coupling, respectively. While simplifying the mathematics, it ignores the physiological fact that the type of synaptic coupling is determined by the value of e_r and the coupling changes sign with $(e_r - v_k)$. In addition, the synaptic gating variable s_i is affected by the firing of presynaptic neurons and $s_i = s$ for an all-to-all coupling network (see details in Sec. 3.2). For a single exponential synapse, the governing equation is

$$s'(t) = -s(t)/\tau_s + s_{\text{jump}} u(t), \tag{4.3}$$

where τ_s and s_{jump} are parameters and $u(t)$ represents the mean spike train injected from all presynaptic neurons, given by

$$u(t) = \frac{1}{N} \sum_{j=1}^{N} \sum_{k} \delta(t - t_j^{(k)}) \tag{4.4}$$

When the number of neurons in the network goes to infinity, that is, $N \to \infty$, we have

$$r(t) = u(t), \tag{4.5}$$

where $r(t)$ is the population firing rate, i.e., the population-averaged number of spikes per unit time (see Sec. 3.3.1). In the limit $v_{\text{peak}} = -v_{\text{reset}} = \infty$, the model (4.1) represents a network of adaptive theta neurons defined in the domain $\theta \in [-\pi, \pi)$ [117, 85, 104, 126] via the transform $v = \tan(\theta/2)$. Such a network satisfies the conditions for the existence of the low-dimensional OA manifold in terms of θ [163] or the Lorentzian ansatz in terms of v [150] that guarantees the evolution of network dynamics as $N \to \infty$. Further reduction in the dimensionality of the resulting mean-field system can be achieved by choosing a Lorentzian distribution for the current parameters η_i with half-width at half-maximum (HWHM) Δ_η, centered at $\bar{\eta}$,

$$\mathcal{L}(\eta) = \frac{1}{\pi} \frac{\Delta_\eta}{(\eta - \bar{\eta})^2 + \Delta_\eta^2}. \tag{4.6}$$

Thus, together with Eqs. (4.3) and (4.4), we can obtain a mean-field system in terms of the population firing rate r, mean membrane potential $\langle v \rangle$ and mean adaptation current $\langle w \rangle$, given by

$$\begin{aligned}
r' &= \Delta_\eta/\pi + 2r\langle v \rangle - \big(\alpha + g_{\text{syn}} s\big) r, \\
\langle v \rangle' &= \langle v \rangle^2 - \alpha \langle v \rangle - \pi^2 r^2 - \langle w \rangle + g_{\text{syn}} s\big(e_r - \langle v \rangle\big) + \bar{\eta} + I_{\text{ext}}, \\
\langle w \rangle' &= a\big(b\langle v \rangle - \langle w \rangle\big) + w_{\text{jump}} r.
\end{aligned} \tag{4.7}$$

In the thermodynamic limit, $N \to \infty$, this mean-field model is valid to represent a heterogeneous all-to-all coupled population of N Izhikevich neurons without synaptic delay. See details in Chapter 3. Note that the assumption of $v_{\text{peak}} = -v_{\text{reset}} = \infty$ is not realistic for biophysiological neurons, as their specific and finite values influence the spiking behavior of individual neurons [113, 115]. However, the study in [97] shows that the realistic reset rule leads mainly to an increase in the population firing rate, which can be compensated for by rescaling the current I_{ext} (equivalently, $\bar{\eta}$) in the mean-field model. In addition, the symmetry constraint between v_{peak} and v_{reset} can be addressed by introducing their ratio [151]. While the limit $v_{\text{peak}} \to \infty$, $v_{\text{reset}} \to -\infty$ is still taken for the mean-field approximation, the ratio is held fixed and different from -1.

If communication between neurons is not instantaneous, that is, there exists a delay between spike emission and reception, then for any neuron in an all-to-all network, the spike train resulting from all other neurons obeys the following equation,

$$u(t) = \frac{1}{N} \sum_{j=1}^{N} \sum_{k} \delta(t - t_j^{(k)} - \tau_j), \tag{4.8}$$

where τ_j is the synaptic delay of the signal sending from the jth neurons. For the fixed, homogeneous delay, $\tau_j = D$ and the mean spike train is changed to

$$u(t) = \frac{1}{N} \sum_{j=1}^{N} \sum_{k} \delta(t - t_j^{(k)} - D). \tag{4.9}$$

If the delay is heterogeneous and follows some probability density function $h(\tau)$ such that $h(\tau)d\tau$ represents the fraction of links with delays between τ and $\tau + d\tau$. In the thermodynamic limit, the mean spike train can be approximated by the integral in terms of $r(t)$ [133, 178],

$$u(t) = \int_0^\infty r(t - \tau)h(\tau)d\tau. \tag{4.10}$$

Thus, the resulting mean-field description for the network with general distributed delay is characterized by Eqs. (4.3), (4.7) and (4.10). Further simplification can be achieved by a proper choice of the distribution function $h(\tau)$. We will show some examples in the following section.

4.2.2 Example Mean-Field Models

Removing the integral (4.10) from the general mean-field model can be accomplished by appropriately selecting the distribution function $h(\tau)$. In this section, we present some typical distributions of $h(\tau)$ and the corresponding mean-field models.

For example, $h(\tau)$ may be given by the gamma distribution

$$h(\tau) = \frac{A_n}{D^n} \tau^{n-1} e^{-\frac{n\tau}{D}} = \frac{A_n}{D^n} \tau^{n-1} e^{-\tau/\tau_u} \tag{4.11}$$

with a natural number, $n = 1, 2, \ldots$. Here, D is the mean value of delays, $A_n = n^n/(n-1)!$ is a normalization parameter, and $\tau_u = D/n$ is related to the standard deviation of τ,

$$\delta\tau = \sqrt{\langle \tau^2 \rangle - \langle \tau \rangle^2} = D/\sqrt{n}. \tag{4.12}$$

Next, we will transform the integral in Eq. (4.10) into a nth order ordinary differential equations (ODEs) using the so-called linear chain trick [193, 178]. For convenience, we rewrite the gamma distribution as

$$h_\beta^n(\tau) = \frac{\beta^n}{(n-1)!} \tau^{n-1} e^{-\beta\tau},$$

where $\beta = n/D$. An important property is that the functions $h_\beta^l(0)$ satisfy the equations,

$$\begin{aligned} h_\beta^1(0) &= \beta, \\ h_\beta^l(0) &= 0, \quad l = 2, \ldots, n. \end{aligned}$$

Define functions $u^l(t)$ for $l = 1, 2, \ldots, n$ by

$$u^l(t) = \int_0^\infty r(t-\tau) h_\beta^l(\tau) d\tau = \int_{-\infty}^t r(\tau) h_\beta^l(t-\tau) d\tau.$$

Then for $l > 1$, where $h_\beta^l(0) = 0$, we have

$$\begin{aligned} \frac{du^l}{dt} &= \frac{d}{dt}\left[\int_{-\infty}^t r(\tau) h_\beta^l(t-\tau) d\tau\right] \\ &= r(t) h_\beta^l(0) + \int_{-\infty}^t r(\tau) \frac{d}{dt} h_\beta^l(t-\tau) d\tau \\ &= \int_{-\infty}^t r(\tau) \beta \left[h_\beta^{l-1}(t-\tau) - h_\beta^l(t-\tau)\right] d\tau \\ &= \int_0^\infty r(t-\tau) \beta \left[h_\beta^{l-1}(\tau) - h_\beta^l(\tau)\right] d\tau \\ &= \beta \left[u^{l-1}(t) - u^l(t)\right]. \end{aligned}$$

Whereas for $l = 1$, where $h_\beta^1(0) = \beta$, the same argument gives

$$du^1/dt = \beta \left[r(t) - u^1(t)\right].$$

For consistency, let $u^0(t) = r(t)$. Thus, we obtain a set of equivalent ODEs for the mean spike train with the gamma-distributed kernel,

$$\begin{aligned} \tau_u du^l/dt &= u^{l-1}(t) - u^l(t), \quad l = 1, \cdots, n, \\ u^0(t) &= r(t), \\ u^n(t) &= u(t), \end{aligned}$$

where $\tau_u = 1/\beta = D/n$. In a more compact form, we can rewrite these equations as

$$\left(\tau_u \frac{d}{dt} + 1\right)^n u(t) = r(t). \tag{4.13}$$

For example, for $n = 2$, Eq. (4.13) becomes

$$\left(\tau_u \frac{d}{dt} + 1\right)^2 u(t) = r(t) \;\Rightarrow\; \tau_u^2 \frac{d^2}{dt^2} u(t) + 2\tau_u \frac{d}{dt} u(t) + u(t) = r(t).$$

Therefore, the Izhikevich network with gamma-distributed delay can be reduced to a mean-field system composed of a set of ODEs (4.3), (4.7) and (4.13).

Moreover, if we consider a gamma distribution with a nonzero minimum delay,

$$h(\tau) = \begin{cases} 0, & 0 \le \tau < \tau_{\min}, \\ \frac{A_n}{D^n}(\tau - \tau_{\min})^{n-1} e^{-(\tau-\tau_{\min})/\tau_u}, & \tau_{\min} \le \tau, \end{cases} \tag{4.14}$$

then the integral in Eq. (4.10) is changed into a nth order differential equation

$$\left(\tau_u \frac{d}{dt} + 1\right)^n u(t) = r(t - \tau_{\min}), \tag{4.15}$$

and the equivalent system of equations is given by

$$\begin{aligned} \tau_u du^l/dt &= u^{l-1}(t) - u^l(t), \quad j = 1, \cdots, n \\ u^0(t) &= r(t - \tau_{\min}), \\ u^n(t) &= u(t). \end{aligned}$$

Thus, the resulting mean-field system is characterized by delay differential equation (DDE)s with a constant delay $\tau_{\min}$.

Furthermore, we can relate the mean spike train (4.8) to the population firing rate $r(t)$ using the integral (4.10). It can be seen that as $n \to \infty$, the gamma distribution (4.11) becomes the Dirac delta function $h(\tau) = \delta(\tau - D)$ when the width of the distribution, the standard deviation of the delay (4.12), approaches zero. This situation corresponds to the fixed homogeneous delay on all links, that is, $\tau_j = D$ for all j in Eq. (4.8), and the integral (4.10) becomes

$$u(t) = r(t - D). \tag{4.16}$$

The resulting mean-field system is characterized by DDEs with a constant delay D, that is, Eqs. (4.3), (4.7) and (4.16). Additionally, when $D = 0$, meaning $h(\tau) = \delta(\tau)$, this scenario corresponds to a neural network without delay (see (4.9) with $D = 0$). We have

$$u(t) = \frac{1}{N} \sum_{j=1}^{N} \sum_{k} \delta(t - t_j^{(k)}) = r(t).$$

This is consistent with the argument in Chapter 3, where we establish the connection between the population firing rate r and the mean spike activity u based on the definition of the number of spikes (see Eq. (3.13)-(3.15)).

4.3 Linear Stability Analysis of Delayed Mean-Field Systems

In this section, we investigate the existence of EPs and their linear stability for the mean-field system with general distributed delay. Specifically, we examine the mean-field system with the limit of heterogeneity $\Delta_\eta \to 0$ from the perspective of stationary states, i.e., EPs.

4.3.1 Existence of Equilibrium for Weak Heterogeneity

The mean-field system (4.3), (4.7) and (4.10) is defined by four macroscopic variables: $r(t)$, $v(t)$, $w(t)$ and $s(t)$. We denote the EP as (r_*, v_*, w_*, s_*). Standard analysis shows that it obeys the following equations,

$$\begin{aligned}
\Delta_\eta/\pi + 2r_*v_* - \big(\alpha + g_{\text{syn}}s_*\big)r_* &= 0,\\
v_*^2 - \alpha v_* - \pi^2 r_*^2 + g_{\text{syn}}s_*\big(e_r - v_*\big) - w_* + \bar{\eta} + I_{\text{ext}} &= 0,\\
a\,(bv_* - w_*) + w_{\text{jump}}r_* &= 0,\\
-s_*/\tau_s + s_{\text{jump}}r_* &= 0.
\end{aligned}$$

Here, we employ the normalization condition

$$\int_0^\infty h(\tau)d\tau = 1.$$

After some algebraic manipulations, we have

$$\begin{aligned}
v_* &= \frac{J}{2}r_* - \frac{\Delta_\eta}{2\pi}\frac{1}{r_*} + \frac{\alpha}{2},\\
w_* &= bv_* + \frac{w_{\text{jump}}}{a}r_*,\\
s_* &= \tau_s s_{\text{jump}} r_*,
\end{aligned}$$

where $J = g_{\text{syn}}\tau_s s_{\text{jump}}$ and r_* satisfies the quartic equation

$$C_4 r_*^4 + C_3 r_*^3 + C_2 r_*^2 + C_1 r_* + C_0 = 0, \tag{4.17}$$

with

$$\begin{aligned}
C_4 &= J^2 + 4\pi^2,\\
C_3 &= 2J(\alpha + b - 2e_r) + 4w_{\text{jump}}/a,\\
C_2 &= \alpha^2 + 2\alpha b - 4I_{\text{ext}} - 4\bar{\eta},\\
C_1 &= -2b\Delta_\eta/\pi,\\
C_0 &= -\Delta_\eta^2/\pi^2.
\end{aligned} \tag{4.18}$$

Note that for biophysical interpretation, the population firing rate r should be non-negative and the proportion of open ion channels s should be bounded by 1. So we have $0 \leq r_* \leq 1/(\tau_s s_{\text{jump}})$.

The neural network we consider has heterogeneous input currents η_i. It follows a Lorentzian distribution (4.6) with Δ_η measuring its width. The value of Δ_η determines the level of heterogeneity. $\Delta_\eta = 0$ implies a homogeneous network, where each neuron is given the same current η. The larger Δ_η, the more heterogeneous the network is. Since $\Delta_\eta = 0$ corresponds to the neurons in the network being strictly identical, the correct approach to derive the mean-field model is to apply the Watanabe-Strogatz theory [213, 214], rather than the OA theory [163] used in this paper. However, it has been shown that the OA mean-field model for identical neurons is representative of the existence but not stability of solutions of the full network [174]. Since the mean-field model equations (4.7) are continuous functions of Δ_η, we expect that the EP is to vary continuously with Δ_η. To investigate this further, we focus on the case of weak heterogeneity, that is, the limit $\Delta_\eta \to 0$, and apply perturbation analysis.

We suppose that Δ_η is a small parameter and define $\Delta_\eta = \epsilon \ll 1$. Then, we rewrite the equation for r_* as

$$C_4 r_*^4 + C_3 r_*^3 + C_2 r_*^2 + \widetilde{C}_1 \epsilon r_* + \widetilde{C}_0 \epsilon^2 = 0,$$

where $\widetilde{C}_1 = -2b/\pi$ and $\widetilde{C}_0 = -1/\pi^2$. We then look for its roots in the form

$$r_* = r_{*,0} + r_{*,1}\epsilon + r_{*,2}\epsilon^2 + O(\epsilon^3). \tag{4.19}$$

Substituting this expression, expanding and collecting terms in like powers of ϵ yield the $O(1)$ equation

$$C_4 r_{*,0}^4 + C_3 r_{*,0}^3 + C_2 r_{*,0}^2 = 0.$$

This has the solutions $r_{*,0} = 0, 0$ and

$$r_{*,0}^{\pm} = \frac{-C_3 \pm \sqrt{C_3^2 - 4C_4C_2}}{2C_4}. \tag{4.20}$$

The $O(\epsilon)$ equation is

$$4C_4 r_{*,0}^3 r_{*,1} + 3C_3 r_{*,0}^2 r_{*,1} + 2C_2 r_{*,0} r_{*,1} + \widetilde{C}_1 r_{*,0} = 0,$$

where $\widetilde{C}_1 = C_1/\epsilon = -2b/\pi$. With $r_{*,0} = 0$, this gives no constraint on $r_{*,1}$. With $r_{*,0} \neq 0$, we have

$$r_{*,1}^{\pm} = \frac{-\widetilde{C}_1}{4C_4 r_{*,0}^2 + 3C_3 r_{*,0} + 2C_2}, \quad \text{when} \quad r_{*,0} \neq 0.$$

The $O(\epsilon^2)$ equation is

$$\left(4C_4r_{*,0}^3+3C_3r_{*,0}^2+2C_2r_{*,0}\right)r_{*,2}+\left(6C_4r_{*,0}^2+3C_3r_{*,0}+C_2\right)r_{*,1}^2+\widetilde{C}_1r_{*,1}+\widetilde{C}_0=0,$$

where $\widetilde{C}_0=C_0/\epsilon^2=-1/\pi^2$. With $r_{*,0}=0$, this gives no constraint on $r_{*,2}$. However, $r_{*,1}$ should satisfy

$$\left(6C_4r_{*,0}^2+3C_3r_{*,0}+C_2\right)r_{*,1}^2+\widetilde{C}_1r_{*,1}+\widetilde{C}_0=0,$$

which gives

$$r_{*,1}^{\pm}=\frac{-\widetilde{C}_1\pm\sqrt{\widetilde{C}_1^2-4\widetilde{C}_0C_2}}{2C_2},\quad \text{when } r_{*,0}=0.$$

Substituting it into the solution (4.19) yields

$$r_*=r_{*,1}^{\pm}\cdot\epsilon=\frac{-\widetilde{C}_1\pm\sqrt{\widetilde{C}_1^2-4\widetilde{C}_0C_2}}{2C_2}\cdot\epsilon,\quad \text{when } r_{*,0}=0. \tag{4.21}$$

Since $0<\epsilon\ll 1$, these solutions are very close to zero.

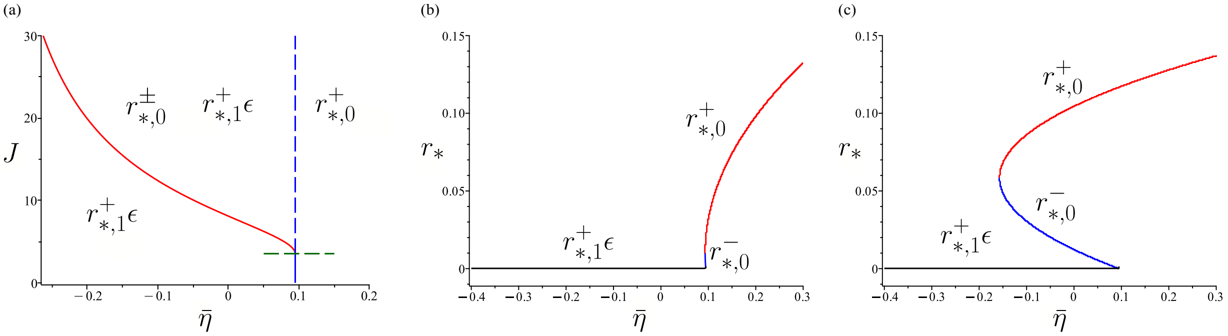

Figure 4.1: Perturbation analysis of the mean-field system (4.3), (4.7) and (4.10) for the excitatory neural network with weak heterogeneity. (a): Existence of EP with biophysically realistic value of r_* in the $(\bar{\eta}, J)$ parameter space is determined by the curves defined from Eq. (4.22). Red corresponds to $C_3^2-4C_4C_2=0$, blue to $C_2=0$, and green to $C_3=0$. Variation of r_* with $\bar{\eta}$ when (b): $\Delta_\eta=10^{-4}$ and $J=3.94$, (c): $\Delta_\eta=10^{-4}$ and $J=16.00$. Other parameter values are from Table 4.1.

In summary, the perturbation analysis shows that the mean-field system with weak heterogeneity has at most four biophysically relevant values for r_*, given to lowest order by

$$
\begin{aligned}
r_* &= r_{*,0}^{\pm} = \frac{-C_3 \pm \sqrt{C_3^2 - 4C_4C_2}}{2C_4}, \\
r_* &= r_{*,1}^{\pm} \cdot \epsilon = \frac{-\widetilde{C}_1 \pm \sqrt{\widetilde{C}_1^2 - 4\widetilde{C}_0C_2}}{2C_2} \cdot \epsilon.
\end{aligned}
\tag{4.22}
$$

Whether or not these are biophysically relevant depends on the parameter values. The first two solutions can be expressed in parametric form in terms of $\bar{\eta}$ and J. The other two solutions are close to zero, since they are $O(\epsilon)$. No solution with exactly $r_* = 0$ exists, except when $\Delta_\eta = 0$. However, our perturbation analysis reveals that the small EP $r_* \to 0$ as $\Delta_\eta \to 0$. This suggests that the scenario involving weak heterogeneity can be considered as a small perturbation of the homogeneous counterpart. For certain publications in the literature, such as [178, 169, 69], the analysis of the OA-based mean-field model with $\Delta_\eta = 0$ can be interpreted as describing a weakly heterogeneous system.

Further, from Eq. (4.22), we can obtain regions in the parameter space where the different perturbation solutions for r_* exist. It is shown that at most three biophysically relevant solutions can co-exist for a given set of parameter values. Here, we focus on an example using the parameter values shown in Table 4.1. Fig. 4.1(a) illustrates the regions of existence in the $(\bar{\eta}, J)$ plane. For the excitatory neural network where the dimensionless value of the reversal potential is $e_r = 1$, the system has one positive EP, $r_* = r_{*,1}^{+}\epsilon \approx 0$, in the region to the left of the blue line and below the red curve, and three EPs, $r_* = r_{*,0}^{\pm} > 0$ and $r_* = r_{*,1}^{+}\epsilon \approx 0$, in the region to the left of the blue line and above the red curve. To the right of the blue line, there is a very small region (not shown) where the system has three EPs, $r_* = r_{*,0}^{+} > 0$ and $r_* = r_{*,1}^{\pm}\epsilon \approx 0$ exist, further to the right only one EP, $r_* = r_{*,0}^{+} > 0$, remains. Fig. 4.1 (b) and (c) show the variation of r_* with respect to $\bar{\eta}$ for different values of J. Both diagrams show the same bifurcations and transitions, but in (b) they occur in a much smaller range of values of $\bar{\eta}$, thus we focus on (c). In (c) $J = 16.00$, i.e., $g_{\text{syn}} = 5$. For $\bar{\eta} > 0.0946$ only the EP with $r_* = r_{*,0}^{+} > 0$ (red) exists. For $\bar{\eta} < -0.1570$ only the EP with $r_* = r_{*,1}^{+}\epsilon \approx 0$ (black) exists. Between the two ranges, there are three EPs. For the inhibitory neural network where $e_r < 0$, we always have $C_3 > 0$. Thus, only one EP, $r_* = r_{*,0}^{+} > 0$, exists to the right of the blue line in Fig. 4.1(a), that is, $\bar{\eta} > 0.0946$, and only one EP, $r_* = r_{*,1}^{+}\epsilon \approx 0$, to the left. Fig. 4.1 was created using Maple [148]. The existence of EPs was numerically verified by XPPAUT [83] (not shown here).

4.3.2 Linear Stability of Equilibria

In this section, we show how to derive the characteristic equation of the linearized mean-field system and the parametric equations for the Andronov-Hopf (HP) bifurcation.

Defining small deviations $\delta r = r - r_*$, $\delta v = v - v_*$, $\delta w = w - w_*$ and $\delta s = s - s_*$, we substitute $r = r_* + \delta r$, $v = v_* + \delta v$, $w = w_* + \delta w$ and $s = s_* + \delta s$ into the mean-field model with a general distribution of delays (4.3), (4.7) and (4.10) and linearize them with respect to small deviations $(\delta r, \delta v, \delta w, \delta s)$. Then we get the linearized equations

$$\begin{aligned}
\delta r'(t) =&(2v_* - \alpha - g_{\text{syn}} s_*)\delta r + 2r_* \delta v - g_{\text{syn}} r_* \delta s, \\
\delta v'(t) =& -2\pi^2 r_* \delta r + (2v_* - \alpha - g_{\text{syn}} s_*)\delta v \\
&- \delta w + g_{\text{syn}}(e_r - v_*)\delta s, \\
\delta w'(t) =& w_{\text{jump}} \delta r + ab\delta v - a\delta w, \\
\delta s'(t) =& -\delta s/\tau_s + s_{\text{jump}} \int_0^\infty \delta r(t-\tau) h(\tau) d\tau.
\end{aligned}$$

We look for the solution of the linearized equations in the form

$$(\delta r, \delta v, \delta w, \delta s) = (K_r, K_v, K_w, K_s) \exp(\lambda t),$$

where K_j are constants. Then, we have

$$[\mathbf{A}(\lambda) - \lambda \mathbf{I}]\,\mathbf{K} = \mathbf{0},$$

where $\mathbf{K} = (K_r, K_v, K_w, K_s)^T$ and

$$\mathbf{A}(\lambda) = \begin{bmatrix} 2v_* - \alpha - g_{\text{syn}} s_* & 2r_* & 0 & -g_{\text{syn}} r_* \\ -2\pi^2 r_* & 2v_* - \alpha - g_{\text{syn}} s_* & -1 & g_{\text{syn}}(e_r - v_*) \\ w_{\text{jump}} & ab & -a & 0 \\ s_{\text{jump}} H(\lambda) & 0 & 0 & -1/\tau_s \end{bmatrix},$$

where $H(\cdot)$ is the Laplace transform of $h(\cdot)$, that is,

$$H(\lambda) = \int_0^\infty e^{-\lambda \tau} h(\tau) d\tau.$$

Then, we derive the characteristic equation

$$\Lambda(\lambda) = P(\lambda) H^{-1}(\lambda) + Q(\lambda), \tag{4.23}$$

where

$$\begin{aligned}
P(\lambda) =& \Big[(\lambda+a)(\lambda+K)^2 + ab(\lambda+K) + 4\pi^2 r_*^2(\lambda+a) + 2w_{\text{jump}} r_*\Big](\tau_s\lambda+1),\\
Q(\lambda) =& \Big[Jr_*(\lambda+K)(\lambda+a) - 2Jr_*(e_r - v_*)(\lambda+a) + abJr_*\Big].
\end{aligned}$$

Here, we denote $J = \tau_s g_{\text{syn}} s_{\text{jump}}$ and $K = \alpha + Jr_* - 2v_*$.

We can obtain some general information about the stability region:

- $H(0) = 1$
- for real roots of $\Lambda(\lambda) = 0$, if $\lambda \geq 0$, then $e^{-\lambda\tau} \leq 1$, and thus $H(\lambda) \leq 1$.
- for some parameter values, the characteristic equation can have a zero root for any distribution, that is, $\Lambda(0) = P(0)\cdot 1 + Q(0) = 0$.

In addition, we can derive the potential HP bifurcation curves in parametric form by imposing the condition of marginal stability $\lambda = i\omega$ on the characteristic equation (4.23). Substituting $\lambda = i\omega$, $K = \alpha + Jr_* - 2v_*$ into the characteristic equation and collecting terms in like powers of r_*, we have

$$\begin{aligned}
P(i\omega) &= R_2 r_*^2 + R_1 r_* + R_0 + i\omega\left(D_2 r_*^2 + D_1 r_* + D_0\right),\\
Q(i\omega) &= \hat{R}_2 r_*^2 + \hat{R}_1 r_* + i\omega\left(\hat{D}_2 r_*^2 + \hat{D}_1 r_*\right),
\end{aligned}$$

where

$$\begin{aligned}
R_2 &= -\tau_s(J^2+4\pi^2)\omega^2 + aJ^2 + 4a\pi^2,\\
R_1 &= -2J\left[1+\tau_s(a+\alpha-2v_*)\right]\omega^2 + 2aJ(\alpha-2v_*) + abJ + 2w_{\text{jump}},\\
R_0 &= \tau_s\omega^4 - \big[\tau_s(\alpha-2v_*)^2 + 2(\alpha-2v_*)(\tau_s a+1) + \tau_s ab + a\big]\omega^2\\
&\qquad + a(\alpha-2v_*)(\alpha-2v_*+b),\\
D_2 &= (J^2+4\pi^2)(1+a\tau_s),\\
D_1 &= -2J\tau_s\omega^2 + 2J(a+\alpha-2v_*) + \tau_s\big[2aJ(\alpha-2v_*) + abJ + 2w_{\text{jump}}\big],\\
D_0 &= -\big[1+\tau_s(a+2\alpha-4v_*)\big]\omega^2 + (\alpha-2v_*)^2 + 2a(\alpha-2v_*) + ab\\
&\qquad + a\tau_s\big[(\alpha-2v_*)(\alpha-2v_*+b)\big],
\end{aligned}$$

and

$$
\begin{aligned}
\hat{R}_2 &= aJ^2, \\
\hat{R}_1 &= -J\omega^2 + aJ(\alpha + b - 2e_r), \\
\hat{D}_2 &= J^2, \\
\hat{D}_1 &= J(a + \alpha - 2e_r),
\end{aligned}
$$

Denote $H^{-1}(i\omega) = A(\omega) + iB(\omega)$ in Eq. (4.23). Separating the real and imaginary parts of the characteristic equation yields the parametric equations for the Hopf bifurcation curves,

$$
\begin{aligned}
0 =&(R_2 r_*^2 + R_1 r_* + R_0)A - (D_2 r_*^2 + D_1 r_* + D_0)B\omega + (\hat{R}_2 r_*^2 + \hat{R}_1 r_*), \\
0 =&(R_2 r_*^2 + R_1 r_* + R_0)B + (D_2 r_*^2 + D_1 r_* + D_0)A\omega + (\hat{D}_2 r_*^2 + \hat{D}_1 r_*)\omega.
\end{aligned}
\tag{4.24}
$$

A proper choice of the distribution function for the synaptic delay can further simplify the stability analysis. The simplest case is the neural network without synaptic delay, where $h(\tau) = \delta(\tau)$ and the reciprocal of the Laplace transform at the Hopf point is $H^{-1}(j\omega) = 1$. For the network with homogeneous delay D, the distribution function is $h(\tau) = \delta(\tau - D)$ and the reciprocal of the Laplace transform is given by

$$
H^{-1}(i\omega) = e^{i\omega D} = \cos(\omega D) + i\sin(\omega D) \equiv A(D, \omega) + iB(D, \omega).
$$

We determine r_* as a function of parameters from Eq. (4.22) and substitute it into Eq. (4.24). Then we can derive the value of one parameter and ω at which a Hopf bifurcation may occur. Alternatively, we could solve for two parameters as parametric equations in ω to get two-parameter curves. To fully verify the existence of Hopf bifurcation, one must check the transversality and nondegeneracy conditions [193]. This task becomes challenging for our model, given the complex dependence of the EPs and hence the coefficients of the characteristic equation on the parameters. Therefore, the remainder of this chapter pivots towards numerical approaches.

4.4 Numerical Bifurcation Analysis of Mean-Field Systems

In this section, we are mainly concerned about the fixed, homogeneous delay across the network and the consequent mean-field system of DDEs (4.3), (4.7) and (4.16). The resulting dynamics are fascinating enough to warrant a careful investigation, and the approach can be extended to the resulting mean-field system composed of ODEs for gamma-distributed delay or DDEs for gamma-distribution with a minimum delay. We study the macroscopic dynamics through numerical bifurcation analysis of the mean-field system and mainly investigate the impact of three factors: the heterogeneity of the current Δ_η, the level of adaptation w_{jump} and the synaptic delay D. Furthermore, we investigate whether the OA-based mean-field system with extremely weak heterogeneity has a smooth transition to its homogeneous counterpart in terms of the bifurcation structure. All the variables and parameters in this section are dimensionless, and are given in Table 4.1, unless otherwise indicated in a figure caption. To transform them into dimensional ones where the parameters have physiological interpretation, one can refer to Sec. 3.2. All values are taken from [158] for the excitatory coupled neural network (E-net), which were initially fit by [78] to hippocampal CA3 pyramidal neuron data from [107]. The parameters for the inhibitory network (I-net) are the same except that the reversal potential ($E_r = -75$ mV, that is, $e_r = -0.1538$) is taken from [181]. To perform the bifurcation analysis, we consider the physiologically plausible ranges of parameter values [159, 34, 84], as shown in Table 4.2. Our results are obtained using standard continuation packages: XPPAUT [83] and MatCont [71] for the system with no delay, and DDE-Biftool [81] when the delay is nonzero. To verify and extend these results, numerical simulations are carried out in Matlab (R2022b) [145] and Julia (v1.8) [26].

Parameter	Value	Parameter	Value
α	0.6215	τ_s	2.6
a	0.0077	b	-0.0062
I_{ext}	0	s_{jump}	1.2308
g_{syn}	1.2308	w_{jump}	0.0189
$e_{r,E}$	1	$e_{r,I}$	-0.1538

Table 4.1: Dimensionless parameter values for the Izhikevich neural network ($e_{r,E}/e_{r,I}$ for excitatory/inhibitory network, respectively).

4.4.1 Typical Macroscopic Behaviors

To motivate the bifurcation analysis, we present some typical macroscopic behaviors observed in our models, as illustrated in Fig. 4.2. The raster plots are generated through numerical simulation of the neural network model (4.1)-(4.3) and (4.9), with neurons arranged in ascending order of the current η_i, while time series of the macroscopic variables

Parameter	Dimensionless value	Dimensional Value
$\bar{\eta}$	$0 - 0.5$	$0 - 5000$ pA
Δ_η	$0 - 0.1$	$0 - 1056$ pA
g_{syn}	$0 - 5$	$0 - 800$ nS
w_{jump}	$0 - 0.1$	$0 - 1056$ pA
D	$0 - 20$	$0 - 30$ ms

Table 4.2: Physiologically plausible ranges of parameters for bifurcation analysis.

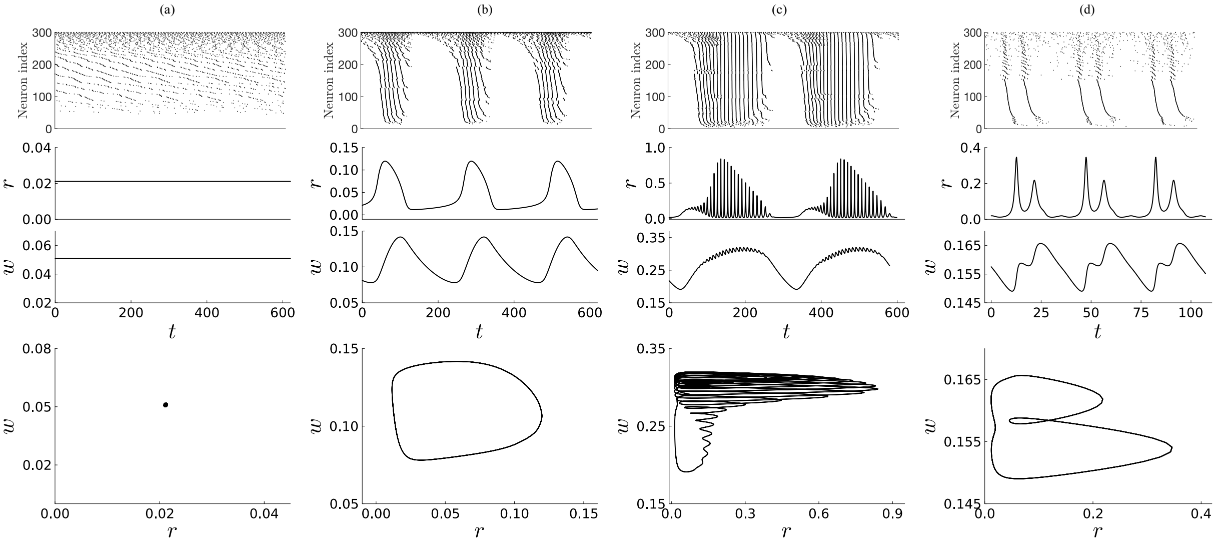

Figure 4.2: Examples of macroscopic behaviors. The first row shows raster plots of 300 neurons randomly selected from 5000 neurons of the network (4.1)-(4.3) and (4.9). The dots correspond to the firing events and the neurons are arranged in order of increasing current η_i. The last two rows give time evolution and phase portraits of $r(t)$ and $w(t)$ of the delayed mean-field equations (4.3), (4.7) and (4.16). Parameter values: Column (a) (E-net): $D = 1$, $g_{\text{syn}} = 0.2$, $w_{\text{jump}} = 0.0189$, $\bar{\eta} = 0.12$ and $\Delta_\eta = 0.02$; Column (b) (E-net): $D = 1$, $g_{\text{syn}} = 1$, $w_{\text{jump}} = 0.0189$, $\bar{\eta} = 0.12$ and $\Delta_\eta = 0.02$; Column (c) (E-net): $D = 4$, $g_{\text{syn}} = 1.1$, $w_{\text{jump}} = 0.025$, $\bar{\eta} = 0.25$ and $\Delta_\eta = 0.02$; Column (d) (I-net): $D = 14$, $g_{\text{syn}} = 1$, $w_{\text{jump}} = 0.0189$, $\bar{\eta} = 0.4$ and $\Delta_\eta = 0.02$. Other parameters are given in Table 4.1.

result from integrating the corresponding mean-field equations (4.3), (4.7) and (4.16). Starting with the column of Fig. 4.2(a), the raster plot reveals that a small group of neurons with low current remain quiescent, while the rest exhibit asynchronous tonic firing with different frequencies determined by current values. From the macroscopic viewpoint, the system eventually settles on an EP, corresponding to a point in the (r, w) phase plane. Moving to the column of Fig. 4.2(b), the dynamics shows regular COs. Neurons undergo bursting, characterized by an alternation between silent and active states. During a burst, neurons spike asynchronously, with those having higher currents η firing before those with lower values. The mean-field system converges to a periodic orbit (PO) with a unique oscillation period. In Fig. 4.2(c), neurons also exhibit bursting behavior. The distinction lies in the fact that during a burst, most neurons fire synchronously, manifested by straight lines in the raster plot, instead of the "traveling waves" observed in Fig. 4.2(b). The mean-field system exhibits quasi-periodic behavior characterized by fast oscillations with a slowly varying envelope. These COs involve two oscillation periods: the slow one responsible for the population bursting rhythm and the fast one corresponding to the spiking period of individual neurons. We refer to this phenomenon as slow-fast nested COs, or population bursting, by analogy to the similar activity of single neurons [191, 90]. Another type of interesting CO is shown in Fig. 4.2(d). In this case, a subpopulation of neurons bursts, alternating with short and long quiescent periods. The limit cycle in the mean variables of $r(t)$ and $w(t)$, observed in the time series and phase portrait, resembles those arising in period-doubling bifurcations.

In summary, we present four dynamical regimes that occur in our delayed mean-field system. The first two dynamics are common phenomena observed in neural networks, regardless of whether we consider the delay in spike transmission. The last two regimes are novel and more complex COs found in the neural system with the SFA mechanism and synaptic delay. To better understand these macroscopic behaviors and the transition between them, we delve into numerical bifurcation analysis in the following sections.

4.4.2 Bifurcation of Neural Network without Synaptic Delay

Looking for HP bifurcations is the first step of bifurcation analysis to separate COs from stationary states. For comparison, we begin with the system without synaptic delay. The corresponding mean-field model is composed of ODEs (4.3), (4.4) and (4.7). Hopf boundaries are shown in Fig. 4.3 in different pairs of parameter planes. The COs occur in the highlighted yellow areas, with boundaries that vary with the corresponding parameter. Note that the diagrams for the excitatory network (E-net) complement those in Chapter 3 for the same system with the same parameter values.

First, we explore the effect of heterogeneity. For the excitatory neural network (E-net), we start with the Hopf bifurcation in the $(g_{\text{syn}}, \bar{\eta})$ plane for different values of Δ_η,

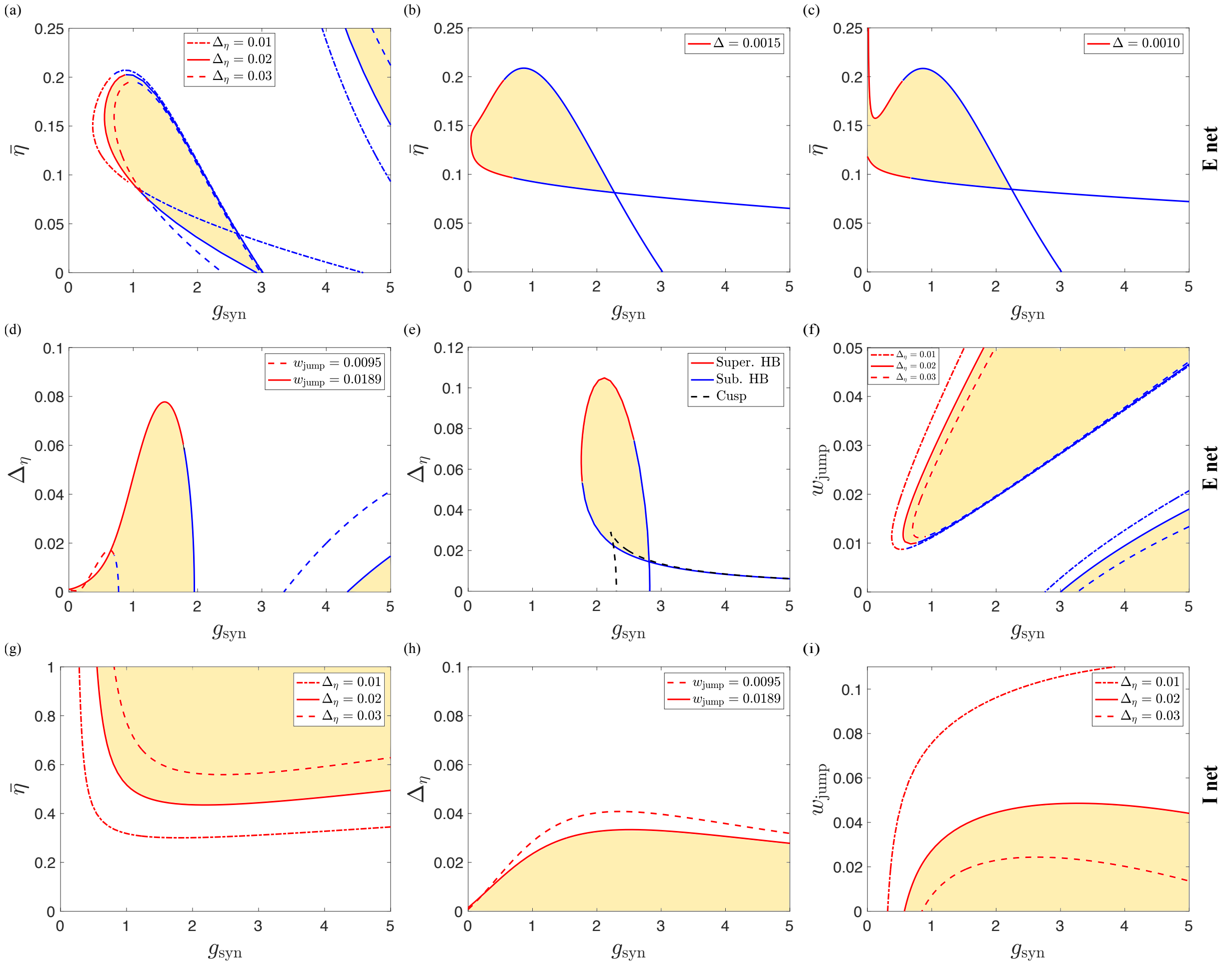

Figure 4.3: Effect of heterogeneity and adaptation on the excitatory (first two rows) and inhibitory (last row) neural networks without synaptic delay. Red/blue: supercritical/subcritical Hopf boundaries. The yellow areas depict COs with boundaries adapting to corresponding parameters. Parameter values: (a)-(c) $w_{\text{jump}} = 0.0189$, (d) $\bar{\eta} = 0.12$, (e) $\bar{\eta} = 0.02$, (f) $\bar{\eta} = 0.12$, (g) $w_{\text{jump}} = 0.0189$, (h)-(i) $\bar{\eta} = 0.6$. Other parameter values are given in Table 4.1.

shown in Fig. 4.3(a). Two Hopf branches appear. One looks like a straight line in the biological range of parameter values, with the Hopf being subcritical (blue); the other is a closed loop and exhibits two codimension-2 Bautin (or generalized Hopf) bifurcations, with the Hopf being supercritical (red) between these points and subcritical (blue) outside. In the region bounded by two Hopf branches (white), the mean-field system settles on an EP, where neurons exhibit asynchronous tonic firing, similar to the behavior shown in

Fig. 4.2(a). Inside the closed loop and in the top right corner (yellow), COs emerge, and neurons exhibit bursting behavior. This behavior is similar to that shown in Fig. 4.2(b), although the oscillation frequency depends on the particular parameter values where the Hopf bifurcation occurs. Additionally, note that the closed curves with different values of Δ_η appear to intersect at a point $(g_{syn,c}, \bar{\eta}_c) \approx (1, 0.09)$. For $\bar{\eta} > \bar{\eta}_c$, the g_{syn} value of the Hopf closed loop associated with the left boundary moves to the right when Δ_η increases, while the right boundary does not change appreciably. This leads to the CO area getting smaller as Δ_η grows. The same phenomenon occurs in the top right corner. Consistent results are found in Fig. 4.3(d) where $\bar{\eta} = 0.12 > \bar{\eta}_c$. On the contrary, the CO region gets bigger as Δ_η grows in the region where $\bar{\eta} < \bar{\eta}_c$. Consistent results are shown in Fig. 4.3(e) for the range $\Delta_\eta < 0.06$ approximately. However, the opposite effect appears when $\Delta_\eta > 0.06$. Here, $\bar{\eta} = 0.02 < \bar{\eta}_c$. Therefore, the heterogeneity of the current η makes the bursting behavior of neurons more robust (larger CO area) or less robust (smaller CO area), depending on the different region of the parameter space in which the system lies. Our findings may help explain the contradictory conclusions obtained in [208] and [159], where the former claimed that heterogeneity favors the emergence of bursting as opposed to hindering, as the latter found. Although it is difficult to directly compare our model with that in [208], we can compare it with that of [159], since both of us start from the same neural network model and use equivalent parameter values. Due to the distinct mean-field modeling approach, the study in [159] exclusively examined the domain where the current exceeded 1000 pA (equivalent dimensionless value $\bar{\eta} > \bar{\eta}_c$). Our findings within this range are consistent with those in [159]; however, a contrast appears when $\bar{\eta} < \bar{\eta}_c$.

It may be noted that when Δ_η is reduced to 0.01 in Fig. 4.3(a), the left Hopf branch crosses the right one, forming another region. From the dynamics in the plane $(\Delta_\eta, g_{\mathrm{syn}})$ shown in Fig. 4.3(e), we know that the EP is an attractor and the system undergoes cusp bifurcations, implying the presence of a hysteresis phenomenon, which is often accompanied by bistability [52].

Finally, we investigate the effect of weak heterogeneity on the bifurcation structure. As Δ_η decreases, see Fig. 4.3(b), the two-parameter Hopf curves move to the left, but the CO region remains qualitatively similar to Fig. 4.3(a) for sufficiently high Δ_η. However, when Δ_η close enough to zero, the closed Hopf branch splits, with the lower part limiting on the $\bar{\eta}$ axis and the upper part approaching large current values as g_{syn} approaches zero (see Fig. 4.3(c)). This scenario represents a population of neurons with extremely weak or zero coupling ($g_{\mathrm{syn}} < 0.2$) and nearly homogeneous injected currents ($\Delta_\eta \approx 0$).

For the inhibitory neural network (I-net), as shown in the last row of Fig. 4.3, the bifurcation diagram is relatively simpler. Only supercritical Hopf bifurcations (red) are observable for the present choice of parameter values. The COs emerge for sufficiently large $\bar{\eta}$, (see Fig. 4.3(g)) and almost any value of g_{syn} (see Fig. 4.3(h) and (i)). Increasing the heterogeneity in the applied current via Δ_η does not favor neurons' bursting behavior, as shown in Fig. 4.3(g)-(i). A higher $\bar{\eta}$ or a lower w_{jump} is required to overcome the increasing Δ_η to generate COs (see Fig. 4.3(g) and (i)).

Next, we investigate the effect of adaptation via the intensity parameter w_{jump}. The relevance of adaptation for emergent collective dynamics can be appreciated by considering the bifurcation diagram in the $(g_{\text{syn}}, w_{\text{jump}})$ plane, as shown in Fig. 4.3(f) for the excitatory neural network and (i) for the inhibitory case. In the excitatory case, COs emerge for sufficiently large w_{jump} or g_{syn}. A generalized Hopf point occurs, separating supercritical (red) from subcritical (blue) Hopf bifurcations. The adaptation favors the emergence of COs with the region expanding as w_{jump} increases. For the inhibitory case, COs appear even at $w_{\text{jump}} = 0$ with medium values of g_{syn}. Adaptation in the inhibitory network has the opposite effect as in the excitatory case. The interval of g_{syn} where COs occur shrinks as w_{jump} grows, thus adaptation hinders the formation of COs.

From the analysis above, the current heterogeneity Δ_η and the adaptation intensity w_{jump} appear to have intricate effects on the emergence of COs. Essentially, all the findings align with a fundamental principle underlying the spiking dynamics governed by the membrane potential equation (4.1). The emergence of COs in the synaptically coupled neural network is due to a balance between the fixed (η) and time-varying (I_{ext}) currents, which cause neurons to spike, the slow adaptation current w, which terminates spiking, and the synaptic current (I_{syn}), which favors spiking in the excitatory network because it is positive most of the time, but hinders spiking in the inhibitory network as it is always negative. The greater heterogeneity implies that the excitatory drive η is distributed over a wider range of values. If the mean current $\bar{\eta}$ is sufficiently large, e.g., $\bar{\eta} = 0.12$ in Fig. 4.3(d), larger Δ_η indicates that more neurons have input currents too small to invoke spiking, resulting in a smaller bursting area. If $\bar{\eta}$ is relatively small, e.g., $\bar{\eta} = 0.02$ and $\Delta_\eta \in [0.02, 0.06]$ in Fig. 4.3(e), bigger Δ_η indicates more neurons have large enough currents to spike, resulting in a bigger bursting area. The synaptic current I_{syn} has different effects in the excitatory and inhibitory networks. As shown in Eq. (4.2), the sign of I_{syn} is determined by the value of the membrane potential $v(t)$ relative to the reversal potential e_r. Thus, it can be positive or negative in the excitatory network, but it is always negative in the inhibitory case. Consequently, the bifurcation diagrams in the excitatory case are more complicated than those in the inhibitory one. In the excitatory network, the primary source of inhibition arises from adaptation. The interaction between excitatory and inhibitory sources leads to multiple areas for COs, e.g., Fig. 4.3(a) and (d), including (f), where even at $w_{\text{jump}} = 0$, strong coupling (approximately $g_{\text{syn}} > 3$) introduces an inhibition effect. In the inhibitory case, both the negative synaptic current and the adaptation act to suppress COs. Thus, the COs appear even at $w_{\text{jump}} = 0$ and disappear for sufficiently large w_{jump}, e.g., Fig. 4.3(h) and (i).

4.4.3 Bifurcation of Neural Network with Synaptic Delay

In this section, we consider the system with constant homogeneous synaptic delay. The corresponding network model is composed of (4.1)-(4.3) and (4.9) and its mean-field system consists of delayed differential equations (4.3), (4.7) and (4.16).

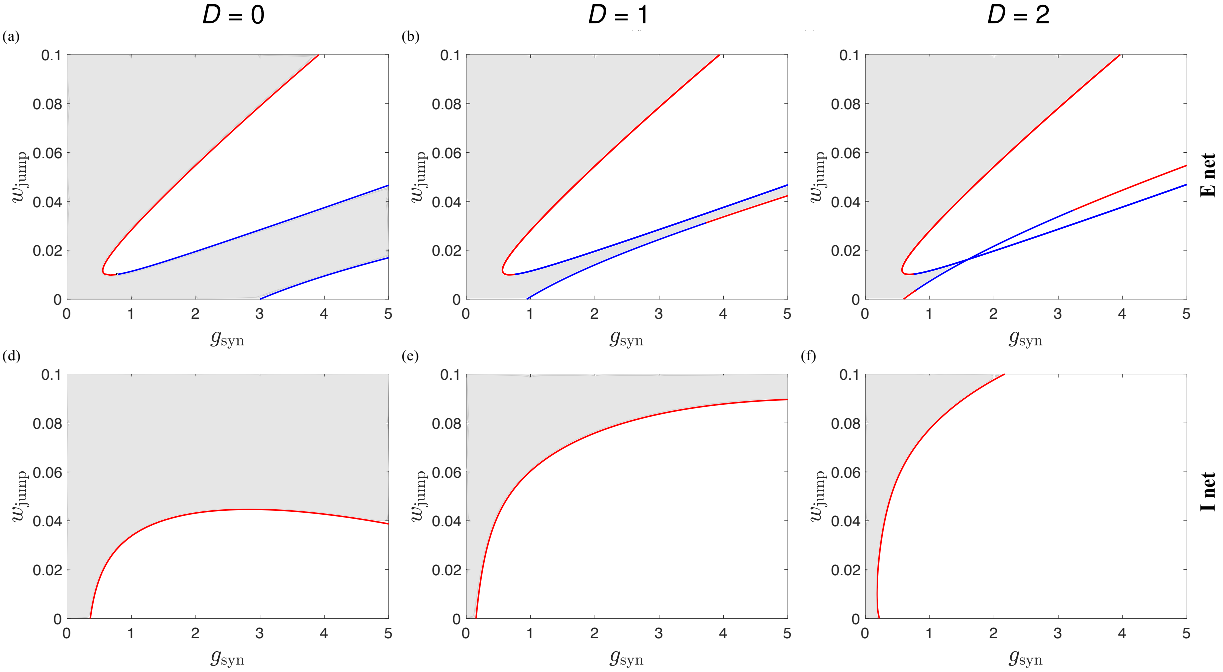

Figure 4.4: Effect of delay on excitatory (1st row) and inhibitory (2nd row) neural networks. Boundaries of Hopf bifurcation (red/blue for supercritical/subcritical) are shown in the $(g_{\text{syn}}, w_{\text{jump}})$ plane for different values of delay $D = 0$ (1st column), $D = 1$ (2nd column) and $D = 2$ (3rd column). Gray regions depict the stable EP. Parameter values: $\bar{\eta} = 0.12$, $\Delta_\eta = 0.02$ for the excitatory network, $\bar{\eta} = 0.4$, $\Delta_\eta = 0.01$ for the inhibitory network. Other parameter values are given in Table 4.1.

We start with an investigation of Hopf bifurcations. Fig. 4.4 shows the Hopf boundaries reported in the $(g_{\text{syn}}, w_{\text{jump}})$ plane for different values of delay D. Generally, delay favors the emergence of COs and generates new dynamics. Specifically, in the inhibitory network (2nd row of Fig. 4.4), the collective oscillation areas (white) under the supercritical Hopf curves (red) expand with an increase of D. In the excitatory case (1st row of Fig. 4.4), the delay not only promotes COs by the expansion of the white regions, but also enriches the collective dynamics. In particular, as the delay increases, the Hopf branch at the lower right corner moves toward the upper one, shrinking the EP area (gray), creating a Hopf-Hopf bifurcation. A generalized Hopf bifurcation also moves into the parameter range considered. Numerical simulations of macroscopic variables show that the mean-field system with $D = 0$ exhibits slow oscillations in the upper white region and fast oscillations in the lower white region, similar to the behavior shown in Fig. 4.2(b), but with different periods. When D increases to 2, these two dynamics persist in the upper and lower white regions. However, in the middle white region created by the intersection of the two Hopf curves, the system exhibits slow-fast nested COs, similar to those shown in Fig. 4.2(c).

To further study the impact of the current heterogeneity and adaptation on the time-delayed mean-field system, we plot the Hopf bifurcation curves in the (D, g_{syn}) plane for different values of Δ_η and w_{jump}, as shown in Fig. 4.5 for the excitatory network and Fig. 4.6 for the inhibitory case. The adaptation strength increases from top to bottom, with $w_{\text{jump}} = 0.0095$ (100 pA) representing weakly adapting and $w_{\text{jump}} = 0.0189$ (200 pA) strongly adapting [158]. The amount of heterogeneity increases from left to right, with $\Delta_\eta = 0$ representing homogeneous input currents. The numerical continuation in both Fig. 4.5 and Fig. 4.6 shows that there are no abrupt qualitative changes when Δ_η grows from 0 to 10^{-4}, except for the replacement of blue subcritical Hopf bifurcations by red supercritical ones in some intervals of D. Combined with the perturbation analysis in Sec. 4.3.1, it is reasonable to interpret the mean-field model with $\Delta_\eta = 0$ as an approximation of the system with very weak heterogeneity. Additionally, when g_{syn} approaches zero, accounting for a population of neurons with significantly weak coupling, the system undergoes a splitting of the Hopf branch when Δ_η drops from 0.01 to 10^{-4}, similar to the phenomenon shown in Fig. 4.3(b) and (c), where the system does not have a synaptic delay.

Now we concentrate on the bifurcation diagrams in the last two columns of Fig. 4.5, where the input currents have moderate heterogeneity. The gray areas show the regions of the parameters where EPs are stable, and thus neurons exhibit asynchronous tonic firing. For weak adaptation, $w_{\text{jump}} = 0.0095$, there are alternating intervals of D where stable EPs exist. A similar phenomenon has been observed in many models with delay including coupled oscillator models [13], a single oscillator with delayed feedback [45] and even scalar delay equations with multiple delays [17]. It indicates that there does not exist a single threshold for the delay, above which the system tends to oscillate. As w_{jump} grows, these EP intervals (gray) shrink and disappear, due to Hopf branches moving to the right toward the larger delay values and new branches emerging from the g_{syn} axis. At the same time, the blue curves representing subcritical Hopf bifurcation become shorter. There-

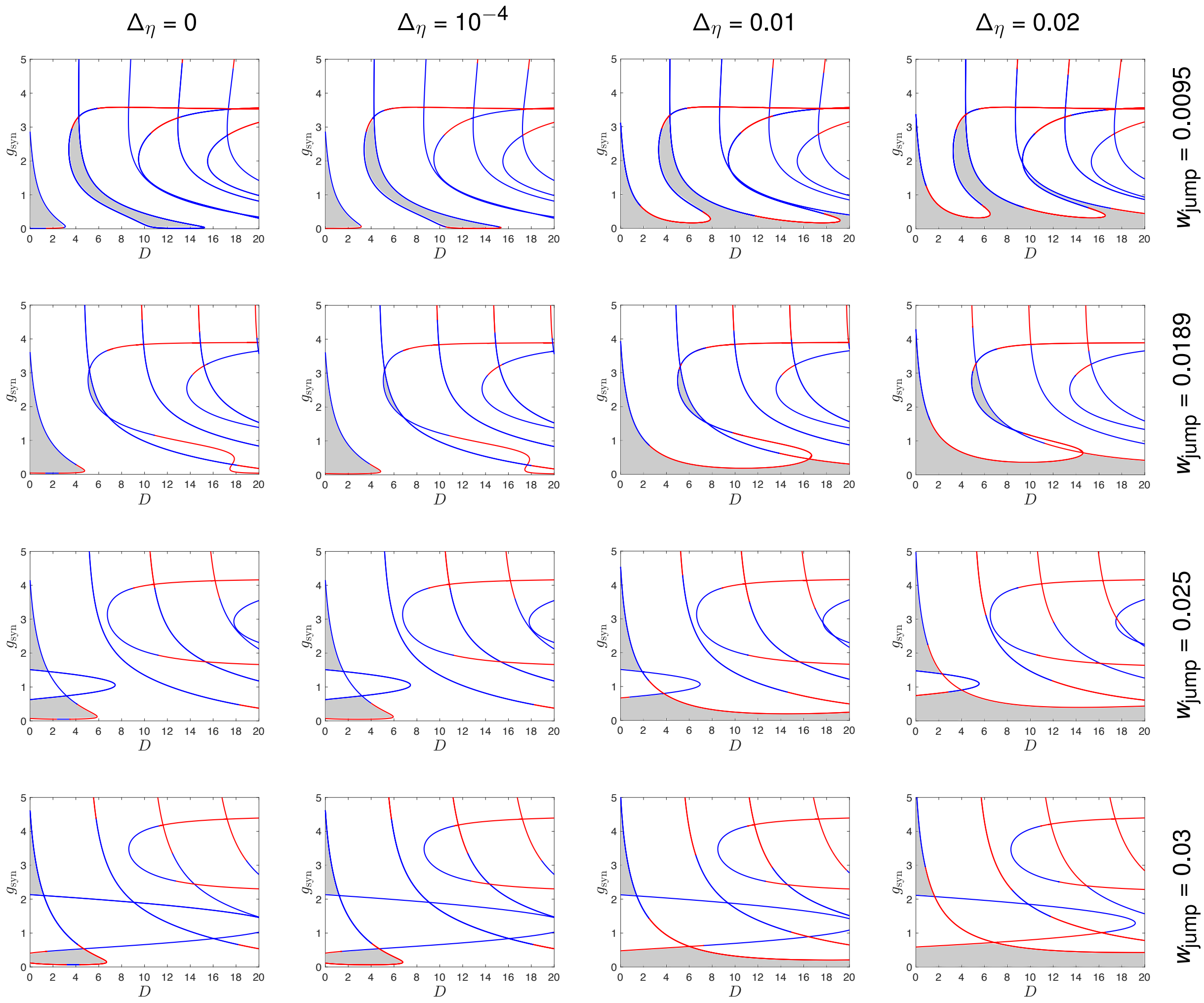

Figure 4.5: Excitatory neural network with homogeneous synaptic delay. Hopf curves (red/blue for supercritical/subcritical) are shown in the (D, g_{syn}) plane for various values of Δ_η and w_{jump} when $\bar{\eta} = 0.25$. Gray regions depict the stable EP. Other parameters are given in Table 4.1.

fore, adaptation favors the emergence of COs in the delayed excitatory neural network, as demonstrated by the shrinking EP areas. By comparison, the increase of Δ_η from 0.01 to 0.02 expands the EP areas as the Hopf curves move upward, but also shortens the blue parts of the curves. Therefore, heterogeneity promotes EP for small values of g_{syn}. Regarding the effect of synaptic delay D, it has no influence on the emergence of COs when the synaptic coupling strength is small enough (see $g_{\text{syn}} < 0.5$ approximately), since a stable

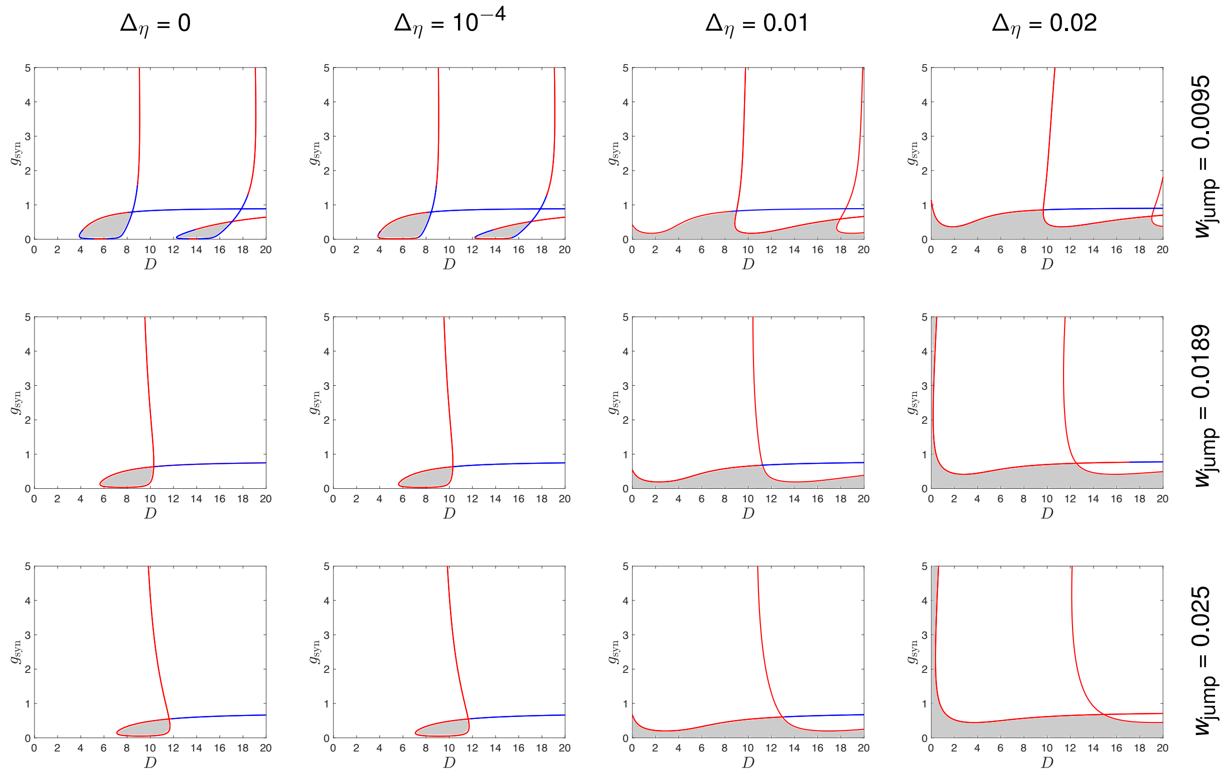

Figure 4.6: Inhibitory neural network with homogeneous synaptic delay. Hopf curves are shown in the (D, g_{syn}) plane for different values of Δ_η and w_{jump} when $\bar{\eta} = 0.4$. Gray regions depict the stable EP. Other parameters are given in Table 4.1.

EP area exists for all delays. But when g_{syn} is large enough, the delay generally promotes COs for strong adaptation ($w_{\text{jump}} \geq 0.0189$) since white areas exist for most values of D. As the adaptation weakens, e.g., $w_{\text{jump}} = 0.0095$, things become complicated: increasing the delay can both induce and destroy COs.

When it comes to the moderately heterogeneous current in the inhibitory network, as shown in the last two columns of Fig. 4.6, one can see that the trends are the same as those in the excitatory network. The gray EP areas are independent of D for small g_{syn}. The Hopf branches move to the right and up, whereas the blue subcritical parts shrink with increasing w_{jump} and Δ_η. However, these changes yield different effects from the excitatory network because of the different bifurcation structure. Specifically, both Δ_η and w_{jump} do not favor the emergence of COs for $D < 2$ or $g_{\text{syn}} < 0.5$, approximately. In addition, the inhibitory coupling is more favorable for macroscopic oscillations than the excitatory one in the range of $D < 2$ because the gray area is smaller than in the excitatory case. The white collective oscillation areas for inhibitory and excitatory couplings are comparable for $D > 2$, except for the weak adaptation case $w_{\mathrm{jump}} = 0.0095$. More Hopf branches appear in the same range of D for the excitatory coupling, producing complicated oscillating dynamics.

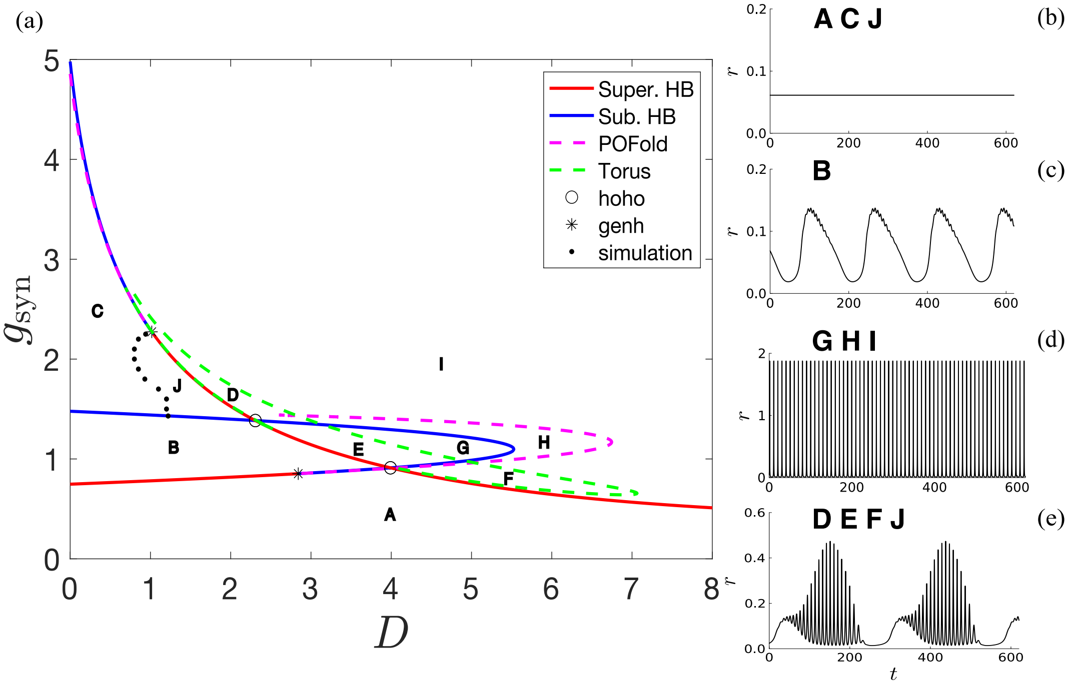

Figure 4.7: Excitatory neural network with homogeneous synaptic delay. (a) Bifurcation diagram in the (D, g_{syn}) plane showing supercritical/subcritical HP bifurcations (solid red/blue lines), POFold (pink dashed line), and Torus bifurcation (green dash line). The symbols refer to codimension-two bifurcation points: Hopf-Hopf (hoho) (circle) and generalized Hopf (genh) (star). The black dotted line, which separates the regions C and J, is determined by direct simulations of the mean-field model. The sample time traces of $r(t)$ and $w(t)$ are shown in panels (b)-(d) for the three possible dynamical regimes: (b) Region A, C, EP at $(D, g_{\mathrm{syn}}) = (2, 0.6)$, (c) Region B, slow PO at $(D, g_{\mathrm{syn}}) = (2, 1)$, (d) Region G, H, I, fast PO at $(D, g_{\mathrm{syn}}) = (6, 1.6)$, (e) Region D, E, F, slow-fast nested COs at $(D, g_{\mathrm{syn}}) = (4, 1)$. Region J: coexistence between EP and slow-fast nested COs. Other parameter values: $\bar{\eta} = 0.25$, $\Delta_\eta = 0.02$ and $w_{\mathrm{jump}} = 0.025$. Other parameter values are given in Table 4.1.

HP bifurcations can only separate stationary solutions and oscillating states. However, different types of COs have been observed in the neural network, such as those shown in

Fig. 4.2. To explore such rich macroscopic dynamics and understand the bifurcation mechanism underlying their emergence, further bifurcation analysis is necessary. For simplicity, we take two typical sets of parameters, one for the excitatory network and one for the inhibitory, and focus on bifurcations in a subset of the parameter space. As shown in Fig. 4.7 for the excitatory network, in addition to the Hopf-Hopf bifurcations (circle hoho points) and generalized Hopf bifurcations (star genh points) seen in previous figures, we find two bifurcations of POs, thus creating different regions with distinct types of dynamics. One is the fold bifurcation of POs (pink dashed line) that originates from the generalized Hopf points and forms the boundaries where stable and unstable POs meet and disappear. The other is the Torus (or Neimark-Sacker) bifurcation (green dashed line) emanating from the Hopf-Hopf points and connecting with each other. The location of these bifurcation curves is consistent with the normal form coefficients of the two Hopf-Hopf points obtained by DDE-BIFTOOL. For both points, the system is in subcase IV ($\theta > 0$, $\delta < 0$) of the difficult case ($\mathrm{Re}(g2100) \cdot \mathrm{Re}(g0021) < 0$) of Hopf-Hopf bifurcations (see [125]). Given the regions where the slow-fast nested COs occur, it is evident that the Torus bifurcation is the main mechanism for the emergence of these solutions. Samples of the time evolution of $r(t)$ are shown to the right of the bifurcation diagram, and they correspond to the following regimes:

(1) Region A and C: stable EPs

(2) Region B: stable POs with low frequency

(3) Region G, H and I: stable POs with high frequency

(4) Region D, E and F: slow-fast nested COs

(5) Region J: coexistence of stable EPs and slow-fast nested COs.

The black dotted line, which separates Region J from Region C, was identified by direct simulations of the mean-field model. Note that the PO exhibited in Fig. 4.7(c) is not strictly a regular spiking PO as that shown in Fig. 4.2(b). Small ripples appear in the time series of $r(t)$. Actually, it is a typical behaviour of a system with multiple time scales and characterized by a limit cycle with a period related to the slow dynamics of the adaptation variable $w(t)$ and fast-damped oscillations on the amplitude resulting from the focus type of solutions of the fast subsystem involving $r(t)$, $v(t)$ and $s(t)$ variables. This can be explained by standard slow-fast analysis, e.g., [23]. Based on the bifurcation diagram in Fig. 4.7(a) and the smooth oscillations of $w(t)$ (see difference between Fig. 4.2(b) and (c)), we do not categorize this behavior as slow-fast nested COs.

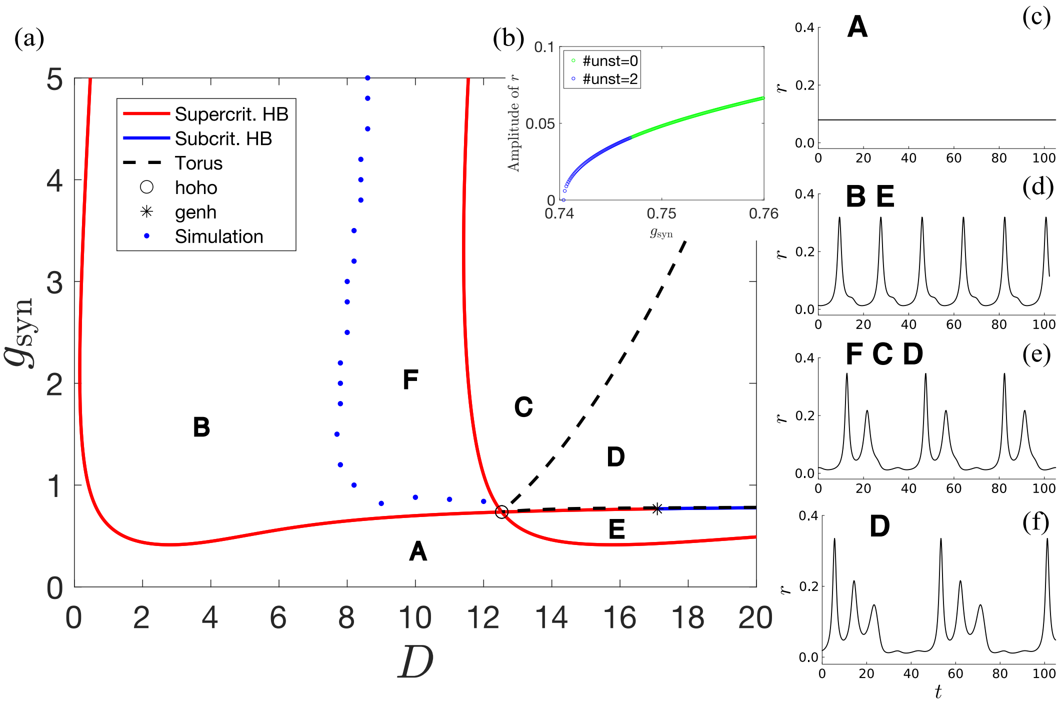

Figure 4.8: Inhibitory neural network with homogeneous synaptic delay. (a) Bifurcation diagram in the (D, g_{syn}) plane showing supercritical/subcritical Hopf bifurcations (solid red/blue lines) and Torus bifurcations (black dashed line). The symbols refer to codimension-two bifurcation points: Hopf-Hopf (hoho) (circle), generalized Hopf (genh) (star). The blue dotted line, which separates regions B and F, has been determined by direct simulations of the mean-field model. (b) Branch of PO emanating from close to the Hopf-Hopf point ($D = 13$). Green/blue represents zero/two unstable Floquet multipliers. Sample time traces of $r(t)$ are shown in panels (c)-(f) for the four possible dynamical regimes: (c) Region A, EP at $(D, g_{\mathrm{syn}}) = (6, 0.4)$, (d) Region B and E, PO at $(D, g_{\mathrm{syn}}) = (6, 1)$, (e) Region F, C and D, double-period limit cycle at $(D, g_{\mathrm{syn}}) = (14, 1)$, (f) Region D, three-period limit cycle at $(D, g_{\mathrm{syn}}) = (20, 1)$. Parameter values: $\bar{\eta} = 0.4$, $\Delta_\eta = 0.02$, $w_{\mathrm{jump}} = 0.0189$. Other parameter values are given in Table 4.1.

By comparison, Fig. 4.8 presents the detailed bifurcation diagram for the inhibitory network. The system undergoes a Hopf-Hopf bifurcation (circle hoho point) and a generalized Hopf bifurcation (star genh point) as seen before. The normal form coefficients show that the system is in subcase I ($\theta > 0$, $\delta > 0$, $\theta\delta > 1$)) of the simple case (($\mathrm{Re}(g2100) \cdot \mathrm{Re}(g0021) > 0$) of the Hopf-Hopf bifurcation (see [125]). As predicted, there are two Torus bifurcation curves (black dashed lines) emanating from the Hopf-Hopf point; see Fig. 4.8(a), and the Torus bifurcation curves lie between the two Hopf branches emanating from the Hopf-Hopf point. The sample time evolutions of $r(t)$ are shown in Fig. 4.8(c)-(f), and they correspond to the following regimes:

(1) Region A: stable EPs

(2) Region B and E: stable POs

(3) Region F, C: double-period limit cycles

(4) Region D: double-, triple-period limit cycles.

The blue dotted line, which separates Region F from Region B, was identified by direct simulations of the mean-field model.

There are two discrepancies between the prediction of the bifurcation analysis and the time evolution. First, the observable period-doubled limit cycles in Region F indicate that the system undergoes a period-doubling bifurcation when D crosses the blue dotted line. Unfortunately, we can only find the boundary by direct simulations of the mean-field model. It was not found by numerical continuation. Second, according to the prediction of the normal form coefficients in [125], there should be two stable POs between the Torus bifurcation curves near the Hopf-Hopf point, that is, in Region D. The numerical continuation supports this conclusion. Fig. 4.8(b) shows the occurrence of a Torus bifurcation, where the number of unstable Floquet multipliers changes from 2 to 0, stabilizing the PO (green line). Unfortunately, our numerical simulations in Region D found only one stable PO in this region, which is of double-, and even triple-period type. In addition, we did not see a cascade of period-doubling bifurcations, well known for their capability of inducing chaos, in our present choice of parameter values. These interesting findings may arise from other complexities in the bifurcation structure of our mean-field model. We note that the two frequencies of the POs near the Hopf-Hopf, (0.21 vs 0.53), are close to the ratio $1:2$. Period doubling bifurcations are known to occur in $1:2$ resonant Hopf-Hopf bifurcations [131]. We leave further investigation of these and other phenomena for future work.

4.5 Discussion

In this chapter, we thoroughly investigated the macroscopic dynamics of the heterogeneous network of Izhikevich neurons with global constant-delay coupling by means of a mean-field model, valid in the thermodynamic limit. Our study emphasized the effect of the input current heterogeneity Δ_η, the adaptation intensity w_{jump} and the synaptic delay D on the emergence of coherent oscillations. Furthermore, we addressed the problem of whether the OA-based mean-field system with $\Delta_\eta = 0$ can characterize the system with extremely weak heterogeneity, although the Watanabe-Strogatz (WS) approach [213], instead of the OA approach, is conventionally considered as the appropriate framework for deriving the mean-field model when neurons are strictly identical.

Our perturbation and bifurcation analysis reveals that the mean-field model, characterized by $\Delta_\eta = 0$, can be regarded as a good approximation of the neural network exhibiting extremely weak heterogeneity. We observe a smooth variation of the EPs and the bifurcation structure as $\Delta_\eta \to 0$, particularly when g_{syn} is sufficiently large. These results support studies [178, 169, 70], where the dynamic analysis built on the OA-based mean-field model with $\Delta_\eta = 0$ is interpreted as representative of the dynamics of networks with weak heterogeneity. It is important to note that for $\Delta_\eta = 0$, the OA manifold is marginally stable [174], thus the dynamics of the OA-based mean-field model cannot be expected to be predictive of the dynamics in the full network. This paper and previous studies for QIF network [178, 169, 70] do not analyze the attractiveness of the OA manifold theoretically, although the correspondence between numerical simulations and mean-field predictions supports the hypothesis that it is attractive for $\Delta > 0$. Recent work [49, 172] has theoretically confirmed this. The mean-field model with weak heterogeneity may also be able to represent a homogeneous neural network under small random perturbations. The paper [150] showed near quantitative agreement between the network of identical quadratic integrate-and-fire (QIF) neurons driven by Gaussian noise and the corresponding mean-field model derived under the OA theory. Recent studies also demonstrated the ability of the OA theory to be applied exactly to the network of Kuramoto oscillators [201, 203] and QIF neurons [57] with Cauchy white noise. For our mean-field model derived from Izhikevich neurons, we leave this for future investigation.

In addition, the impacts of the heterogeneity of the injected current Δ_η and the adaptation strength w_{jump} on the macroscopic dynamics change depending on the choice of parameter values (see Fig. 4.3–4.6). In essence, their effects are determined by the balance of excitatory drives, which cause neurons to spike, and inhibitory drives, which terminate spiking. The constant and time-varying input currents η and I_{ext} are typical excitatory drives, and the adaptation current w is the inhibitory drive. The role of the synaptic current I_{syn} depends on the sign of $e_r - v_i$, which is negative in the inhibitory network and positive/negative in the excitatory case. This also leads to a more complicated bifurcation structure in the system with excitatory coupling than in the one with inhibitory coupling.

Regarding the effect of synaptic delay on COs, our analysis shows that delay does not affect the number or position of EPs, but does influence their stability. This is typical for time-delayed neural systems [43]. For our present set of parameter values, delays work mostly as an excitatory drive to promote the emergence of COs and generate new dynamics, including slow-fast nested COs resulting from Torus bifurcations (see Fig. 4.7). Moreover, we have found some other interesting regimes. Delays exhibit little influence on the generation of COs when the heterogeneity is moderate and g_{syn} is small, indicating weak coupling; and this influence becomes more pronounced with larger heterogeneity (refer to the two right columns in Figs. 4.5 and 4.6). The delays are expected to have no impact when there is no coupling in the network, i.e., $g_{syn} = 0$. However, with the addition of extremely weak heterogeneity, the influence of delays on the emergence of COs becomes evident under conditions of weak coupling (see the two left columns in Figs. 4.5 and 4.6). We need further exploration to understand the nuanced interplay between the double limits of weak coupling and weak heterogeneity. Additionally, with larger g_{syn} and weaker adaptation, the domains for the emergence of COs may appear and disappear as the delay increases. It implies that a longer delay does not necessarily increase the probability of the occurrence of COs (see Figs. 4.5 and 4.6 for $w_{\mathrm{jump}} = 0.0095$.)

There are many papers in the literature studying the neural network with delayed coupling. To our knowledge, these three papers [178, 169, 69] are closely related to ours. These papers all used the same theoretical framework to derive the mean-field model as we do, and they used the model to study the collective dynamics induced by the coupling delay. However, in this chapter, we derived mean-field models from neural networks with greater neurological plausibility and performed more detailed bifurcation analysis. First, we took into account the SFA in each neuron. This is a fundamental neuronal mechanism and plays a significant role in promoting synchronous bursting of neurons. Second, we employed a realistic expression for the synaptic current (4.2) in the network connections. This model is widely used in neuroscience, but is often simplified for analysis. This simplification loses physiological insight and may lead to discrepancies in the prediction of system behaviors. Increased biological relevance results in our more complicated mean-field model. It is four-dimensional due to the addition of the adaptation variable and contains new nonlinear terms arising from the more complicated synapse model. Thus, analytic Hopf bifurcation analysis such as in [169, 69, 178] is not tractable. Instead, we used numerical approaches. This has the added benefit of allowing us to locate higher-codimension bifurcations and study their effect on the macroscopic dynamics.

The introduction of enhanced biological plausibility into our mean-field system gives rise to significantly different Hopf bifurcation structures compared to those documented in [169, 69], especially for the excitatory coupling system. Numerous Bautin/generalized Hopf bifurcations emerge in the excitatory network, signifying points where the Hopf bifurcation switches between supercritical and subcritical. Moreover, Hopf-Hopf bifurcations manifest themselves in both excitatory and inhibitory networks. Further exploration of these newly identified structures has revealed Fold bifurcation of periodic orbits (POFold), marking points where stable and unstable POs meet and disappear, and Torus bifurcations, which consistently appear in the vicinity of the Hopf-Hopf bifurcation. In the excitatory network, Torus bifurcations lead to the creation of a stable torus solution, corresponding to slow-fast nested COs, not observed in [178, 169, 69]. In the inhibitory network, the numerical bifurcation analysis found a different arrangement of Torus bifurcations, leading to bistability between two different POs. However, using a direct numerical simulation, we did not observe the bistability. Instead, we found evidence for a period-doubling bifurcation. Interestingly, we did not find a cascade of period-doubling bifurcations leading to chaos, as observed in the inhibitory network in [169, 178]. The discrepancy between the numerical continuation and numerical simulation in the inhibitory network may be due to a further complication in the system: the frequencies at the Hopf-Hopf points we investigated are close to the 1:2 resonance. Such resonant Hopf-Hopf points can lead to isolated period-doubling bifurcations [131]. We will leave this for further investigation in the future.

Some recent work has also examined variations of the QIF neural network and their mean-field dynamics. For instance, in the papers [96] and [198], additional equations were introduced to the QIF neuron to account for different short-term plasticity (STP). STP represents a different mechanism from SFA in the Izhikevich neuron we used, although some researchers (though not common) regard it as another form of adaptation. SFA in the Izhikevich neuron occurs at the soma, whereas STP occurs in the synaptic connection. The bursting dynamics in our system is induced by the slow adaptation variable and the delayed coupling, while those described in [198] are caused by a slow periodic current, and those in [96] result from slow synaptic dynamics. The slow-fast COs arising from Torus bifurcations in the excitatory network differ from those observed in [90], where they consist of a small-amplitude fast "ripple" riding on a large-amplitude slow oscillation. In this chapter, fast oscillations may exhibit a large amplitude, with slow oscillations modulating this amplitude, similar to the recordings observed in the hippocampus and various regions of the brain [136]. Other papers have shown that fast oscillations can fall in the γ range (30–100 Hz) and slow modulation in the θ band (4–8 Hz) by choosing appropriate parameter values, e.g., the adaptation intensity w_{jump} [90]. In our COs, slow oscillations are generated by adaptation, whereas fast oscillations are due to the intrinsic spiking frequency of neurons and time delay. For the parameters of Fig. 4.2 (c), the slow oscillations correspond to 2 Hz and the fast oscillations to 70 Hz when converted to dimensional values. These two values can be modified by adjusting the adaptation intensity and the time delay size, respectively. The $\theta - \gamma$ nested oscillations have been observed in the hippocampus and have been shown to be relevant to cognitive tasks, such as navigation, sensory association, and working memory [18, 33, 37, 58, 136]. Generally, this interaction between different frequency bands belongs to a phenomenon called cross-frequency-coupling (CFC), which is potentially relevant to understanding healthy and pathological brain functions [46, 12, 136]. The emergence of CFC has been reported for mean-field systems, for example, for two coupled neural networks [48, 90], or for a network with an external $\theta-$drive [191]. In contrast, we have shown that CFC can emerge in a single population of neurons with SFA and delayed excitatory coupling.

Chapter 5

Mean-Field Modeling for Spiking Neural Networks with Short-Term Synaptic Plasticity

In previous two chapters, we discussed the effect of spike frequency adaptation (SFA) and synaptic delay in phenomenological models where the SFA mechanism is carried out by an adaptation variable w in the Izhikevich neuron and the non-instantaneous communication is represented by an explicit time delay term in the coupling between neurons. In this chapter, we consider a kinetic model of synapses with short-term plasticity (STP). This feature has the potential to impact the spiking activity of postsynaptic neurons and introduce an inherent time delay in synaptic transmission. This chapter aims to develop a mean-field model to capture the collective dynamics of a large neural network that incorporates STP. We establish a kinetic model to describe this calcium-dependent synaptic dynamics in Sec. 5.2. For a network of quadratic integrate-and-fire (QIF) neurons with STP (Sec. 5.3), we develop a macroscopic description using the Ott-Antonsen (OA) mean-field theory (Sec. 5.4). We show their agreement by numerical analysis and investigate the muscarinic effect at hippocampal synapses through the proposed mean-field model in Sec. 5.5.

5.1 Introduction

Synapses exhibit remarkable alterations in the strength and efficacy of connections between neurons. These dynamics can be categorized into two main types: long-term synaptic plasticity and short-term synaptic plasticity. Long-term plasticity refers to long-lasting changes in synaptic strength that can persist for hours, days, or even longer. It typically involves structural and molecular changes at the synapse, such as the number or sensitivity of neurotransmitter receptors [56, 21]. STP refers to transient changes in synaptic strength that last from milliseconds to minutes [144, 225]. It is typically associated with the dynamic properties of neurotransmitter release and availability under stimulation of presynaptic activity and may then lead to adaptation of the spike frequency of the postsynaptic neuron [225, 20]. For a review of the development in both types of synaptic plasticity, we refer the reader to articles [56, 142, 21].

STP exerts profound effects on network activity and information processing capabilities. For example, it may generate a dynamic gain control mechanism by assigning a high / low gain to a slow / rapid input firing rate to achieve optimal synaptic transmission [3, 1]; it may work as a temporal filter to regulate neural information transmission that is fundamental for a variety of healthy and pathological brain functions [94, 184, 183]; and it may provide a mechanism to implement working memory in the neocortical network [149, 190, 199].

Synapses may exhibit different characteristics at different locations [29]. In experiments, two types of STP, with opposite effects on synaptic efficacy, have been observed: short-term depression (STD) and short-term facilitation (STF). STD reduces the postsynaptic response to repetitive presynaptic activity, while synaptic facilitation increases the efficacy of connection. These two phenomena act on different timescales and can be activated by a variety of different processes [212]. More importantly, they are not mutually exclusive and can occur within the same synaptic terminal [74].

Increasing efforts have been made to develop mathematical models for synaptic STP [108], beginning in the 1950s [134]. Some models specifically describe STF dynamics ([223, 24]) whereas some for STD ([210, 222]). Recently, integrative models that unify both STP dynamics have been proposed. Among them, a simple phenomenological model, proposed by Tsodyks and Markram [205], has gained significant popularity and has been applied in many studies, e.g., [149, 171, 199]. Although mathematically simple, the Tsodyks-Markram (TM) model lacks essential information on synaptic transmission, and some parameters do not have direct and measurable correlations with experiments [132]. On the other hand, detailed biophysical processes underlying STP are introduced in the models, e.g., [138, 74]. These physiologically well-defined models may incorporate an abundance of details, making them less conducive to investigation at the level of networks. A class of kinetic STP models was recently proposed in [132, 195], which retain central biophysical processes in a relatively simple mathematical form. They should be an appropriate candidate for studying large neural networks.

Furthermore, muscarinic acetylcholine receptors (mAChRs) is a type of G protein-coupled receptor that binds to the neurotransmitter acetylcholine (ACh). They derive their name from their selective activation by muscarine, a toxic compound found in certain mushrooms that mimics some effects of ACh. These receptors are involved in numerous diseases and conditions, and are targets for various drugs used to treat disorders such as Alzheimer's disease, Parkinson's disease, and schizophrenia [124, 120, 63]. Activation of mAChRs has various effects at the synapse, depending on the specific subtype of mAChRs and the location of the synapse [215]. In particular, by binding to the mAChRs located on the presynaptic membrane, ACh reduces the release of neurotransmitters from both excitatory and inhibitory inputs to hippocampal pyramidal neurons [206]. This is often achieved by modulating voltage-gated calcium channels on the presynaptic terminal in response to the arrival of an action potential [197, 176]. The reduced influx of calcium ions into the presynaptic terminal leads to a decrease in the amount of neurotransmitter, thereby inhibiting synaptic transmission. Similarly, muscarine can also trigger the inhibitory effect of mAChRs by reducing the amount of calcium influx into the presynaptic terminal [99]. Since calcium plays a crucial role in shaping the strength and dynamics of synaptic transmission, it is necessary to include the calcium dynamics in the STP model.

In this chapter, we will incorporate the calcium-dependent kinetic STP model in [132, 195] into the network of QIF neurons and analytically develop a mean-field model to describe collective behaviors. To our knowledge, such a macroscopic description has not yet been achieved for networks of spiking neurons with the kinetic STP model. Furthermore, we will investigate the muscarinic effect on the STP mechanism in the context of collective dynamics using parameter values fitted to the hippocampal GABAergic synapses [195].

5.2 Kinetic Model of Synapse with STP

This section aims to formulate a system model that captures the kinetics of short-term synaptic plasticity between two neurons.

5.2.1 Synaptic transmission process

To identify the required variables in the models, we begin with a quick overview of the main processes in synaptic transmission, as illustrated in Fig. 5.1. When a neuron fires a spike, the resulting action potential, or impulse input, travels down its axon terminal, triggering the opening of voltage-gated calcium channels and the subsequent inflow of calcium Ca^{2+}.

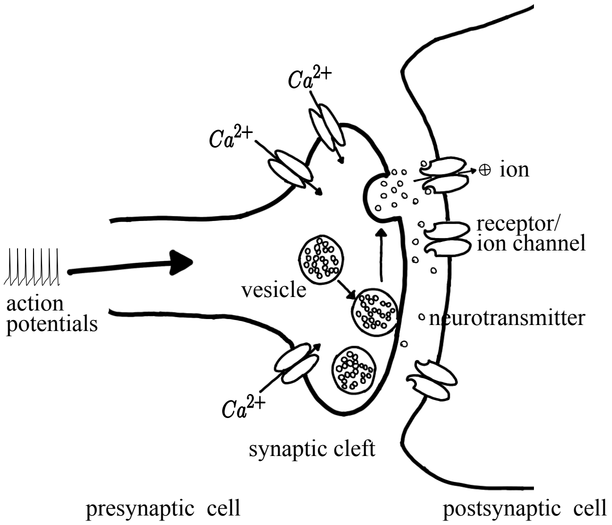

Figure 5.1: Schematic structure of chemical synapses and signal transmission pathways involved.

A brief surge in calcium concentration increases the probability of vesicle fusion with the terminal membrane, releasing neurotransmitters, a chemical messenger, into the synaptic cleft. Neurotransmitters diffuse across the synaptic cleft and bind to receptors on the postsynaptic cell. Receptor activation leads to the opening or closing of ion channels in the cell membrane. This may increase or decrease the membrane potential, depending on the ions involved, ultimately causing the postsynaptic cell to be more/less likely to fire its own action potential, called the excitatory/inhibitory postsynaptic response. Synaptic facilitation occurs when the accumulated calcium concentration encourages vesicle release, ultimately causing an increase in the amplitude of the postsynaptic response. Depletion of vesicles during ongoing activity can lead to suppression of the postsynaptic response; thus, synaptic depression occurs.

Presynaptic vesicles are a limited resource. After release, empty vesicles are retrieved and replenished. During this period, the synapses are in a refractory state. The recovery rate from the refractory state is usually not constant and is influenced by the calcium concentration at the presynaptic terminal [75].

5.2.2 Discrete STP Model with Periodic Inputs

To study the principles of synaptic plasticity, experiments commonly involve trains of action potentials at specific fixed frequencies to replicate the recurrent input from the presynaptic cell [195]. In this section, we focus on this scenario and aim to derive a discrete dynamical system for the microscopic STP variables. This model is based on the work in [195], and we present it here to help motivate and validate the subsequent neural network model.

Generally, the synaptic transmission process described above has three main components: presynaptic calcium buffering, presynaptic calcium-dependent vesicle trafficking, and postsynaptic response. Our discrete model will follow this structure, expanding on the mechanisms delineated in [132].

Presynaptic calcium buffering

When modeling synaptic dynamics, a common approach is to use a simple calcium model where the intracellular calcium concentration, denoted C, follows the first-order decay kinetics towards a baseline concentration with a decay time constant of τ_c. Without loss of generality, let the baseline concentration be zero [74, 195]. Thus, the calcium concentration is governed by

$$\tau_c \frac{dC}{dt} = -C(t). \tag{5.1}$$

We assume that the presynaptic neuron spikes periodically with an interspike interval (ISI) of T, which is consistent with the experimental design. Let us start at the time $t = 0$ just after the first spike occurs. By solving the equation for C, we obtain a solution at the end of the first interspike interval: $C(T) = C(0)e^{-T/\tau_c}$. The second spike closely follows the first spike, leading to a rapid and significant increase in local calcium concentration, denoted $C(T) + C_{\text{jump}}$. Thus, the overall process is such that the calcium concentration reaches its maximum just after this spike and then decays to its minimum before the arrival of the next spike.

We denote C as $C^-(k)$ just before the kth spike (left limit) and as $C^+(k)$ just after the kth spike (right limit). Using the value after the kth spike as the initial condition, i.e., $C(0) = C^+(k)$, yields $C(T) = C^-(k+1)$ as the value just before the $(k+1)$th spike arrives, and then this concentration rapidly accumulates due to the $k+1$th spike. Thus, we have a discrete expression given by

$$C^-(k+1) = C^+(k)e^{-T/\tau_c}, \tag{5.2a}$$

$$C^+(k+1) = C^-(k+1) + C_{\text{jump}}. \tag{5.2b}$$

After some manipulation, we can reformulate these equations into an iterative map:

$$C^-(k+1) = \big(C^-(k) + C_{\text{jump}}\big)e^{-T/\tau_c}, \tag{5.3a}$$

$$C^+(k+1) = C^+(k)e^{-T/\tau_c} + C_{\text{jump}}. \tag{5.3b}$$

Presynaptic vesicle trafficking

When stimulated, an increase in calcium concentration triggers exocytosis with a release probability P. This process involves vesicle docking, priming, and fusion with the terminal membrane, followed by the release of neurotransmitters into the synaptic cleft, as illustrated in Fig. 5.1. The release probability P relies on how quickly specific transmitter-release proteins respond to the instantaneous influx of calcium [132]. Since we focus on modulation at hippocampal GABAeric synapses, we adopt a scheme proposed in [195] to be consistent with the experimental data. In this scheme, the release probability P is determined by the calcium concentration and obeys a Hill equation with coefficient 4,

$$P = P_{\max}\frac{C^4}{C^4 + K_P^4}, \tag{5.4}$$

where the parameter $P_{\max}$ denotes the maximum release probability and K_p is the calcium concentration when $P = 1/2P_{\max}$.

Presynaptic vesicles are a limited resource. Simultaneously with exocytosis, empty vesicles are recovered (recycled and replenished with neurotransmitters) from the refractory state. Denote R as the fraction in the vesicle pool ready to release and assume that the total quantity of vesicles remains constant [132]. Then, the ratio of empty vesicles is $(1-R)$. Before an input spike, the variable R is governed by the equation [132]

$$\frac{dR}{dt} = k_{\text{rev}}(t)(1-R). \tag{5.5}$$

The recovery rate k_{rev} depends on residual calcium according to experimental observation [112]. It involves a Hill equation with coefficient 1 starting at $k_{\text{rev,min}}$ [132], given by

$$k_{\text{rev}}(t) = k_{\text{rev,min}} + (k_{\text{rev,max}} - k_{\text{rev,min}})\frac{C(t)}{C(t) + K_{\text{rev}}}, \tag{5.6}$$

where C follows the decay equation (5.1) during the interval of spikes. The value of k_{rev} decreases to $k_{\text{rev,min}}$ when C approaches the baseline and reaches $k_{\text{rev,max}}$ when C is sufficiently large relative to the affinity constant K_{rev}. Solving equations (5.1), (5.5) and (5.6), we obtain a continuous solution

$$\begin{aligned} R(t) &= 1 - \big[1 - R(0)\big] e^{-k_{\text{rev,min}} t} \left(\frac{C(0) e^{-t/\tau_c} + K_{\text{rev}}}{C(0) + K_{\text{rev}}} \right)^{\tau_c (k_{\text{rev,max}} - k_{\text{rev,min}})}, \\ &\equiv 1 - \big[1 - R(0)\big] e^{-k_{\text{rev,min}} t} \gamma\big(C(0)\big), \end{aligned} \tag{5.7}$$

where

$$\gamma\left(C\right) = e^{-k_{\text{rev,min}} T} \left(\frac{C e^{-T/\tau_c} + K_{\text{rev}}}{C + K_{\text{rev}}} \right)^{\tau_c (k_{\text{rev,max}} - k_{\text{rev,min}})}.$$

Employing the discrete scheme as before and replacing $R(t)$ with $R^{-}(k+1)$, the variable before the $(k+1)$th spike, $R(0)$ with $R^{+}(k)$ and $C(0)$ with $C^{+}(k)$, the variables after the kth spike, yields

$$R^{-}(k+1) = 1 - \big(1 - R^{+}(k)\big) e^{-k_{\text{rev,min}} T} \gamma\left(C^{+}(k)\right).$$

Furthermore, the releasable vesicle ratio R decreases due to the the spike-triggered neurotransmitter release, yielding

$$R^{+}(k) = R^{-}(k) - \beta P^{+}(k) R^{-}(k) = R^{-}(k)\left(1 - \beta P^{+}(k)\right),$$

where β is the scaling factor, and the right-limit release probability P^{+} is adopted because P instantly varies with $[C]$ as described by Eq. (5.4) due to the spike stimulus, whereas the synapse needs time to response from R^{-} to R^{+} especially when the spike stimulus occurs closely after the former one [74, 205]. Then, we can reformulate the above expressions into the following iteration map for the variable R:

$$R^{-}(k+1) = 1 - \left[1 - \left(1 - \beta P^{+}(k)\right) R^{-}(k)\right] \gamma\left(C^{+}(k)\right), \tag{5.8a}$$

$$R^{+}(k+1) = \left(1 - \beta P^{+}(k+1)\right) \left[1 - \left(1 - R^{+}(k)\right) \gamma\left(C^{+}(k)\right)\right]. \tag{5.8b}$$

Postsynaptic response with periodic input

Synaptic facilitation occurs when the accumulated calcium concentration encourages vesicle release, ultimately causing an enhancement in the amplitude of the postsynaptic response. On the other hand, synaptic depression occurs when vesicles are depleted at a rate faster than their recovery, resulting in a reduced postsynaptic response.

If the kth spike input is followed closely by the next one without allowing the synapse to recovered from the refractory state, then the kth postsynaptic current (PSC) will be determined by the product of the increased release probability P^+ (just after the kth spike) and the remaining releasable vesicles R^- (just before the kth spike) in the form

$$\mathrm{PSC}(k) \propto P^+(k)R^-(k). \tag{5.9}$$

Note that only the values (P^+, R^-) at right-limit and left-limit spike times matter for the PSC [74, 205, 195, 188].

In summary, we have developed a discrete dynamical system (5.3), (5.4), (5.8) and (5.9) to represent the microscopic dynamics of signal transmission between two neurons modulated by synaptic STP. To gain a deeper understanding of the synaptic dynamics, we illustrate the temporal changes of the variables using a spike-train input with a frequency of 50 Hz. The parameter values can be found in Table 5.1. These values, obtained from [195], were specifically fitted to the synapses from the parvalbumin-containing basket cell (PV BC) to the pyramidal cell in the CA1 region of the hippocampus. The evolution of the variables between spikes is captured by plotting the continuous functions (5.1), (5.4) and (5.7). As shown in Fig. 5.2, the calcium concentration $C(t)$ and the recovery variable $R(t)$ exhibit first-order kinetics between the spikes. With the arrival of the stimulus, there is a rapid increase in C and a rapid decrease in R. Throughout this process, the release probability $P(t)$ changes with $C(t)$ by Eq. (5.4). The postsynaptic response follows the law in Eq. (5.9) and eventually reaches a stable value. In addition, we observe that the application of muscarine leads to a smaller postsynaptic response, since muscarinic activation reduces the influx of calcium concentration (see the scale difference in C in Fig. 5.2) into the presynaptic cell [195].

5.3 Neural Network with Synaptic STP

Previously, we described the synaptic transmission between two neurons and built the discrete STP model motivated by experimentally designed studies that generated the periodic spike-train input manually. However, neurons always work as a population and network couplings make individual neurons exhibit irregular spiking patterns at various rates [194]. In this section, we go back to our initial problem of a large neural network with synaptic STP, where the spike input is from coupled presynaptic neurons and its frequency varies with time. We will construct a continuous dynamical system by formulating the spike train stimuli as repetitive input impulses.

Parameters	Values	Description
τ_m	1 ms	Time constant for membrane potential
τ_c	1.5 ms	Time constant for calcium
C_{jump}	1 (control) 0.17 (muscarine)	After-spike jump size for calcium
β	1	Scaling factor
$P_{\max}$	0.87	Maximum release probability
$k_{\min}$	0.0017 ms^{-1}	Minimum recovery rate constant
$k_{\max}$	0.0057 ms^{-1}	Maximum recovery rate constant
K_P	0.2	Half calcium concentration for probability of release function
K_{rev}	0.1	Half calcium concentration for rate of recovery function

Table 5.1: Parameter values for hippocampal GABAergic synapses [195].

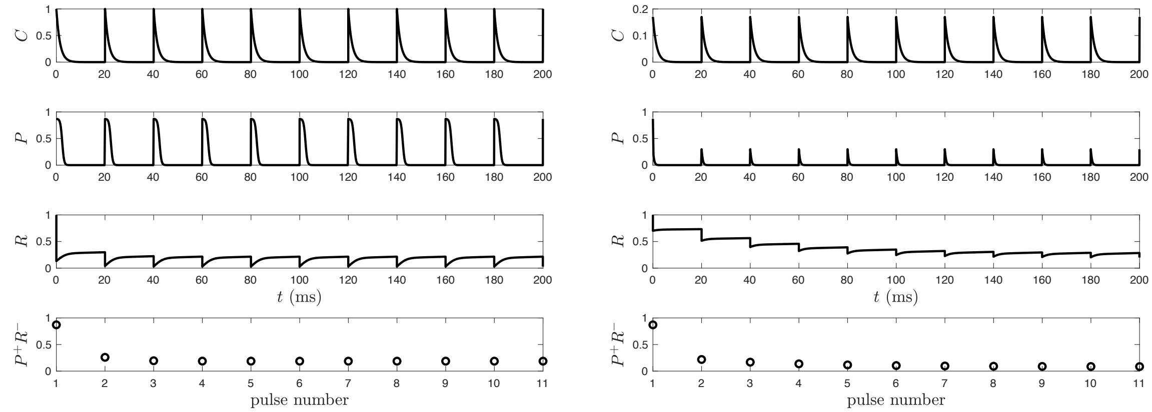

Figure 5.2: Time evolution of the synaptic system with STP (5.1), (5.4), (5.7) and (5.9) for the control case $C_{\text{jump}} = 1$ (left column) and the muscarine case $C_{\text{jump}} = 0.17$ (right column). The initial conditions are $C(0) = C_{\text{jump}}$, $P(0) = P_{\max}$ and $R(0) = 1$. Parameter values are given in Table 5.1.

5.3.1 Network Setting and Postsynaptic Response

We consider a network of N all-to-all coupled QIF neurons with synaptic STP. The QIF neuron is the canonical model for type I excitability and is suitable for studying network dynamics. Details of the QIF neuron are provided in Chapter 2.

The microscopic dynamics of the QIF network is described by the membrane potentials obeying the following equations:

$$\begin{aligned} \tau_m \frac{dv_i}{dt} &= v_i^2(t) + \eta_i + I_{\text{ext}}(t) + \tau_m I_{\text{syn},i}(t), \\ \text{if} \ \ v_i \geq v_{\text{peak}}, & \ \ \text{then} \ v_i \leftarrow v_{\text{reset}}, \end{aligned} \tag{5.10}$$

for $i = 1, 2, \ldots, N$. A neuron i emits its spike when it reaches the peak value v_{peak}, on which v_i is reset to v_{reset}. In the limit $v_{\text{peak}} = -v_{\text{reset}} = \infty$, the model (5.10) represents a network of theta neurons defined in the domain $\theta \in [-\pi, \pi)$ [117, 85, 104, 126] via the transform $v = \tan(\theta/2)$. Each neuron receives the input current from three distinct sources: a shared, time-varying external component $I_{\text{ext}}(t)$, an individualized static component η_i drawn from a probability distribution, and a recurrent component representing the postsynaptic response of neuron i resulting from presynaptic neurons through synapses, denoted as $I_{\text{syn},i}$. This PSC is the cumulative outcome of contributions from all the coupled presynaptic neurons,

$$I_{\text{syn},i} = (e_r - v_i)\bar{g}_i s_i = (e_r - v_i)\sum_{j=1}^{N} \bar{g}_{ij} s_{ij} = (e_r - v_i)\frac{g_{\text{syn}}}{N}\sum_{j=1}^{N} s_{ij}, \tag{5.11}$$

where e_r is the reversal potential, whose value determines whether the synapses are excitatory or inhibitory, i.e, whether they increase or decrease the likelihood of firing of the postsynaptic neuron; $\bar{g}_{ij}$ is the maximal synaptic conductance between neurons i and j, determining the strength of the coupling. For all-to-all connectivity, the neuron i is coupled with all N neurons in the network, including itself. Thus, we can take $\bar{g}_{ij} = g_{\text{syn}}/N$ where g_{syn} is the maximal synaptic conductance of the neuron i and homogeneous across the network [158]. Furthermore, s_{ij} is the synaptic gating variable, representing the proportion of ion channels open in the membrane of the postsynaptic neuron i as the result of firing in the presynaptic neuron j. Due to the effect of STP, we modulate s_{ij} by a dynamic factor $M_{ij}(t)$ [132, 188], then the postsynaptic current is modified as

$$I_{\text{syn},i} = (e_r - v_i)\frac{g_{\text{syn}}}{N}\sum_{j=1}^{N} M_{ij} s_{ij} = (e_r - v_i) g_{\text{syn}} s_i, \tag{5.12}$$

where

$$s_i = \frac{1}{N}\sum_{j=1}^{N} M_{ij} s_{ij}$$

is the gating variable of postsynaptic neuron i due to all presynaptic neurons. Under the assumption of all-to-all coupling, $s_i = s$ for all i since every postsynaptic neuron receives the same summed input from all presynaptic neurons [158]. Thus, we omit the index i in all s and rewrite it as follows,

$$s = \frac{1}{N}\sum_{j=1}^{N} M_j s_j. \tag{5.13}$$

We can also interpret it as the mean synaptic activation [150]. Recall from Sec. 2.4.2 that the single exponential synapse is governed by

$$\tau_s \frac{ds_j}{dt} = -s_j(t) + \sum_k \delta(t - t_j^{(k)}), \tag{5.14}$$

where $\delta(t)$ is the Dirac delta function and t_j^k is the time at which the neuron j emits its kth spike. In the limit $\tau_s \to 0$, we have

$$s_j(t) = \sum_k \delta(t - t_j^{(k)}) \;\equiv\; s_j^0(t), \quad \tau_s \to 0, \tag{5.15}$$

which represents the instantaneous effect resulting from the input spike train. To find the relationship between the synaptic activity $s_j^0(t)$ and the firing rate $r_j(t)$ of neuron j, we define the function $n_j(t)$ to be the number of spikes fired by the jth neuron in the time interval $[0, t]$,

$$n_j(t) = \int_0^t \sum_k \delta(t' - t_j^{(k)}) \mathrm{d}t'. \tag{5.16}$$

Then, we define the firing rate $r_j(t)$ as the number of spikes emitted per unit time in the limit $\Delta t \to 0$ [158], given by

$$r_j(t) = \lim_{\Delta t \to 0} \frac{n_j(t + \Delta t) - n_j(t)}{\Delta t} = \frac{d}{dt} n_j(t) = \sum_k \delta(t - t_j^{(k)}) = s_j^0(t).$$

For a spike train with an experimentally designed period of T_j, we have

$$r_j(t) = 1/T_j, \tag{5.17}$$

which represents that there is only one spike within each spike interval $T_j(t)$ [95].

5.3.2 Synaptic Dynamics in Network

As we already know, spike stimuli from the presynaptic neuron activate calcium channels, causing the intracellular calcium concentration to increase rapidly by an amount C_{jump}; between spike intervals, the calcium concentration decays with first-order kinetics. Thus, we can describe the time course of the concentration $C_j(t)$ for the neuron j in the network by the following equation in terms of the spike trains s_j [132]:

$$\tau_c \frac{dC_j}{dt} = -C_j + \tau_c C_{\text{jump}} s_j. \tag{5.18}$$

An increase in calcium concentration initiates the exocytosis process, where the release probability P is determined by the value of calcium concentration; see Eq. (5.4). The question then arises: what value of C should be substituted into this equation? Various studies in the literature have used different values, reflecting the varied responses of specific neurotransmitters to calcium influx. For example, the minimum value before the arrival of the next spike was adopted in [74]; the steady state obtained from Eq. (5.18) was chosen in [132], while the equivalent post-spike effect was utilized in [205]. Our strategy is to select a value for C that ensures the consistency of synaptic dynamics, whether considered in isolation or within the network environment. Thus, we need to establish the relationship of C between the network model (5.18) and the microscopic model (5.3) developed for the individual synapse.

For comparison, we adopt the idea used to develop the microscopic STP map (5.3) and apply regular spike trains to each neuron of the all-to-all coupled neural network. In this scenario, the presynaptic neuron j spikes periodically with a period T_j, giving rise to a spike train $s_j^0 = \sum_{k=0}^{\infty} \delta(t - kT_j)$ with a constant firing rate of $r_j = 1/T_j$. By replacing the spike train in the network model (5.18) by $s_j = r_j = 1/T_j$ in the limit $\tau_s \to 0$, we obtain the steady-state calcium concentration given by

$$C_* = \tau_c C_{\text{jump}}/T. \tag{5.19}$$

Here, we omit the neuron index j for brevity. On the other hand, in the context of periodic input, we have derived the iteration maps (5.3) for the calcium concentrations before and after the kth spike, $C^-(k)$ and $C^-(k)$. Thus, we can find the corresponding stationary solutions $C^-(k) = C^-(k+1) = C_*^-$ and $C^+(k) = C^+(k+1) = C_*^+$, given by

$$C_*^- = \frac{C_{\text{jump}}}{e^{T/\tau_c} - 1} \approx \frac{\tau_c}{T} C_{\text{jump}}, \tag{5.20a}$$

$$C_*^+ = \frac{C_{\text{jump}}}{e^{T/\tau_c} - 1} e^{T/\tau_c} \approx \frac{\tau_c}{T} C_{\text{jump}} + C_{\text{jump}}, \tag{5.20b}$$

where the second terms are the first-order approximations of C_*^- and C_*^+ at moderate to high frequencies, specifically when $T/\tau_c \ll 1$. Comparing Eq. (5.19) and (5.20), we find that the network steady state C_* closely corresponds to the left-limit value C_*^- obtained from the microscopic system. Given that the right-limit release probability P^+ is crucial in the exocytosis process and dependent on the calcium concentration (see Eq. (5.4) and (5.9)), we calculate P_j for neuron j in the network model as follows:

$$C_j^+(t) = C_j(t) + C_{\text{jump}}, \tag{5.21a}$$

$$P_j(t) = P_{\max}\frac{(C_j^+)^4}{(C_j^+)^4 + K_P^4}, \tag{5.21b}$$

which is consistent with the scheme in [205] and the analysis in [95]. Regarding the recovery variable $R(t)$, we utilize the same strategy in developing the microscopic models. Then, we have

$$\frac{dR_j}{dt} = k_{\text{rev},j}(1 - R_j) - \beta P_j^+ R_j^- s_j, \tag{5.22a}$$

$$k_{\text{rev},j}(t) = k_{\text{rev,min}} + (k_{\text{rev,max}} - k_{\text{rev,min}})\frac{C_j}{C_j + K_{\text{rev}}}. \tag{5.22b}$$

Here, $R^- = R$ and $P^+ = P$ in Eq. (5.21). We add the superscripts "–" and "+" to the prefactors of s_j to emphasize that only the values (P^+, R^-) at right-limit and left-limit spike times matter for the PSC; see Eq. (5.9). Meanwhile, we can specifically write the synaptic current in Eq. (5.12) as

$$I_{\text{syn},i} = (e_r - v_i)\frac{g_{\text{syn}}}{N}\sum_{j=1}^{N} P_{ij}^+ R_{ij}^- s_{ij} = (e_r - v_i)\frac{g_{\text{syn}}}{N}\sum_{j=1}^{N} P_j^+ R_j^- s_j. \tag{5.23}$$

5.3.3 Summary of the Network Model and Its Simplification

We have developed the network model for the all-to-all coupled QIF neurons with calcium-dependent synaptic STP, which is summarized by the system comprising a set of ordinary differential equations (ODEs) and algebraic equations as follows,

$$\tau_m \frac{dv_i}{dt} = v_i^2(t) + \eta_i + I_{\text{ext}}(t) + \tau_m g_{\text{syn}}(e_r - v_i)\frac{1}{N}\sum_{j=1}^{N} P_j^+ R_j^- s_j, \tag{5.24a}$$

$$\tau_c \frac{dC_i}{dt} = -C_i + \tau_c C_{\text{jump}} s_i, \tag{5.24b}$$

$$\frac{dR_i}{dt} = k_{\text{rev},i}(1 - R_i) - \beta P_i^+ R_i^- s_i, \tag{5.24c}$$

$$\tau_s \frac{ds_i}{dt} = -s_i + \sum_k \delta(t - t_i^{(k)}), \tag{5.24d}$$

$$C_i^+ = C_i + C_{\text{jump}}, \tag{5.24e}$$

$$P_i = P_{\max}\frac{(C_i^+)^4}{(C_i^+)^4 + K_P^4}, \tag{5.24f}$$

$$k_{\text{rev},i} = k_{\text{rev,min}} + (k_{\text{rev,max}} - k_{\text{rev,min}})\frac{C_i}{C_i + K_{\text{rev}}}. \tag{5.24g}$$

In the literature, some common choices are made to simplify the neural network system, with the aim of concentrating the study on the pertinent dynamics. One choice involves taking the limit of infinitely fast synapses, i.e., $\tau_s \to 0$ in Eq. (5.24d) [150]. Moreover, the time-varying component of the coupling strength $(e_r - v)$ in Eq. (5.24a) is frequently assumed to be constant, especially for inhibitory neural networks [167]. This assumption replaces the term $g_{\text{syn}}(e_r - v)$ with a constant J. The case $J > 0$ represents the excitatory coupling and $J < 0$ represents the inhibitory coupling [150]. Additionally, the dependency of the recovery rate on calcium may demonstrate linearity at some synapses. For example, the paper [195] replaced Eq. (5.24g) by its first-order approximation around $C = 0$, a linear equation,

$$k_{\text{rev},i} = k_{\text{rev,min}} + \frac{k_{\text{rev,max}} - k_{\text{rev,min}}}{K_{\text{rev}}} C_i \equiv k_{\text{rev,min}} + \alpha C_i. \tag{5.25}$$

In this chapter, we retain the nonlinear form of k_{rev}, while adopting the first two simplifications. As a result, we have the simplified network model given by

$$
\begin{aligned}
\tau_m \frac{dv_i}{dt} &= v_i^2(t) + \eta_i + I_{\text{ext}}(t) + \frac{J\tau_m}{N} \sum_{j=1}^{N} P_j^+ R_j^- s_j, && \text{(5.26a)}\\
\tau_c \frac{dC_j}{dt} &= -C_j + \tau_c C_{\text{jump}} s_j, && \text{(5.26b)}\\
\frac{dR_j}{dt} &= k_{\text{rev},j}(1 - R_j) - \beta P_j^+ R_j^- s_j, && \text{(5.26c)}\\
s_j &= \sum_k \delta(t - t_j^{(k)}), && \text{(5.26d)}\\
C_j^+ &= C_j + C_{\text{jump}}, && \text{(5.26e)}\\
P_j &= P_{\max} \frac{(C_j^+)^4}{(C_j^+)^4 + K_P^4}, && \text{(5.26f)}\\
k_{\text{rev},j} &= k_{\text{rev,min}} + (k_{\text{rev,max}} - k_{\text{rev,min}}) \frac{C_j}{C_j + K_{\text{rev}}}. && \text{(5.26g)}
\end{aligned}
$$

Here, we specifically use the subscript j to emphasize the activities that occur in presynaptic neurons and i for the postsynaptic ones. For all-to-all connectivity, there is no discrimination between them. All subsequent analyses will be conducted on this model.

5.4 The Derivation of the Mean-field System

In this section, our aim is to develop a low-dimensional mean-field model to describe the collective dynamics of the neural network (5.26). The main difference from previous chapters lies in introducing a kinetic model of synapse into the neural network.

To steamline the derivation, we denote

$$
r_{\text{eff}}(t) = \frac{1}{N} \sum_{j=1}^{N} P_j^+ R_j^- s_j = \frac{1}{N} \sum_{j=1}^{N} P_j^+ R_j^- \sum_k \delta(t - t_j^{(k)}) \tag{5.27}
$$

as the effective mean-field network activity that arrives at each neuron. Without synaptic STP, we have $P(t) = R(t) = 1$ and r_{eff} becomes the population firing rate $r(t)$,

$$
r(t) = \lim_{N\to\infty} \frac{1}{N} \sum_{j=1}^{N} \sum_k \delta(t - t_j^{(k)}). \tag{5.28}
$$

See details in Sec. 3.3.1. The population firing rate $r(t)$ and the mean membrane potential $\langle v(t)\rangle$ over all neurons can be derived using a similar procedure presented in Chapter 3. Here, we offer a brief overview.

In the thermodynamic limit, $N \to \infty$, the network satisfies the conditions for the existence of the low-dimensional OA manifold [163] or the equivalent Lorentzian ansatz [150], that is, the membrane potentials v_i are distributed according to a Lorentzian probability density for the current parameter η at time t,

$$\rho(t, v|\eta) = \frac{1}{\pi} \frac{x(t,\eta)}{\big[v - y(t,\eta)\big]^2 + x^2(t,\eta)}. \tag{5.29}$$

The center $y(t,\eta)$ and half-width at half-maximum (HWHM) $x(\eta, t)$ are associated with $r(t)$ and $\langle v(t)\rangle$ via the equations

$$r(t) = \int_{\partial\eta} r(t,\eta)\mathcal{L}(\eta)\mathrm{d}\eta = \int_{\partial\eta} \frac{1}{\pi} x(t,\eta)\mathcal{L}(\eta)\mathrm{d}\eta, \tag{5.30a}$$

$$\langle v(t)\rangle = \int_{\partial\eta} y(t,\eta)\mathcal{L}(\eta)\mathrm{d}\eta, \tag{5.30b}$$

where $\mathcal{L}(\eta)$ is the probability distribution function for the current parameters η_i. The time evolution of the probability density $\rho(t)$ is governed by the continuity equation, given by

$$\partial_t\rho + \partial_v \left[\left(\frac{v^2 + \eta + I_{\text{ext}}}{\tau_m} + J r_{\text{eff}}\right)\rho\right] = 0. \tag{5.31}$$

Substituting Eq. (5.29) into the above equation yields the dynamics of $x(\eta, t)$ and $y(\eta, t)$, thus $r(\eta, t)$ and $\langle v(\eta, t)\rangle$, obeying

$$\partial_t z(\eta, t) = i\left[\frac{-z^2(\eta,t) + \eta + I_{\text{ext}}}{\tau_m} + J r_{\text{eff}}\right] \tag{5.32}$$

for any η, with $z(\eta, t) = x(\eta, t) + iy(\eta, t) = \pi r(\eta, t) + i\langle v(\eta, t)\rangle$. Further reduction in the dimensionality of the resulting mean-field system can be achieved by choosing a Lorentzian distribution for the current parameters η_k with HWHM Δ_η, centered at $\bar{\eta}$,

$$\mathcal{L}(\eta) = \frac{1}{\pi} \frac{\Delta_\eta}{(\eta - \bar{\eta})^2 + \Delta_\eta^2}. \tag{5.33}$$

Using the residue theorem of complex analysis and evaluating the integral at the pole of $\mathcal{L}(\eta)$ given by $\bar{\eta} - i\Delta_\eta$, i.e., $z(\bar{\eta} - i\Delta_\eta, t) = \pi r(t) + iv(t)$, we obtain the mean-field system for r and $\langle v\rangle$ as follows,

$$\tau_m \frac{dr}{dt} = \frac{\Delta_\eta}{\pi\tau_m} + 2r\langle v\rangle, \tag{5.34a}$$

$$\tau_m \frac{d\langle v\rangle}{dt} = \langle v\rangle^2 + \bar{\eta} + I_{\text{ext}}(t) + J\tau_m r_{\text{eff}} - (\pi\tau_m r)^2. \tag{5.34b}$$

Further, we can obtain the mean-field approximation for the presynaptic dynamics (5.26b)-(5.26g) as below,

$$\tau_c \frac{d\langle C\rangle}{dt} = -\langle C\rangle + \tau_c C_{\text{jump}} r, \tag{5.35a}$$

$$\frac{d\langle R\rangle}{dt} = \langle k_{\text{rev}}\rangle\big(1 - \langle R\rangle\big) - \beta r_{\text{eff}}, \tag{5.35b}$$

$$\langle C^+\rangle = \langle C\rangle + C_{\text{jump}}, \tag{5.35c}$$

$$\langle k_{\text{rev}}\rangle = k_{\text{rev,min}} + (k_{\text{rev,max}} - k_{\text{rev,min}})\frac{\langle C\rangle}{\langle C\rangle + K_{\text{rev}}}, \tag{5.35d}$$

$$\langle P\rangle = P_{\max}\frac{\langle C^+\rangle^4}{\langle C^+\rangle^4 + K_P^4}. \tag{5.35e}$$

Here, the equation of $\langle C\rangle$ is derived by following a similar procedure as for $\langle w\rangle$ in Chapter 3 under the analogous assumption that $\langle C|\eta\rangle \gg C_{\text{jump}}$; the equation for $\langle R\rangle$ is the result of the first-order moment closure method by assuming $\langle k_{\text{rev}} \cdot R\rangle = \langle k_{\text{rev}}\rangle \cdot \langle R\rangle$; the equations for $\langle P\rangle$ and $\langle k_{\text{rev}}\rangle$ come from heuristic, but simple estimations. Our numerical simulations in the following section will demonstrate acceptable agreement between the network system and our mean-field approximation.

Now, we come to the last step of mean-field derivation about how to obtain the expression of r_{eff} in Eq. (5.34b) and (5.35b) in terms of the existing macroscopic variables. It is the key to closing the mean-field system. Neurophysiological studies revealed that individual neurons fire irregularly and can occur at any rate [194]. This irregularity in firing rates is compared to a Poisson process, which means that the timing of each neuron's firing is independent of the timing of previous firings and occurs randomly [205]. So we can assume that the spike trains of all neurons $\{s_j\}_{j=1,\dots,N}$ follow independent Poisson processes [205, 188]. Under this assumption, the original spike train is statistically equivalent to the ones, given by

$$\frac{1}{N}\sum_{j=1}^{N}\sum_{k}\delta(t - t_j^{(k)}) = \frac{1}{N}\sum_{k\in\mathbb{Z}_+}\delta(t - t^{(k)}). \tag{5.36}$$

It implies that synapse identities j can be randomized, that is, the spike times $\{t^{(k)}\}_{k\in\mathbb{Z}_+}$ matter, but not the synapse at which the spikes occur. From the definition (5.16), we have $n_j(t)$ as the number of spikes fired by the jth neuron in the time interval $[0,t]$. Then, we define the network averaged firing rate, the mean spike numbers in per unit time, as in Eq. (3.14),

$$r(t) = \lim_{\Delta t\to 0} \lim_{N\to\infty} \frac{1}{N}\sum_{j=1}^{N} \frac{n_j(t+\Delta t) - n_j(t)}{\Delta t}.$$

Due to the effect of STP, the spike trains are modulated by a dynamic factor $M_j(t) = P_j R_j$. Thus, we define the effective mean-field network activity as

$$\begin{aligned} r_{\text{eff}}(t) &= \lim_{\Delta t\to 0} \lim_{N\to\infty} \frac{1}{N}\sum_{j=1}^{N} M(P_j, R_j)\frac{n_j(t+\Delta t) - n_j(t)}{\Delta t} \\ &= \lim_{\Delta t\to 0} \frac{1}{\Delta t} \lim_{N\to\infty} \frac{1}{N}\sum_{j=1}^{N} M(P_j, R_j)\Big(n_j(t+\Delta t) - n_j(t)\Big) \end{aligned} \tag{5.37}$$

Under the Poisson process, that is, Eq. (5.36), we assume that at most one spike can occur in the entire network in an infinitesimally small time interval $\Delta t \to 0$ [188]. Thus, there exists one and only one neuron j for which $n_j(t+\Delta t) - n_j(t) = 1$. We define the average of $\langle n_j(t)\rangle$ across the network as [158]

$$\langle n_j(t)\rangle = \lim_{N\to\infty} \frac{1}{N}\sum_{j=1}^{N} n_j(t). \tag{5.38}$$

From the network averaged perspective, we have $\big\langle n_j(t+\Delta t)\big\rangle - \langle n_j(t)\rangle = 1$ in the interval $\Delta t \to 0$. This implies that we can factor out any modulation function $M(P_j, R_j)$ as follows [188],

$$\begin{aligned} r_{\text{eff}}(t) &= \lim_{\Delta t\to 0} \frac{1}{\Delta t} \lim_{N\to\infty} \frac{1}{N}\sum_{j=1}^{N} M(P_j, R_j)\Big(n_j(t+\Delta t) - n_j(t)\Big) \\ &= \lim_{\Delta t\to 0} \frac{M\Big(\langle P\rangle, \langle R\rangle\Big)\Big(\big\langle n_j(t+\Delta t)\big\rangle - \langle n_j(t)\rangle\Big)}{\Delta t} \\ &= M\Big(\langle P\rangle, \langle R\rangle)\Big)\frac{d}{dt}\langle n_j(t)\rangle. \end{aligned} \tag{5.39}$$

Substituting Eqs. (5.16) and (5.38) yields

$$\begin{aligned} r_{\text{eff}}(t) &= M\Big(\langle P\rangle, \langle R\rangle\Big) \lim_{N\to\infty} \frac{1}{N} \sum_{j=1}^{N} \sum_{k} \delta(t - t_j^{(k)}) \\ &= M\Big(\langle P\rangle, \langle R\rangle\Big) r(t). \end{aligned} \tag{5.40}$$

For our case, we have

$$r_{\text{eff}}(t) = \langle P\rangle \langle R\rangle r(t) \tag{5.41}$$

Thus, the mean-field system is closed by expressing r_{eff} in terms of the existing macroscopic variables. Finally, we reduce the network of QIF neurons with synaptic STP (5.26) to the mean-field system composed of (5.34), (5.35) and (5.41).

5.5 Numerical Analysis

In this section, we will numerically analyze the dynamics of the proposed mean-field system, showing its ability to accurately replicate the collective behaviors of the QIF network with synaptic STP. Additionally, we will investigate the effect of muscarine within the mean-field framework. By binding to the presynaptic mAChRs, muscarine triggers the inhibition of calcium channels, leading to a reduction in the influx of calcium into the presynaptic terminal upon arrival of an action potential [99]. Therefore, in the muscarine case, we will employ a smaller value for C_{jump} compared to the control case [195].

The parameter values for all numerical experiments are given in Table 5.1 and Table 5.2, unless otherwise specified in a figure. Mainly sourced from [195], these values were originally fitted for the hipocampal CA1 GABAergic synapses between the parvalbumin-containing basket cell (PV BC) and the pyramidal cell. These synapses are characterized by their inhibitory nature, thus the coupling strength $J < 0$. Note that all values are dimensionless, except for time, which is measured in milliseconds (ms). Numerical simulations were performed using Euler's method in MATLAB [145], with a time step $dt = 10^{-3}$ and numerical continuation using XPPAUT software [83].

We begin our investigation by performing a bifurcation analysis of the mean-field system. In Fig. 5.3(a), we present qualitative changes in the population firing rate r as the mean current parameter $\bar{\eta}$ varies. When $\Delta_\eta = 0.05$, both the control ($C_{\text{jump}} = 1$) and the muscarinic ($C_{\text{jump}} = 0.17$) systems converge to stable equilibrium points (EPs) (red), while the muscarinic one exhibits higher values of r. This observation agrees with our previous

Parameters	Values	Description
$I_{\text{ext}}(t)$	0	Common, time-varying external current
N	1000	Number of cells in the network
$v(0)$	0	Initial membrane potential
$C(0)$	1	Initial calcium concentration
$P(0)$	0.5	Initial release probability
$R(0)$	1	Initial ratio of releasable vesicles
$r(0)$	0	Initial population firing rate

Table 5.2: Parameter values & initial conditions of the QIF-STP system.

findings, where the muscarinic effect reduces the postsynaptic response; see Fig. 5.2. In the inhibitory network, the reduced PSC implies that fewer negative currents are introduced into postsynaptic cells, thus improving their excitability. Consequently, the average firing rate across the network is elevated in the muscarine case. Furthermore, the bifurcation diagrams also indicate that the application of muscarine enriches the system dynamics. This can be seen in the bottom row of Fig. 5.3, where the muscarinic system is able to stabilize at periodic orbits (POs) (below the green line in (b), inside the green loop in (d), and to the left of the green line in (c)). It suggests that muscarine may induce synchronous bursting behaviors between neurons. In addition, we illustrate qualitative changes in the population firing rate r with varying coupling strength J in Fig. 5.4 for the QIF neural network (a), the QIF system with STP in the control case (b) and the QIF-STP system in the muscarine case (c), respectively. It should be noted that most of our parameter values were obtained by fitting data from the inhibitory synapse, suggesting that J should always be negative. Driven by curiosity, we extend the range of J to the positive region and observe an interesting phenomenon. When $J < 0$, all three neural systems have EPs as the sole attractor, as indicated by the red color in Fig. 5.4. It is consistent with results in Fig. 5.3(a) and (b) with $\Delta_\eta = 0.5$. When $J > 0$, the system in the absence of synaptic STP still only shows the EP attractor; see Fig. 5.4(a). In contrast, when synaptic plasticity is taken into account, the system can exhibit stable POs in the region to the right of the supercritical Hopf boundaries (green), where $J > 0$ (refer to Fig. 5.4(b) for the control case and (c) for the muscarine case). Observe that a higher positive value of J is required to compensate for the reduced PSC due to muscarine.

The time evolution of the macroscopic variables is depicted in Fig. 5.5 for the full neural network (in blue) and the derived mean-field system (in red) simultaneously. Both cases,

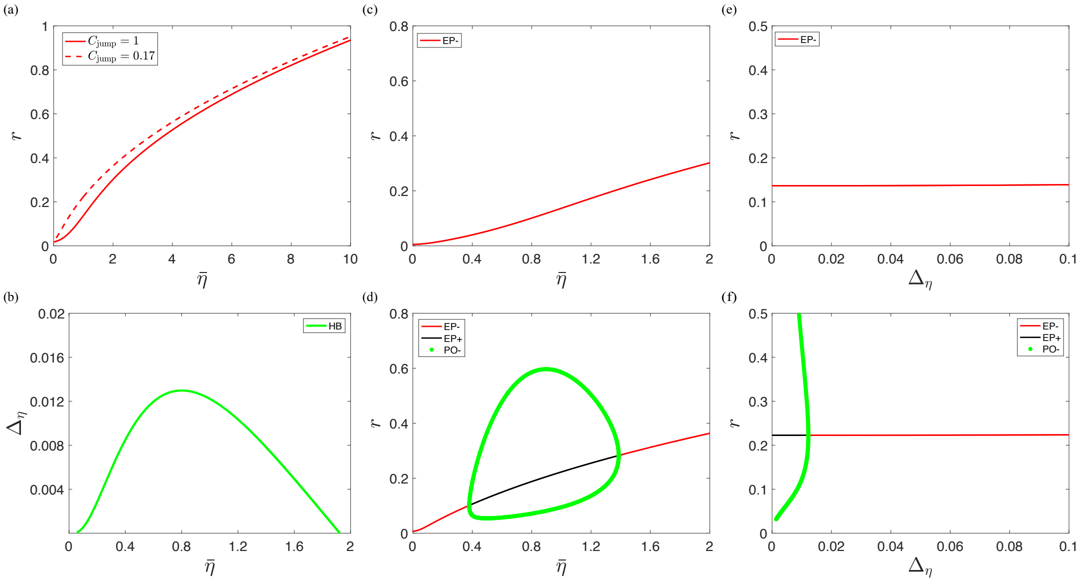

Figure 5.3: Bifurcation diagrams of the mean-field system (5.34), (5.35) and (5.41) for the control case $C_{\text{jump}} = 1$ (first row) and the muscarine case $C_{\text{jump}} = 0.17$ (second row), respectively. We depict stable/unstable EP in red/black and supercritical Hopf boundaries in green. (a): the $(\bar{\eta}, r)$ plane when $\Delta_\eta = 0.05$, combining the curves in both cases for comparison. (b): the $(\bar{\eta}, \Delta_\eta)$ plane, where stable POs exist under the green curve. (c) & (d): the $(\bar{\eta}, r)$ plane when $\Delta_\eta = 0.008$. (e) & (f): the (Δ_η, r) plane when $\bar{\eta} = 1$. To the left of the green curve, there are stable POs. Parameter values: $J = -30$ and others are given in Tables 5.1 and 5.2.

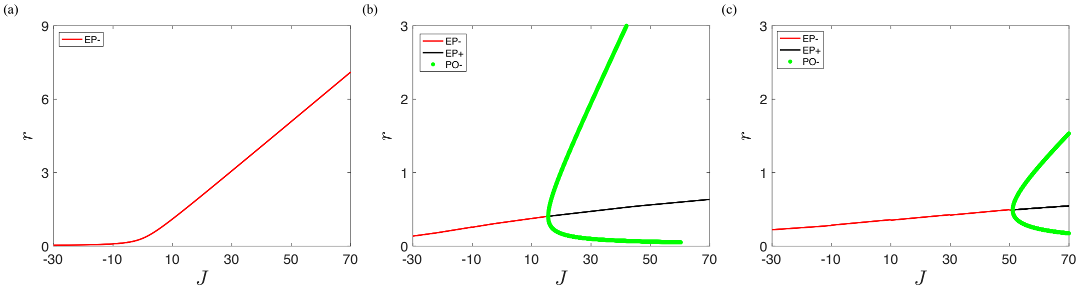

Figure 5.4: Comparison of bifurcation diagrams in the plane (J, r) for (a) the QIF network without STP, (b) the QIF-STP system for the control case $C_{\text{jump}} = 1$ and (c) the QIF-STP system for the muscarine case $C_{\text{jump}} = 0.17$. We depict stable/unstable EP in Red/black and supercritical Hopf boundaries in green. Stable POs exist the right of the green line. Parameter values: $\bar{\eta} = 1$ and $\Delta_\eta = 0.05$, others are given in Tables 5.1 and 5.2.

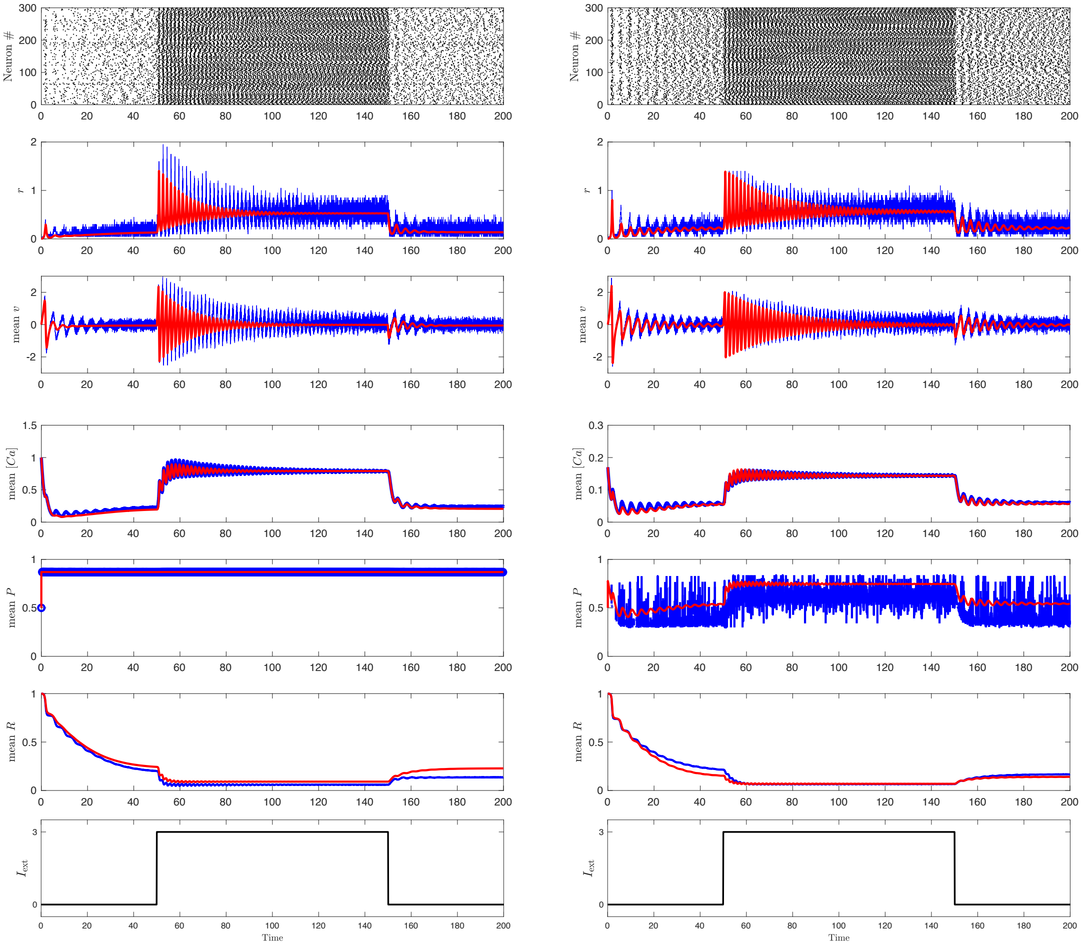

Figure 5.5: Time evolution for the QIF-STP network (5.26) (blue) and the corresponding mean-field model (5.34), (5.35) and (5.41) (red) for the control case $C_{\text{jump}} = 1$ (left column) and muscarine case $C_{\text{jump}} = 0.17$ (right column). A current $I_{\text{ext}}(t) = 3$ is applied to all neurons when $t = (50 - 150)$ ms and $I(t) = 0$ at all other times (bottom row). The top row shows raster plots of 300 randomly selected neurons of the $N = 1000$ in the population. The dots correspond to the firing events. The macroscopic variables $r(t)$ (2nd row), $\langle v(t) \rangle$ (3rd row), $\langle C(t) \rangle$ (4th row), $\langle P(t) \rangle$ (5th row) and $\langle R(t) \rangle$ (6th row) are presented, respectively. Parameter values: $\bar{\eta} = 1$, $\Delta_\eta = 0.05$ and $J = -30$. Others are given in Tables 5.1 and 5.2.

the control case (left column) and the muscarine case (right column), exhibit consistent behaviors, including damped oscillations and changes with the varying applied current. Despite the slight discrepancy observed in the muscarine case for the mean release probability

$P(t)$, the mean-field estimation still consistently reflects a trend similar to that observed in the network. Moreover, these temporal behaviors agree with the bifurcation results for the mean-field system, as shown in Fig. 5.3(a) and (b) for $\Delta_\eta = 0.05$. Note that the effects of constants I and $\bar{\eta}$ on the mean-field system are identical; see Eq. (5.34). These consistent findings suggest that our mean-field model reliably predicts the dynamic of the full neural network that incorporates synaptic STP. Furthermore, we identified a novel muscarinic effect from the time series illustrated in Fig. 5.5. Specifically, the muscarinic system exhibits a longer transient oscillatory process compared to the control system. This phenomenon arises from muscarinic activation, which causes weaker inhibitory PSCs and consequently increases excitability in postsynaptic neurons, leading to a longer convergence process of the full network. In addition, we performed some numerical experiments (not shown) using the parameter values in [195], where the authors proposed a linear equation for k_{rev}; see Eq. (5.25) instead of (5.26g). Our findings indicate that the mean-field system exhibits a relatively slower decay towards EPs and agrees worse with the network's transient behavior when employing the linear form rather than the nonlinear one.

Furthermore, we consider a scenario where the neural system has a smaller heterogeneity. As predicted from the bifurcation diagram of the mean-field system in Fig. 5.3(c) and (d), the system under control conditions converges to an EP, while the system under muscarine conditions exhibits oscillating behaviors when $\bar{\eta} = 1$ and $\Delta_\eta = 0.08$. Fig. 5.6 shows the corresponding temporal collective dynamics in the last 50 ms. The time series of the mean-field system agree with the bifurcation results, while there are some inconsistencies between the network simulation and the mean-field approximation. These discrepancies may be due to the limitations of the mean field system in accurately representing neural networks with weaker heterogeneity, especially when considering synaptic STP. Some amendments are suggested in [95] to improve the mean-field approximation in such scenarios, although these modifications are somewhat complex. However, Fig. 5.6 still exhibits some different features between the expected EP behavior in the control system (left column) and the expected PO behavior in the muscarinic system (right column). These include a cluster of neurons that alternate between active and static states in the muscarine scenario (right column), in contrast to the comparatively unpredictable activity in the control scenario (left column); larger oscillating amplitudes in the time series of $r(t)$ and $\langle v(t) \rangle$, and the variation of $\langle P(t) \rangle$ in the right column. The subtle distinctions may be partly due to the fast oscillations frequently observed in the inhibitory neural network [70]. We anticipate a more insightful observation if one introduces a slow variable, such as by removing the simplification assumption $\tau_s \to 0$ for $s_j(t)$ and using a relatively larger value of it, or by replacing QIF neurons with Izhikevich neurons, which include an extra slow adaptation variable. As demonstrated in Chapter 3, the interaction between slow-fast

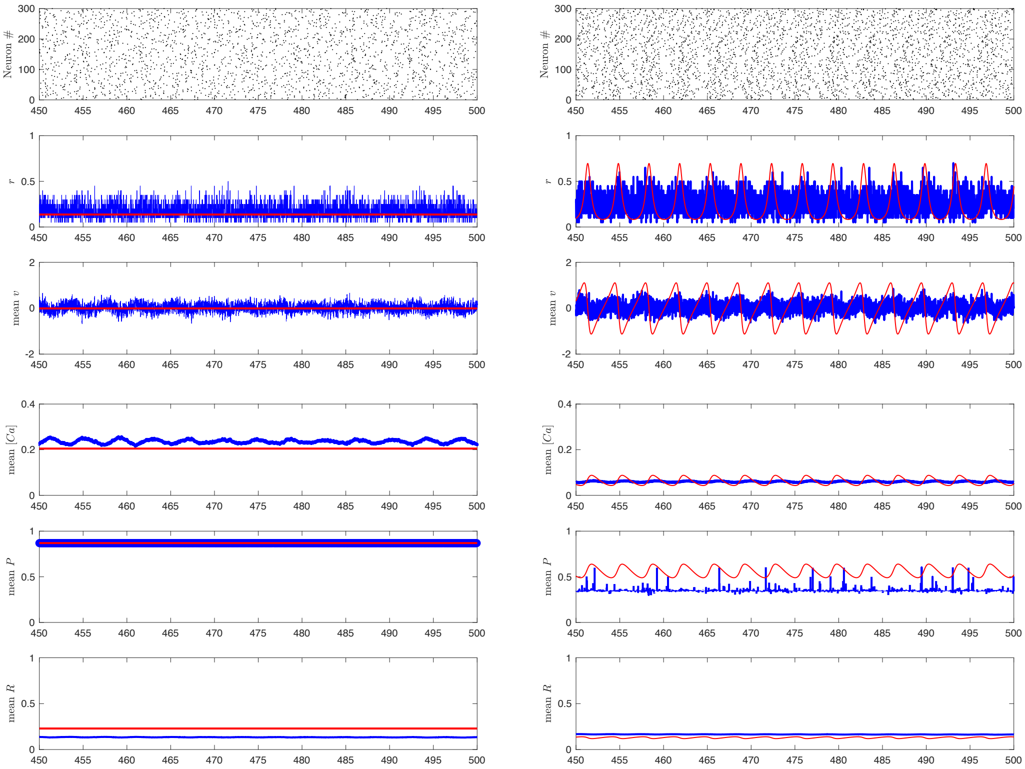

Figure 5.6: Time evolution for the QIF-STP network (5.26) (blue) and the corresponding mean-field model (5.34), (5.35) and (5.41) (red) for the control case $C_{\text{jump}} = 1$ (left column) and the muscarine case $C_{\text{jump}} = 0.17$ (right column). A current $I_{\text{ext}}(t) = 0$ is applied to all neurons. The top row shows the last 50 ms raster plots of 300 randomly selected neurons of $N = 1000$ in the population. The dots correspond to the firing events. The macroscopic variables $r(t)$ (2nd row), $\langle v(t)\rangle$ (3rd row), $\langle C(t)\rangle$ (4th row), $\langle P(t)\rangle$ (5th row) and $\langle R(t)\rangle$ (6th row) are presented, respectively. Parameters: $\bar{\eta} = 1$, $\Delta_\eta = 0.008$ and $J = -30$. Others are given in Tables 5.1 and 5.2.

dynamics is the primary mechanism for generating bursting behaviors, characterized by the alternation between silent and active states with a longer period. We believe that these modifications could facilitate the observation of oscillatory patterns and agreement between the network and our mean-field system. We leave this avenue for future research.

Fig. 5.7 illustrates an additional set of time evolutions of macroscopic variables for the system with moderate heterogeneity $\Delta_\eta = 0.05$ and positive coupling strength $J = 30$ so as

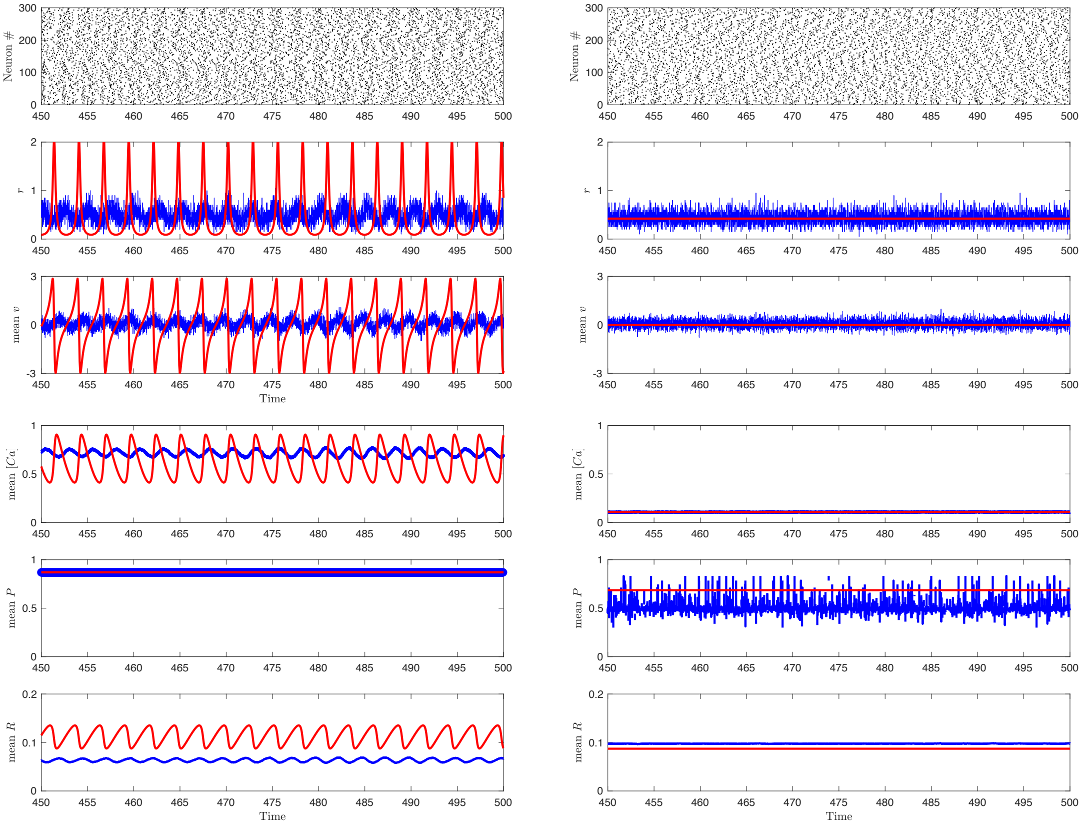

Figure 5.7: Time evolution for the QIF-STP network (5.26) (blue) and the corresponding mean-field model (5.34), (5.35) and (5.41) (red) for the control case $C_{\text{jump}} = 1$ (left column) and the muscarine case $C_{\text{jump}} = 0.17$ (right column). A current $I_{\text{ext}}(t) = 0$ is applied to all neurons. The top row shows the last 50 ms raster plots of 300 randomly selected neurons of $N = 1000$ in the population. The dots correspond to the firing events. The macroscopic variables $r(t)$ (2nd row), $\langle v(t)\rangle$ (3rd row), $\langle C(t)\rangle$ (4th row), $\langle P(t)\rangle$ (5th row) and $\langle R(t)\rangle$ (6th row) are presented, respectively. Parameter values: $\bar{\eta} = 1$, $\Delta_\eta = 0.05$ and $J = 30$. Others are given in Tables 5.1 and 5.2.

to provide more insight into oscillatory behaviors. The muscarinic system (right column) converges to EP, and the mean-field system gives a reliable approximation for the neural network, as anticipated in the bifurcation diagram of Fig. 5.4(c) ($J = 30$). By comparison, the control system (left column) stabilizes at PO, consistent with the anticipation of Fig. 5.4(b) ($J = 30$). Despite discrepancies in the oscillating amplitude between the network model (in blue) and the mean-field approximation (in red), the mean-field model is still capable of capturing oscillations with a frequency consistent with that of the network model. Although it is challenging to distinguish the difference from the raster plot, it is still possible to observe that a cluster of neurons exhibits alternative activity between active and static states in the control scenario in contrast to comparatively random activity in the muscarine scenario, in addition to the different network simulations of $\langle P(t) \rangle$ between the expected mean-field EP in Fig. 5.7 (right column) and PO in Fig. 5.6 (right column). We anticipate a more insightful observation could be achieved using experimentally fitted parameters in a real excitatory network.

At last, we introduce a periodic drive with a relatively slower oscillation than that in Fig. 5.7 to assess the accuracy of the mean-field model in capturing the network's oscillatory behaviors. Fig. 5.8 shows the response of the system to a periodic current $I_{\text{ext}}(t) = I_0 \sin(\omega t)$. Great consistency is exhibited between the network model and the derived mean-field model in all macroscopic variables. The periodic bursting behavior alternates with a quiescent state with $r \approx 0$. An interesting phenomenon was observed in the QIF network without synaptic STP, where a quasi-periodic trajectory was reported in [150]. Further investigation is needed to explore the effect of synaptic STP to the periodic input that comes from other areas of the brain or associates with different rhythms.

5.6 Results and Discussions

We proposed a network model for a population of heterogeneous QIF neurons with calcium-dependent presynaptic STP dynamics inspired by the idea in [132, 195]. This network system captures the central biophysical processes involved in synaptic transmission and integrates various forms of short-term synaptic plasticity, including facilitation, depression, and mixed effects, in a relatively simple mathematical form. Following the theoretical framework of OA theory [163] or the equivalent Lorentzian ansatz [150], we analytically derived a mean-field model, valid in the thermodynamic limit $N \to \infty$. Furthermore, we investigate the STP effect on collective dynamics, particularly by examining the effect of muscarinic activation at inhibitory hippocampal synapses using the parameters fitted for the CA1 PV BC-pyramidal cell synapses in [195]. Our numerical simulations demonstrate satisfactory agreement between the network system and our mean-field model. The introduction of muscarine results in a decreased postsynaptic response, leading to an extended transient oscillating process toward steady state (see Fig. 5.5) and a decreased tendency to oscillate in the excitatory network (see Fig. 5.4). Additionally, it may increase the possibility of the emergence of collective oscillations (COs) in the inhibitory network (see

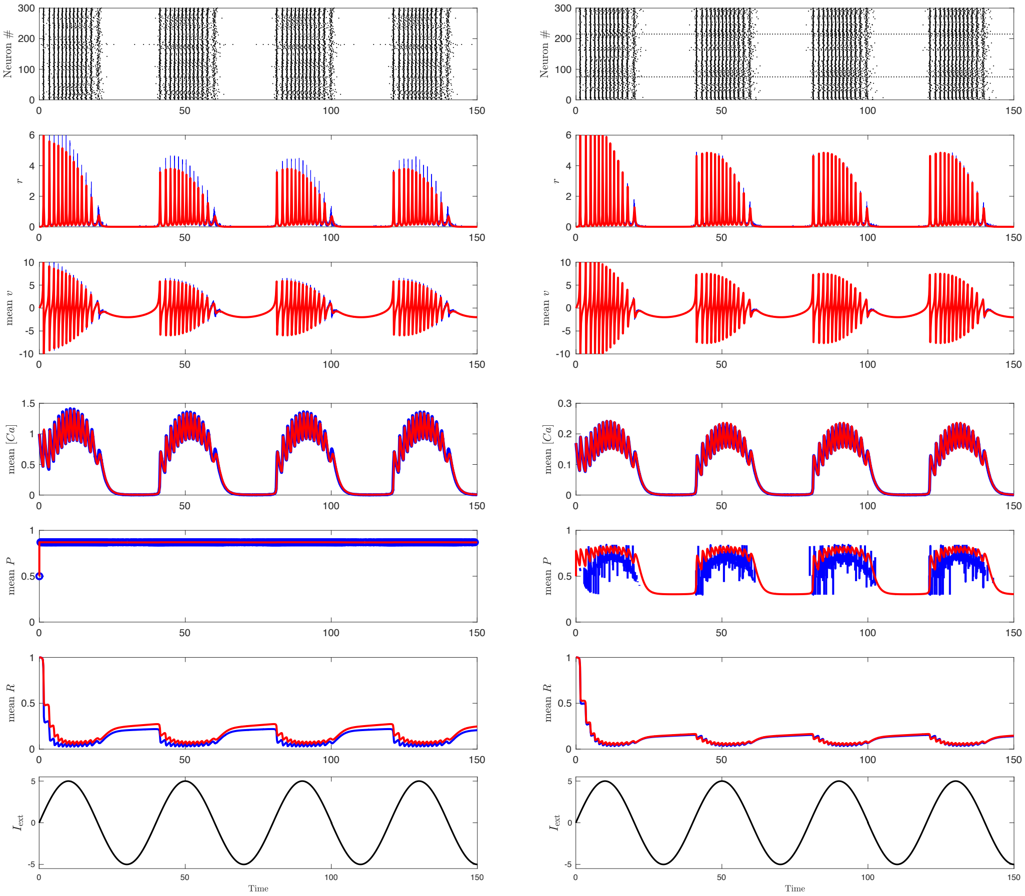

Figure 5.8: Time evolution for the QIF-STP network (5.26) (blue) and the corresponding mean-field model (5.34), (5.35) and (5.41) (red) for the control case $C_{\text{jump}} = 1$ (left column) and the muscarine case $C_{\text{jump}} = 0.17$ (right column). A sinusoidal current is applied to all neurons $I_{\text{ext}}(t) = I_0 \sin(\omega t)$ with $I_0 = 5$, $\omega = \pi/20$. The top row shows raster plots of 300 randomly selected neurons of the $N = 1000$ in the population. The dots correspond to the firing events. The macroscopic variables $r(t)$ (2nd row), $\langle v(t) \rangle$ (3rd row), $\langle C(t) \rangle$ (4th row), $\langle P(t) \rangle$ (5th row) and $\langle R(t) \rangle$ (6th row) are presented, respectively. Parameters: $J = -15$, others are given in Tables 5.1 and 5.2.

Fig. 5.3).

To our knowledge, we were the first to analytically derive the mean-field system ODEs (5.34), (5.35) and (5.41) to represent spiking neural networks with the kinetic STP model. Most studies in the literature are based on the phenomenological synaptic model proposed by Tsodyks and Markram [205], as seen in works such as [188, 95, 198]. However, calcium dynamics plays a crucial role in synaptic plasticity [99, 176, 197] and it is important to investigate the contribution of physiologically defined STP processes to neural networks through experimentally measurable models. Our models reflect biophysical properties, have direct functional implications, and support analysis and comparison with experiment data. Furthermore, muscarine is important in the regulation of numerous physiological processes and its modulation is of great interest in the fields of pharmacology and medical research. Our mean-field framework will greatly facilitate the understanding of its effects in networks, as well as its relevance to both normal and abnormal brain functions.

Chapter 6

Conclusions and Outlook

6.1 Summary and Conclusions

The brain is a complex system, and its functions are the result of the emergent collective dynamics of a large number of interacting neurons. The development of mathematically tractable models with experimentally measurable parameters allows us to understand these collective dynamics associated with both normal functions and neurological disorders from a dynamical system perspective. This thesis revolves around this key idea.

The entire thesis project covers three aspects: mean-field modeling for neural networks with spike frequency adaptation (SFA) (Chapter 3), time delay impact on collective dynamics of such a network with delayed coupling (Chapter 4) and mean-field modeling for neural networks with synaptic short-term plasticity (STP) (Chapter 5). The SFA mechanism and the synaptic time delay are two crucial factors in shaping the collective dynamics of neural networks. In the first two topics, we implemented them in phenomenological models. The SFA mechanism is carried out by introducing a slow variable w into the canonical quadratic integrate-and-fire (QIF) neuron model, thus the Izhikevich neuron (3.2), so as to initiate synchronous bursting behaviors due to the interaction of fast and slow dynamics. In addition, we adopted a phenomenological model for synapses (3.4) and incorporated an explicit time-delay term in the coupling (4.8) to represent non-instantaneous communication between neurons. In the last topic, we integrated a kinetic model for synapses into the network (5.24), which exhibits calcium-dependent STP. This kinetics also implies an implicit time delay between neurons and may influence the spike frequency of postsynaptic neurons.

Consideration of the two-dimensional Izhikevich neuron as the single neural model is a result of balance between neurological plausibility, theoretical/ computational tractability and efficiency for studying large-scale neural networks. It is also a result of the observation that its fast subsystem involves a quadratic form for the membrane potential, like the QIF neuron, allowing the use of the Ott-Antonsen (OA) mean-field theory to obtain an exact macroscopic description for neural networks. For the added slow subsystem, the moment closure method was used to eliminate the dependence of the slow variable on the fast membrane potential, so that it achieved the closure of the mean-field system. Moreover, the interaction of different time-scale processes may induce a synchronous bursting behavior between neurons (e.g., Fig. 3.2(e)), which is one of the important features of cognition and perception and cannot be reproduced in the network of QIF neurons represented only by a one-dimensional system [150]. For connectivity within the neural network, we considered all-to-all coupling. It is reasonable for the application to the CA3 region of the hippocampus in this thesis, as this region is highly recurrently coupled [8, 9, 35]. We can generalize it to sparsely coupled networks using the formalism in [89, 50, 127, 27]. We also considered all-to-all connectivity between two cross-coupled neural networks with strong and weak adaptation and saw the impact on collective dynamics by varying the proportion of neurons of each type (Sec. 3.5).

To validate our proposed mean-field models, we performed a set of numerical experiments to compare with the time evolutions of the full network models. We also discussed the bifurcation agreement between the network system and its mean-field approximation (Fig. 3.2(c) and Fig. 3.3). We examined all the assumptions that were imposed during the derivation (Sec. 3.6). Basically, they are not truly indispensable for the applicability of the developed mean-field models. Some choices are simply mathematical convenience, and insights gained from the macroscopic description are more generally applicable.

Stability influences neural activities, structure, and physiology of the neural system [101]. We performed a linear stability analysis for the mean-field system with a general distributed delay (Sec. 4.3). Theoretical analysis presents considerable challenges, even for the single neuron with delayed feedback, or for the delayed Wilson-Cowan (WC) network composed of phenomenological mean-field models (not shown in this thesis; see our published articles [52, 6]). Therefore, this thesis primarily focused on numerical bifurcation analysis. This technique allows us to deal with the more complex mean-field system, such as incorporating the SFA mechanism and the conductance-based synaptic current (4.2). It also enables us to explore more complicated collective oscillations (COs) induced by higher codimension bifurcations. Our findings revealed a novel mechanism for the emergence of synchronous bursting in the network via a saddle-node bifurcation on invariant circle (SNIC) or homoclinic bifurcation; see Fig. 3.6(c). We also discovered that synaptic delay promotes the emergence of population bursting with two nested frequencies induced by Torus bifurcations, which occurs in a single population of neurons without an external drive; see Fig. 4.7. Furthermore, through perturbation theory and numerical bifurcation analysis, we investigated the OA-based mean-field model in the limit where the heterogeneity approaches zero. It can represent a system with extremely weak heterogeneity. Additionally, interesting transitions appear in addition to the limit of $g_{\text{syn}} \to 0$; see Fig. 4.5 and 4.6. Moreover, our analysis indicated that synaptic delay has little impact on the generation of COs in weakly coupled heterogeneous networks, with this effect becoming more pronounced as heterogeneity increases. Additionally, a larger delay does not necessarily enhance the likelihood of oscillations, especially in a weakly adapting neural network; see Fig. 4.5.

Short-term synaptic plasticity is also a critical factor in shaping neural network activity. An intriguing question is whether integrating presynaptic forms of synaptic plasticity driven by single-neuron activity would still allow for the derivation of mean-field models using the OA theory. Previous studies [188, 95, 198] have employed the phenomenological STP model proposed by Tsodyks and Markram [205]. However, it is important to investigate the contribution of physiologically defined STP processes to neural networks through experimentally measurable models, especially those incorporating calcium dynamics. This exploration forms the crux of our last research topic. To our knowledge, we were the first to propose a macroscopic description analytically derived from the neural network with a kinetic STP model. Through the derived mean-field system, we found that introduction of muscarine results in a decreased postsynaptic response, leading to an extended transient oscillating process towards stationary states and a decreased tendency to oscillate in the excitatory network. Additionally, it may increase the possibility of the emergence of collective oscillations in the inhibitory network. Our mean-field model captures biophysical properties, offers direct functional implications, and facilitates analysis and comparison with experimental data.

Parameter values in this thesis are mainly from the hippocampal CA3 pyramidal neuron data [107, 78] for Chapter 3 and 4, and the hippocampal CA1 GABAergic synapse data [195] for Chapter 5. We performed all numerical simulations using the Euler method for the non-smooth network model with the resetting rule, and ODE45 or DDE23 in MATLAB [145] for the smooth ordinary differential equations (ODEs) or delay differential equations (DDEs) of the mean-field system. We obtained all bifurcation diagrams using the softwares XPPAUT [83] and MATCONT [71] for ODEs and DDE-BIFTOOL [81] for DDEs. Both MATCONT and DDE-BIFTOOL are MATLAB software packages.

6.2 Outlook

The research presented in this thesis opens up a wide range of options worthy of further exploration. The exact mean-field models proposed in this thesis serve as a bridge between neural networks and individual neurons, providing accurate descriptions of synaptic processing in terms of population firing rates and mean membrane potentials. They are particularly well-suited for investigating brain functions and disorders. For instance, drawing from the computational analysis conducted by Rich et al. [181], which involved simulating a network of 500 Izhikevich neurons to explore a hypothesis about seizure initiation, our mean-field model for the Izhikevich network and bifurcation analysis results in Chapter 3 can be utilized to investigate the underlying mechanism of seizure initiation from a theoretical neuroscience perspective. We anticipate that this study will offer guidance on the design of appropriate and efficient experiments to examine this hypothesis. Moreover, the slow-fast nested COs discussed in Chapter 4 offer potential insights into the treatment of pathological brain functions. This treatment essentially involves transitioning the system between synchronous and asynchronous, or the pattern of neural synchronization at different rhythms. For example, according to the hypothesis that the coding information of multiple items is organized by theta-gamma nested oscillations [136, 137], a decrease in the number of coded items indicates a reduction in the effectiveness of neural coding. Ferrara et al. [90] showed in a different model that a higher adaptation intensity, a parameter equivalent to w_{jump} in our model (4.7), can reduce the number of gamma oscillation events within a single theta cycle, thus decreasing neural coding ability. The drug linopirdine (DuP996) has been studied for its potential use in the treatment of conditions such as Alzheimer's disease and ADHD (attention deficit/hyperactivity disorder) [200]. It primarily reduces SFA in pyramidal cells by enhancing the release of the neurotransmitter acetylcholine (ACh) and thus reducing the slow inward potassium current [4]. In addition, the model framework developed in Chapter 5 is suitable to investigate the effects of activation of muscarinic acetylcholine receptors (mAChRs) at synapses. Their modulation is of significant interest in pharmacology and medical research [124, 120, 63] and can be achieved by adjusting the parameter C_{jump} in our mean-field model (5.35) [99].

From a modeling point of view, our study only considered constant delays in the coupling of neural networks. A more sophisticated approach is to integrate a delay plasticity mechanism into the network. It is inspired by evidence showing that axonal white matter exhibits adaptability through learning and behavior [91], and the process of myelination around the axons continues in an activity-dependent manner in the mature neural system [7, 16]. These findings suggest the presence of varying propagation delays. We can account for these phenomena by incorporating a time-varying delay term $\tau(t)$ or equations for state-dependent delays, as discussed in [106]. Derivation of the corresponding mean-field models would be challenging. An initial step could be inspired by the effort of Park et al. [168], where they applied perturbation theory to the Kuramoto network of neural oscillators around a constant baseline delay.

Note that our results on short-term synaptic dynamics are preliminary. Extending the approach in Chapter 5 to the more realistic network model (5.24), such as non-instantaneous synapses and conductance-based synaptic current, rather than the simplified version (5.26), is straightforward. The resulting mean-field system is expected to exhibit richer dynamics, including synaptic facilitation or mixed synaptic effect [195]. Moreover, incorporating parameter values fitted from experimental data, especially for excitatory neural networks, is anticipated to reveal more interesting phenomena. Additionally, the neurotransmitter ACh plays a crucial role in various body functions, such as muscle contraction, learning, and memory [121]. At the microscopic level, it not only contributes to synaptic plasticity, but also induces SFA through muscarinic receptors. Therefore, incorporating SFA via the Izhikevich neuron model into the network with synaptic STP would be a foundational step in exploring the dual effect of ACh on macroscopic network dynamics using the mean-field framework developed in this thesis. Furthermore, we can extend our approach to multiple populations of spiking neurons [53, 199], realistic network topologies [89], networks featuring other or multiple sources of heterogeneity [97, 159].

Letter of Copyright Permission

SPRINGER NATURE LICENSE TERMS AND CONDITIONS

Mar 26, 2024

This Agreement between Liang Chen ("You") and Springer Nature ("Springer Nature") consists of your license details and the terms and conditions provided by Springer Nature and Copyright Clearance Center.

License Number	5756531251512
License date	Mar 26, 2024
Licensed Content Publisher	Springer Nature
Licensed Content Publication	Journal of Computational Neuroscience
Licensed Content Title	Exact mean-field models for spiking neural networks with adaptation
Licensed Content Author	Liang Chen et al
Licensed Content Date	Jul 14, 2022
Type of Use	Thesis/Dissertation
Requestor type	academic/university or research institute
Format	print and electronic
Portion	full article/chapter
Will you be translating?	no
Circulation/distribution	2000 - 4999
Author of this Springer Nature content	yes
Title of new work	Collective Dynamics of Large-Scale Spiking Neural Networks by Mean-Field Theory
Institution name	University of Waterloo
Expected presentation date	May 2024
Order reference number	123
Requestor Location	Liang Chen
Billing Type	
Billing Address	
Total	**0.00 CAD**

Terms and Conditions

Springer Nature Customer Service Centre GmbH Terms and Conditions

The following terms and conditions ("Terms and Conditions") together with the terms specified in your [RightsLink] constitute the License ("License") between you as Licensee and Springer Nature Customer Service Centre GmbH as Licensor. By clicking 'accept' and completing the transaction for your use of the material ("Licensed Material"), you confirm your acceptance of and obligation to be bound by these Terms and Conditions.

1. Grant and Scope of License

1. 1. The Licensor grants you a personal, non-exclusive, non-transferable, non-sublicensable, revocable, world-wide License to reproduce, distribute, communicate to the public, make available, broadcast, electronically transmit or create derivative works using the Licensed Material for the purpose(s) specified in your RightsLink Licence Details only. Licenses are granted for the specific use requested in the order and for no other use, subject to these Terms and Conditions. You acknowledge and agree that the rights granted to you under this License do not include the right to modify, edit, translate, include in collective works, or create derivative works of the Licensed Material in whole or in part unless expressly stated in your RightsLink Licence Details. You may use the Licensed Material only as permitted under this Agreement and will not reproduce, distribute, display, perform, or otherwise use or exploit any Licensed Material in any way, in whole or in part, except as expressly permitted by this License.

1. 2. You may only use the Licensed Content in the manner and to the extent permitted by these Terms and Conditions, by your RightsLink Licence Details and by any applicable laws.

1. 3. A separate license may be required for any additional use of the Licensed Material, e.g. where a license has been purchased for print use only, separate permission must be obtained for electronic re-use. Similarly, a License is only valid in the language selected and does not apply for editions in other languages unless additional translation rights have been granted separately in the License.

1. 4. Any content within the Licensed Material that is owned by third parties is expressly excluded from the License.

1. 5. Rights for additional reuses such as custom editions, computer/mobile applications, film or TV reuses and/or any other derivative rights requests require additional permission and may be subject to an additional fee. Please apply to journalpermissions@springernature.com or bookpermissions@springernature.com for these rights.

2. Reservation of Rights

Licensor reserves all rights not expressly granted to you under this License. You acknowledge and agree that nothing in this License limits or restricts Licensor's rights in or use of the Licensed Material in any way. Neither this License, nor any act, omission, or statement by Licensor or you, conveys any ownership right to you in any Licensed Material, or to any element or portion thereof. As between Licensor and you, Licensor owns and retains all right, title, and interest in and to the Licensed Material subject to the license granted in Section 1.1. Your permission to use the Licensed Material is expressly conditioned on you not impairing Licensor's or the applicable copyright owner's rights in the Licensed Material in any way.

3. Restrictions on use

3. 1. Minor editing privileges are allowed for adaptations for stylistic purposes or formatting purposes provided such alterations do not alter the original meaning or intention of the Licensed Material and the new figure(s) are still accurate and representative of the Licensed Material. Any other changes including but not limited to, cropping, adapting, and/or omitting material that affect the meaning, intention or moral rights of the author(s) are strictly prohibited.

3. 2. You must not use any Licensed Material as part of any design or trademark.

3. 3. Licensed Material may be used in Open Access Publications (OAP), but any such reuse must include a clear acknowledgment of this permission visible at the same time as the figures/tables/illustration or abstract and which must indicate that the Licensed Material is not part of the governing OA license but has been reproduced with permission. This may be indicated according to any standard referencing system but must include at a minimum 'Book/Journal title, Author, Journal Name (if applicable), Volume (if applicable), Publisher, Year, reproduced with permission from SNCSC'.

4. STM Permission Guidelines

4. 1. An alternative scope of license may apply to signatories of the STM Permissions Guidelines ("STM PG") as amended from time to time and made available at https://www.stm-assoc.org/intellectual-property/permissions/permissions-guidelines/.

4. 2. For content reuse requests that qualify for permission under the STM PG, and which may be updated from time to time, the STM PG supersede the terms and conditions contained in this License.

4. 3. If a License has been granted under the STM PG, but the STM PG no longer apply at the time of publication, further permission must be sought from the Rightsholder. Contact journalpermissions@springernature.com or

bookpermissions@springernature.com for these rights.

5. Duration of License

5. 1. Unless otherwise indicated on your License, a License is valid from the date of purchase ("License Date") until the end of the relevant period in the below table:

Reuse in a medical communications project	Reuse up to distribution or time period indicated in License
Reuse in a dissertation/thesis	Lifetime of thesis
Reuse in a journal/magazine	Lifetime of journal/magazine
Reuse in a book/textbook	Lifetime of edition
Reuse on a website	1 year unless otherwise specified in the License
Reuse in a presentation/slide kit/poster	Lifetime of presentation/slide kit/poster. Note: publication whether electronic or in print of presentation/slide kit/poster may require further permission.
Reuse in conference proceedings	Lifetime of conference proceedings
Reuse in an annual report	Lifetime of annual report
Reuse in training/CME materials	Reuse up to distribution or time period indicated in License
Reuse in newsmedia	Lifetime of newsmedia
Reuse in coursepack/classroom materials	Reuse up to distribution and/or time period indicated in license

6. Acknowledgement

6. 1. The Licensor's permission must be acknowledged next to the Licensed Material in print. In electronic form, this acknowledgement must be visible at the same time as the figures/tables/illustrations or abstract and must be hyperlinked to the journal/book's homepage.

6. 2. Acknowledgement may be provided according to any standard referencing system and at a minimum should include "Author, Article/Book Title, Journal name/Book imprint, volume, page number, year, Springer Nature".

7. Reuse in a dissertation or thesis

7. 1. Where 'reuse in a dissertation/thesis' has been selected, the following terms apply: Print rights of the Version of Record are provided for; electronic rights for use only on institutional repository as defined by the Sherpa guideline (www.sherpa.ac.uk/romeo/) and only up to what is required by the awarding institution.

7. 2. For theses published under an ISBN or ISSN, separate permission is required. Please contact journalpermissions@springernature.com or bookpermissions@springernature.com for these rights.

7. 3. Authors must properly cite the published manuscript in their thesis according to current citation standards and include the following acknowledgement: '*Reproduced with permission from Springer Nature*'.

8. License Fee

You must pay the fee set forth in the License Agreement (the "License Fees"). All amounts payable by you under this License are exclusive of any sales, use, withholding, value added or similar taxes, government fees or levies or other assessments. Collection and/or remittance of such taxes to the relevant tax authority shall be the responsibility of the party who has the legal obligation to do so.

9. Warranty

9. 1. The Licensor warrants that it has, to the best of its knowledge, the rights to license reuse of the Licensed Material. **You are solely responsible for ensuring that the material you wish to license is original to the Licensor and does not carry the copyright of another entity or third party (as credited in the published version).** If the credit

line on any part of the Licensed Material indicates that it was reprinted or adapted with permission from another source, then you should seek additional permission from that source to reuse the material.

9. 2. EXCEPT FOR THE EXPRESS WARRANTY STATED HEREIN AND TO THE EXTENT PERMITTED BY APPLICABLE LAW, LICENSOR PROVIDES THE LICENSED MATERIAL "AS IS" AND MAKES NO OTHER REPRESENTATION OR WARRANTY. LICENSOR EXPRESSLY DISCLAIMS ANY LIABILITY FOR ANY CLAIM ARISING FROM OR OUT OF THE CONTENT, INCLUDING BUT NOT LIMITED TO ANY ERRORS, INACCURACIES, OMISSIONS, OR DEFECTS CONTAINED THEREIN, AND ANY IMPLIED OR EXPRESS WARRANTY AS TO MERCHANTABILITY OR FITNESS FOR A PARTICULAR PURPOSE. IN NO EVENT SHALL LICENSOR BE LIABLE TO YOU OR ANY OTHER PARTY OR ANY OTHER PERSON OR FOR ANY SPECIAL, CONSEQUENTIAL, INCIDENTAL, INDIRECT, PUNITIVE, OR EXEMPLARY DAMAGES, HOWEVER CAUSED, ARISING OUT OF OR IN CONNECTION WITH THE DOWNLOADING, VIEWING OR USE OF THE LICENSED MATERIAL REGARDLESS OF THE FORM OF ACTION, WHETHER FOR BREACH OF CONTRACT, BREACH OF WARRANTY, TORT, NEGLIGENCE, INFRINGEMENT OR OTHERWISE (INCLUDING, WITHOUT LIMITATION, DAMAGES BASED ON LOSS OF PROFITS, DATA, FILES, USE, BUSINESS OPPORTUNITY OR CLAIMS OF THIRD PARTIES), AND WHETHER OR NOT THE PARTY HAS BEEN ADVISED OF THE POSSIBILITY OF SUCH DAMAGES. THIS LIMITATION APPLIES NOTWITHSTANDING ANY FAILURE OF ESSENTIAL PURPOSE OF ANY LIMITED REMEDY PROVIDED HEREIN.

10. Termination and Cancellation

10. 1. The License and all rights granted hereunder will continue until the end of the applicable period shown in Clause 5.1 above. Thereafter, this license will be terminated and all rights granted hereunder will cease.

10. 2. Licensor reserves the right to terminate the License in the event that payment is not received in full or if you breach the terms of this License.

11. General

11. 1. The License and the rights and obligations of the parties hereto shall be construed, interpreted and determined in accordance with the laws of the Federal Republic of Germany without reference to the stipulations of the CISG (United Nations Convention on Contracts for the International Sale of Goods) or to Germany´s choice-of-law principle.

11. 2. The parties acknowledge and agree that any controversies and disputes arising out of this License shall be decided exclusively by the courts of or having jurisdiction for Heidelberg, Germany, as far as legally permissible.

11. 3. This License is solely for Licensor's and Licensee's benefit. It is not for the benefit of any other person or entity.

Questions? For questions on Copyright Clearance Center accounts or website issues please contact springernaturesupport@copyright.com or +1-855-239-3415 (toll free in the US) or +1-978-646-2777. For questions on Springer Nature licensing please visit https://www.springernature.com/gp/partners/rights-permissions-third-party-distribution

Other Conditions:

Version 1.4 - Dec 2022

Questions? E-mail us at customercare@copyright.com.

References

[1] L. F. Abbott and W. G. Regehr. Synaptic computation. *Nature*, 431(7010):796–803, 2004.

[2] L. F Abbott and C. van Vreeswijk. Asynchronous states in networks of pulse-coupled oscillators. *Physical Review E*, 48(2):1483, 1993.

[3] L. F. Abbott, J. A. Varela, Kamal Sen, and S. B. Nelson. Synaptic depression and cortical gain control. *Science*, 275(5297):221–224, 1997.

[4] S. P. Aiken, B. J. Lampe, and B. S. Brown. Reduction of spike frequency adaptation and blockade of m-current in rat CA1 pyramidal neurones by linopirdine (dup 996), a neurotransmitter release enhancer. *British Journal of Pharmacology*, 115(7):1163–1168, 1995.

[5] I. Al-Darabsah and S. A. Campbell. A phase model with large time delayed coupling. *Physica D*, 411:132559, 2020.

[6] I. Al-Darabsah, L. Chen, W. Nicola, and S. A. Campbell. The impact of small time delays on the onset of oscillations and synchrony in brain networks. *Frontiers in Systems Neuroscience*, 15:688517–688517, 2021.

[7] R. G. Almeida and D. A. Lyons. On myelinated axon plasticity and neuronal circuit formation and function. *Journal of Neuroscience*, 37(42):10023–10034, 2017.

[8] D. G. Amaral and M. P. Witter. The three-dimensional organization of the hippocampal formation: a review of anatomical data. *Neuroscience*, 31(3):571–591, 1989.

[9] P. Andersen, R. Morris, D. Amaral, T. Bliss, and J. O'Keefe. *The Hippocampus Book*. Oxford university press, 2006.

[10] J. A. Anderson and E. Rosenfeld, editors. *Talking Nets : An Oral History of Neural Networks*. MIT Press, Cambridge, Mass, 1998.

[11] F. Apfaltrer, C. Ly, and D. Tranchina. Population density methods for stochastic neurons with realistic synaptic kinetics: Firing rate dynamics and fast computational methods. *Network: Computation in Neural Systems*, 17(4):373–418, 2006.

[12] J. Aru, J. Aru, V. Priesemann, M. Wibral, L. Lana, G. Pipa, W. Singer, and R. Vicente. Untangling cross-frequency coupling in neuroscience. *Current Opinion in Neurobiology*, 31:51–61, 2015.

[13] F. M. Atay. Distributed delays facilitate amplitude death of coupled oscillators. *Physical Review Letters*, 91(9):094101, 2003.

[14] M. Augustin, J. Ladenbauer, F. Baumann, and K. Obermayer. Low-dimensional spike rate models derived from networks of adaptive integrate-and-fire neurons: Comparison and implementation. *PLOS Computational Biology*, 13(6):e1005545–e1005545, 2017.

[15] A. Bandyopadhyay, C. Bernard, V. Jirsa, and S. Petkoski. Mean-field approximation of network of biophysical neurons driven by conductance-based ion exchange. *bioRxiv*, 2022.

[16] M. E. Bechler, M. Swire, and ffrench Constant C. Intrinsic and adaptive myelination-a sequential mechanism for smart wiring in the brain. *Developmental Neurobiology*, 78(2):68–79, 2018.

[17] Jacques Bélair and Sue Ann Campbell. Stability and bifurcations of equilibria in a multiple-delayed differential equation. *SIAM Journal on Applied Mathematics*, 54(5):1402–1424, 1994.

[18] M. A. Belluscio, K. Mizuseki, R. Schmidt, R. Kempter, and G. Buzsáki. Cross-frequency phase–phase coupling between theta and gamma oscillations in the hippocampus. *Journal of Neuroscience*, 32(2):423–435, 2012.

[19] R. Benavides-Piccione, I. Fernaud-Espinosa, V. Robles, R. Yuste, and J. DeFelipe. Age-based comparison of human dendritic spine structure using complete three-dimensional reconstructions. *Cerebral Cortex*, 23(8):1798–1810, 2013.

[20] J. Benda and J. Tabak. Spike-frequency adaptation. In D. Jaeger and R. Jung, editors, *Encyclopedia of Computational Neuroscience*, pages 2814–2824. Springer New York, New York, NY, 2015.

[21] R. Berner, T. Gross, C. Kuehn, J. Kurths, and S. Yanchuk. Adaptive dynamical networks. *Physics Reports*, 1031:1–59, 2023.

[22] R. Bertram, M. J. Butte, T. Kiemel, and A. Sherman. Topological and phenomenological classification of bursting oscillations. *Bulletin of Mathematical Biology*, 57(3):413–439, 1995.

[23] R. Bertram and J. E. Rubin. Multi-timescale systems and fast-slow analysis. *Mathematical Biosciences*, 287:105–121, 2017.

[24] R. Bertram, A. Sherman, and E. F. Stanley. Single-domain/bound calcium hypothesis of transmitter release and facilitation. *Journal of Neurophysiology*, 75(5):1919–1931, 1996.

[25] R. L. Beurle. Properties of a mass of cells capable of regenerating pulses. *Philosophical Transactions of the Royal Society of London. Series B, Biological Sciences*, 240(669):55–94, 1956.

[26] J. Bezanson, S. Karpinski, V. B. Shah, and A. Edelman. Julia: A fast dynamic language for technical computing. *arXiv:1209.5145*, 2012.

[27] H. Bi, M. di Volo, and A. Torcini. Asynchronous and coherent dynamics in balanced excitatory-inhibitory spiking networks. *Frontiers in Systems Neuroscience*, 15:752261–752261, 2021.

[28] C. Bick, M. Goodfellow, C. R. Laing, and E. A. Martens. Understanding the dynamics of biological and neural oscillator networks through exact mean-field reductions: a review. *Journal of Mathematical Neuroscience*, 10:9, 2020.

[29] D. M. Blitz, K. A. Foster, and W. G. Regehr. Short-term synaptic plasticity: a comparison of two synapses. *Nature Reviews Neuroscience*, 5(8):630–640, 2004.

[30] J. M. Bower and D. Beeman. *The Book of GENESIS: Exploring Realistic Neural Models with the GEneral NEural SImulation System.* Springer-Verlag, New York, 1998.

[31] P. C. Bressloff. Spatiotemporal dynamics of continuum neural fields. *Journal of Physics A, Mathematical and Theoretical*, 45(3):033001, 2012.

[32] R. Brette and W. Gerstner. Adaptive exponential integrate-and-fire model as an effective description of neuronal activity. *Journal of Neurophysiology*, 94(5):3637–3642, 2005.

[33] J. L. Butler, P. R. F. Mendonça, H. P. C. Robinson, and O. Paulsen. Intrinsic cornu ammonis area 1 theta-nested gamma oscillations induced by optogenetic theta frequency stimulation. *Journal of Neuroscience*, 36(15):4155–4169, 2016.

[34] G. Buzsáki. *Rhythms of the Brain*. Oxford University Press, Oxford, UK, 2006.

[35] G. Buzsáki. Hippocampus. *Scholarpedia*, 6(1):1468, 2011.

[36] G. Buzsáki and A. Draguhn. Neuronal oscillations in cortical networks. *Science*, 304(5679):1926–1929, 2004.

[37] G. Buzsáki and X. Wang. Mechanisms of gamma oscillations. *Annual Review of Neuroscience*, 35(1):203–225, 2012.

[38] Á. Byrne, D. Avitabile, and S. Coombes. Next-generation neural field model: the evolution of synchrony within patterns and waves. *Physical Review E*, 99(1-1):012313–012313, 2019.

[39] Á. Byrne, R. D. O'Dea, M. Forrester, J. Ross, and S. Coombes. Next-generation neural mass and field modeling. *Journal of Neurophysiology*, 123(2):726–742, 2020.

[40] Á. Byrne, J. Ross, R. Nicks, and S. Coombes. Mean-field models for EEG/MEG: from oscillations to waves. *Brain Topography*, 35(1):36–53, 2022.

[41] C. Cakan and K. Obermayer. Biophysically grounded mean-field models of neural populations under electrical stimulation. *PLOS Computational Biology*, 16(4):1–30, 04 2020.

[42] C. Cakan and K. Obermayer. Correction: Biophysically grounded mean-field models of neural populations under electrical stimulation. *PLOS Computational Biology*, 17(2):1–3, 02 2021.

[43] S. A. Campbell. Time delays in neural systems. In Viktor K. Jirsa and AR McIntosh, editors, *Handbook of Brain Connectivity*, pages 65–90. Springer Berlin Heidelberg, 2007.

[44] S. A. Campbell and Z. Wang. Phase models and clustering in networks of oscillators with delayed coupling. *Physica D*, 363:44–55, 2018.

[45] Sue Ann Campbell, Jacques Belair, Toru Ohira, and John Milton. Complex dynamics and multistability in a damped harmonic oscillator with delayed negative feedback. *Chaos: An Interdisciplinary Journal of Nonlinear Science*, 5(4):640–645, 1995.

[46] R. T. Canolty and R. T. Knight. The functional role of cross-frequency coupling. *Trends in Cognitive Sciences*, 14(11):506–515, 2010.

[47] M. Carlu, O. Chehab, L. Dalla Porta, D. Depannemaecker, C. Héricé, M. Jedynak, E. Köksal Ersöz, P. Muratore, S. Souihel, C. Capone, Y. Zerlaut, A. Destexhe, and M. di Volo. A mean-field approach to the dynamics of networks of complex neurons, from nonlinear integrate-and-fire to Hodgkin-Huxley models. *Journal of Neurophysiology*, 123(3):1042–1051, 2020.

[48] A. Ceni, S. Olmi, A. Torcini, and D. Angulo-Garcia. Cross frequency coupling in next generation inhibitory neural mass models. *Chaos: An Interdisciplinary Journal of Nonlinear Science*, 30(5):053121, 2020.

[49] R. Cestnik and A. Pikovsky. Exact finite-dimensional reduction for a population of noisy oscillators and its link to Ott–Antonsen and Watanabe–Strogatz theories. *Chaos: An Interdisciplinary Journal of Nonlinear Science*, 32(11):113126, 2022.

[50] S. Chandra, D. Hathcock, K. Crain, T. M. Antonsen, M. Girvan, and E. Ott. Modeling the network dynamics of pulse-coupled neurons. *Chaos*, 27(3):033102, 2017.

[51] T. R. Chay and D. L. Cook. Endogenous bursting patterns in excitable cells. *Mathematical Biosciences*, 90(1-2):139–153, 1988.

[52] L. Chen and S. A. Campbell. Hysteresis bifurcation and application to delayed FitzHugh-Nagumo neural systems. *Journal of Mathematical Analysis and Applications*, 500(1):125–151, 2021.

[53] L. Chen and S. A. Campbell. Exact mean-field models for spiking neural networks with adaptation. *Journal of Computational Neuroscience*, 50(5):445–469, 2022.

[54] L. Chen and S. A. Campbell. Synaptic delay induced macroscopic dynamics of the large-scale network of Izhikevich neurons. *arXiv*, 2310.04596, 2023.

[55] M. Ciszak, S. Olmi, G. Innocenti, A. Torcini, and F. Marino. Collective canard explosions of globally-coupled rotators with adaptive coupling. *Chaos, Solitons and Fractals*, 153:111592, 2021.

[56] A. Citri and R. C. Malenka. Synaptic plasticity: Multiple forms, functions, and mechanisms. *Neuropsychopharmacology*, 33(1):18–41, 2008.

[57] Pau Clusella and Ernest Montbrió. Exact low-dimensional description for fast neural oscillations with low firing rates. *Physical Review E*, 109(1):014229, 2024.

[58] L. L. Colgin, T. Denninger, M. Fyhn, T. Hafting, T. Bonnevie, O. Jensen, M. Moser, and E. I. Moser. Frequency of gamma oscillations routes flow of information in the hippocampus. *Nature*, 462:353–357, 2009.

[59] S. Coombes and Á. Byrne. Next generation neural mass models. In F. Corinto and A. Torcini, editors, *Nonlinear Dynamics in Computational Neuroscience*, pages 1–16. Springer, Cham, 2019.

[60] S. Coombes, P. beim Graben, R. Potthast, and J. Wright, editors. *Neural Fields Theory and Applications*. Springer, Berlin, 2014.

[61] S. Coombes and G. J. Lord. Intrinsic modulation of pulse-coupled integrate-and-fire neurons. *Physical Review E*, 56:5809–5818, Nov 1997.

[62] J. J Crofts, M Forrester, and R. D O'Dea. Structure-function clustering in multiplex brain networks. *Europhysics Letters*, 116(1):18003, 2016.

[63] B. Dean, G. Bakker, H. R. Ueda, A. B. Tobin, A. Brown, and R. A. A. Kanaan. A growing understanding of the role of muscarinic receptors in the molecular pathology and treatment of schizophrenia. *Frontiers in Cellular Neuroscience*, 17, 2023.

[64] G. Deco, V. K. Jirsa, P. A. Robinson, M. Breakspear, and K. Friston. The dynamic brain: from spiking neurons to neural masses and cortical fields. *PLOS Computational Biology*, 4(8):e1000092–e1000092, 2008.

[65] A. Destexhe, Z. F. Mainen, and T. J. Sejnowski. An efficient method for computing synaptic conductances based on a kinetic model of receptor binding. *Neural Computation*, 6(1):14–18, 1994.

[66] A. Destexhe, Z. F. Mainen, and T. J. Sejnowski. Synthesis of models for excitable membranes, synaptic transmission and neuromodulation using a common kinetic formalism. *Journal of Computational Neuroscience*, 1:195–230, 1994.

[67] A. Destexhe, Z. F. Mainen, and T. J. Sejnowski. Kinetic models of synaptic transmission. In Christof Koch and Idan Segev, editors, *Methods in Neuronal Modeling: From Ions to Networks*. MIT Press, 1998.

[68] A. Destexhe and T. J. Sejnowski. The Wilson-Cowan model, 36 years later. *Biological Cybernetics*, 101(1):1–2, 2009.

[69] F. Devalle, E. Montbrió, and D. Pazó. Dynamics of a large system of spiking neurons with synaptic delay. *Physical Review E*, 98:042214, 2018.

[70] F. Devalle, A. Roxin, and E. Montbrió. Firing rate equations require a spike synchrony mechanism to correctly describe fast oscillations in inhibitory networks. *PLOS Computational Biology*, 13(12):e1005881–e1005881, 2017.

[71] A. Dhooge, W. Govaerts, l. A. Kuznetsov, H. G. E. Meijer, and B. Sautois. New features of the software matcont for bifurcation analysis of dynamical systems. *Mathematical and Computer Modelling of Dynamical Systems*, 14(2):147–175, 2008.

[72] M. di Volo and A. Destexhe. Optimal responsiveness and information flow in networks of heterogeneous neurons. *Scientific Reports*, 11:17611, 2021.

[73] M. di Volo, A. Romagnoni, C. Capone, and A. Destexhe. Biologically realistic mean-field models of conductance-based networks of spiking neurons with adaptation. *Neural Computation*, 31(4):653–680, 2019.

[74] J. S. Dittman, A. C. Kreitzer, and W. G. Regehr. Interplay between facilitation, depression, and residual calcium at three presynaptic terminals. *Journal of Neuroscience*, 20(4):1374–1385, 2000.

[75] J. S. Dittman and W. G. Regehr. Calcium dependence and recovery kinetics of presynaptic depression at the climbing fiber to purkinje cell synapse. *Journal of Neuroscience*, 18(16):6147–6162, 1998.

[76] G. Dumont, G. B. Ermentrout, and B. Gutkin. Macroscopic phase-resetting curves for spiking neural networks. *Physical Review E*, 96(4-1):042311, 2017.

[77] G. Dumont and B. Gutkin. Macroscopic phase resetting-curves determine oscillatory coherence and signal transfer in inter-coupled neural circuits. *PLOS Computational Biology*, 15(5):e1007019, 2019.

[78] M. Dur-e-Ahmad, W. Nicola, S. A. Campbell, and F. K. Skinner. Network bursting using experimentally constrained single compartment CA3 hippocampal neuron models with adaptation. *Journal of Computational Neuroscience*, 33(1):21–40, 2012.

[79] S. El Boustani and A. Destexhe. A master equation formalism for macroscopic modeling of asynchronous irregular activity states. *Neural Computation*, 21(1):46–100, 2009.

[80] A. K. Engel and W. Singer. Temporal binding and the neural correlates of sensory awareness. *Trends in Cognitive Sciences*, 5(1):16–25, 2001.

[81] K. Engelborghs, T. Luzyanina, and D. Roose. Numerical bifurcation analysis of delay differential equations using dde-biftool. *ACM Transactions on Mathematical Software*, 28(1):1–21, 2002.

[82] B. Ermentrout. Type I membranes, phase resetting curves, and synchrony. *Neural Computation*, 8(5):979–1001, 1996.

[83] B. Ermentrout. *Simulating, Analyzing, and Animating Dynamical Systems: A Guide to XPPAUT for Research and Students*. SIAM, Philadephia, USA, 2002.

[84] B. Ermentrout and T. Ko. Delays and weakly coupled neuronal oscillators. *Philosophical Transactions of the Royal Society A: Mathematical, Physical and Engineering Sciences*, 367(1891):1097–1115, 2009.

[85] B. Ermentrout and N. Kopell. Parabolic bursting in an excitable system coupled with a slow oscillation. *SIAM Journal on Applied Mathematics*, 46(2):233–253, 1986.

[86] B. Ermentrout, M. Pascal, and B. Gutkin. The effects of spike frequency adaptation and negative feedback on the synchronization of neural oscillators. *Neural Computation*, 13(6):1285–1310, 2001.

[87] B. Ermentrout, J. Rubin, and R. Osan. Regular traveling waves in a one-dimensional network of theta neurons. *SIAM Journal on Applied Mathematics*, 62(4):1197–1221, 2002.

[88] B. Ermentrout and D. H Terman. *Mathematical Foundations of Neuroscience*, volume 35 of *Interdisciplinary Applied Mathematics*. Springer, New York, 2010.

[89] K. A. Ferguson, F. Njap, W. Nicola, F. K. Skinner, and S. A. Campbell. Examining the limits of cellular adaptation bursting mechanisms in biologically-based excitatory networks of the hippocampus. *Journal of Computational Neuroscience*, 39(3):289–309, 2015.

[90] A. Ferrara, D. Angulo-Garcia, A. Torcini, and S. Olmi. Population spiking and bursting in next-generation neural masses with spike-frequency adaptation. *Physical Review E*, 107:024311, Feb 2023.

[91] R. D. Fields. A new mechanism of nervous system plasticity: activity-dependent myelination. *Nature Reviews Neuroscience*, 16(12):756–767, 2015.

[92] H. Fitz, M. Uhlmann, D. van den Broek, R. Duarte, P. Hagoort, and K. M. Petersson. Neuronal spike-rate adaptation supports working memory in language processing. *Proceedings of the National Academy of Sciences*, 117(34):20881–20889, 2020.

[93] R. FitzHugh. Impulses and physiological states in theoretical models of nerve membrane. *Biophysical Journal*, 1(6):445–466, 1961.

[94] E. S. Fortune and G. J. Rose. Short-term synaptic plasticity as a temporal filter. *Trends in Neurosciences*, 24(7):381–385, 2001.

[95] R. Gast, T. R. Knösche, and H. Schmidt. Mean-field approximations of networks of spiking neurons with short-term synaptic plasticity. *Physical Review E*, 104(4):044310, 2021.

[96] R. Gast, H. Schmidt, and T. R. Knösche. A mean-field description of bursting dynamics in spiking neural networks with short-term adaptation. *Neural Computation*, 32(9):1615–1634, 2020.

[97] R. Gast, S. A. Solla, and A. Kennedy. Macroscopic dynamics of neural networks with heterogeneous spiking thresholds. *Physical Review E*, 107(2):024306, 2023.

[98] W. Gerstner and W. M. Kistler. *Spiking neuron models: Single neurons, populations, plasticity.* Cambridge University Press, 2002.

[99] J. C. González, G. Lignani, M. Maroto, P. Baldelli, and J.M. Hernández-Guijo. Presynaptic muscarinic receptors reduce synaptic depression and facilitate its recovery at hippocampal GABAergic synapses. *Cerebral Cortex*, 24(7):1818–1831, 2014.

[100] D. F. M. Goodman and R. Brette. The brian simulator. *Frontiers in Neuroscience*, 3, 2009.

[101] R. T. Gray and P. A. Robinson. Stability constraints on large-scale structural brain networks. *Frontiers in Computational Neuroscience*, 7:31, 2013.

[102] J. Guckenheimer and P. J. Holmes. *Nonlinear Oscillations, Dynamical Systems and Bifurcations of Vector Fields.* Springer-Verlag, New York, 1983.

[103] G. J. Gutierrez and S. Denève. Population adaptation in efficient balanced networks. *eLife*, 8, 2019.

[104] B. Gutkin. Theta neuron model. In Dieter Jaeger and Ranu Jung, editors, *Encyclopedia of Computational Neuroscience*, pages 3412–3419. Springer New York, 2022.

[105] G. Hahn, A. Ponce-Alvarez, G. Deco, A. Aertsen, and A. Kumar. Portraits of communication in neuronal networks. *Nature Reviews Neuroscience*, 20:117–127, 2019.

[106] F. Hartung, T. Krisztin, H. Walther, and J. Wu. Chapter 5 functional differential equations with state-dependent delays: Theory and applications. In A. CaÑada, P. DrÁbek, and A. Fonda, editors, *Handbook of Differential Equations: Ordinary Differential Equations*, volume 3, pages 435–545. North-Holland, 2006.

[107] P. Hemond, D. Epstein, A. Boley, M. Migliore, G. A. Ascoli, and D. B. Jaffe. Distinct classes of pyramidal cells exhibit mutually exclusive firing patterns in hippocampal area CA3b. *Hippocampus*, 18(4):411–424, 2008.

[108] M. H. Hennig. Theoretical models of synaptic short term plasticity. *Frontiers in Computational Neuroscience*, 7:45, 2013.

[109] M. L. Hines and N. T. Carnevale. The neuron simulation environment. *Neural Computation*, 9(6):1179–1209, 1997.

[110] J. Hlinka and S. Coombes. Using computational models to relate structural and functional brain connectivity. *European Journal of Neuroscience*, 36(2):2137–2145, 2012.

[111] A. L. Hodgkin and A. F. Huxley. A quantitative description of membrane current and its application to conduction and excitation in nerve. *The Journal of Physiology*, 117(4):500–544, August 1952.

[112] N. Hosoi, T. Sakaba, and E. Neher. Quantitative analysis of calcium-dependent vesicle recruitment and its functional role at the calyx of held synapse. *Journal of Neuroscience*, 27(52):14286–14298, 2007.

[113] M. D. Humphries, R. Wood, and K. Kevin Gurney. Dopamine-modulated dynamic cell assemblies generated by the gabaergic striatal microcircuit. *Neural Networks*, 22(8):1174–1188, 2009.

[114] E. M. Izhikevich. Neural excitability, spiking and bursting. *International Journal of Bifurcation and Chaos*, 10(6):1171–1266, 2000.

[115] E. M. Izhikevich. Simple model of spiking neurons. *IEEE Transactions on Neural Networks*, 14(6):1569–1572, 2003.

[116] E. M. Izhikevich. Which model to use for cortical spiking neurons? *IEEE Transactions on Neural Networks*, 15(5):1063–1070, 2004.

[117] E. M. Izhikevich. *Dynamical Systems in Neuroscience: the geometry of excitability and bursting.* Computational neuroscience. MIT Press, Cambridge, 2007.

[118] E. M. Izhikevich and G. M. Edelman. Large-scale model of mammalian thalamocortical systems. *Proceedings of the national academy of sciences*, 105(9):3593–3598, 2008.

[119] B. H. Jansen and V. G. Rit. Electroencephalogram and visual evoked potential generation in a mathematical model of coupled cortical columns. *Biological Cybernetics*, 73(4):357–366, 1995.

[120] C. R. Johnson, B. D. Kangas, E. M. Jutkiewicz, J. Bergman, and A. Coop. Drug design targeting the muscarinic receptors and the implications in central nervous system disorders. *Biomedicines*, 10(2):398, 2022.

[121] E. R. Kandel, J. D. Koester, S. H. Mack, and S. A. Siegelbaum. *Principles of Neural Science.* McGraw-Hill, New York, 6th edition, 2021.

[122] Z. P. Kilpatrick and B. Ermentrout. Sparse gamma rhythms arising through clustering in adapting neuronal networks. *PLOS Computational Biology*, 7(11):e1002281–e1002281, 2011.

[123] V. Klinshov, S. Kirillov, and V. Nekorkin. Reduction of the collective dynamics of neural populations with realistic forms of heterogeneity. *Physical Review E*, 103:L040302, Apr 2021.

[124] A. Kruse, B. Kobilka, D. Gautam, Patrick M. Sexton, Arthur Christopoulos, and Jürgen Wess. Muscarinic acetylcholine receptors: novel opportunities for drug development. *Nature Reviews Drug Discovery*, 13:549–560, 2014.

[125] Y. A. Kuznetsov. *Elements of Applied Bifurcation Theory (4th Ed.).* Springer, 2023.

[126] C. R. Laing. The dynamics of networks of identical theta neurons. *Journal of Mathematical Neuroscience*, 8(1):1–24, 2018.

[127] C. R. Laing and C. Bläsche. The effects of within-neuron degree correlations in networks of spiking neurons. *Biological Cybernetics*, 114(3):337–347, 2020.

[128] P. E. Latham, B. J. Richmond, P. G. Nelson, and S. Nirenberg. Intrinsic dynamics in neuronal networks. i. theory. *Journal of Neurophysiology*, 83(2):808–827, 2000.

[129] S. B. Laughlin and T. J. Sejnowski. Communication in neuronal networks. *Science*, 301(5641):1870–1874, 2003.

[130] M. Layer, J. Senk, S. Essink, A. van Meegen, H. Bos, and M. Helias. NNMT: Mean-field based analysis tools for neuronal network models. *Frontiers in Neuroinformatics*, 16, 2022.

[131] V. G. LeBlanc and W. F. Langford. Classification and unfoldings of 1:2 resonant Hopf bifurcation. *Archive for Rational Mechanics and Analysis*, 136:305–357, 1996.

[132] C. J. Lee, M. Anton, C. Poon, and G. J. McRae. A kinetic model unifying presynaptic short-term facilitation and depression. *Journal of Computational Neuroscience*, 26(3):459–473, 2009.

[133] W. S. Lee, E. Ott, and T. M. Antonsen. Large coupled oscillator systems with heterogeneous interaction delays. *Physical Review Letters*, 103(4):044101, 2009.

[134] A. W. Liley and K. A. North. An electrical investigation of effects of repetitive stimulation on mammalian neuromuscular junction. *Journal of Neurophysiology*, 16(5):509–527, 1953.

[135] D. T. J. Liley, P. J. Cadusch, and M. P. Dafilis. A spatially continuous mean field theory of electrocortical activity. *Network: Computationsal in Neural Systems*, 13(1):67–113, 2002.

[136] J. E. Lisman and G. Buzsáki. A neural coding scheme formed by the combined function of gamma and theta oscillations. *Schizophrenia Bulletin*, 34(5):974–980, 2008.

[137] J. E. Lisman and O. Jensen. The theta-gamma neural code. *Neuron*, 77(6):1002–1016, 2013.

[138] T. Lu and L. O. Trussell. Inhibitory transmission mediated by asynchronous transmitter release. *Neuron*, 26(3):683–694, 2000.

[139] M. Lukoševičius and H. Jaeger. Reservoir computing approaches to recurrent neural network training. *Computer Science Review*, pages 127–149, 2009.

[140] C. Ly and D. Tranchina. Critical analysis of dimension reduction by a moment closure method in a population density approach to neural network modeling. *Neural Computation*, 19(8):2032–2092, 2007.

[141] R. Maex and E. De Schutter. Resonant synchronization in heterogeneous networks of inhibitory neurons. *Journal of Neuroscience*, 23(33):10503–10514, 2003.

[142] J. C. Magee and C. Grienberger. Synaptic plasticity forms and functions. *Annual Review of Neuroscience*, 43:95–117, 2020.

[143] H. Markram. The blue brain project. *Nature Reviews. Neuroscience*, 7(2):153–160, 2006.

[144] H. Markram and M. Tsodyks. Redistribution of synaptic efficacy between neocortical pyramidal neurons. *Nature*, 382(6594):807–810, 1996.

[145] The Mathworks, Inc., Natick, Massachusetts, United States. *MATLAB version: 9.13.0 (R2022b)*, 2022.

[146] S. McKennoch, T. Voegtlin, and L. Bushnell. Spike-timing error backpropagation in theta neuron networks. *Neural Computation*, 21(1):9–45, 2009.

[147] M. Michael Okun, A. Naim, and I. Lampl. The subthreshold relation between cortical local field potential and neuronal firing unveiled by intracellular recordings in awake rats. *Journal of Neuroscience*, 30(12):4440–4448, 2010.

[148] M. B. Monagan, K. O. Geddes, K. M. Heal, G. Labahn, S. M. Vorkoetter, J. S. Devitt, M. L. Hansen, D. Redfern, K. M. Rickard, et al. *Maple V Programming Guide: For Release 5.* Springer Science & Business Media, 2012.

[149] G. Mongillo, O. Barak, and M. Tsodyks. Synaptic theory of working memory. *Science (New York, N.Y.)*, 319(5869):1543–1546, 2008.

[150] E. Montbrió, D. Pazó, and A. Roxin. Macroscopic description for networks of spiking neurons. *Physical Review X*, 5:021028, Jun 2015.

[151] Ernest Montbrió and Diego Pazó. Exact mean-field theory explains the dual role of electrical synapses in collective synchronization. *Physical Review Letters*, 125(24):248101, 2020.

[152] M. Monteforte and F. Wolf. Dynamical entropy production in spiking neuron networks in the balanced state. *Physical Review Letters*, 105:268104, Dec 2010.

[153] S. A. Moosavi1, V. K. Jirsa, and W. Truccolo. Critical dynamics in the spread of focal epileptic seizures: Network connectivity, neural excitability and phase transitions. *PLOS ONE*, 17(8):e0272902, 2022.

[154] R. Moran, D. A. Pinotsis, and K. Friston. Neural masses and fields in dynamic causal modeling. *Frontiers in Computational Neuroscience*, 7:57, 2013.

[155] C. Morris and H. Lecar. Voltage oscillations in the barnacle giant muscle fiber. *Biophysical Journal*, 35(1):193–213, 1981.

[156] R. Naud, N. Marcille, C. Clopath, and W. Gerstner. Firing patterns in the adaptive exponential integrate-and-fire model. *Biological Cybernetics*, 99(4):335–347, 2008.

[157] W. H. Nesse, A. Borisyuk, and P. C. Bressloff. Fluctuation-driven rhythmogenesis in an excitatory neuronal network with slow adaptation. *Journal of Computational Neuroscience*, 25(2):317–333, 2008.

[158] W. Nicola and S. A. Campbell. Bifurcations of large networks of two-dimensional integrate and fire neurons. *Journal of Computational Neuroscience*, 35(1):87–108, 2013.

[159] W. Nicola and S. A. Campbell. Mean-field models for heterogeneous networks of two-dimensional integrate and fire neurons. *Frontiers in Computational Neuroscience*, 7:184, 2013.

[160] D. Q. Nykamp and D. Tranchina. A population density approach that facilitates large-scale modeling of neural networks: Analysis and an application to orientation tuning. *Journal of Computational Neuroscience*, 8(1):19–50, 2000.

[161] A. Omurtag, B. W. Knight, and L. Sirovich. On the simulation of large populations of neurons. *Journal of Computational Neuroscience*, 8(1):51–63, 2000.

[162] R. Osan and B. Ermentrout. Two dimensional synaptically generated traveling waves in a theta-neuron neural network. *Neurocomputing*, 38-40:789–795, 2001. Computational Neuroscience: Trends in Research 2001.

[163] E. Ott and T. M. Antonsen. Low dimensional behavior of large systems of globally coupled oscillators. *Chaos*, 18(3):037113, 2008.

[164] E. Ott and T. M. Antonsen. Long time evolution of phase oscillator systems. *Chaos*, 19(2):023117, 2009.

[165] E. Ott, B. R. Hunt, and T. M. Antonsen. Comment on “long time evolution of phase oscillator systems” [chaos 19, 023117 (2009)]. *Chaos*, 21(2):025112, 2011.

[166] B. Pakkenberg and H. J. Gundersen. Neocortical neuron number in humans: effect of sex and age. *The Journal of Comparative Neurology*, 384(2):312–320, 1997.

[167] G. Palkar, J. Wu, and B. Ermentrout. The inhibitory control of traveling waves in cortical networks. *PLOS Computational Biology*, 19(9):e1010697, 2023.

[168] S. H. Park and J. Lefebvre. Synchronization and resilience in the kuramoto white matter network model with adaptive state-dependent delays. *Journal of Mathematical Neuroscience*, 10(1):16–16, 2020.

[169] D. Pazó and E. Montbrió. From quasiperiodic partial synchronization to collective chaos in populations of inhibitory neurons with delay. *Physical Review Letters*, 116:238101, 2016.

[170] S. E. Petersen and O. Sporns. Brain networks and cognitive architectures. *Neuron*, 88(1):207–219, 2015.

[171] J. Pfister, P. Dayan, and M. Lengyel. Synapses with short-term plasticity are optimal estimators of presynaptic membrane potentials. *Nature Neuroscience*, 13(10):1271–1275, 2010.

[172] B. Pietras, R. Cestnik, and A. Pikovsky. Exact finite-dimensional description for networks of globally coupled spiking neurons. *Physical Review E*, 107:024315, 2023.

[173] A. Pikovsky and M. Rosenblum. Partially integrable dynamics of hierarchical populations of coupled oscillators. *Physical Review Letters*, 101(26):264103, 2008.

[174] A. Pikovsky and M. Rosenblum. Dynamics of heterogeneous oscillator ensembles in terms of collective variables. *Physica D: Nonlinear Phenomena*, 240(9):872–881, 2011.

[175] V. Pyragas and K. Pyragas. Dynamics of a network of quadratic integrate-and-fire neurons with bimodal heterogeneity. *Physics letters A*, 416:127677–, 2021.

[176] B. M. Radu, A. M. M. Osculati, and E. et al. Suku. All muscarinic acetylcholine receptors (m1-m5) are expressed in murine brain microvascular endothelium. *Scientific Reports*, page 5083, 2017.

[177] W Rall. Distinguishing theoretical synaptic potentials computed for different soma-dendritic distributions of synaptic input. *Journal of Neurophysiology*, 30(5):1138–1168, 1967.

[178] I. Ratas and K. Pyragas. Macroscopic oscillations of a quadratic integrate-and-fire neuron network with global distributed-delay coupling. *Physical Review E*, 98(5):052224, 2018.

[179] D. V. R. Reddy, A. Sen, and G. L. Johnston. Time delay induced death in coupled limit cycle oscillators. *Physical Review Letters*, 80(23):5109, 1998.

[180] C. Reis, A. Sharott, P. J. Magill, B. C. M. van Wijk, T. Parr, P. Zeidman, K. J. Friston, and H. Cagnan. Thalamocortical dynamics underlying spontaneous transitions in beta power in parkinsonism. *NeuroImage*, 193:103–114, 2019.

[181] S. Rich, H. M. Chameh, M. Rafiee, K. Ferguson, F. K. Skinner, and T. A. Valiante. Inhibitory network bistability explains increased interneuronal activity prior to seizure onset. *Frontiers in Neural Circuits*, 13:81, 2020.

[182] J. Rinzel and G. B. Ermentrout. Analysis of neural excitability and oscillations. In C. Koch and I. Segev, editors, *Methods in Neuronal Modeling*. The MIT Press, Cambridge, 1989.

[183] R. Rosenbaum, J. Rubin, and B. Doiron. Short term synaptic depression imposes a frequency dependent filter on synaptic information transfer. *PLOS Computational Biology*, 8(6):e1002557, 2012.

[184] Z. Rotman, P. Deng, and V. A. Klyachko. Short-term plasticity optimizes synaptic information transmission. *Journal of Neuroscience*, 31(41):14800–14809, 2011.

[185] D. Salaj, A. Subramoney, C. Kraisnikovic, G. Bellec, R. Legenstein, and W. Maass. Spike frequency adaptation supports network computations on temporally dispersed information. *eLife*, 10, 2021.

[186] E. Salinas and T. Sejnowski. Correlated neuronal activity and the flow of neural information. *Nature Reviews Neuroscience*, 2:539–550, 2001.

[187] P. Sanz-Leon, S. A. Knock, A. Spiegler, and V. K. Jirsa. Mathematical framework for large-scale brain network modeling in the virtual brain. *NeuroImage (Orlando, Fla.)*, 111:385–430, 2015.

[188] V. Schmutz, W. Gerstner, and T. Schwalger. Mesoscopic population equations for spiking neural networks with synaptic short-term plasticity. *The Journal of Mathematical Neuroscience*, 10(1):5, 2020.

[189] A. Schüz and G. Palm. Density of neurons and synapses in the cerebral cortex of the mouse. *The Journal of Comparative Neurology*, 286(4):442–455, 1989.

[190] A. Seeholzer, M. Deger, and W. Gerstner. Stability of working memory in continuous attractor networks under the control of short-term plasticity. *PLOS Computational Biology*, 15(4):e1006928, 2019.

[191] M. Segneri, H. Bi, S. Olmi, and A. Torcini. Theta-nested gamma oscillations in next generation neural mass models. *Frontiers in Computational Neuroscience*, 14:47, 2020.

[192] L. P. Shayer and S. A. Campbell. Stability, bifurcation, and multistability in a system of two coupled neurons with multiple time delays. *SIAM Journal on Applied Mathematics*, 61(2):673–700, 2000.

[193] H. Smith. Distributed delay equations and the linear chain trick. In *An Introduction to Delay Differential Equations with Applications to the Life Sciences*, pages 119–130. Springer, New York, NY, 2011.

[194] W. R. Softky and C. Koch. The highly irregular firing of cortical cells is inconsistent with temporal integration of random EPSPs. *Journal of Neuroscience*, 13(1):334–350, 1993.

[195] E. Stone, H. Haario, and J. J. Lawrence. A kinetic model for the frequency dependence of cholinergic modulation at hippocampal GABAergic synapses. *Mathematical Biosciences*, 258:162–175, 2014.

[196] S. H. Strogatz and R. E Mirollo. Stability of incoherence in a population of coupled oscillators. *Journal of Statistical Physics*, 63(3):613–635, 1991.

[197] T. C. Südhof. Calcium control of neurotransmitter release. *Cold Spring Harbor Perspectives in Biology*, 4(1):a011353, 2012.

[198] H. Taher, D. Avitabile, and M. Desroches. Bursting in a next generation neural mass model with synaptic dynamics: a slow–fast approach. *Nonlinear Dynamics*, 108(4):4261–4285, 2022.

[199] H. Taher, A. Torcini, and S. Olmi. Exact neural mass model for synaptic-based working memory. *PLOS Computational Biology*, 16(12):e1008533, 2020.

[200] S. W. Tam and R. Zaczek. Linopirdine. a depolarization-activated releaser of transmitters for treatment of dementia. *Advances in Experimental Medicine and Biology*, 363:47–56, 1995.

[201] Takuma Tanaka. Low-dimensional dynamics of phase oscillators driven by cauchy noise. *Physical Review E*, 102:042220, 2020.

[202] K. Tateno, H. Hayashi, and S. Ishizuka. Complexity of spatiotemporal activity of a neural network model which depends on the degree of synchronization. *Neural Networks*, 11(6):985–1003, 1998.

[203] Ralf Tönjes and Arkady Pikovsky. Low-dimensional description for ensembles of identical phase oscillators subject to cauchy noise. *Physical Review E*, 102:052315, 2020.

[204] A. Treves. Mean-field analysis of neuronal spike dynamics. *Network: Computation in Neural Systems*, 4(3):259, 1993.

[205] M. Tsodyks, K. Pawelzik, and H. Markram. Neural networks with dynamic synapses. *Neural Computation*, 10(4):821–835, 1998.

[206] R. J. Valentino and R. J. Dingledine. Presynaptic inhibitory effects of acetylcholine in the hippocampus: A 40-year evolution of a serendipitous finding. *Journal of Neuroscience*, 41(21):4550–4555, 2021.

[207] C. van Vreeswijk and D. Hansel. Patterns of synchrony in neural networks with spike adaptation. *Neural Computation*, 13(5):959–992, 2001.

[208] B. B. Vladimirski, J. Tabak, and M. J. O'Donovan. Episodic activity in a heterogeneous excitatory network, from spiking neurons to mean field. *Journal of Computational Neuroscience*, 25:39–63, 2008.

[209] E. Vogel, A. McCollough, and M. Machizawa. Neural measures reveal individual differences in controlling access to working memory. *Nature*, 438:500–503, 2005.

[210] H. von Gersdorff, R. Schneggenburger, S. Weis, and E. Neher. Presynaptic depression at a calyx synapse: the small contribution of metabotropic glutamate receptors. *Journal of Neuroscience*, 17(21):8137–8146, 1997.

[211] X. J. Wang and G. Buzsáki. Gamma oscillation by synaptic inhibition in a hippocampal interneuronal network model. *Journal of Neuroscience*, 16(29):6402–6413, 1996.

[212] Y. Wang, H. Markram, P. H. Goodman, T. K. Berger, J. Ma, and P. S. Goldman-Rakic. Heterogeneity in the pyramidal network of the medial prefrontal cortex. *Nature Neuroscience*, 9(4):534–542, 2006.

[213] S. Watanabe and S. H. Strogatz. Integrability of a globally coupled oscillator array. *Physical Review Letters*, 70(16):2391, 1993.

[214] S. Watanabe and S. H. Strogatz. Constants of motion for superconducting josephson arrays. *Physica D: Nonlinear Phenomena*, 74(3-4):197–253, 1994.

[215] J. Wess. Muscarinic acetylcholine receptor knockout mice: novel phenotypes and clinical implications. *Annual Review of Pharmacology and Toxicology*, 44:423–450, 2004.

[216] M. J. West, L. Slomianka, and H. J. G. Gundersen. Unbiased stereological estimation of the total number of neurons in the subdivisions of the rat hippocampus using the optical fractionator. *The Anatomical Record*, 231(4):482–497, 1991.

[217] H. R. Wilson and J. D. Cowan. Excitatory and inhibitory interactions in localized populations of model neurons. *Biophysical Journal*, 12(1):1–24, 1972.

[218] H. R Wilson and J. D Cowan. A mathematical theory of the functional dynamics of cortical and thalamic nervous tissue. *Biological Cybernetics*, 13(2):55–80, 1973.

[219] H. R. Wilson and J. D. Cowan. Evolution of the Wilson–Cowan equations. *Biological Cybernetics*, 115(6):643–653, 2021.

[220] J. Wu. *Introduction to Neural Dynamics and Signal Transmission Delay*, volume 6. Walter de Gruyter, 2011.

[221] J. Wu, S. A. Campbell, and J. Bélair. Time-delayed neural networks: Stability and oscillations. In *Encyclopedia of Computational Neuroscience*, pages 3434–3440. Springer, 2022.

[222] L. G. Wu and W. J. Betz. Kinetics of synaptic depression and vesicle recycling after tetanic stimulation of frog motor nerve terminals. *Biophysical Journal*, 74(6):3003–3009, 1998.

[223] W. M. Yamada and R. S. Zucker. Time course of transmitter release calculated from simulations of a calcium diffusion model. *Biophysical Journal*, 61(3):671–682, 1992.

[224] L. H. Zetterberg, L. Kristiansson, and K. Mossberg. Performance of a model for a local neuron population. *Biological Cybernetics*, 31(1):15–26, 1978.

[225] R. S. Zucker and W. G. Regehr. Short-term synaptic plasticity. *Annual Review of Physiology*, 64(1):355–405, 2002.